



# Towards a new dimension in analytical TEM: EELS, Tomography and the Spectrum Volume

Lluís Yedra Cardona

**ADVERTIMENT.** La consulta d'aquesta tesi queda condicionada a l'acceptació de les següents condicions d'ús: La difusió d'aquesta tesi per mitjà del servei TDX ([www.tdx.cat](http://www.tdx.cat)) i a través del Dipòsit Digital de la UB ([diposit.ub.edu](http://diposit.ub.edu)) ha estat autoritzada pels titulars dels drets de propietat intel·lectual únicament per a usos privats emmarcats en activitats d'investigació i docència. No s'autoritza la seva reproducció amb finalitats de lucre ni la seva difusió i posada a disposició des d'un lloc aliè al servei TDX ni al Dipòsit Digital de la UB. No s'autoritza la presentació del seu contingut en una finestra o marc aliè a TDX o al Dipòsit Digital de la UB (framing). Aquesta reserva de drets afecta tant al resum de presentació de la tesi com als seus continguts. En la utilització o cita de parts de la tesi és obligat indicar el nom de la persona autora.

**ADVERTENCIA.** La consulta de esta tesis queda condicionada a la aceptación de las siguientes condiciones de uso: La difusión de esta tesis por medio del servicio TDR ([www.tdx.cat](http://www.tdx.cat)) y a través del Repositorio Digital de la UB ([diposit.ub.edu](http://diposit.ub.edu)) ha sido autorizada por los titulares de los derechos de propiedad intelectual únicamente para usos privados enmarcados en actividades de investigación y docencia. No se autoriza su reproducción con finalidades de lucro ni su difusión y puesta a disposición desde un sitio ajeno al servicio TDR o al Repositorio Digital de la UB. No se autoriza la presentación de su contenido en una ventana o marco ajeno a TDR o al Repositorio Digital de la UB (framing). Esta reserva de derechos afecta tanto al resumen de presentación de la tesis como a sus contenidos. En la utilización o cita de partes de la tesis es obligado indicar el nombre de la persona autora.

**WARNING.** On having consulted this thesis you're accepting the following use conditions: Spreading this thesis by the TDX ([www.tdx.cat](http://www.tdx.cat)) service and by the UB Digital Repository ([diposit.ub.edu](http://diposit.ub.edu)) has been authorized by the titular of the intellectual property rights only for private uses placed in investigation and teaching activities. Reproduction with lucrative aims is not authorized nor its spreading and availability from a site foreign to the TDX service or to the UB Digital Repository. Introducing its content in a window or frame foreign to the TDX service or to the UB Digital Repository is not authorized (framing). Those rights affect to the presentation summary of the thesis as well as to its contents. In the using or citation of parts of the thesis it's obliged to indicate the name of the author.

# **Towards a new dimension in analytical TEM: EELS, Tomography and the Spectrum Volume**

Tesi que presenta **Lluís Yedra Cardona** per a optar al títol de Doctor per la Universitat de Barcelona en el marc del Programa de Doctorat en Nanociències

Directores de la Tesi:

**Dr. Francesca Peiró Martínez**

**Dr. Sònia Estradé Albiol**

LENS, MIND- IN<sup>2</sup>UB, Departament d'Electrònica, Universitat de Barcelona



---

**B** Universitat de Barcelona



**Dr. Francesca Peiró Martínez**, Professor titular del Departament d'Electrònica i  
**Dr. Sònia Estradé Albiol**, Professor Associat del Departament d'Electrònica

certifiquen que la tesi "**Towards a new dimension in analytical TEM: EELS, Tomography and the Spectrum Volume**", que presenta **Lluís Yedra Cardona** per optar al títol de Doctor de la Universitat de Barcelona en el marc del Programa de Doctorat en Nanociències, ha estat realitzada sota la seva direcció.

A Barcelona, el 23 d'octubre del 2013.

Les directores:

Dr. Francesca Peiró Martínez

Dr. Sònia Estradé Albiol



**Tribunal:**

President:

**Dr. Raúl Arenal de la Concha**

Instituto de Nanociencia de Aragón (INA)

Secretari:

**Dr. Joaquim Portillo Serra**Centres Científics i Tecnològics de la Universitat de  
Barcelona & Nanomegas SL

Vocal

**Dr. Zineb Saghi**Department of Materials Science and Metallurgy,  
University of Cambridge

Membres suplents

**Dr. Marta Estrader Bofarull**, Departament de Química Inorgànica, Universitat de  
Barcelona**Dr. Eva Pellicer Vila**, Departament de Física, Universitat Autònoma de Barcelona**Dr. Daniel Prades García**, Departament d'Electrònica, Universitat de Barcelona



People who look for the first time through a microscope say now I see this and then I see that and even a skilled observer can be fooled. On these observations I have spent more time than many will believe, but I have done them with joy.

**Antonie van Leeuwenhoek**, 1701

When you employ the microscope, shake off all prejudice, nor harbor any favorite opinions; for, if you do, 'tis not unlikely fancy will betray you into error, and make you see what you wish to see.

**Henry Baker** in *The Microscope Made Easy*, 1742

One can be fooled by appearances, which happens only too frequently, whether one uses a microscope or not.

**Voltaire** in *Micromégas*, 1752



## Acknowledgements

When I started working on this specific subject, it seemed that the end would never come; it was apparently so far away. We knew completing the task was going to be difficult, and it came as unexpectedly as the Spanish Inquisition, to say the least. Yet, it was possible, indeed, thanks to people ready to give advice and lend a hand. Recalling their efforts, I proceed here to tell them “thank you”. The whole process of the thesis to this point has been a long, windy, road going up and down, let us focus on the ups.

I would like to thank the staff at Scientific and Technological Centers of the University of Barcelona (CCiTUB), who have also become my colleagues for more than two years now, for their help in the understanding and operation of the electron microscopes; especially Dr. Quim Portillo, Joan Mendoza and Fèlix Mata. I would also like to thank the management of the CCiTUB, Dr. José Ramón Seoane and Eva Jané, for their trust and support.

I also want to thank Dr. Alfonso Ibarra and Dr. César Magén from the INA Zaragoza for their help in the microscope. From the INA Zaragoza I would also like to thank Dr. Raúl Arenal, for the long hours spent in EELS-SI tomography acquisitions and result discussions. His views have been of great help.

I would like to express my deepest gratitude to the HRTEM group in the Department of Materials Science and Metallurgy of the University of Cambridge for their hospitality, advice and for taking me to the pub whenever it was needed. My gratitude is for all of them and especially for Prof. Paul A. Midgley for accepting me to stay in his group for 10 weeks and for the advice, and for Dr. Zineb Saghi for teaching me a great deal about electron tomography, for her tireless aid in tomogram acquisition and reconstruction, and for lending me some much needed pans and cutlery. Thanks to Dr. Caterina Ducati, Dr. Jonathan Barnard and Dr. Giorgio Divitini for their help in the

microscope; and to Dr. Olivia Nicoletti, Dr. Alex Eggeman, Dr. Martin Ritter, Dr. Florian Hue and the rest of the group for scientific and non-scientific support.

I would like to convey my gratitude to Appfive Inc. in Tempe, Arizona, for allowing me to use their microscope for (mostly unsuccessful) experiments, for the borrowed (and highly necessary) bike and for their warm welcome; noting that warm acquired a whole new meaning for me in the Arizona summer. I would like to thank Dr. J.K. Weiss, Doug Cosart, Dr. Steve Kim, Dr. Bruno Janssens, Dr. Raman Narayan, Erik Herbrandson and Kenny Kohlmeier for all their guidance. Special thanks to Dr Amith Darbal, who painstakingly helped me in the entire microscope work. Also thanks to the wife and daughter of Dr. Weiss, who took me and Amith to a wonderful weekend journey to Sedona and the Grand Canyon. I would also like to thank Dr. Stavros Nicolopoulos, from Nanomegas SL for his support.

I would like to thank Dr. Sara Bals, Dr. Bart Goris and Dr. Hamed Heidari from the Electron Microscopy for Materials Science (EMAT), University of Antwerp for the help in full tilt tomography, needle sample preparation in the FIB and tomography discussions.

I would also like to thank Dr. Francisco de la Peña, now at the HRTEM group in Cambridge and Dr. Michael Walls from the STEM group at the Laboratoire de Physique des Solides, in Paris, for teaching me how to use EELS Lab, now Hyperspy.

This work would not have been possible without our collaborators who provided the samples used during this thesis, and it would not have been the same without the discussions following their characterization. I would like to thank Dr. Carlos Martínez-Boubeta, Dr. Daniel Prades and collaborators, from the Electronics Department of the University of Barcelona (UB); Dr. Elena Xuriguera from the Electronics Department and the Department of Materials Science and Metallurgical Engineering, UB ; Dr. Marta Estrader, from the Inorganic Chemistry Department, UB; Prof. Jordi Sort, Dr. Maria Dolors Baró, Dr. Eva Pellicer and Dr. Moisès Cabo from the Physics Department of the Universitat Autònoma de Barcelona; Prof. Josep Nogués, from the Institut Català de Nanociència i Nanotecnologia (ICN<sup>2</sup>); Dr. Alberto López-Ortega, now at the Chemistry department of the Università degli Studi di Firenze; Prof. Josep Fontcuberta, Dr. Florencio Sánchez and Dr. Nico Dix from the Institut de Ciència dels Materials de Barcelona (ICMAB); Dr. Andreu Cabot, Dr. Albert Tarancón and Laura Almar from the Institut de Recerca en Energia de Catalunya (IREC). Also thanks to Dr. María Varela, from Oak Ridge National Laboratory, Tennessee, and the Applied Physics III

Department of the Complutense University, for the data provided and the thoughtful comments.

I want to express my gratitude to all my colleagues in the MIND (Micro i nanoscòpies per a dispositius electronics) group of the electronics department for all the shared colloquiums. Special thanks to Dr. Albert Cirera for sharing his computer cluster for tomographic reconstructions.

I would like to express my deepest gratitude to my colleagues in the LENS group. I am thankful in equal parts for scientific work and procrastination. It can get long, but they deserve it. Let us start with Jose Manuel Rebled, my only fellow when it all got started. I would like to thank him for teaching me all he knew about tomography (and he knew a great deal), for the coffees and for the fruitful discussions; special mention to our discussion in Antwerp, where the EELS-SV (which I love to call the Data Tesseract) found its way to life. Alberto Eljarrat also deserves a special mention. He has been involved in all the multivariate analysis, so sorry for all the pressure. Thanks to Lluís López-Conesa, who made me to change my signature in informal emails from Lluís to Lluís Yedra to avoid confusion. I am not thankful for that, but all his knowledge in imaging (and the shared Gatan prize) made up for that. To Gemma Martín, for all the shared moments in the microscope. To Alícia Ruiz, for the help with administrative work. To my former colleagues Dr. Marie H el ene Chambrier, Dr. Yuanbin Qin and Dr. S onia Conesa, for all I have learnt from them, and to the newest colleagues, Pau Torruella and Laura G omez.

Special thanks to my two advisors. To Dr. S onia Estrad e for the patience, efforts and will put into teaching me the many details of experimental electron microscopy; for the long discussions about theory (for the many things I learnt in them), for always lending a hand and for the continuous feedback. To Dr. Francesca Peir o for the opportunity given to start collaborating in the LENS group which led to this thesis, for the time spent in the microscope, but mostly for the tons of corrections and comments that upgraded my work. To both of them, I am thankful for the years working together, for the science and the conversations spiced up with pop culture references. It has been a great experience.

And last but not least, I would like to thank my family and partner, for their support and understanding.



## Foreword

Transmission electron microscopy (TEM) offers several tools to characterize materials at the nanoscale. From imaging to spectroscopy, TEM allows us to extract advanced structural and chemical information with resolutions below the Å in space and the 100 meV in spectroscopic information. However, all this information is always a two-dimensional (2D) projection of the actual three-dimensional (3D) structure of the samples. To overcome this limitation, electron tomography was developed, based on the already established X-ray computer tomography.

Tomography is related to obtaining higher dimensional information from lower dimensional data. This thesis is concentrated in the recovery of the information from projections of the object in a lower dimension, namely the reconstruction of 3D volumes from 2D projections.

Electron energy loss spectroscopy (EELS) is one of those techniques previously bonded to the 2D space of projections. Inspired by the many applications of electron tomography, this thesis develops the 3D reconstruction of chemical information of the EEL spectrum. We will show how to extract information suitable for tomography from EEL spectra. Conversely, we will also propose how to use tomography to expand EELS and obtain the three dimensional distribution of energy loss. Electron tomography will be used to further the possibilities of EELS as much as EELS will offer us new ways to expand the application of electron tomography.



# *Index*

<b>1. Introduction.....</b>	<b>21</b>
<b>1.1. Tomography.....</b>	<b>25</b>
1.1.1. Basics of tomography in the transmission electron microscope.....	26
1.1.1.a. Signals for tomography: the projection requirement.....	27
1.1.1.b. Resolution and missing wedge.....	28
1.1.1.c. Reconstruction approaches.....	29
1.1.2. Structural electron tomography: state of the art.....	31
<b>1.2. Electron energy loss in the TEM .....</b>	<b>34</b>
1.2.1. The EEL spectrum.....	35
1.2.2. Core loss edge nomenclature.....	38
1.2.3. The data cube.....	39
1.2.4. EELS compared to EDS.....	40
<b>1.3. Analytical electron tomography.....</b>	<b>42</b>
1.3.1.State of the art.....	43
1.3.1.a. EDS tomography.....	43
1.3.1.b. EFTEM tomography.....	43
1.3.1.c. EELS-SI tomography.....	45
<b>1.4. Actual instrumentation.....</b>	<b>47</b>
<b>1.5. Aim of this work.....</b>	<b>48</b>
<b>1.6. References.....</b>	<b>50</b>

<b>2. Tomography.....</b>	<b>55</b>
<b>2.1. Scope of the chapter.....</b>	<b>59</b>
<b>2.2. Reconstruction methods.....</b>	<b>60</b>
2.2.1. Fourier Methods.....	60
2.2.2. Weighted Back-projection Methods.....	63
2.2.2.a. <i>The simple Back-projection.....</i>	63
2.2.2.b. <i>Weighting function.....</i>	66
2.2.2.c. <i>The weighting function for single axis and equal tilt increments.....</i>	68
2.2.3. Iterative methods.....	71
2.2.3.a. <i>The Algebraic Reconstruction Technique.....</i>	72
2.2.3.b. <i>The Simultaneous Iterative Reconstruction Technique.....</i>	74
<b>2.3. Methodology.....</b>	<b>75</b>
2.3.1. Materials: iron oxide nanocubes for in-vivo applications.....	75
2.3.2. Data acquisition.....	76
2.3.3. Data treatment.....	78
2.3.3.a. <i>Image alignment and tilt axis identification.....</i>	79
2.3.3.b. <i>Reconstruction.....</i>	81
2.3.3.c. <i>Visualization.....</i>	82
<b>2.4. Faceting of Cu<sub>2</sub>O nanoparticles: an application of HAADF tomography.....</b>	<b>85</b>
2.4.1. Experimental details.....	86
2.4.2. Results and discussion.....	87
2.4.3. Conclusions.....	91
<b>2.5. References.....</b>	<b>93</b>

<b>3. Electron Energy Loss Spectroscopy.....</b>	<b>97</b>
<b>3.1. Scope of the chapter.....</b>	<b>101</b>
<b>3.2. Core-loss EELS. Physics of electron scattering.....</b>	<b>102</b>
3.2.1. Elastic scattering.....	102
3.2.2. Lenz formalism of inelastic scattering.....	104
3.2.3. Bethe Theory.....	106
3.2.4. Generalized Oscillator Strength calculations.....	110
3.2.5. Single, Plural and Multiple Scattering. Poisson's law. Effects of plural scattering.....	111
3.2.6. ELNES.....	113
<b>3.3. Quantification of the core-loss edges.....</b>	<b>116</b>
3.3.1. Background to core loss edges.....	120
<b>3.4. Precession assisted EELS.....</b>	<b>123</b>
3.4.1. Electron precession and EELS.....	123
3.4.2. Considered EELS edges and methods.....	126
3.4.3. Signal enhancement as a function of precession angle.....	126
3.4.4. Conclusions.....	129
<b>3.5. Oxide Wizard.....</b>	<b>130</b>
3.5.1. Procedures to determine oxidation states from the ELNES.....	131
3.5.2. Steps of the analysis.....	134
3.5.3. Calibration test on $Mn_xO_y$ oxides.....	141
3.5.4. Application: Mn oxidation state determination in core-shell nanoparticles.....	143
3.5.5. Conclusions.....	147
<b>3.6. References.....</b>	<b>148</b>

<b>4. EELS Tomography.....</b>	<b>153</b>
<b>4.1. Scope of the chapter.....</b>	<b>157</b>
<b>4.2. Preliminary characterization: HAADF tomography and EELS.....</b>	<b>158</b>
4.2.1. Materials: Mesoporous $\text{Fe}_x\text{Co}_{(3-x)}\text{O}_4@\text{Co}_3\text{O}_4$ .....	158
4.2.2. HAADF STEM tomography of mesoporous.....	160
4.2.3. EEL Spectroscopy across pore walls.....	165
4.2.4. Discussion of HAADF STEM tomography and EELS as independent tools.....	168
<b>4.3. EELS Spectrum Image tomography of mesoporous materials.....</b>	<b>169</b>
4.3.1. Acquisition of the tomographic SI series.....	170
4.3.2. Noise reduction by PCA.....	171
4.3.2.a. <i>Principal Component Analysis (PCA) theory</i> .....	171
4.3.2.b. <i>Noise reduction: experimental and results</i> .....	178
4.3.3. Edge intensity maps.....	181
4.3.4. Identification of the independent components.....	184
4.3.4.a. <i>Blind Source Separation /</i> <i>Independent Component Analysis (ICA) theory</i> .....	184
4.3.4.b. <i>Results: independent components</i> .....	185
4.3.5. EELS-SI tomography reconstruction.....	188
4.3.6. Conclusions.....	190
<b>4.4. A step beyond: enhanced resolution EELS-tomography     of the mesoporous material.....</b>	<b>194</b>
4.4.1. Spectra acquisition and data treatment.....	194
4.4.2. EELS tomography resolving porous structure.....	196
4.4.3. Conclusions.....	202
<b>4.5. Conclusions.....</b>	<b>203</b>
<b>4.6. References.....</b>	<b>205</b>

<b>5. EELS Spectrum Volumes.....</b>	<b>211</b>
5.1. Antecedents of the spectrum volume.....	215
5.2. Materials: multiferroic nanocomposites.....	217
5.3. Sample preparation and data acquisition.....	219
5.4. EELS-SI tomography reconstruction from edge intensity maps.....	222
5.5. EELS-SI tomography from independent components.....	226
5.5.1. Bayesian Linear Unmixing.....	227
5.5.2. 3D reconstruction from BSS components.....	228
5.6. Recovering the Spectrum Volume.....	230
5.7. Conclusions.....	233
5.8. References.....	234
<b>6. Conclusions.....</b>	<b>237</b>
<b>Appendixes.....</b>	<b>243</b>
A. Experimental.....	247
A.1. Nanoparticles.....	247
A.2. Focused Ion Beam .....	249
B. Resum en català.....	253
C. Scientific curriculum.....	257



# ***1. Introduction***



<b>1.1. Tomography .....</b>	<b>25</b>
1.1.1. Basics of tomography in the transmission electron microscope .....	26
1.1.1.a. Signals for tomography: the projection requirement.....	27
1.1.1.b. <i>Resolution and missing wedge</i> .....	28
1.1.1.c. <i>Reconstruction approaches</i> .....	29
1.1.2. Structural electron tomography: state of the art .....	31
<b>1.2. Electron energy loss in the TEM.....</b>	<b>34</b>
1.2.1. The EEL spectrum.....	35
1.2.2. Core loss edge nomenclature .....	38
1.2.3. The data cube .....	39
1.2.4. EELS compared to EDS .....	40
<b>1.3. Analytical electron tomography .....</b>	<b>42</b>
1.3.1. State of the art.....	43
1.3.1.a. <i>EDS tomography</i> .....	43
1.3.1.b. <i>EFTEM tomography</i> .....	43
1.3.1.c. <i>EELS-SI tomography</i> .....	45
<b>1.4. Actual instrumentation.....</b>	<b>47</b>
<b>1.5. Aim of this work.....</b>	<b>48</b>
<b>1.6. References .....</b>	<b>50</b>



## 1.1. Tomography

The reconstruction of 3D volumes from 2D projections stems from mathematical principles described by Radon in 1917<sup>1</sup>. In two dimensions, Radon transform is an integral transform consisting in the integral of a function over straight lines. In three dimensions, integrals are taken over planes.

In the space of straight lines  $L$  in  $\mathbb{R}^2$ , the transform of a function  $f(x)=f(x,y)$  can be written as

$$Rf(L) = \int_L f(x)|dx| . \quad [1.1]$$

If the straight line  $L$  is parameterized,

$$(x(t), y(t)) = ((t \sin \alpha + s \cos \alpha), (-t \cos \alpha + s \sin \alpha)) , \quad [1.2]$$

then the Radon transform can be expressed as

$$Rf(L) = \int_{-\infty}^{\infty} f(x(t), y(t))dt = \int_{-\infty}^{\infty} f((t \sin \alpha + s \cos \alpha), (-t \cos \alpha + s \sin \alpha))dt , \quad [1.3]$$

where  $s$  is the distance to  $L$  from the origin and  $\alpha$  is related to the angle between  $L$  and  $y$  axis, as shown in Figure 1.1. For a high enough number of projections, inverse Radon transform is theoretically capable of reconstructing the object in real space. However, due to the lack of computational tools, these calculi could not be applied at that time.

It was not until 1956 that Bracewell<sup>2</sup> applied Radon principles to a practical problem, using them to reconstruct two-dimensional maps of microwave emission from the sun from one-dimensional data obtained from a microwave telescope. This opened

the door to obtaining data of higher dimensions from data of lower dimensions in many fields of science.

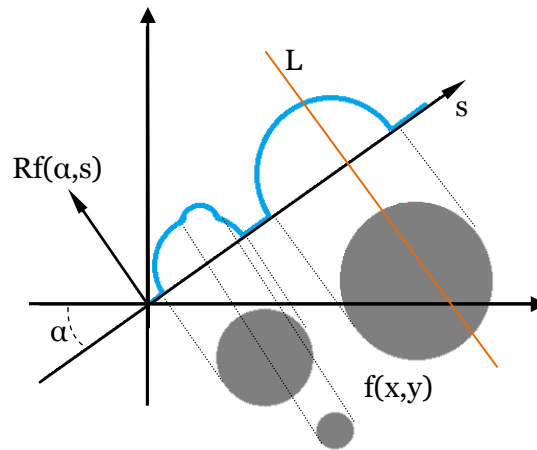


**Figure 1.1:** Plot of the Radon transform ( $Rf(\alpha, s)$ ) for a given  $\alpha$  of a body with a property  $f(x, y)$ . It can be described as the integration of  $f(x, y)$  along all lines  $L$  with normal angle  $\alpha$  and distance  $s$  to the origin.

The first application to x-rays appeared in 1963, when Cormack<sup>3</sup> applied the same principles to reconstruct a wood and aluminum model. Five years later, the first macromolecule studies using bright field (BF) in the TEM appeared<sup>4, 5</sup>.

### 1.1.1. Basics of tomography in the transmission electron microscope

For the first applications of electron tomography, used for the reconstruction of biological macromolecules<sup>4, 5</sup>, instead of using the Radon space, took advantage of the relationship between real and Fourier spaces, namely the central section theorem. This theorem states that the projection of an object at a given angle is a central section through the Fourier transform of the object. If a series of projections at different tilt

angles is obtained, every projection is equivalent to a part of the Fourier transform of the object. Tomographic reconstruction is possible through inverse Fourier transform of the superposition of the Fourier transforms of the projections (see Figure 1.2 (a)). This technique is known as “direct Fourier reconstruction”. Understanding this technique allows for discussing electron tomography in the TEM from the point of view of the signals used, the resolution of the technique and the alternative reconstruction approaches.

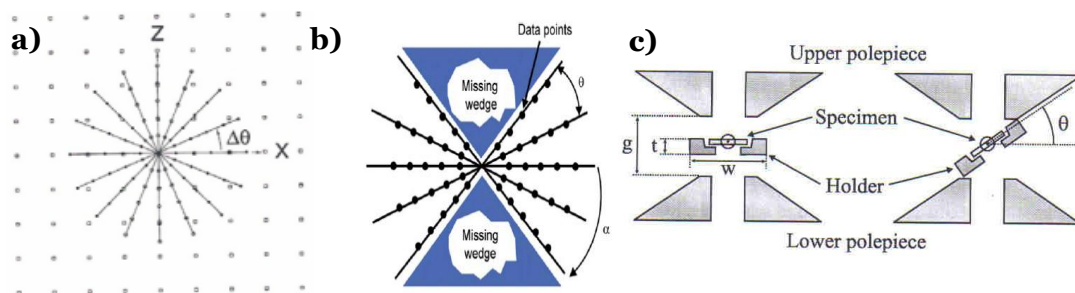


**Figure 1.2:** **a)** Sampling of the Fourier space through a series of images at regular angles. It can be observed that low frequencies are better sampled than higher frequencies. **b)** Missing wedge in Fourier space due to tilt angle limitations, as shown in **c)**.

#### 1.1.1.a. Signals for tomography: the projection requirement

Electron tomography cannot be applied to any kind of image obtained in the microscope. The signal must fulfill the projection requirement<sup>6</sup>. For a successful reconstruction, the used images must have a contrast that changes monotonically with the properties of the sample, which discards any image with coherent contributions.

Several signals have been used which fulfill the projection requirement. While in biological or polymer samples, bright field TEM has been the most used technique, in crystalline samples, high angle annular dark field has been the preferred approach. See the state of the art in section 1.1.2 for more details.

Alternatively Precession Assisted Electron Tomography (PAET)<sup>7</sup> has been recently proven to overcome the spurious contrast changes in crystalline samples from Fresnel and diffraction contrast in BF mode.

Spectroscopic signals can also be considered, as it will be shown later in this chapter.

### 1.1.1.b. Resolution and missing wedge

Spatial resolution of the reconstruction for a single tilt axis, which is the most implemented method, is anisotropic. Parallel to the tilt axis, resolution  $d_x$  is equal to the resolution of the projections, if the series has been perfectly aligned. In perpendicular directions, resolution is controlled by the number of acquired projections ( $N$ ) and the diameter ( $D$ ) of the volume to be reconstructed, following the equation  $d_y = d_z = (\pi D)/N$ , assuming a tilt angle of  $\pm 90^\circ$ .

When working in the TEM, the tilting angle is limited by the space between the polar piece of the objective lenses and the finite thickness of the sample holder (see Figure 1.2 (c)), causing a missing angle, the so called missing wedge (Figure 1.2 (b)). The missing wedge in the data leads to a degradation of the resolution,  $d_z$ , along the optical axis, by an elongation factor  $e_{yz}$  so that  $d_y \cdot e_{yz} = d_z$ . This is related to the missing wedge angle  $\alpha$  by  $e_{yz} = \sqrt{(\alpha + \sin \alpha \cos \alpha)/(\alpha - \sin \alpha \cos \alpha)}$ .

In order to deal with the missing wedge, other techniques have been proposed. First, the acquisition of two tilt series with perpendicular axes, transforming the missing wedge into a missing pyramid<sup>8</sup>. Thinking in Fourier space, not only is the missing wedge greatly reduced, but this space is better sampled. However, there is always a direction in which the results suffer from degradation. Other drawbacks of the technique is the need for a special holder able to turn the sample  $90^\circ$  in plane, as turning the sample ex-situ to the correct angle and locating the region of interest afterwards is extremely difficult and unreliable. This technique has mainly been applied to nanoparticle samples. A second way of dealing with the missing wedge is the acquisition of full tilt series. In this case, the technique is not applied to particles supported on a film, as the grid would always prevent the full tilting, but to nanoneedle shaped samples<sup>9,10</sup>. These kinds of samples are obtained from bulk or nanostructured materials in the form of layers supported on substrates by using focused ion beam (FIB) preparation. The microscopic sample is milled in the form of a round pillar and thinned at the tip to leave the thinnest possible sample area. These narrow samples, held by their base in special holders, can be then fully rotated, as no shadow from the

holder or the grid is encountered at any tilt angle. The main drawback of the technique is that it cannot be applied to nanoparticle samples, as already mentioned.

#### *1.1.1.c. Reconstruction approaches*

Reconstruction in Fourier space has two main drawbacks. First, sampling is carried out at discrete angles, leaving regular spaces (see Figure 1.2). Inverse Fourier transform requires a continuous function; hence there is a need to interpolate in order to fill the gaps, which greatly affects the quality of the reconstruction. Second, sampling is greater at the central part when compared to the peripheral part of the Fourier space (see Figure 1.2 (a)). Last, it is necessary to note that direct Fourier reconstruction is difficult to implement and it requires great computing power.

To overcome their limitations, Radon and Fourier methods have been replaced by the back-projection method, which uses less computing power and can solve the problems of sampling inhomogeneities in Fourier space using filters. A simple weighting filter (radial linear function in Fourier space, going through zero at the origin and reaching its maximum at the border, plus a smoothing filter, which reduces high frequency noise) enhances the frequency distribution. This technique is known as filtered back-projection. This method consists in the inversion of the obtained images and their projection in real space at the angles in which they were recorded (as illustrated in Figure 1.3). With a sufficiently high number of projections at all experimentally possible angles, the object can be reconstructed. The smaller the tilt step and the larger the tilt range, the better the reconstruction<sup>11</sup>. However, the reconstruction is never perfect, due to the limited number of experimentally possible projections and the low signal-to-noise ratio.

In the seventies, iterative methods appeared. Among them, the most used are the Algebraic Reconstruction Techniques (ART)<sup>12</sup> and the Simultaneous Iterative Reconstruction Techniques (SIRT)<sup>13</sup>. SIRT, first used in materials science by Midgley and Weyland (reviewed in <sup>14</sup>), enhances the quality of tomograms by reprojecting the reconstructed volume as a new tilt series and finding the difference between the original and the new projection, which is characteristic of filtered back-projection. This difference is back-projected and subtracted from the reconstructed volume so that the

reconstruction gets more similar to the real volume. This method is implemented recursively until the best solution is found.

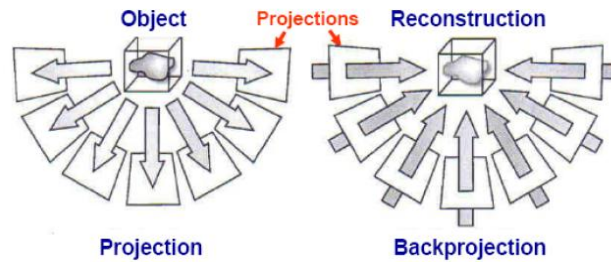


**Figure 1.3:** Reconstruction using back-projection. An object is sampled at a series of tilt angles and these images are back-projected through the angles at which they were acquired.

Some other algorithms have been proposed which effectively reduce the inconvenient missing wedge effects. First of all, the Discrete Algebraic Reconstruction Technique (DART)<sup>15</sup> eliminates the problem by imposing the fact that every material present in the sample should yield only one grey level in the reconstruction. Compared to ART or SIRT, it adds discretization steps in every iteration, finding the boundary pixels and the bulk pixels for every component and applying iterative algorithms only to the boundary ones, while the inner pixels remain fixed. This algorithm requires fewer projections than the previous ones. Even if the usefulness of this algorithm has been proved, it is not yet widely spread, as it requires the imposition of previous knowledge onto the reconstruction, biasing the results and leading to error if the nominal the number of present materials happens to be wrong. Therefore, new algorithms with less constraints, known as “partially discrete” are currently under development<sup>16</sup>.

More recent algorithms also explore the possibilities of avoiding the missing wedge artifacts and reduce the number of projections required for a reconstruction using Compressed Sensing (CS)<sup>17-20</sup>. CS, widely used in image compression in formats such as JPEG, is based on the assumption that the signal is sparse in some domain. The sparsity of the signal means that the number of non-zero values is significantly lower than the total number of elements. Another requisite is that the signal has to be incoherent with respect to the basis in which the signal is sparsely represented. Two conditions follow from this requisite: first, each data point must contain information about many points of the original source, and second, the artifacts from incomplete

measuring must not be sparse. In electron tomography, the projections contain integrated information about the sample, and the artifacts are spread through most of the reconstructed volume, the true signal being relatively more intense, so the two conditions are met. The domain in which the electron tomography signals are sparse can be as simple as the image domain or the gradient domain, usually referred to as 'total variation'. Then the reconstruction algorithms are based on finding the sparsest solution consistent with the data. The grey levels obtained in the solution from these algorithms can be used as an input to DART in order to objectively determine the number of components.

DART and CS have the advantage of reconstructing the volumes from a smaller number of projections, both reducing the acquisition time and the damage of the sample during acquisition. However, the algorithm used throughout this work will be SIRT, as it is still the most widely spread technique and the aim of the work is to discuss signals that can be used for tomography, regardless of the reconstruction technique.

### **1.1.2. Structural electron tomography: state of the art**

Electron tomography started as a structural technique, where the only interest was to recover the morphology of a nanostructure. In this section we will focus on the two main techniques used for structural tomographic reconstruction: bright field TEM and HAADF STEM.

Bright Field (BF) TEM images are acquired by illuminating the whole area to be imaged with a broad beam. Provided that the sample is sufficiently thin, weakly scattering, large unit cell crystalline or amorphous, so that contrast is a function of the thickness and atomic number, BF fulfills the projection requirement. Therefore, BF has been the signal of choice for biological samples. Several applications of BF tomography include cilia<sup>21</sup>, mitochondria<sup>22</sup>, Golgi apparatus<sup>23, 24</sup>, basal bodies<sup>25</sup> and primary cilium<sup>26</sup>. However, for most samples in physical sciences, BF contrast strongly depends on diffraction conditions of the crystals, leading to artifacts in the images. Thus, bright-field cannot fulfill that requirement for crystalline specimens. Moreover, if the

specimen is amorphous or weakly diffracting, Fresnel contrast can still impair 3D reconstruction<sup>27</sup>.

The HAADF detector (see Figure 1.4), as its name implies, is ring-shaped, so that the inner angle is greater than any of the relevant Bragg reflections. Therefore, the signal is related to the unscreened elastic and quasi-elastic nuclei-scattered electrons (Rutherford scattering). This incoherent signal is monotonically sensitive to the thickness of the sample and its Z number, approximately to  $Z^2$  at the angle limit. HAADF signal fulfils the projection requirement, except near a major zone axis, where channeling concentrates the beam onto atomic columns and thus increases HAADF signal. However it is only relevant at a small number of orientations and tends to be irrelevant on the tomographic reconstruction.

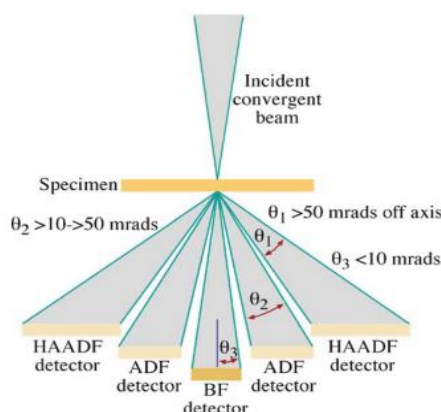


**Figure 1.4:** Scheme of the detectors that can be used in STEM. The inner angle of the HAADF detector is over 50 mrad off axis.

The first applications of electron tomography in the physical sciences followed what had been established for biological sciences, and used bright field images as projections. Spontak et al.<sup>28</sup> characterized in the eighties the order of styrene in styrene-butadiene-styrene block copolymers using bright field images. As the sample gave little contrast, the staining with osmium tetroxide was necessary. Applications in the nineties remained in the field of polymers<sup>29-31</sup>.

In the year 2000, the first application outside the polymers field appeared. Koster et al.<sup>32</sup> applied bright field images to reconstruct the three-dimensional mesoporous channel system of a metal/zeolite crystal (Ag/NaY). One year later, Midgley et al.<sup>33, 34</sup> proposed the use of HAADF STEM as a signal. In the two mentioned

publications, they applied this technique to Pt-Ru heterogeneous catalysts on MCM-41 mesoporous silica. As the silica and the metals have a high difference in effective Z number, HAADF yielded different intensities for both, and the position of the bimetallic particles with respect to the mesoporous network could be elucidated.

While bright field tomography is still used for materials science (mainly for polymers<sup>35-40</sup> and zeolites<sup>41, 42</sup>), HAADF STEM has become the most usual technique. It was applied by Midgley and Weyland to characterize magnetite nanoparticle chains inside magnetotactic bacteria<sup>14</sup>, that they found to be linked through {111} planes.

In 2005, Arslan et al.<sup>8</sup> used HAADF STEM tomography to extract the distribution of Sn quantum dots embedded in a Si matrix. A year later, Yates et al.<sup>43</sup> proposed a new model of the mesoporous structure MCM-48 again using HAADF tomography. Another application in the same year came from Inoke et al.<sup>44</sup>, who studied the deformation in Al-Ag alloys by characterizing the deformation of Ag-rich precipitates.

An interesting application of HAADF STEM tomography in heterogeneous catalysts was carried out by Ward et al.<sup>45</sup>. In this work, The reconstruction of a Grace Davison 634-type mesoporous silica supporting bimetallic nanoparticles allowed for analyzing the relationship between the nanoparticles positions within the support and the local curvature. Saddle shaped areas were preferred inside the sample, while cup shaped areas remained the preferential sites at the external surface.

More recent developments concerning electron tomography using HAADF STEM include the long sought atomically resolved reconstructions, recently achieved by van Aert et al.<sup>46</sup>. In this work, a silver nanocluster in an aluminum matrix is imaged in an aberration corrected microscope, with atomic resolution, in two different zone axes. As the HAADF signal is related to the quantity of atoms in each atomic column, this quantity can be extracted and compared in the two images to reconstruct the three dimensional distribution of the atoms.

Our group recently demonstrated<sup>7</sup> that beam precession reduced contrast artifacts due to diffraction and curvature in thin foils, reconstructing the morphology of Sn precipitates embedded in an Al matrix

Once some applications of structural tomography have been explained, it is necessary to introduce the other great field in which this thesis is involved, the spectroscopic signals containing chemical information: analytical TEM.

## 1.2. Electron energy loss in the TEM

Electron energy loss spectroscopy (EELS) deals with the interaction of highly energetic electrons with thin solid state materials inside the transmission electron microscope. Highly energetic here means in an energy range between 80 keV and 300 keV. A sample is considered thin when its thickness is well below the mean free path between scattering events of the electrons in the specimen, which usually means a thickness in the order of the tenths of nanometers. When accelerated electrons encounter matter, elastic and inelastic interactions are expected.

EELS is centered on inelastic interactions related to the change of energy of the incoming electrons. When interacting with the sample, the fast electrons can transfer part of their energy to the electrons of the sample in a specific amount, related to different excitations of the sample electrons. A magnetic prism at the end of the TEM column deflects the electrons according to their energy, which, coupled with a CCD, gives us the EEL spectrum (as shown in Figure 1.5), where the abscise axis corresponds to the amount of lost energy and the ordinate axis to the counts (i.e., the number of electrons having lost that amount of energy).

### 1.2.1. The EEL spectrum

The spectrum obtained in EELS can be arbitrarily divided in three regions according to the information they can provide: the zero-loss peak, the low-loss region and the core-loss region in increasing loss of energy of the incoming electrons.

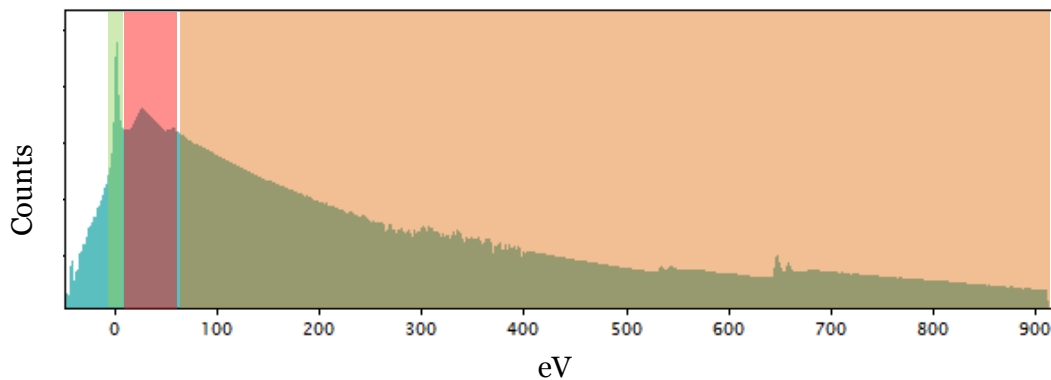


**Figure 1.5:** Electron energy loss spectrum in logarithmic intensity scale. The zero-loss peak is highlighted in green, the low-loss region is highlighted in red and the core-loss region is highlighted in orange.

- **The zero-loss peak**

Even if we deal with energy losses, implying the inelastic nature of the signal, elastic scattered electrons also appear in the EEL spectrum. Together with electrons which have suffered indiscernible inelastic scattering they form the zero-loss peak (ZLP). As its name indicates, electrons in the ZLP are the origin of the energy loss abscise in the spectrum.

This peak can be several orders of magnitude more intense than the rest of the spectrum features. It contains two main informations: the energy resolution of the spectrum and the thickness of the sample. The energy spread of the electrons not suffering from energy losses will determine the resolution of the experiment. Therefore, the FWHM of the zero loss peak is a good estimator of this resolution.

The thickness of the sample can be estimated thanks to the relationship between the zero loss peak and the rest of the spectrum using the following equation:

$$\frac{t}{\lambda} = \ln\left(\frac{I_{ZLP}}{I_{Tot}}\right) , \quad [1.4]$$

where  $I_{ZLP}$  is the integrated intensity of the ZLP and  $I_{Tot}$  is the integrated intensity over the entire spectrum.

- **Low-loss region**

The low loss region spans approximately from the ZLP to 50 eV energy loss. In this region, most of the features can be attributed to interactions with outer shell electrons, which means chemical sensitivity as well as electronic properties information. The bulk plasmon losses are remarkable and occur typically in the range of 5-25 eV. Other features at lower losses are the bandgap transitions in semiconductors and insulators, and radiation losses or surface plasmons in metallic-dielectric contacts.

The simplest way of analyzing the low loss spectrum is by comparison with reference low-loss spectra, the so called fingerprinting technique. The experimental spectra are fitted to a linear combination of well-known spectra in order to determine the composition. The main problem of this technique is that the details in low loss spectra are easily blurred out when electrons are scattered more than once.

Plasmons, which are collective loose bound electron oscillations, are preeminent in materials with free electron structures like Na, Al or Mg. Nevertheless, they do occur in all materials with more or less strength, even in insulators as polymers and biological tissue. This is so because the highly energetic electrons from the beam easily excite electrons to the conduction band.

Assuming that electrons in the conduction band are free, the energy lost by the generation of a plasmon of frequency  $\omega_p$  (resonant frequency for plasma oscillation) is given by the following expression:

$$E_p = \frac{h}{2\pi} \omega_p = \frac{h}{2\pi} \left(\frac{ne^2}{\epsilon_0 m}\right)^{\frac{1}{2}} , \quad [1.5]$$

Where  $h$  is Plank's constant,  $e$  and  $m$  are the electron charge and mass,  $\epsilon_0$  is the permittivity of free space and  $n$  is the free electron density. This shows the sensitivity of plasmon position to the bonding of the material. Thus, plasmon position can be used to

discriminate compounds in some cases. Moreover, the width of the plasmon can be related to the damping of the oscillations. Therefore, lattice defects, such as grain boundaries, will generate a broadening of the peak, as they introduce more desexcitation modes. Multiple scattering will produce multiple plasmon peaks at multiples of its energy, giving the plasmon a hump like structure. This can be also used to estimate the thickness of the sample.

In semiconductors or insulating materials, valence band excitations can be observed. Immediately after the ZLP and before the plasmon rise there is a region of forbidden transitions corresponding to the band gap. However, in order to determine the actual rise of the plasmon it is necessary to subtract the tail of the ZLP, as the plasmon is superimposed to it. Subtraction of the ZLP tail is usually achieved through a Gaussian or Lorentzian fit, by acquiring the ZLP in vacuum and then fourier-log deconvolving it from the low-loss or even by approximation of the tail by a power law function<sup>47-49</sup>.

The low loss region together with the ZLP is sometimes acquired to be used as an instrument function. Then, it can be deconvoluted from the high loss region in order to enhance its details. This is the well known Fourier-ratio deconvolution method.

- **Core-loss region.**

The high energy loss spectrum consists mainly in ionizations of electrons from the core states. These ionizations appear in the form of edges above 50 eV on a rapidly decreasing background. Only edges up to 2000 eV are commonly used, as the intensity decreases with energy and transitions at higher energies are easily observed in EDX.

Core states of atoms can be regarded as eigenvalues rather than energy bands. It is straightforward to identify core-loss edges, simply by comparing their energy positions with a reference table. These edges can be sometimes slightly shifted, which can also be used as information from the sample.

Once the specific edges of the sample have been identified, quantification procedures can determine the actual composition of the sample. Also, the shape of the edges, the energy loss near edge structure (ELNES), can be analyzed to extract more information about chemical bonding, such as valence state.

### 1.2.2. Core loss edge nomenclature

In EELS, the names of the edges correspond to the initial state of the sample electron involved in the scattering process. All possible ionizations are shown in Figure 1.6 (b), along with their quantum numbers and degeneracy. In Figure 1.6 (a) the dual edges such as  $L_{2,3}$  are indicated.

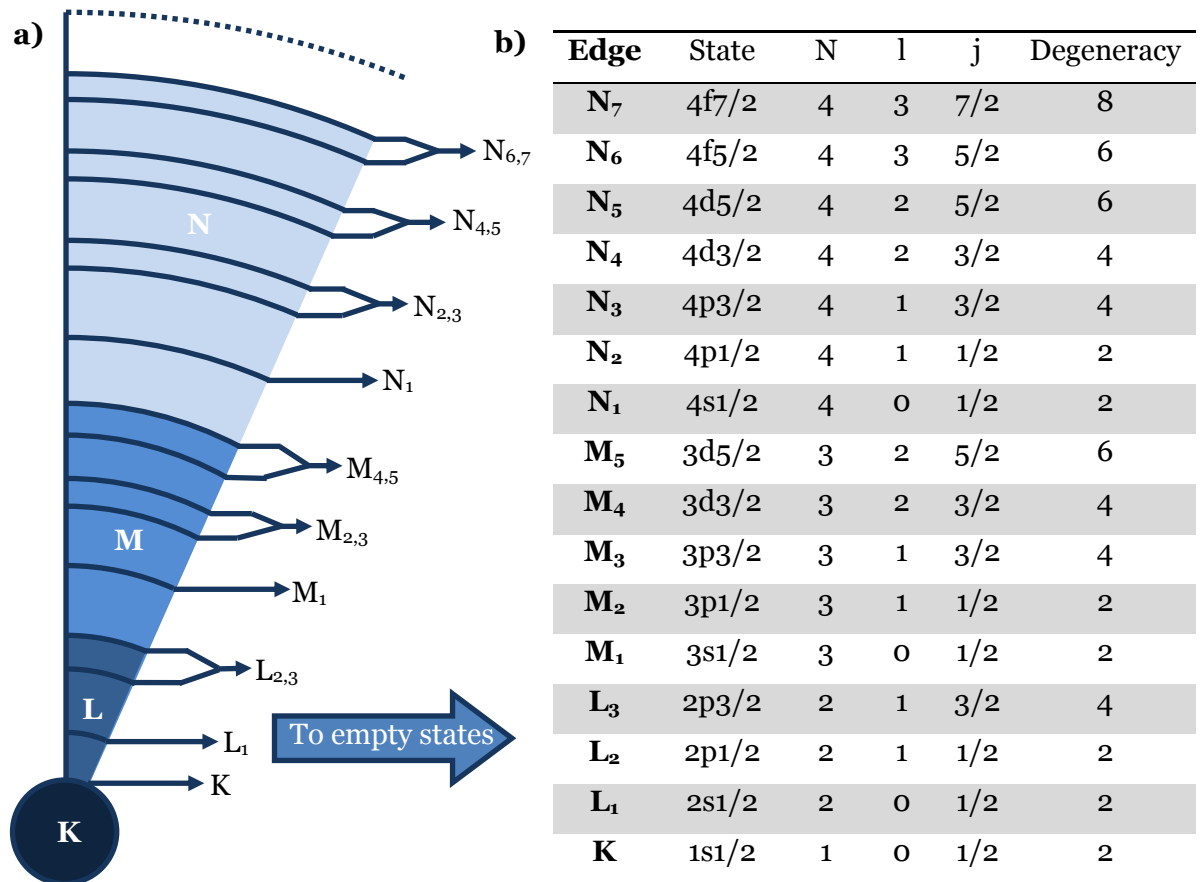


**Figure 1.6:** **a)** Naming of the core levels and transitions represented in atomic shells. **b)** Table presenting the corresponding state, quantum numbers and degeneracy of the initial state of the different EELS edges.

### 1.2.3. The data cube

EELS is a spectroscopic technique, which means that all data from EELS will have an energy axis. The most simple case is that of a single spectrum (Figure 1.7 (a)), where the data can be expressed as intensity as a function of energy loss ( $\Delta E$ ). Moreover, EELS information can be extracted from a very small volume of material (as small as an atomic column) when focusing the electron beam to a small spot. Taking advantage of the high spatial resolution of the signal, a whole set of spectra can be obtained from a line (Figure 1.7 (c)), yielding a so-called spectrum line, or an area (Figure 1.7 (d)) of the sample, which is known as spectrum imaging (SI). As a result, the data set does not only contain information about the energy, but also about the position, leading to a  $(\Delta E, x, y)$  matrix of information.. This is known as the EELS data cube. This dataset has been available since the seventies<sup>50</sup>, but , as it requires a great deal of computer memory, as well as a good synchronization of the control computer, the camera and the scanning and voltage offset modules, it has taken many years for it to become a routine technique. The acquisition of an EELS spectrum image is often coupled with HAADF imaging, which is used to measure and correct for the spatial drift during the acquisition.

Another approach to obtain the data cube is energy filtered TEM (EFTEM), where instead of acquiring  $\Delta E$  for a given  $(x, y)$  position on the sample, a whole image  $(x, y)$  is acquired at a given energy  $\Delta E$  (Figure 1.7 (b)). The resulting dataset has been called an image spectrum. It has the advantage that the spatial resolution is better. However, the energy resolution is limited by the width of the selecting slit (a slit placed after the magnetic prism used to select an energy range), and it is much more inefficient than spectrum imaging, since the electrons blocked by the slit do not contribute to the measure.

The data cube, also called spectrum image, has traditionally been the upper dimensional limit of the EELS datasets. In chapters 4 and 5, we will show how to extend the dataset to a spectrum volume, which contains three spatial dimensions and an energy dimension.

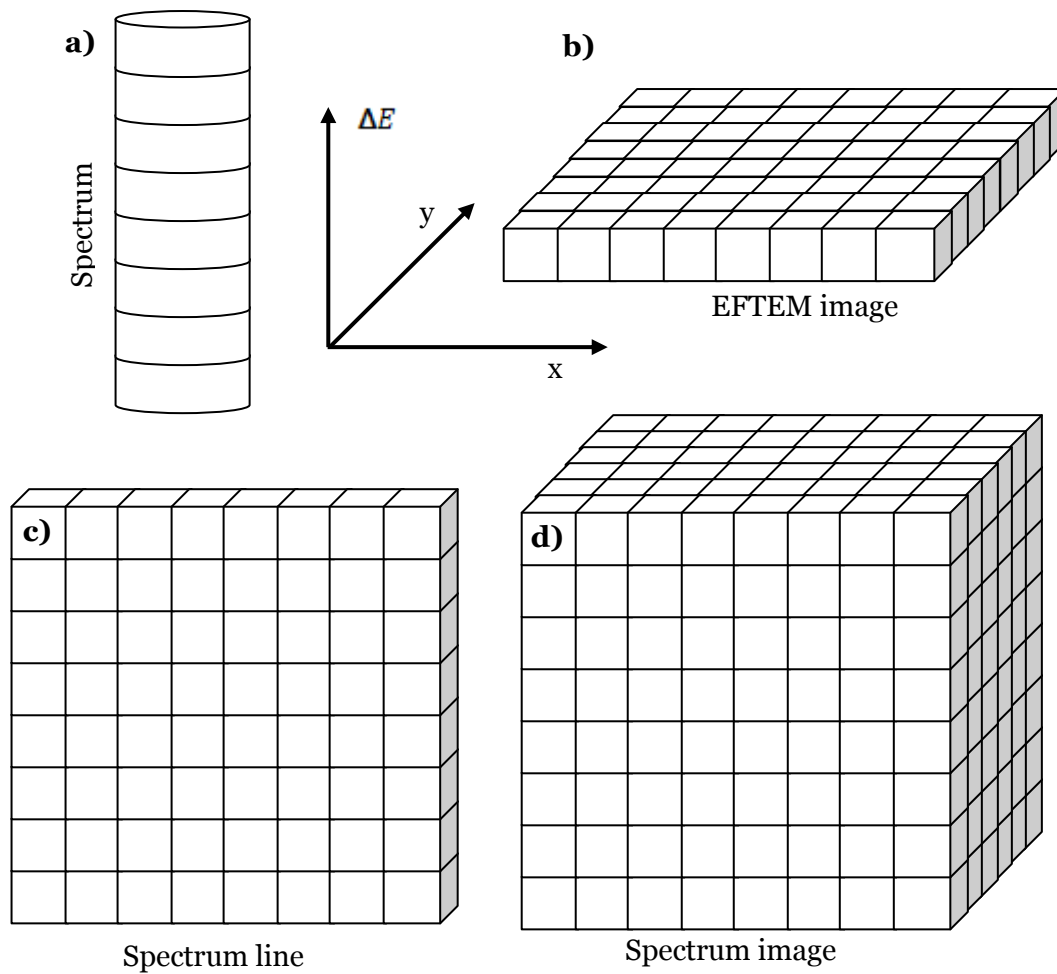


**Figure 1.7:** Schematic of the different ways to probe a datacube: **a)** single spectrum, **b)** EFTEM image, **c)** Spectrum line and **d)** spectrum image.

#### 1.2.4. EELS compared to EDS

The origin of the x-rays in the microscope are the beam electrons, which ionize an atom of the specimen by ejecting an inner-shell electron, leaving a hole in its shell behind. Then, a cascade of electron transitions is generated, each hole filled with an electron of a more weakly bound shell. This electron leaves a hole, so the process is repeated until, ultimately, an electron from the conduction band fills the last hole in the

valence band. Depending on the fluorescence yield, each transition results in either a characteristic x-ray or an Auger electron. The characteristic x-rays have a well-defined energy and a natural line width<sup>51</sup>. By working in STEM mode, it is possible to generate elemental maps by integrating the area under the characteristic peaks. The signal yielded by the sample is generally low, as the characteristic x-rays are emitted in any direction, and the detectors only cover a small solid angle.

Despite the poor energy resolution, EDS is often preferred to EELS because quantification requires less sophisticated methods. When it is installed and adjusted, the EDS silicon diode detector requires no further tuning from the operator. Acquisition of the X-ray spectra is straightforward and elemental-quantification software produces elemental ratios, also in a straightforward manner, but accuracy can rarely be considered better than 10%<sup>52</sup>. EDS becomes more problematic for low Z elements as for them the main deexcitation mechanism is Auger (the x-ray fluorescence yield is below 1% for  $Z < 10$ )<sup>52</sup> and the detection of low-energy x rays is considerably affected by absorption effects in the specimen and in the detector window. Moreover, EDS spectrometers have a small collection solid angle (at most a few tenths of a steradian), limited by the size of the detector crystal and the specimen–detector distance.

Using calibration specimens, it was showed as early as 1993 that EELS can detect smaller amounts of an element than EDS spectroscopy for elements below sodium ( $Z < 11$ ) based on K-shell excitation, or below iron ( $Z < 26$ ) using L excitation, given that cross section elemental ratios were experimentally obtained from controlled stoichiometry samples (as opposed to calculated from a physical model)<sup>53</sup>.

## **1.3. Analytical electron tomography**

The aforementioned analytical techniques (EDS, EFTEM and EELS) offer signals that can be used for tomographic reconstruction. Analytical electron tomography refers to the three-dimensional reconstruction of signals extracted using analytical techniques. Just as structural techniques often contain some information about the components of the samples, analytical techniques also reconstruct the morphology of the sample. Therefore analytical reconstruction has the great advantage of recovering the structural information along with chemical information about the species present in the sample.

There have been two ways of recovering chemical information in the TEM which can be used for tomographic reconstruction. Both of them are related to the interactions between the fast travelling electrons and the electrons of the sample. The most usual techniques deal with the analysis of the loss of energy of the beam electrons, while, recently, x-ray fluorescence has been also used for energy dispersive x-ray spectroscopy (EDS) tomography<sup>54-56</sup>.

### 1.3.1. State of the art

#### 1.3.1.a. EDS tomography

In EDS, the intensities of each characteristic peak are related to the absolute amount of each element<sup>54</sup>, so it can be considered a valid signal for tomographic reconstruction, as shown by Möbus et al.<sup>57</sup> in a sample containing Y, Zr, Al, Fe and O. The most extensive work up to date is the publication by A. Genç et al.<sup>55</sup>, in which, thanks to a high brightness electron gun and four large area silicon drift detectors (0.9 sr), it was possible to extract elemental maps for O, Ni and Mn in a  $\text{Li}_{1.2}\text{Ni}_{0.2}\text{Mn}_{0.6}\text{O}_2$  nanoparticle. The distribution of the elements was not visible in HAADF, but the elemental maps extracted at different tilt angles could be successfully reconstructed.

#### 1.3.1.b. EFTEM tomography

Energy Filtering in the Transmission Electron Microscope (EFTEM) can be used to restrict the images to some properties fulfilling the projection requirement. The first applications of EFTEM tomography concerned the elimination of all the energy loss contribution to the images (zero-loss filtering)<sup>58</sup>. Nowadays, it is used mainly to obtain energy-loss related signals from inelastically scattered electrons.

In order to obtain maps of a specific core loss, one can filter the image leaving only the energies under the edge. However, in this image, most of the intensity will correspond to the background, and then, it will not be specific for the edge. In order to correct for the background, two techniques are used: jump ratio maps, where one extra image is acquired prior to the edge and then subtracted, and three (or more) windows method, where a series of images prior to the edge are acquired to model the background with a potential law.

The first chemical sensitive elemental maps (three window method) and jump ratio maps as projections for tomographic reconstruction were obtained in 2001 by Möbus and Inkson<sup>59</sup>. In this paper, the possibility of reconstructing chemical distributions in 3D is reported for  $\text{FeAlY}_2\text{O}_3$  nanocomposite particles. The presence of residual elastic scattering in the images was acknowledged for the elemental maps, but it was averaged throughout the tilt series. Jump ratios were found to better suppress

the scattering contrast, but to hardly fulfill the projection requirement, whilst the quality of the reconstruction was worse.

Jump ratio has been favored in the biological sciences, as the electron dose is reduced. Leapman et al.<sup>60</sup> used it to extract ribosome maps in the nematode *Caenorhabditis elegans* thanks to the high content in phosphorous. Leapman and Aronova<sup>61</sup> also used phosphorous jump ratio maps to reveal the distribution of DNA in the cell nucleus, and iron jump ratio maps to describe the distribution of ferritin, the iron storing protein. An inaccuracy in the quantification of samples with varying thicknesses was detected, and Aronova et al.<sup>62</sup> proposed correcting the effects of plural inelastic scattering in the jump ratio maps by acquiring unfiltered and zero filtered images to determine the thickness and correcting the data.

In materials science, Weyland and Midgley<sup>14, 63</sup> applied both techniques to a well characterized chromium carbide sample. The changes of the Cr jump ratio with thicknesses were investigated. The ratio changed monotonically with thicknesses up to  $t/\lambda=0.7$  (where  $\lambda$  is the mean free path of the electrons). For higher thickness, the intensity dropped. Under those thicknesses, the jump ratio provided a better reconstruction of the sample. It was also used in the reconstruction of the  $\text{Fe}_3\text{O}_4$  particle chains in magnetotactic bacteria, using both iron and oxygen jump ratios, as the elemental maps showed considerable diffraction contrast. In reference <sup>14</sup>, EFTEM results are compared to those obtained by HAADF electron tomography, and the better quality of the HAADF reconstructions can be observed. However, elemental maps were preferred for the reconstruction of iron and nickel oxide nanoparticles a few years later by Weyland et. al<sup>64</sup>.

In more recent examples, Jin-Phillipp et al.<sup>65</sup> proposed a method for correcting the multiple scattering using the zero loss image and proved its validity in a copper nanowire. They defined a new element specific relative thickness ( $t_E/\lambda$ ):

$$t_E/\lambda \approx \ln[(I_{0,exp} + I_{E,exp})/I_{0,exp}] \quad , \quad [1.5]$$

where  $I_{0,exp}$  and  $I_{E,exp}$  are the experimentally recorded zero loss and the background-subtracted core loss intensities, respectively, using energy windows of equal size. Another example can be found in Ileana et al.<sup>66</sup>, who used EFTEM with the three window method to elucidate the role of nitrogen in the curvature of arches inside multiwalled carbon nanotubes.

Another procedure of EFTEM tomography, extracting single energy loss images as projections, has been considered for copolymer studies<sup>67</sup> and bulk plasmon maps have been applied to semiconductors<sup>68</sup>. This approach was used by Gass et al.<sup>69</sup> on multiwall carbon nanotubes filled with nylon. In this case, for every tilt angle, a series of filtered images in the low-loss region from 0 to 29 eV were acquired with 3 eV slit width. Then, every energy slice was reconstructed in 3D, so that voxel specific spectra could be recovered from all the reconstructions. These “volume spectra” had been already mentioned as a possibility by Möbus et al.<sup>57</sup>. The approach by Gass et al has more recently been used, also in low-loss, in silicon/alumina/titanium nitride nanowires by Haberfehlner et al.<sup>70</sup>, recovering voxel specific low loss spectra.

The main drawback of EFTEM is the low energy resolution, limited by the width of the energy selecting slit. However, it has the advantage of the lower acquisition times and more favorable conditions for sample stability<sup>57, 60, 63</sup>. Only a few images (i.e. energy windows) per tilt angle are acquired in EFTEM, which reduces the time of acquisition as well as the energy dose received by the sample when compared to EELS-SI tomography.

### 1.3.1.c. *EELS-SI tomography*

Electron Energy Loss Spectroscopy Spectrum Imaging (EELS-SI) tomography, is a much more recent approach when compared to EFTEM tomography. The literature in the field is very scarce, with only one paper dealing with core loss EELS-SI tomography and another one based on surface plasmons.

EELS-SI tomography presents the drawback of high acquisition times and therefore high energy dose. This technique consists in acquiring a series of spectrum images, i.e., images where every pixel contains a full EEL spectrum, at different tilt angles. However, the new generations of transmission electron microscopes (including Cs correctors, monochromators, C<sub>c</sub> correctors, cold field emission and more sensitive detectors) have enabled higher spatial and energy resolution as well as a decrease in the acquisition time of images and spectra<sup>71</sup>. It is thanks to the use of an ultra fast reading EELS detector that the first results were published in 2009 by Jarausch et al.<sup>72</sup> (although the feasibility of the technique had already been proposed by Möbus et al.<sup>57</sup>). In this paper<sup>72</sup> a few extracted signals from EELS SI were explored and discussed in

terms of the projection requirement. Volumetric maps of different properties were obtained where those met the requirement. For those failing the projection requirement, the results were expressed in the form of angle dependent charts. 3D reconstructions were achieved for integrated edge intensities (equivalent to the 3 window method in EFTEM) and for the MLLS fitting of the fine structure of a Si L<sub>2,3</sub> edge, which could not have been done using EFTEM. It was also pointed out that anisotropic characteristics cannot be reconstructed, which was shown for a ZnO sample.

Even more recently, in 2013, (that is, after the experiments carried out in the context of this thesis were published in 2012<sup>73</sup>), the use of low-loss EELS was also reported to successfully recover the three dimensional distribution of surface plasmon resonance modes by Nicoletti et al.<sup>74</sup>. In this work, five EELS-SI with an extremely high energy resolution were acquired in the energy range of 1-4 eV from a silver nanocube. Thanks to multivariate analysis for data extraction and compressed sensing in the reconstruction, it was possible to distinguish five surface plasmon modes in 3D.

In the context of EELS-SI tomography, it is important to note that the literature is scarce and that the only application of core loss tomography<sup>72</sup> is limited to specific instrumentation not widely available.

## 1.4. Actual instrumentation

In the context of this thesis, the following transmission electron microscopes have been used:

- JEOL JEM 2100, LaB<sub>6</sub> cathode operated at 200 kV. Located at the Scientific and Technical Centers of the University of Barcelona (CCiT-UB), Barcelona, Spain.
- JEOL JEM 2010F, Shottky field emission gun operated at 200 kV. Fitted with a Gatan GIF spectrometer. Located at the Scientific and Technical Centers of the University of Barcelona (CCiT-UB), Barcelona, Spain.
- Low base probe corrected FEI Titan, equipped with a XFEG source and operated at 80 kV. Fitted with a Gatan Tridiem EEL spectrometer. Located at the Laboratorio de Microscopias Avanzadas (LMA), Instituto de Nanociencia de Aragón (INA), Zaragoza, Spain.
- FEI Tecnai F20-G2 FEGTEM operated at 200 kV of the High Resolution Electron Microscopy group of the Department of Materials Science and Metallurgy of the University of Cambridge, Cambridge, UK.
- Nion UltraSTEM200 operated at 200 kV and equipped with a Gatan Enfium spectrometer. Located at Oak Ridge National Laboratory, Oak Ridge, TN, USA.

## 1.5. Aim of this work

The objective of this work is the combination of electron energy loss spectroscopy spectrum imaging (EELS-SI) and electron tomography in order to recover the maximum amount of chemical information in 3D in commonly used microscopes (either Cs corrected and uncorrected), with an ultimate goal of proposing the recovery of a full four dimensional dataset with three spatial dimensions plus an energy loss dimension. This work is divided in four main chapters after this introduction.

In **chapter 2**, the principles of tomographic reconstruction in the TEM will be further explained, with special focus on the reconstruction algorithms and the experimental procedures that are used in the following chapters. Two different cases of HAADF STEM tomography will be shown. First, iron oxide nanocubes are reconstructed to illustrate the procedure, showing every step in the data treatment. Then, a series of cuprous oxide nanoparticles are reconstructed to exemplify the application of HAADF STEM tomography to a problem in materials science as the faceting of functional nanoparticles.

**Chapter 3** will deal with EELS, explaining the theoretical basis of the EEL spectrum and two new applications, developed in the framework of this doctoral thesis. On the one hand, we demonstrate for the first time the enhancement of the EELS signal by means of electron beam precession, in strontium titanate and crystalline silicon in major zone axis conditions. This discovery has been also object of a patent application. On the second hand, a new homemade software for the quantification of oxidation state in transition metal oxides has been developed. A calibration test has been designed so as to get appropriate references for different manganese oxides. The use of this software for disentangling the core-shell structure in manganese oxides nanoparticles will be presented.

Then, **chapter 4** shows how EELS-SI tomography can benefit from multivariate statistical analysis (MVA) to get the most out of the spectra and recover chemical information in 3D.  $\text{Fe}_x\text{Co}_{(3-x)}\text{O}_4@\text{Co}_3\text{O}_4$  mesoporous nanocomposite particles

are first characterized by means of HAADF STEM tomography and EEL spectroscopy as independent TEM tools. Then, the acquisition and MVA treatment of the tilted series of EELS-SI is explained, ending by the 3D reconstruction of chemical information extracted from the spectra.

Finally, in **chapter 5**, EELS-SI tomography assisted by MVA analysis is applied to a nanoneedle-prepared sample of multiferroic cobalt ferrite – bismuth ferrite nanocomposite. A full 4D dataset is successfully retrieved, where the whole structural and chemical information are combined in the so called spectrum volume.

## 1.6. References

1. Radon, J. Über die Bestimmung von Funktionen durch ihre Integralwerte längs gewisser Mannigfaltigkeiten. *Ber. Verh. Sächs. Akad. Wiss.* **69**, 262-277 (1917).
2. Bracewell, R. N. Two-dimensional aerial smoothing in radio astronomy. *Australian Journal of Physics* **9**, 297-314 (1956).
3. Cormack, A. M. Representation of a Function by Its Line Integrals, with Some Radiological Applications. *Journal of Applied Physics* **34**, 2722-2727 (1963).
4. Hoppe, W., Langer, R., Knesch, G. & Poppe, C. Protein-Kristallstrukturanalyse mit Elektronenstrahlen. *Naturwissenschaften* 333-336 (1968).
5. de Rosier, D. J. & Klug, A. Reconstruction of Three Dimensional Structures from Electron Micrographs. *Nature* **217**, 130-134 (1968).
6. Hawkes, P. W. The Electron Microscope as a Structure Projector. 83-111 (2006).
7. Rebled, J. M., Yedra, L., Estradé, S., Portillo, J. & Peiró, F. A new approach for 3D reconstruction from bright field TEM imaging: Beam Precession Assisted Electron Tomography. *Ultramicroscopy* **111**, 1504-1511 (2011).
8. Arslan, I., Yates, T. J. V., Browning, N. D. & Midgley, P. A. Embedded Nanostructures Revealed in Three Dimensions. *Science* **309**, 2195-2198 (2005).
9. Miller, M., Russell, K. & Thompson, G. Strategies for fabricating atom probe specimens with a dual beam FIB. *Ultramicroscopy* **102**, 287-298 (2005).
10. Goris, B., Bals, S., Van den Broek, W., Verbeeck, J. & Van Tendeloo, G. Exploring different inelastic projection mechanisms for electron tomography. *Ultramicroscopy* **111**, 1262-1267 (2011).
11. Crowther, R., de Rosier, D. & Klug, A. Reconstruction of 3 Dimensional Structure from Projections and its Application to Electron Microscopy. *Proceedings of the Royal Society of London Series A-Mathematical and Physical Sciences* **317**, 319-340 (1970).
12. Gordon, R., Bender, R. & Herman, G. T. Algebraic Reconstruction Techniques (ART) for three-dimensional electron microscopy and X-ray photography. *J.Theor.Biol.* **29**, 471-481 (1970).
13. Gilbert, P. Iterative methods for the three-dimensional reconstruction of an object from projections. *J.Theor.Biol.* **36**, 105-117 (1972).

14. Midgley, P. A. & Weyland, M. 3D electron microscopy in the physical sciences: the development of Z-contrast and EFTEM tomography. *Ultramicroscopy* **96**, 413-431 (2003).
15. Batenburg, K. J., et al. 3D imaging of nanomaterials by discrete tomography. *Ultramicroscopy* **109**, 730-740 (2009).
16. Roelandts, T., et al. Accurate segmentation of dense nanoparticles by partially discrete electron tomography. *Ultramicroscopy* **114**, 96-105 (2012).
17. Goris, B., Van den Broek, W., Batenburg, K. J., Mezerji, H. H. & Bals, S. Electron tomography based on a total variation minimization reconstruction technique. *Ultramicroscopy* **113**, 120-130 (2012).
18. Saghi, Z., et al. Three-Dimensional Morphology of Iron Oxide Nanoparticles with Reactive Concave Surfaces. A Compressed Sensing-Electron Tomography (CS-ET) Approach. *Nano Lett.* **11**, 4666-4673 (2011).
19. Leary, R., Midgley, P. A. & Thomas, J. M. Recent Advances in the Application of Electron Tomography to Materials Chemistry. *Acc.Chem.Res.* **45**, 1782-1791 (2012).
20. Thomas, J. M., Leary, R., Midgley, P. A. & Holland, D. J. A new approach to the investigation of nanoparticles: Electron tomography with compressed sensing. *J.Colloid Interface Sci.* **392**, 7-14 (2013).
21. McEwen, B. F., Radermacher, M., Rieder, C. L. & Frank, J. Tomographic three-dimensional reconstruction of cilia ultrastructure from thick sections. *Proceedings of the National Academy of Sciences* **83**, 9040-9044 (1986).
22. Nicastro, D., Frangakis, A. S., Typke, D. & Baumeister, W. Cryo-electron Tomography of Neurospora Mitochondria. *J.Struct.Biol.* **129**, 48-56 (2000).
23. Ladinsky, M. S., Mastronarde, D. N., McIntosh, J. R., Howell, K. E. & Staehelin, L. A. Golgi Structure in Three Dimensions: Functional Insights from the Normal Rat Kidney Cell. *The Journal of Cell Biology* **144**, 1135-1149 (1999).
24. Marsh, B., Mastronarde, D., McIntosh, J. & Howell, K. Structural evidence for multiple transport mechanisms through the Golgi in the pancreatic beta-cell line, HIT-T15. *Biochem.Soc.Trans.* **29**, 461-467 (2001).
25. O'Toole, E. T., Giddings, T. H., McIntosh, J. R. & Dutcher, S. K. Three-dimensional Organization of Basal Bodies from Wild-Type and  $\Delta$ -Tubulin Deletion Strains of *Chlamydomonas reinhardtii*. *Mol.Biol.Cell* **14**, 2999-3012 (2003).
26. Jensen, C. G., et al. Ultrastructural, tomographic and confocal imaging of the chondrocyte primary cilium in situ. *Cell Biol.Int.* **28**, 101-110 (2004).
27. Thomas, J. M., et al. The Chemical Application of High-Resolution Electron Tomography: Bright Field or Dark Field? *Angewandte Chemie* **116**, 6913-6915 (2004).
28. Spontak, R. J., Williams, M. C. & Agard, D. A. 3-Dimensional Study of Cylindrical Morphology in a Styrene Butadiene Styrene Block Copolymer. *Polymer* **29**, 387-395 (1988).
29. Bates, F. S. & Fredrickson, G. H. Block Copolymer Thermodynamics - Theory and Experiment. *Annu.Rev.Phys.Chem.* **41**, 525-557 (1990).

30. Spontak, R. J., et al. Phase behavior of ordered diblock copolymer blends: Effect of compositional heterogeneity. *Macromolecules* **29**, 4494-4507 (1996).
31. Radzilowski, L. H., Carragher, B. O. & Stupp, S. I. Three-dimensional self-assembly of rodcoil copolymer nanostructures. *Macromolecules* **30**, 2110-2119 (1997).
32. Koster, A., Ziese, U., Verkleij, A., Janssen, A. & de Jong, K. Three-dimensional transmission electron microscopy: A novel imaging and characterization technique with nanometer scale resolution for materials science. *J Phys Chem B* **104**, 9368-9370 (2000).
33. Midgley, P., Weyland, M., Thomas, J. & Johnson, B. Z-Contrast tomography: a technique in three-dimensional nanostructural analysis based on Rutherford scattering. *Chem.Commun.* 907-908 (2001).
34. Weyland, M., Midgley, P. A. & Thomas, J. M. Electron Tomography of Nanoparticle Catalysts on Porous Supports: A New Technique Based on Rutherford Scattering. *The Journal of Physical Chemistry B* **105**, 7882-7886 (2001).
35. Jinnai, H., et al. Direct measurement of interfacial curvature distributions in a bicontinuous block copolymer morphology. *Phys.Rev.Lett.* **84**, 518-521 (2000).
36. Jinnai, H., et al. 3D nanometer-scale study of coexisting bicontinuous morphologies in a block copolymer/homopolymer blend. *Macromolecular Rapid Communications* **27**, 1424-1429 (2006).
37. Jinnai, H., Kaneko, T., Matsunaga, K., Abetz, C. & Abetz, V. A double helical structure formed from an amorphous, achiral ABC triblock terpolymer. *Soft Matter* **5**, 2042-2046 (2009).
38. Park, H., Jung, J., Chang, T., Matsunaga, K. & Jinnai, H. New Epitaxial Phase Transition between DG and HEX in PS-b-PI. *J.Am.Chem.Soc.* **131**, 46-47 (2009).
39. Jung, J., et al. Structural characterization of the Fddd phase in a diblock copolymer thin film by electron microtomography. *Soft Matter* **7**, 10424-10428 (2011).
40. Jinnai, H., et al. Transmission electron microtomography in soft materials. *J.Electron Microsc.* **62**, 243-258 (2013).
41. Janssen, A. H., Koster, A. J. & de Jong, K. P. On the shape of the mesopores in zeolite Y: A three-dimensional transmission electron microscopy study combined with texture analysis. *J Phys Chem B* **106**, 11905-11909 (2002).
42. Ziese, U., de Jong, K. P. & Koster, A. J. Electron tomography: a tool for 3D structural probing of heterogeneous catalysts at the nanometer scale. *Applied Catalysis A-General* **260**, 71-74 (2004).
43. Yates, T. J. V., et al. Three-dimensional real-space crystallography of MCM-48 mesoporous silica revealed by scanning transmission electron tomography. *Chemical Physics Letters* **418**, 540-543 (2006).
44. Inoke, K., et al. Severe local strain and the plastic deformation of Guimer-Preston zones in the Al-Ag system revealed by three-dimensional electron tomography. *Acta Materialia* **54**, 2957-2963 (2006).
45. Ward, E. P. W., Yates, T. J. V., Fernandez, J., Vaughan, D. E. W. & Midgley, P. A. Three-dimensional nanoparticle distribution and local curvature of heterogeneous

catalysts revealed by electron tomography. *Journal of Physical Chemistry C* **111**, 11501-11505 (2007).

46. Van Aert, S., Batenburg, K. J., Rossell, M. D., Erni, R. & Van Tendeloo, G. Three-dimensional atomic imaging of crystalline nanoparticles. *Nature* **470**, 374-377 (2011).

47. Eljarrat, A., et al. Optoelectronic Properties of InAlN/GaN Distributed Bragg Reflector Heterostructure Examined by Valence Electron Energy Loss Spectroscopy. *Microscopy and Microanalysis* **18**, 1143-1154 (2012).

48. Eljarrat, A., et al. Structural and compositional properties of Er-doped silicon nanoclusters/oxides for multilayered photonic devices studied by STEM-EELS. *Nanoscale* **5**, 9963-70 (2013).

49. Eljarrat, A., et al. Insight into the Compositional and Structural Nano Features of AlN/GaN DBRs by EELS-HAADF. *Microscopy and Microanalysis* **19**, 698-705 (2013).

50. Jeanguillaume, C., Trebbia, P. & Colliex, C. About use of Electron Energy-Loss Spectroscopy for Chemical Mapping of Thin Foils with High Spatial-Resolution. *Ultramicroscopy* **3**, 237-242 (1978).

51. Williams, D. B. & Carter, B. C. *Transmission Electron Microscopy* (Springer, 2009).

52. Egerton, R. F. & Malac, M. EELS in the TEM. *Journal of Electron Spectroscopy and Related Phenomena* **143**, 43-50 (2005).

53. Hofer, F. & Kothleitner, G. Quantitative Microanalysis using Electron-Energy-Loss Spectrometry .1. Li and be in Oxides. *Microscopy Microanalysis Microstructures* **4**, 539-560 (1993).

54. Genç, A., Cheng, H., Winterstein, J., Pullan, L. & Freitag, B. 3D chemical mapping using tomography with an Enhanced XEDS system. *Microscopy and Analysis* **26**, 23-25 (2012).

55. Genç, A., et al. XEDS STEM tomography for 3D chemical characterization of nanoscale particles. *Ultramicroscopy* **131**, 24-32 (2013).

56. Lepinay, K., Lorut, F., Pantel, R. & Epicier, T. Chemical 3D tomography of 28 nm high K metal gate transistor: STEM XEDS experimental method and results. *Micron* **47**, 43-49 (2013).

57. Möbus, G., Doole, R. C. & Inkson, B. J. Spectroscopic electron tomography. *Ultramicroscopy* **96**, 433-451 (2003).

58. Grimm, R., Koster, A., Ziese, U., Typke, D. & Baumeister, W. Zero-loss energy filtering under low-dose conditions using a post-column energy filter. *J.Microsc.-Oxf.* **183**, 60-68 (1996).

59. Möbus, G. & Inkson, B. J. Three-dimensional reconstruction of buried nanoparticles by element-sensitive tomography based on inelastically scattered electrons. *Appl.Phys.Lett.* **79**, 1369-1371 (2001).

60. Leapman, R. D., Kocsis, E., Zhang, G., Talbot, T. L. & Laquerriere, P. Three-dimensional distributions of elements in biological samples by energy-filtered electron tomography. *Ultramicroscopy* **100**, 115-125 (2004).

61. Leapman, R. D. & Aronova, M. A. Localizing specific elements bound to macromolecules by EFTEM. *Cellular Electron Microscopy* **79**, 593-613 (2007).
62. Aronova, M. A., et al. Three-dimensional elemental mapping of phosphorus by quantitative electron spectroscopic tomography (QuEST). *J.Struct.Biol.* **160**, 35-48 (2007).
63. Weyland, M. & Midgley, P. A. Extending Energy-Filtered Transmission Electron Microscopy (EFTEM) into Three Dimensions Using Electron Tomography. *Microscopy and Microanalysis* **9**, 542-555 (2003).
64. Weyland, M., Yates, T., Dunin-Borkowski, R., Laffont, L. & Midgley, P. Nanoscale analysis of three-dimensional structures by electron tomography. *Scr.Mater.* **55**, 29-33 (2006).
65. Jin-Phillipp, N. Y., Koch, C. T. & van Aken, P. A. Toward quantitative core-loss EFTEM tomography. *Ultramicroscopy* **111**, 1255-1261 (2011).
66. Florea, I., et al. 3D Analysis of the Morphology and Spatial Distribution of Nitrogen in Nitrogen-Doped Carbon Nanotubes by Energy-Filtered Transmission Electron Microscopy Tomography. *J.Am.Chem.Soc.* **134**, 9672-9680 (2012).
67. Yamauchi, K., et al. Microdomain morphology in an ABC 3-miktoarm star terpolymer: A study by energy-filtering TEM and 3D electron tomography. *Macromolecules* **36**, 6962-6966 (2003).
68. Yurtsever, A., Weyland, M. & Muller, D. A. Three-dimensional imaging of nonspherical silicon nanoparticles embedded in silicon oxide by plasmon tomography. *Appl.Phys.Lett.* **89**, 151920 (2006).
69. Gass, M. H., Koziol, K. K. K., Windle, A. H. & Midgley, P. A. Four-Dimensional Spectral Tomography of Carbonaceous Nanocomposites. *Nano Letters* **6**, 376-379 (2006).
70. Haberfehlner, G., et al. Four-dimensional spectral low-loss energy-filtered transmission electron tomography of silicon nanowire-based capacitors. *Appl.Phys.Lett.* **101**, 063108 (2012).
71. Varela, M., et al. Spectroscopic imaging of oxide interfaces with aberration corrected probes RID A-5587-2008. *Microsc.Microanal.* **13**, 142-143 (2007).
72. Jarausch, K., Thomas, P., Leonard, D. N., Twesten, R. & Booth, C. R. Four-dimensional STEM-EELS: Enabling nano-scale chemical tomography. *Ultramicroscopy* **109**, 326-337 (2009).
73. Yedra, L., et al. EEL spectroscopic tomography: Towards a new dimension in nanomaterials analysis. *Ultramicroscopy* **122**, 12-18 (2012).
74. Nicoletti, O., et al. Three-dimensional imaging of localized surface plasmon resonances of metal nanoparticles. *Nature* **502**, 80-84 (2013).

## ***2. Tomography***



<b>2.1. Scope of the chapter .....</b>	<b>59</b>
<b>2.2. Reconstruction methods .....</b>	<b>60</b>
2.2.1. Fourier Methods.....	60
2.2.2. Weighted Back-projection Methods .....	63
2.2.2.a. <i>The simple Back-projection</i> .....	63
2.2.2.b. <i>Weighting function</i> .....	66
2.2.2.c. <i>The weighting function for single axis and equal tilt increments</i> .....	68
2.2.3. Iterative methods .....	71
2.2.3.a. <i>The Algebraic Reconstruction Technique</i> .....	72
2.2.3.b. <i>The Simultaneous Iterative Reconstruction Technique</i> .....	74
<b>2.3. Methodology .....</b>	<b>75</b>
2.3.1. Materials: iron oxide nanocubes for in-vivo applications .....	75
2.3.2. Data acquisition .....	76
2.3.3. Data treatment .....	78
2.3.3.a. <i>Image alignment and tilt axis identification</i> .....	79
2.3.3.b. <i>Reconstruction</i> .....	81
2.3.3.c. <i>Visualization</i> .....	82
<b>2.4. Faceting of Cu<sub>2</sub>O nanoparticles: an application of HAADF tomography .....</b>	<b>85</b>
2.4.1. Experimental details .....	86
2.4.2. Results and discussion .....	87
2.4.3. Conclusions .....	91
<b>2.5. References .....</b>	<b>93</b>



## **2.1. Scope of the chapter**

This chapter is centered on the theoretical and experimental aspects of electron tomography, solely from the structural point of view. First, the theoretical aspects of reconstruction using Fourier, back-projection and iterative methods will be presented. Then, using an iron oxide nanocube sample, the whole process of data acquisition in the case of HAADF STEM, alignment and reconstruction will be illustrated. Finally, HAADF STEM tomography will be applied to solve a materials science problem concerning the morphology and structure of  $\text{Cu}_2\text{O}$  nanoparticles.

The objective of the chapter is to establish the theoretical and experimental basis of electron tomography for the fourth and fifth chapters, where EELS-SI tomography is developed.

## 2.2. Reconstruction methods

The success of electron tomography relies on the reconstruction algorithms which enable the recovery of the three dimensional information from two dimensional projections. In this chapter, a short introduction to reconstruction techniques is given, starting with the Fourier techniques, pioneers in TEM tomography and still relevant for understanding the information contained in the reconstruction. Weighted back-projection (WBP) techniques are introduced afterwards, as they are closely linked to the Fourier techniques. Finally, ART and SIRT iterative methods are explained. In the context of this thesis, SIRT has been used for reconstruction. SIRT has the advantage of yielding better quality reconstructions than the previous techniques; with no prior knowledge imposed to the reconstruction other than positivity (counts in the microscope are always positive). Other algorithms, such as DART<sup>1, 2</sup> or CS<sup>3</sup> impose more constraints to the reconstruction. As we want to show the ability of some signals to reconstruct volumes, the extra constraints would make the interpretation of the validity of those signals more difficult. SIRT is the algorithm that has prevailed for materials science electron tomography and the resulting reconstructions are well known. Therefore, the discussion about validity of the signals will be much clearer.

### 2.2.1. Fourier Methods

DeRosier and Klug<sup>4</sup> first showed that a three dimensional distribution could be recovered from 2D projections in the transmission electron microscope (TEM). Their method consisted on determining the Fourier transform of an object from the Fourier transforms of its projections. Then the original object could be recovered applying an

inverse Fourier transform. The procedure is described as in the original paper, which extended Fourier reconstruction to non symmetrical objects<sup>5</sup>.

In order to perform the reconstruction, the relation between real projections and Fourier sections must be understood. The Fourier Transform of a three dimensional object of density  $\rho(x, y, z)$  is given by:

$$F(X, Y, Z) = \iiint_{\text{object}} \rho(x, y, z) e^{2\pi i(xX + yY + zZ)} dx dy dz \quad . \quad [2.1]$$

Then the central section  $Z = 0$  of the transform is given by

$$F(X, Y, 0) = \iint \sigma(x, y) e^{2\pi i(xX + yY)} dx dy \quad , \quad [2.2]$$

where

$$\sigma(x, y) = \int \rho(x, y, z) dz \quad . \quad [2.3]$$

$\sigma(x, y)$  represents the projected density parallel to the  $z$  axis. This is a single direction, but the following can be derived for any particular direction. Here we see that the central section is equivalent to the Fourier transform of a given projection.

To perform a reconstruction, we need the inverse of [2.1], namely

$$\rho(\mathbf{x}) = \int_{\text{transform}} F(\mathbf{X}) e^{-2\pi i \mathbf{x} \cdot \mathbf{X}} d\mathbf{X} \quad . \quad [2.4]$$

However, for computational purposes, the integral in [2.4] must be discretized

$$\rho(\mathbf{x}) = \delta\mathbf{X} \sum_j F(\mathbf{X}_j) e^{-2\pi i \mathbf{x} \cdot \mathbf{X}_j} \quad [2.5]$$

so that the transform is performed only at sampling points  $\mathbf{X}_j$ . This is a valid inverse Fourier transform only if the sampling is done at regular intervals, and at intervals smaller than the theoretical information limit. In imaging, the highest spatial frequency that can be detected is limited by the pixel size of the detectors or the scanning. If the pixels in an image are at a spatial frequency  $f_s$ , the bandwidth of the information is limited to  $\frac{1}{2}f_s$ <sup>6</sup>. In three dimensions, the simplest regular samplings are either a three dimensional lattice, for which normal Fourier inversion in Cartesian coordinates is used, or a set of equiangularly spaced planes passing through a common line, for which Fourier Bessel inversion in cylindrical polar coordinates is used. In both cases, in order

to make efficient use of the data, some degree of interpolation must be applied, as the original sections will not always coincide with sampling points.

In the case of a single tilt experiment with regular intervals, the cylindrical polar coordinates are more adequate to describe the sampling. The analytical form of the Fourier transform in cylindrical coordinates leads to a simple method of interpolation. We denote the cylindrical polar coordinates  $(r, \phi, z)$  in particle space, and  $(R, \Phi, Z)$  in transform space. We expand the density in cylindric functions

$$\rho(r, \phi, z) = \sum_n \int g_n(r, Z) e^{in\phi} e^{2\pi izZ} dZ \quad . \quad [2.6]$$

The Fourier transform  $F$ , can be expressed in the form

$$F(R, \Phi, Z) = \sum_n G_n(R, Z) e^{in(\phi+\pi/2)} \quad , \quad [2.7]$$

where  $G_n(R, Z)$  is the Fourier-Bessel transform of  $g_n(r, Z)$ :

$$G_n(R, Z) = \int_0^\infty g_n(r, Z) J_n(2\pi Rr) 2\pi r dr \quad [2.8]$$

and

$$g_n(r, Z) G_n(R, Z) = \int_0^\infty G_n(R, Z) J_n(2\pi Rr) 2\pi R dR \quad . \quad [2.9]$$

Equation [2.7] implies that for a fixed  $R$  and  $Z$ , that is, for a given annulus normal to the polar axis,  $F$  is a known function of  $\Phi$  independent of the density  $\rho$ . Therefore, while working on an annulus, the interpretation becomes one-dimensional. The  $G_n(R, Z)$  are the coefficients in a one dimensional Fourier analysis of the transform around the annulus. If the observed transform values  $F$  are available at equally spaced points around the annulus, equations [2.7] are analytically invertible for the  $G_n$ .  $g_n$  are obtained from [2.9] and then  $\rho$  from [2.6]. If the sampling is not done regularly, the previous method can be adapted. As long as there are at least as many observed data points as unknowns,  $G_n$ , on the annulus, it is possible to attempt to solve [2.7] by least squares. The sets of equations are

$$F_j = \sum_n B_{jn} G_n \quad , \quad [2.10]$$

where  $F_j$  are the available points of transform around the annulus at angles  $\Phi_j$ , and  $\mathbf{B}$  is given by equation [2.7]

$$B_{jn} = e^{in(\Phi_j + \pi/2)} \quad . \quad [2.11]$$

The recovery of the densities  $\rho(x, y, z)$  from  $\rho(r, \phi, z)$  would require again another interpolation, as the datasets are discrete, and the points in the polar coordinate system will not coincide with the Cartesian points.

While this technique has been proven capable of reconstructing objects in 3D, the calculations required, mainly for interpolating data, have triggered the development of direct methods, where the calculations are carried out in real space.

## 2.2.2. Weighted Back-projection Methods

### 2.2.2.a. *The simple Back-projection*

The back-projection algorithms were developed as direct (or at least partially direct) methods, direct meaning that no Fourier transformations are required to match the results obtained in Fourier methods<sup>5-7</sup>. As a matter of fact, we will consider a back-projection algorithm with a direct and an indirect part, as the filtering of the simple back-projection is carried out on the Fourier transforms of either the original data or the reconstructed object<sup>8-10</sup>.

The back-projection, also known as summation technique, can be simply understood as the sum of all the projected images (P in Figure 2.1) after smearing them in the original projection angle, which are called the back-projection bodies<sup>11</sup> (B in Figure 2.1).

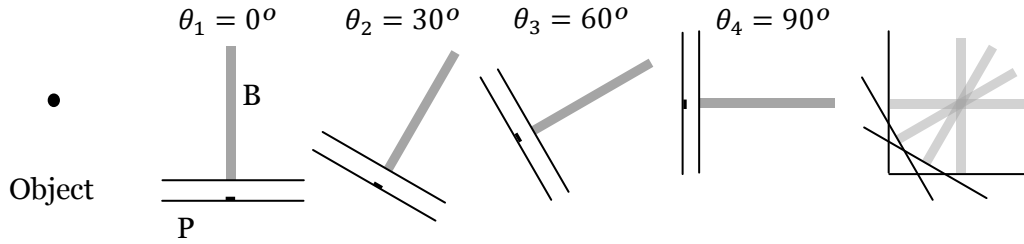


**Figure 2.1:** Simple Back-projection of a binary object projected onto four projections ( $P$ ) at angles  $\theta_1, \theta_2, \theta_3$  and  $\theta_4$ . From the projections, back-projection bodies ( $B$ ) are created (eq. [2.18]). The final figure shows the summation of the four back-projection bodies (eq. [2.19]).

If we consider a 3D distribution  $f(x, y, z)$ , projected under the angles  $\theta_j, \phi_j$ , (as the one in Figure 2.2) it will form a series of projections  $p_j(x^j, y^j)$ . Let  $r^j = (x^j, y^j, z^j)$  be the coordinates of the projection  $p_j$  in the coordinate system in which it forms the  $(x^j, y^j)$  plane. The geometrical relationships between the object coordinates  $\mathbf{r}(x, y, z)$  and  $\mathbf{r}^j = (x^j, y^j, z^j)$  are given by the rotation matrixes  $D_{\theta_j}, D_{\phi_j}$ :

$$\mathbf{r}^j = D_{\theta_j} \cdot D_{\phi_j} \cdot \mathbf{r} \quad , \quad [2.12]$$

with

$$D_{\theta_j} = \begin{pmatrix} \cos\theta_j & 0 & -\sin\theta_j \\ 0 & 1 & 0 \\ \sin\theta_j & 0 & \cos\theta_j \end{pmatrix} \quad [2.13]$$

and

$$D_{\phi_j} = \begin{pmatrix} \cos\phi_j & \sin\phi_j & 0 \\ -\sin\phi_j & \cos\phi_j & 0 \\ 0 & 0 & 1 \end{pmatrix} \quad . \quad [2.14]$$

The object is first rotated around the  $z$  axis by  $\phi_j$  and then around the new  $y$  axis by  $-\theta_j$  and then projected onto the  $(x^j, y^j)$  plane. The third rotation, which would be in the plane of the projection, will be disregarded as it will be zero for random conical tilt or simple geometries as the usual single tilt scenario.

A projection along the  $z^j$  direction with angles  $\theta_j, \phi_j$  can be expressed as

$$p_j = \int f(x^j, y^j, z^j) dz^j \quad , \quad [2.15]$$

as observed in Figure 2.2.

A back-projection body, which could be explained as smearing the intensities of the projection in the  $z^j$  direction, is created by the convolution of the projection  $p_j$  in the  $(x^j, y^j)$  plane with the 3D spread function

$$l_j = \delta(x^j, y^j)c(z^j) \quad [2.16]$$

with

$$c(z^j) = \begin{cases} 1 & \text{for } -a \leq z^j \leq +a \\ 0 & \text{otherwise} \end{cases} \quad [2.17]$$

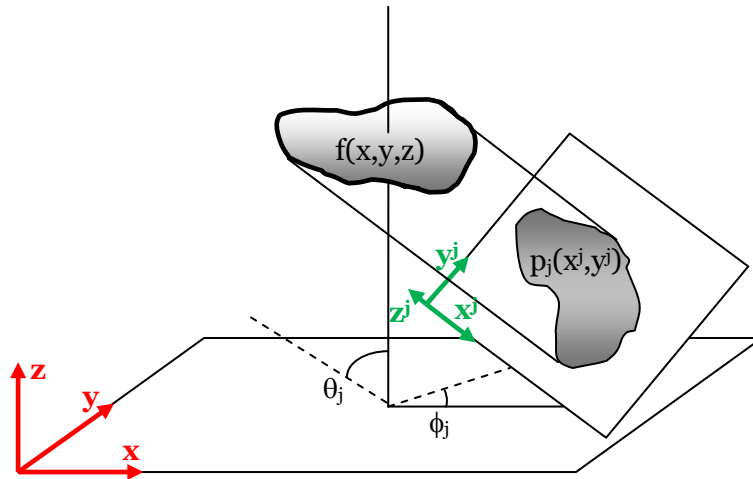


**Figure 2.2:** Figure representing the projection of the function  $f(x, y, z)$  in the  $(x, y, z)$  basis (represented in red) onto the  $(x^j, y^j)$  plane (with its basis in green). The  $(x^j, y^j)$  plane is defined by angles  $\theta_j$  and  $\phi_j$ .

The convolution conditions for an isoplanatic system are fulfilled within a sphere of diameter  $a$  such that  $2 \cdot a$  is at least twice the object diameter. Another condition is that the projections and the reconstruction volume are to be sufficiently large to include all back-projected rays. For theoretical purposes, projections and back-projection bodies can be considered infinite, but in practical applications,  $2 \cdot a$  is the

object diameter for the calculation of the weighting function, and infinite in the back-projection step. Projections and volumes are kept at twice the size of the object for the calculations.

The back-projection body can be written as

$$p_j^b(x^j, y^j, z^j) = \iint p_j(x^j, y^j) \cdot l(x^j - x'^j, y^j - y'^j, z^j) dx'^j dy'^j = \iiint f(x'^j, y'^j, z'^j) dz'^j \cdot l(x^j - x'^j, y^j - y'^j, z^j) dx'^j dy'^j \quad . \quad [2.18]$$

Then, the back-projection algorithm is

$$b(x, y, z) = \sum_j p_j^b(x^j, y^j, z^j) \quad . \quad [2.19]$$

The performance of the algorithm can be described by the convolution of the original object with the point spread function of the reconstruction algorithm. To get a better reconstruction, it must be corrected by deconvoluting with the point spread function, a step known as the weighting of the back-projection.

### 2.2.2.b. Weighting function

The weighting function used for correcting the simple back-projection is based on the point spread function of the experimental technique. The 3D object can be rewritten as a superposition of  $\delta$  functions:

$$f(x, y, z) = \iiint f(\xi, \eta, \zeta) \delta(x - \xi, y - \eta, z - \zeta) d\xi d\eta d\zeta \quad . \quad [2.20]$$

The point spread function can be found by observing the effects of back-projection on a single point in three dimensions described by

$$q = \delta(x, y, z) \quad . \quad [2.21]$$

Then, when projected at angles  $\theta_j, \phi_j$  it becomes

$$p_j(x^j, y^j) = \delta(x^j, y^j) \quad . \quad [2.22]$$

The back-projection body, according to equations [2.16] and [2.18] is

$$p_j^b(x^j, y^j, z^j) = \delta(x^j, y^j)c(z^j) \quad . \quad [2.23]$$

The point back-projected in 3D is found by summation over  $\theta_j, \phi_j$

$$b(x, y, z) = \sum_j \delta(x^j, y^j)c(z^j) \quad . \quad [2.24]$$

The transfer function of the system will be the Fourier transform of [2.24]:

$$\begin{aligned} H(X, Y, Z) &= \mathbf{F}[b(x, y, z)] \\ &= \mathbf{F} \left\{ \sum_j \delta(x^j, y^j)c(z^j) \right\} \\ &= \sum_j \mathbf{F} [\delta(x^j, y^j)c(z^j)] \end{aligned} \quad [2.25]$$

and

$$\begin{aligned} \mathbf{F} [\delta(x^j, y^j)c(z^j)] &= \int_{-\infty}^{\infty} \iint \delta(x^j, y^j)c(z^j)e^{-2\pi i(x^j X^j + y^j Y^j + z^j Z^j)} dx^j dy^j dz^j \\ &= 1 \int_{-a}^a e^{-2\pi i z^j Z^j} dz^j = \frac{(2\pi a Z^j)}{\pi a Z^j} = 2a \operatorname{sinc}(2\pi a Z^j) \end{aligned} \quad [2.26]$$

where  $\operatorname{sinc}(x) = \sin(x)/x$ .

$Z^j$  can be expressed in the coordinate system  $(X, Y, Z)$  of the object with the rotation matrices of equations [2.13] and [2.14]

$$Z^j = X \sin \theta_j \cos \phi_j + Y \sin \theta_j \sin \phi_j + Z \cos \theta_j \quad [2.27]$$

and the transfer function becomes<sup>8</sup>:

$$H(X, Y, Z) = \sum_j 2a \operatorname{sinc}[X \sin \theta_j \cos \phi_j + Y \sin \theta_j \sin \phi_j + Z \cos \theta_j] \quad . \quad [2.28]$$

Therefore, the weighting function for any arbitrary geometry is

$$\begin{aligned} W_a(X, Y, Z) &= \frac{1}{H(X, Y, Z)} \\ &= \left\{ \sum_j 2a \operatorname{sinc}[X \sin \theta_j \cos \phi_j + Y \sin \theta_j \sin \phi_j + Z \cos \theta_j] \right\}^{-1} \quad , \end{aligned} \quad [2.29]$$

which is valid for  $H \neq 0$ . In the implementation of the algorithm,  $H$  is thresholded close to 0 to avoid division by 0 and to limit the noise enhancement. In practice, if a value of 1 would avoid any noise enhancement, a value of 0.6 is chosen to enhance the undersampled areas at high frequencies without great amplification of the noise. The original 3D distribution  $o(x, y, z)$  is recovered from the back-projection  $b(x, y, z)$  by deconvoluting the weighting function, easily done in Fourier space:

$$o(x, y, z) = \mathbf{F}^{-1}[O(X, Y, Z)] = \mathbf{F}^{-1}[B(X, Y, Z)W_a(X, Y, Z)] \quad . \quad [2.30]$$

The three dimensional weighting function [2.29] is applied to the Fourier transform of the object reconstructed by simple back-projection. As stated in the central slice theorem, the Fourier transforms of the projections correspond to central sections of 3D Fourier transform of the object. As the Fourier transform can be applied to the projections before the back-projection as well, the weighting can also be applied to the Fourier transform of the projections. However, in arbitrary tilt geometries, the location of the point in the central section relative to all other central sections is not independent of in-plane rotations, and the third Euler angle should be included in the previous equations. Yet, in simple geometries such as single axis tilting, this angle can be kept 0 by aligning the entire tilt axes to be parallel.

The advantage of applying the weighting to the projection is that, in most cases,  $H$  is non zero along the corresponding sections through the 3D Fourier transform, because each section is also the origin of one of the superimposed sinc-functions in  $H$ . However, the number of calculations required for this method is usually larger. In real applications, the weighting function in [2.29] performs well if the number of projections per angular interval changes smoothly.

### *2.2.2.c. The weighting function for single axis and equal tilt increments*

The previous weighting function is applicable to any tilt geometry. In particular, the solution for a single tilt axis series with equal tilt increments can be found analytically. In single axis tilt geometry, the object is rotated around a single axis in regular tilt increments, a projection recorded for each orientation. Assuming that this axis is the  $y$  axis,  $\theta$  in [2.13] becomes the tilt angle, and  $\phi$  in [2.14] is kept 0. We make two additional assumptions: (i) that the variable  $a$  in equation [2.17] is infinite, which means that the back-projection bodies are infinitely extended in the  $z^i$  direction; and

(ii) that the series of projections are available for  $\theta$  ranging from  $-90^\circ$  to  $90^\circ$ , the full tilting range. For this approximation, we have

$$\lim_{a \rightarrow \infty} a \operatorname{sinc}(a \cdot x) = \delta(x) \quad [2.31]$$

and equation [2.28] becomes

$$H(X, Y, Z) = \sum_j \delta(X \sin \theta_j + Z \cos \theta_j) \quad [2.32]$$

Taking into account condition (ii), the sum in equation [2.32] can be replaced by an integral:

$$H(X, Y, Z) = \int_{-\pi/2}^{\pi/2} \delta(X \sin \theta + Z \cos \theta) d\theta \quad [2.33]$$

Moreover, as the tilt axis is the  $y$ -axis,  $H(X, Y, Z)$  is independent of  $Y$ . Then, if we change the coordinate system to the cylindrical coordinates  $R$  and  $\Gamma$  in the  $XZ$  planes:

$$X = R \cos \Gamma, \quad Z = R \sin \Gamma, \quad Y = Y \quad [2.34]$$

equation [2.34] becomes

$$H(X, Y, Z) = \int_{-\pi/2}^{\pi/2} \delta(R \cos(\Gamma - \Theta)) d\Theta \quad [2.35]$$

Using the following identity, a solution can be found

$$\delta(f(x)) = \sum_n \frac{1}{|f'(x_n)|} \delta(x - x_n), \quad [2.36]$$

for  $f'(x_n) \neq 0$ . The  $x_n$  are zeros of  $f(x)$  in the integration range. In our case, there is only one zero and it corresponds to  $\Theta = \Gamma - \pi/2$ , so the solution of [2.35] is

$$H(R, Y, \Gamma) = \frac{1}{R} \quad [2.37]$$

Thus, the Fourier transform of the back-projections has to be multiplied by the weighting function

$$W_s(R, Y, \Gamma) = R \quad [2.38]$$

where  $R$  is the radius in Fourier space perpendicular to the tilt axis  $Y$ , and it can be applied to either the Fourier transform of the projections or the 3D Fourier transform of the back-projection.

However, this filter has a few inconvenients. First, there are an infinite number of reconstructions consistent with the limited measurements (see how high frequencies are undersampled in Fourier space in Figure 2.3 (a)) if the spatial frequency of the solutions is not limited; second, it enhances high frequency artifacts; and third,  $R$  does not have an inverse Fourier transform. These problems are solved by adding a low pass filter at frequencies up to the information limit or Nyquist frequency, as the one shown on Figure 2.3 (b).

In the actual experimental acquisition of single tilt axis tomography series there is usually a part of the Fourier space which remains unsampled, the so called missing wedge. The missing data will cause distortions which cannot be corrected by a weighting function, because the Fourier transform of the point spread function is zero in these regions, meaning that it cannot be used for deconvolution. This is the reason why the tilt range has been supposed to be complete, as the solution applies to the whole tilting range but the missing wedge.

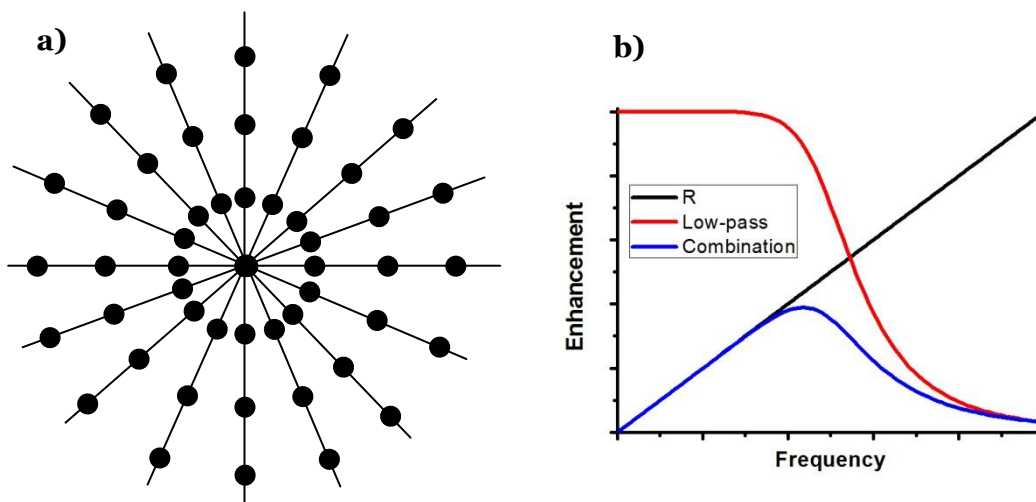


**Figure 2.3:** **a)** Figure representing the sampling distribution in Fourier space once the Fourier transforms of the projections are stacked as slices. Low frequencies are more sampled than high frequencies. **b)** Weighting filter (in blue), created by the combination of the radial filter (black) and a low-pass filter (in red).

It is important to note that the weighted back-projection is equivalent to the reconstruction using Fourier methods<sup>12</sup>. Let us give a simple, illustrative example. In the case of  $p_\phi(q)$ , a 1D projection of a 2D object  $o(x, y)$  at angle  $\phi$ , we have  $q = x \cos \phi + y \sin \phi$  in the coordinate system of the object. Let  $f(q, \phi)$  be the function which describes the set of projections for a continuous angle  $\phi$ . The back-projection in continuous form is

$$b(x, y) = \int_0^\pi f(x \cos \phi + y \sin \phi, \phi) d\phi = \int_0^\pi f(q(x, y, \phi)) d\phi \quad . \quad [2.39]$$

The one dimensional Fourier transform of  $f(q, \phi)$  along  $q$  is

$$F(R, \phi) = \int_{-\infty}^{\infty} f(q, \phi) e^{-2\pi i q R} dq \quad . \quad [2.40]$$

Replacing  $f$  in [2.39] by the inverse Fourier transform of  $F$  we have

$$\begin{aligned} b(x, y) &= \int_0^\pi \int_{-\infty}^{\infty} F(R, \phi) e^{2\pi i q(x, y, \phi) R} dR d\phi = \\ &= \int_0^\pi \int_{-\infty}^{\infty} F(R, \phi) e^{2\pi i (x \cos \phi + y \sin \phi) R} dR d\phi \quad . \end{aligned} \quad [2.41]$$

If we change the coordinates to polar coordinates  $r, \gamma$  with  $x = r \cos \gamma$  and  $y = r \sin \gamma$ , the previous equation becomes

$$\begin{aligned} b(r, \gamma) &= \int_0^\pi \int_{-\infty}^{\infty} F(R, \phi) e^{2\pi i R r \cos(\gamma - \phi)} dR d\phi \\ &= \int_0^\pi \int_{-\infty}^{\infty} \frac{F}{R}(R, \phi) e^{2\pi i R r \cos(\gamma - \phi)} R dR d\phi \quad , \end{aligned} \quad [2.42]$$

which is the inverse Fourier transform of  $F(R, \phi)$  multiplied by  $1/R$ .

### 2.2.3. Iterative methods

Fourier methods, as well as the weighted back-projection, are rigorous methods, and the conditions for a good reconstruction are well understood. However, there is

interest in working with other direct methods to obtain better reconstructions, as it is possible to introduce information about the object in the reconstruction procedure. For instance, in the methods we have introduced so far, it is very difficult to take advantage from the positivity constraint of the signal (the density of the object is always positive). We will see this is not always the case.

### 2.2.3.a. The Algebraic Reconstruction Technique

The first direct iterative method to be proposed was the Algebraic Reconstruction Technique (ART)<sup>13</sup>. From now on, the formalism will be presented for the single tilting experiment. Therefore, all the projections will share a single line, and the density  $f(x, y, z)$ , in any plane of the object perpendicular to this line will contribute to the projections in this plane. As a consequence, the reconstruction can be reduced to a series of two dimensional reconstructions carried out in planes perpendicular to the tilting axis. In other words, the reconstruction is carried out slice per slice using one dimensional projections.

We consider a problem where we want to find the density  $\rho_{ij}$  of an object on a grid of  $n \cdot n$  points  $(i, j), i = 1, 2, \dots, n; j = 1, 2, \dots, n$ . The field of the grid needs to be bigger than the dimensions of the object to be reconstructed. Then, a ray of a projection at an angle  $\theta$  is defined as a band of width  $w$  across the plane at that angle (analogous to the back-projected body). We define  $R_{k\theta}$  as the sum of the densities  $\rho_{ij}$  contained in ray  $k$  of the projection at angle  $\theta$ . Then

$$R_{k\theta} = \sum_{\text{points } (i,j) \text{ in ray } (k,\theta)} \rho_{ij}, \quad k = 1, 2, \dots, r_\theta \quad [2.43]$$

The number of rays  $r_\theta$  depends on  $w$  and the size of the object. The  $k$  points are the midpoints of the rays. The true projected densities of the object at these points are  $P_{k\theta}$ . The reconstruction problem is to find  $\rho_{ij}$  from  $P_{k\theta}$ .

The total density  $T$  of the object can be deduced from the sum of the projected densities  $P_{k\theta}$ . The degree of the approximation will depend of the size of the sampling interval between the points  $P_{k\theta}$  on the projections. The procedure of Gordon et al.<sup>13</sup> is iterative, with an initial state where all the  $\rho_{ij}$  are set equal to the total mean intensity

$$\rho_{ij}^0 = \frac{T}{n^2} \quad i, j = 1, 2, \dots, n \quad [2.44]$$

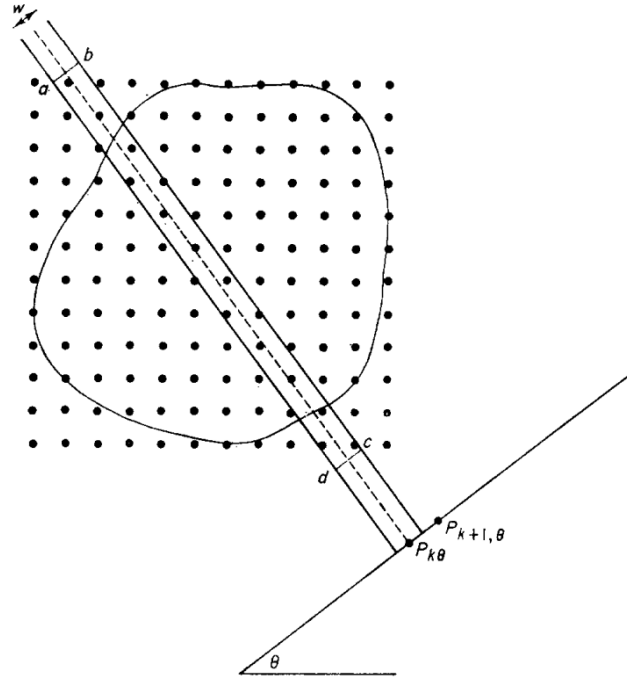


**Figure 2.4:**  $k$ th ray of width  $w$  at an angle  $\theta$ . The length of the ray is  $ad$  and the sum of densities at the points within  $abcd$  at the  $q$ th iteration of the reconstruction algorithm is  $R_{k\theta}$ . The projection density of the object along the middle of the ray is  $P_{k\theta}$  (adapted from P.Gilbert<sup>14</sup>).

Then the intensities are changed iteratively by one of two different procedures, called the multiplicative and the additive method, respectively. Let  $R_{k\theta}^q$  be the sum of intensities  $\rho_{ij}^q$  at the  $q$ th iteration contained within the ray  $k$  of projection  $\theta$ . Then

$$R_{k\theta}^q = \sum_{\text{the } N_{k\theta} \text{ points } (i,j) \text{ in ray } (k,\theta)} \rho_{ij}^q, \quad k = 1, 2, \dots, r_\theta \quad [2.45]$$

In the multiplicative method, the density is changed by the rule

$$\rho_{ij}^{q+1} = (P_{k\theta} / R_{k\theta}^q) / \rho_{ij}^q \quad [2.46]$$

and in the additive method by

$$\rho_{ij}^{q+1} = \max \left[ \rho_{ij}^q + \frac{(P_{k\theta} - R_{k\theta}^q)}{N_{k\theta}}, 0 \right] \quad [2.47]$$

for  $(i, j)$  in ray  $(k, \theta)$ , where  $N_{k\theta}$  is the number of points in the ray.

The formulae in equations [2.46] or [2.47] are applied to all rays of a given projection and then, to the next, subsequently. In these two equations and all the following formulae the rays are taken to have a width equal to the spacings in the reconstruction grid. Projected densities  $P_{k\theta}$  are expressed in terms of the same distance unit. Both algorithms ensure that the reconstructed densities are positive if the projection data are also positive.

### 2.2.3.b. *The Simultaneous Iterative Reconstruction Technique*

An alternative iterative algorithm for reconstructions more similar to the Fourier method can be formulated. This method has been called Simultaneous Iterative Reconstruction Technique (SIRT)<sup>14</sup> because at each iteration the densities are changed by using the data from all the projections simultaneously (in contrast, ART densities are changed by using data from one projection at a time). Analogously to ART, and setting  $\rho_{ij}^0$  to the mean density, the additive SIRT algorithm is

$$\rho_{ij}^{q+1} = \max \left[ \rho_{ij}^q + \frac{\sum P_{k\theta}}{\sum L_{k\theta}} - \frac{\sum R_{k\theta}^q}{\sum N_{k\theta}}, 0 \right], \quad [2.48]$$

where  $L_{k\theta}$  is the length of the ray  $R_{k\theta}$ . The multiplicative algorithm is

$$\rho_{ij}^{q+1} = \frac{\sum P_{k\theta} \cdot \sum N_{k\theta}}{\sum L_{k\theta} \cdot \sum R_{k\theta}^q} \rho_{ij}^q. \quad [2.49]$$

The summations in equations [2.48] and [2.49] are all over the projection points  $(k, \theta)$  where there is contribution of the density point  $\rho_{ij}$ , i.e., the number of projections used.

After the algorithms [2.48] or [2.49] are used for all densities  $\rho_{ij}^q$ , densities  $\rho_{ij}^{q+1}$  are scaled so that their sum over all the grid points is equal to the original sum of  $\rho_{ij}^0$ .

## **2.3. Methodology**

### **2.3.1. Materials: iron oxide nanocubes for in-vivo applications**

Once the theoretical procedure to reconstruct a volume from its projections has been shown, in this section, magnetic iron oxide nanocubes are used to illustrate a practical approach to electron tomography.

Magnetic nanoparticles are widely used for in vivo applications such as magnetic resonance imaging contrast enhancement, tissue repair, immunoassay detoxification of biological fluids, hyperthermia, drug delivery and cell separation<sup>15</sup>. Cellular labeling can be used in in vivo cell separation, as labeled cells are easily detected with magnetic resonance imaging (MRI). Tissue repair using magnetic nanoparticles can be achieved by two different approaches: welding, apposing two tissue surfaces then heating the tissue sufficiently to join, and soldering, where protein or polymer coated particles are placed between two tissues to enhance the junction<sup>16</sup>. Nanoparticles can be also used for site specific drug delivery, covering their large surface area with drugs. This can be used to reduce drug doses and potential side effects to healthy tissues and the costs associated with drug treatment. Magnetic induction hyperthermia is the exposition of cancer tissues to an alternating magnetic field. When magnetic particles are subjected to a variable magnetic field, heat is generated due to hysteresis losses. These particles embedded around a tumor site or endocytosed by malignant cells and placed within an alternating magnetic field can heat up to 43°C, a temperature at which tumor cells are destroyed, but the healthy ones

are not. And lastly, magnetofection is a method in which vector DNA is associated with magnetic nanoparticles in order to be transfected into cells by the application of an external magnetic field<sup>17</sup>.

The particles used in this chapter have been demonstrated to have superior magnetic heating efficiency, especially when assembled in chains, mimicking the bacterial magnetosomes<sup>18</sup>. The geometry of the cluster formed by these nanocubes is then, clearly, most crucial for its final magnetic properties. The HAADF tomography characterization of a cluster of Fe oxide nanocubes will be shown in the following sections.

Iron oxide nanocubes were prepared by heating a solution of iron(III) acetylacetonate ( $\text{Fe}(\text{acac})_3$ ), decanoic acid and dibenzylether. 0.353 g (1 mmol) of  $\text{Fe}(\text{acac})_3$  was mixed with 0.688 g (4 mmol) of decanoic acid in 25 mL of dibenzyl ether. After a short vacuum step at 60  $\mu\text{K}$  (30 minutes), the solution temperature was first raised up to 200  $\mu\text{C}$  with a constant rate of 2.6  $\mu\text{K}/\text{min}$ , and kept at this temperature for 2 h under an argon flow and vigorous stirring. In a second step, the solution was heated to reflux temperature with a heating rate of 1.7  $\mu\text{K}/\text{min}$ . After 1 h the solution was cooled down and acetone was added. Nanoparticles were then collected by centrifugation at 8000 rpm and redispersed in chloroform. This procedure was repeated at least two times in order to get rid of the excess of surfactant.

Electron tomography studies were carried out in the FEI Tecnai F20-G2. Other images were obtained in the JEOL JEM 2100.

This sample was kindly provided by Dr. Carlos Martínez-Boubeta, from the Electronics Department of the University of Barcelona.

### **2.3.2. Data acquisition**

In order to fulfill the projection requirement<sup>19</sup>, the contrast in the image of an object must change monotonically with a property of the object itself. Bright field (BF) images, such as those of iron oxide nanocubes presented in Figure 2.5, have sudden changes in intensity when tilting. The crystalline nature of the samples causes the BF

images (both in CTEM and STEM) to suddenly change contrast when in Bragg conditions, as the dark cubes in Figure 2.5 (b). These changes cause the images to fail the projection requirement. HAADF STEM images yield an intensity which only depends on the thickness and the effective Z of the material and, therefore, are usually chosen for the acquisition of a tilt series.

Before acquiring a tilt series of data, a favorable particle or particle group must be identified. This part of the sample has to be tilted without significant overlapping of its particles and without shadowing from other particles or the copper grid. A preliminary tilting of the sample ensures that none of the previous problems takes place in a sufficiently large range and, therefore, gives the higher and lower bounds of the tilting range, where shadowing happens.

As previously explained, the quality of a reconstruction greatly depends on the number of projections acquired and the missing wedge, the angles at which images cannot be acquired. A tilt series with a missing wedge of over  $60^\circ$  should be avoided.

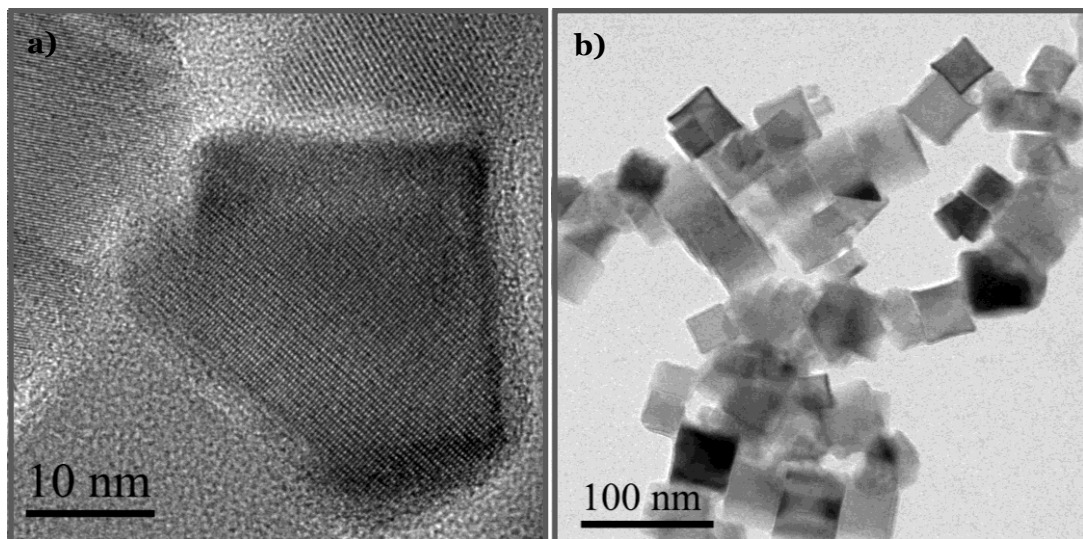


**Figure 2.5:** **a)** HRTEM and **b)** general BF images of iron oxide nanocubes.

As an example, for the Fe nanocubes in Figure 2.5, a series of STEM HAADF images was acquired at angles ranging from  $-64^\circ$  to  $64^\circ$  at intervals of  $4^\circ$  in order to prevent contamination. If the sample is placed at eucentric height, the area used for the acquisition should not move from the imaging area when tilting and it should remain roughly in focus. However, at high magnifications (320k for the nanocubes) the precision of eucentric height determination is not enough to prevent the sample

drifting when tilting. Therefore, for each tilt step and especially at  $4^\circ$  step, which can be considered as a high step size, drift and focus need to be corrected, lest the quality of the reconstruction decreases. Acquisition needs to be carried out up to the highest tilt angle, in order to minimize the missing wedge. The effects of elongation and loss of resolution in the optical axis direction are illustrated in Figure 2.6, where the reconstruction of the nanocubes shows a clear loss in definition in beam direction.

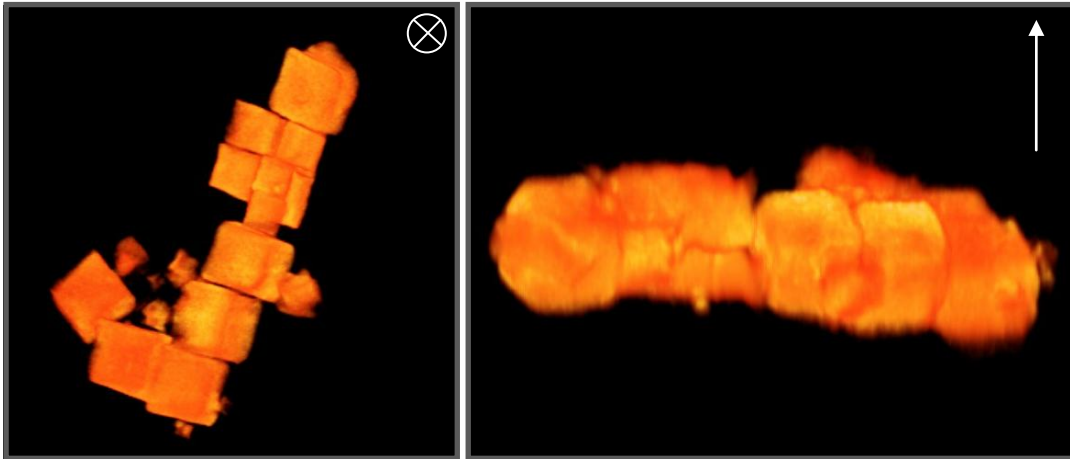


**Figure 2.6:** Direct visualization of the reconstruction of the nanocube tilt series. Arrows indicate the optical axis at  $0^\circ$  tilt, the direction where the elongation due to the missing wedge can be observed. The cubes are roughly 40 nm wide.

### 2.3.3. Data treatment

Data treatment consists of three main steps. First of all, it is necessary to align all images and find the tilt axis, so that the images can be back-projected in angles as precise as possible. Then the reconstruction algorithm is launched, resulting in volume data. Last, these data must be treated with a visualization software so that the information can be appropriately presented.

### 2.3.3.a. Image alignment and tilt axis identification

Accurate alignment of the projection images is of great importance for obtaining high quality tomographic reconstructions. Ideally, all images are a projection of the same 3D object at a known angle. However, during the acquisition, a certain spatial drift between the images is to be expected, having a greater importance in manual acquisitions. As the datasets presented in this work are all single tilt acquisitions, we will suppose that there are no rotations or changes in magnification between the images, a supposition that can be made if the image focus is corrected by adjusting the height of the sample after each tilt.

The shifts between consecutive images are measured by cross-correlation procedures. In order to enhance the details that give a more accurate correlation, the images are previously filtered. There are a number of possible filters in Inspect 3D, which is the usual software of choice for tomographic series alignment. Amongst them, applying a threshold to keep only the brighter parts of the images; a bandpass filter, to enhance the spatial frequencies which best describe the shape of the objects; morphological filters such as erosion or dilation, which reduce or enhance small changes in the image; and a Sobel filter, which enhances the edges by differentiating the image. Once the images are filtered, the cross-correlation between two images  $f$  and  $g$  is calculated either in real space:

$$h(m, n) = \frac{1}{MN} \sum_{M=0}^{M-1} \sum_{N=0}^{N-1} f(j, k)g(j + m, k + n) \quad [2.1]$$

or in Fourier space:

$$H(u, v) = F(u, v)G^*(u, v) \quad [2.2]$$

The cross correlation array will have a maximum at the shift between the two images. The alignment problem means identifying the maxima of the correlations pairwise as the relative shift parameters. This step is much easier for tilt angles below  $2^\circ$ , as the cross correlation gives better results. In Figure 2.7, a representation of the measured shifts in an intermediate aligning step for the nanocubes is shown.

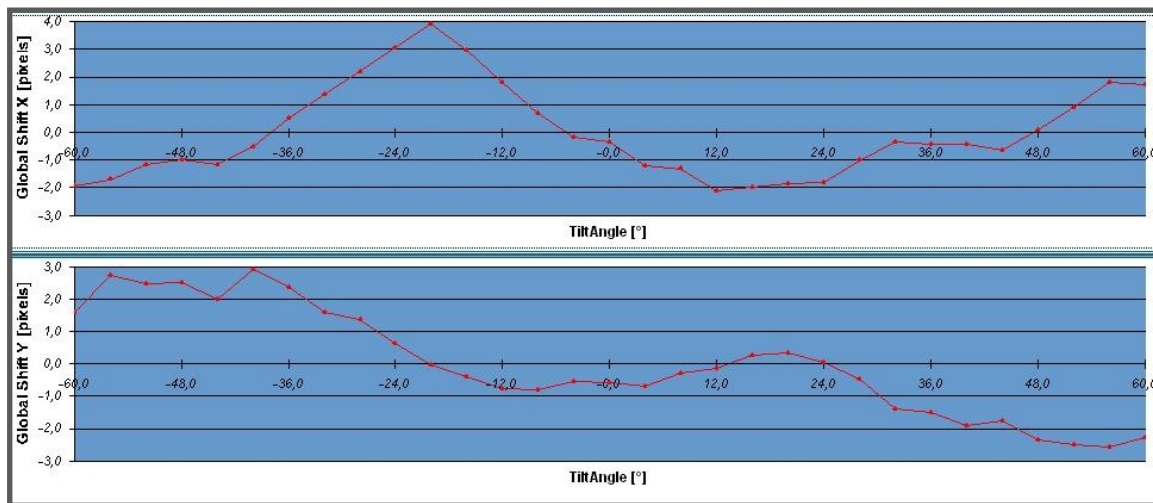


**Figure 2.7:** image shift alignment measurements in x and y directions.

After the image shift is recursively corrected, it is necessary to find the right tilt axis. The software also performs a weighted backprojection (WBP) of three slices in order to find the right tilt axis. The axis has to be shifted and tilted until a correct position is found. For tilt axis correction, the user has to identify banana shaped artifacts, which arise from the misalignment, in the three slices. The direction and intensity of the bananas in a top, center and bottom slice helps manually correcting the axis position. When the artifact is corrected for the central slice by shifting the axis, one point of the axis is already known. If the angle of the tilting axis with respect to the images is not the default vertical one given in the software, the other two slices still present the banana artifacts. By correcting them for the two images we find three points which describe the actual tilt axis.

In Figure 2.8, the major steps in the tilt axis alignment for the nanocube sample are shown. The first row shows bananas in all of the images, all pointing to the same direction (Figure 2.8 (a-c)). The axis is then shifted and manually corrected until no bananas appear in the central slice, as shown in the second row (Figure 2.8 (d-f)). There, it can be observed that top and bottom slices have bananas pointing to opposite directions. Then the axis is tilted until they are minimized for all images, as it is observed in the bottom row (Figure 2.8 (g-i)). Correctly finding the tilt axis will greatly influence the quality of the reconstruction.

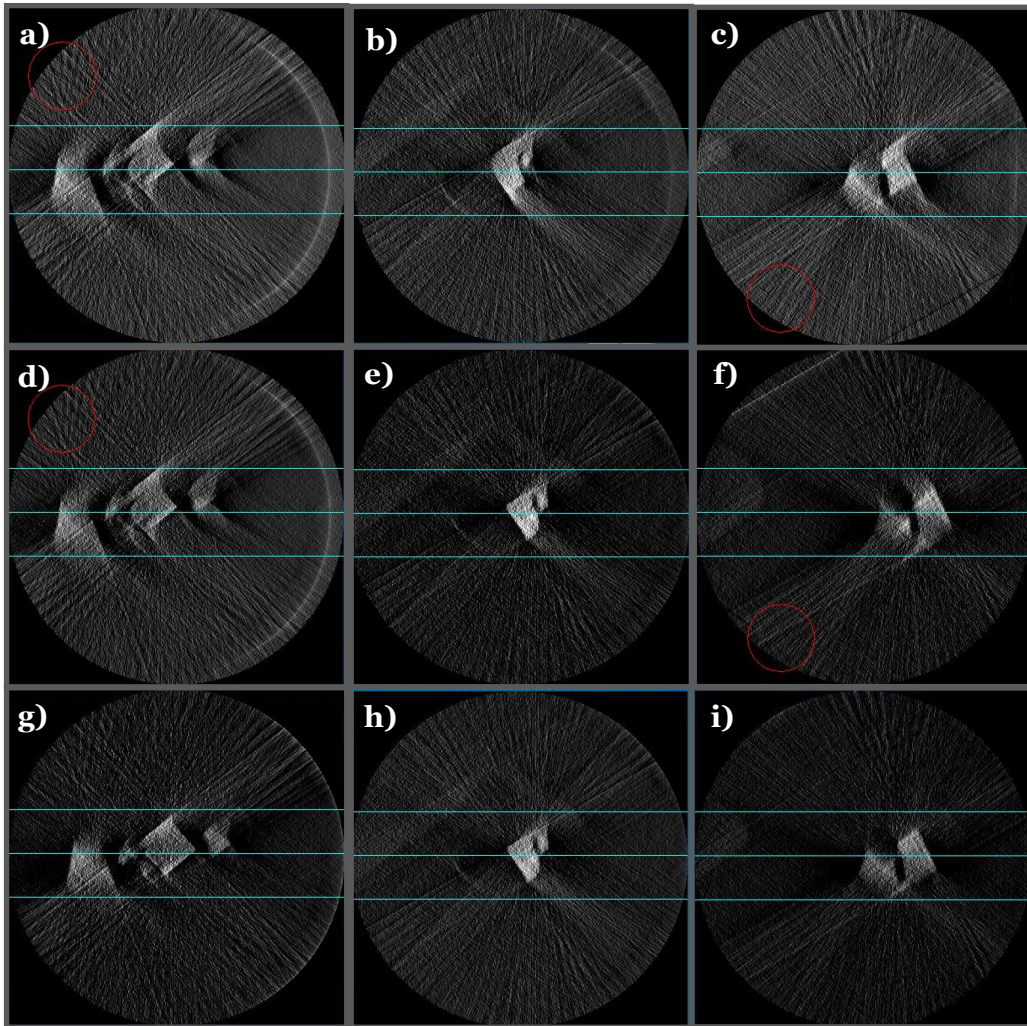


**Figure 2.8:** image tilt axis: images of a top, central and bottom slice WBP reconstruction perpendicular to  $z$  in left, central and right column. **a), b)** and **c)** show “banana” artifacts due to reconstructing using a tilt axis wrongly shifted. **d), e)** and **f)** show “banana” artifacts due to a bad inclination alignment of the axis. **g), h)** and **i)** are reconstructions with a well aligned tilt axis.

### 2.3.3.b. Reconstruction

Inspect3D, the same software used for image alignment, can perform 3D reconstructions. Available algorithms are filtered Back-projection, ART and SIRT. In the context of this thesis, SIRT was mostly used, as this algorithm gives the best results for particle shape recovery and is the most used one in materials science. A higher

number of SIRT iterations yields higher contrast, but increases the noise as well. Therefore, the number of iterations must be a compromise between the contrast needed and the noise that can be handled. In Figure 2.9, a comparison between the three mentioned reconstruction algorithms is shown. WBP is the fastest technique, but with the drawback of producing results with lower signal to background ratio. ART with 40 iterations yields a good signal, but the intensities inside the sample are somewhat incorrect. SIRT with the same number of iterations shows the best definition of the particles while keeping a good signal to background ratio.

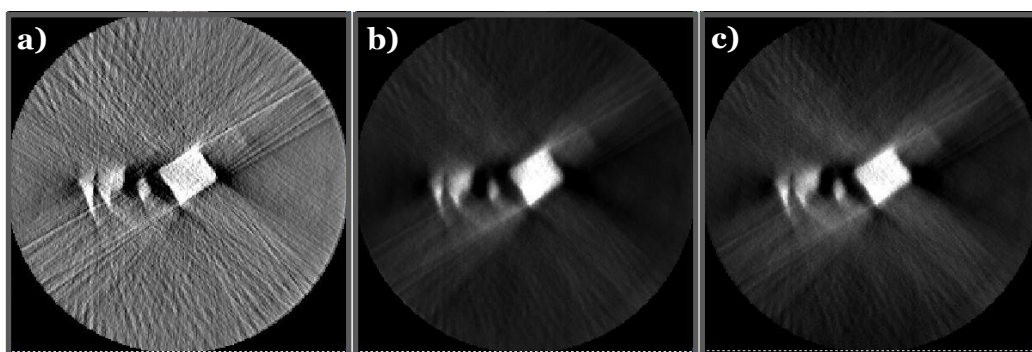


**Figure 2.9:** Reconstruction of a slice of the nanocube cluster using **a)** WBP, **b)** ART (40 iterations) and **c)** SIRT (40 iterations).

### 2.3.3.c. Visualization

Getting the most of the information in a tomogram is the goal of visualization. There are two major objectives in visualization: the first one is to fully understand the structure of the object in the third dimension and the second one is to present the results in a straightforward way so that they can be readily understood. The chosen software was Amira (now Avizo), which is a long running visualization software for life and materials sciences. This software is especially well suited for electron tomography, because it enables the user to manually segment the volume (make it discrete) using orthoslices in the three space axes. Visualization techniques can be divided in two groups: direct or indirect. Direct techniques consist on mapping every value in the dataset to a color and opacity. It is used either in the full volume (Voltex representation) or in 2D slices. Indirect visualization requires much less computing power, as only a few values are shown. For example, isosurfaces only show those voxels

with a given intensity value; thus, by discretizing the volume, only the frontiers of the components are shown.

Examples of direct visualizations are given in Figure 2.10 (a) and (b), which represent 2D slices of the reconstructed volume. In (b), the vertical direction corresponds to the optical axis at  $0^\circ$  tilt, around which the missing wedge is centered. The loss of resolution in this direction can be observed, as well as the streaking that fans out of the reconstruction. The software also allows 3D direct visualization, *voltex* type (Figure 2.11 (a)), in which the user can introduce intensities, colors and transparency to the grey level 3D model.

Indirect visualizations are mainly recovered from isosurfaces or segmented volumes. The visualization of the nanocube cluster with an isosurface is observed in Figure 2.10 (c) and (d). In electron microscopy, isosurfaces are usually a poor representation of the volume, as the changes of intensity in the reconstructed volume are notable (as seen in the orthoslices in Figure 2.10 (a) and (b)). Therefore segmentation is the major step in indirect visualization. It consists on finding surfaces which can describe the sample. In one-compound samples, this surface is the interface between the sample and the environment and in multi-compounds these surfaces can be the frontiers between the different materials. Manual segmentation or semi-manual segmentation can correct for the encountered artifacts, namely elongation, rising from the missing wedge. Moreover, filters can also be applied to the surface, usually low-pass ones, in order to correct smaller artifacts introduced by the manual correction. The results of segmenting the volumes are shown in Figure 2.11 (b), where a single cube is highlighted amongst the cluster. See the animated results in the supplementary files, movie 1.

Summing up this section, the whole procedure of data acquisition, alignment, reconstruction and visualization has been explained using an iron oxide nanocube sample. In the next section, HAADF STEM tomography will be applied to  $\text{Cu}_2\text{O}$  nanoparticles samples. In this case, the focus of the section will be in the materials science problems that can be resolved using electron tomography rather than the experimental procedure of reconstruction.

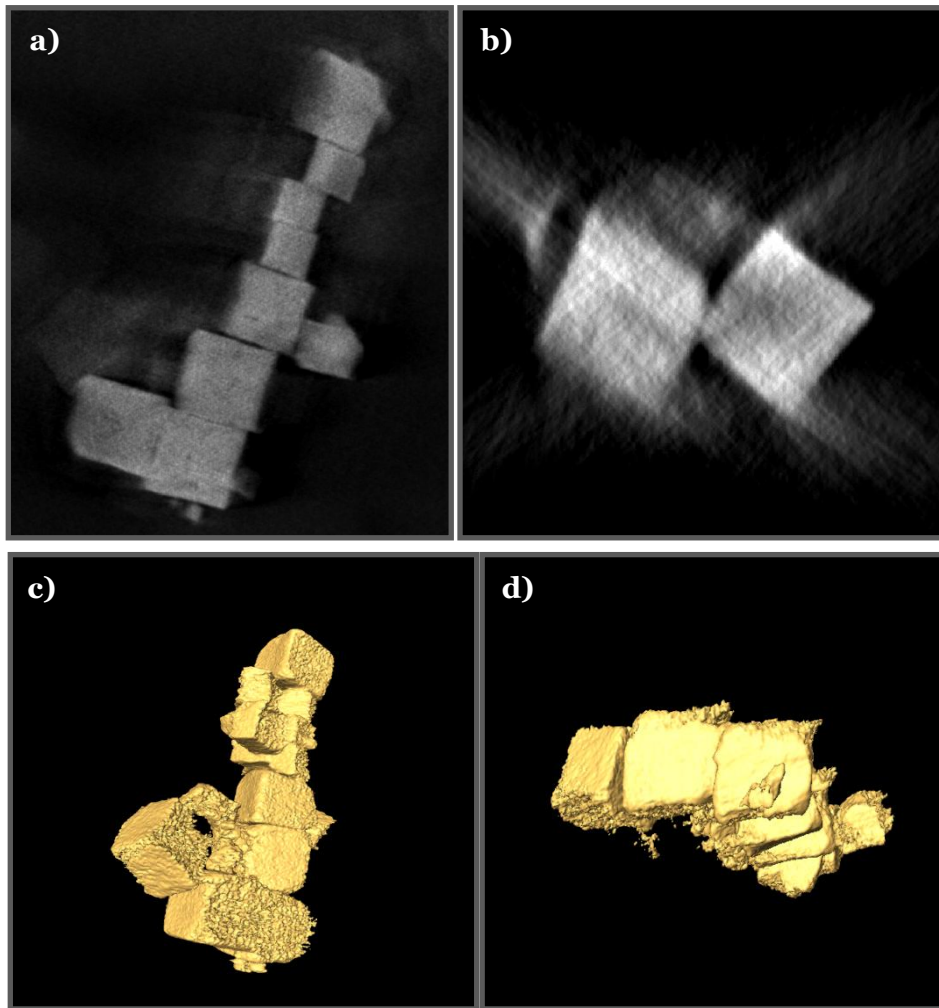


**Figure 2.10:** **a)** Slice through the reconstructed volume perpendicular to the optical axis. **b)** Slice through the reconstructed volume in a plane containing the optical axis. **c)** and **d)** Indirect visualizations (isosurfaces) of the reconstructed volume of the nanocube cluster.

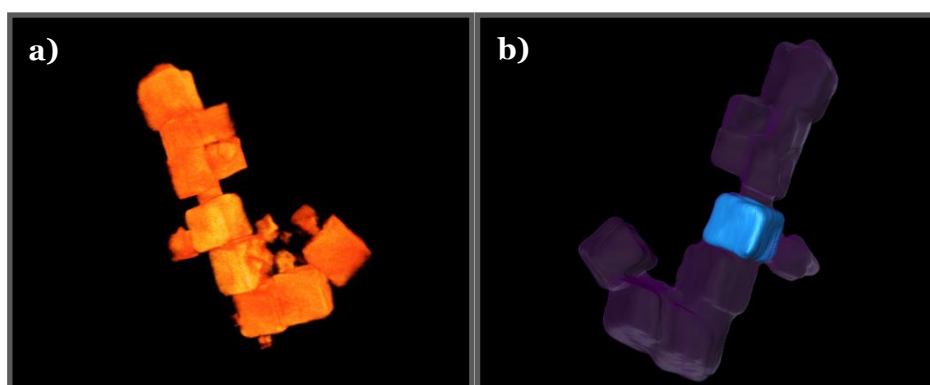


**Figure 2.11:** **a)** 3D volume visualization of the reconstructed volume of the nanocubes and **b)** visualization of the surface of the segmented volume of one nanocube (in blue) amongst the nanocube cluster (in purple)

## 2.4. Faceting of Cu<sub>2</sub>O nanoparticles: an application of HAADF tomography

In this section, a series of Cu<sub>2</sub>O nanoparticles will be characterized by means of electron tomography. Cu<sub>2</sub>O is a p-type semiconductor with a direct band gap of about 2.0 eV and has the advantage of being inexpensive, plentiful, having low toxicity and good environmental acceptability<sup>20</sup>. These characteristics have favored its fundamental and practical research in many fields.

One of the first applications for Cu<sub>2</sub>O was on photovoltaic solar cells. The band gap of 2.0 eV of the material and a high absorption coefficient mean theoretical conversion efficiencies of 23%. Early studies in the seventies and eighties reported a much lower efficiency, of about 1-2%<sup>21</sup>. More recent studies have reached efficiencies of around 4%<sup>22, 23</sup>, the highest reported on all metal oxide absorbers<sup>24</sup>. Copper compounds in the shape of nanoparticles have been used for catalyzing organic reactions. They were first applied as cocatalysts<sup>25-30</sup> to reduce the amount of palladium nanoparticles traditionally used in Stille cross-coupling reactions, thus reducing its costs. Nowadays, the use of copper as a single catalyst is attracting more interest<sup>31-36</sup> and Cu<sub>2</sub>O nanoparticles have shown promising performances as catalysts<sup>37</sup>. They have also been used as electrodes for lithium ion batteries<sup>38-40</sup>, gas sensors<sup>41</sup> and magnetic storage devices<sup>42-44</sup>. One of the most interesting applications of Cu<sub>2</sub>O nanoparticles comes from the combination of the light absorption and catalytic properties. They have been used as photocatalysts for degradation of organic pollutants<sup>45</sup> and water decomposition to O<sub>2</sub> and H<sub>2</sub> under visible light<sup>46-51</sup>.

The properties of the particles are highly dependent on their surface area and their crystallinity<sup>20</sup>. The crystalline plane at the surface is the main source of catalytic

activity and sensor performance. In copper oxide particles, the  $\{111\}$  facets are found to interact well with negatively charged molecules, while  $\{001\}$  facets are less sensitive to molecular charges<sup>52</sup>. Therefore, it is of vital importance to characterize the shape and crystal structure of the nanoparticles in order to correlate the structural properties to their applications. In this section, we will show the three dimensional characterization of a series of  $\text{Cu}_2\text{O}$  nanoparticles as well as its correlation to the crystal structure, in order to determine the surface planes.

### 2.4.1. Experimental details

Three different types of copper oxide nanoparticles have been studied. Small variations in the growth process produced notable changes in the shape of the particles, which is the main interest of this study. In order to grow the particles, water,  $\text{CuCl}_2$  solution, sodium dodecyl sulfate surfactant,  $\text{NH}_2\text{OH}\cdot\text{HCl}$  reductant, and  $\text{NaOH}$  were added in the sequence listed, and the mixture was aged for 2 h to obtain the products. The systematic variation in the product morphology can be controlled by changing the amount of reductant added. By simply varying the amount of  $\text{NH}_2\text{OH}\cdot\text{HCl}$  added from 0.15 to 0.95 ml, different  $\text{Cu}_2\text{O}$  nanocrystals with sharp faces were synthesized. In increasing reductant agent quantity, samples are named (i), (ii) and (iii) respectively.

The samples were kindly provided by Dr. Daniel Prades from the electronics department of the University of Barcelona and Dr. Hao Shen, from the Institut für Halbleitertechnik, Technische Universität Braunschweig.

The acquisition of the tilt series (carried out in the JEOL JEM 2100) for the three samples ranged as follows:

- (i): -70 to 72 degrees, with images acquired each 2 degrees.
- (ii): Two tilt series, ranging from -66 to 70 degrees and from -74 to 70 degrees respectively, at 2 degrees tilt step.
- (iii): -70 to +70 degrees, acquiring an image every 2 degrees.

HAADF STEM images were acquired using the automatic procedure included in Gatan Digital Micrograph. The datasets were aligned and reconstructed in Inspect 3D,

using 40 iterations of the SIRT algorithm. The visualization was obtained in Avizo. The indexation of diffraction patterns was carried out using Digital Micrograph and Carine software. See the supplementary files for the animated reconstructions, movies 2 to 5.

### 2.4.2. Results and discussion

For each individual sample, in conventional TEM images the 3D shape of the particles was not clear and their shape homogeneity was not evident. Moreover, while clearly polyhedral, no further details about the 3D structure could be extracted from the projections. The first objective was to link the actual 3D shape of the particles with the observed projections in the CTEM images.

In the original CTEM images of sample (i), the particles were apparently square, as observed in Figure 2.12 (a). When tilted (Figure 2.12 (c)), the particles were seen as hexagons, so that a good 3D shape candidate could be a cubic particle. The reconstructed particle was not cubic, as seen in Figure 2.13, because two of the cube faces had extra facets, and the four vertices linking these two opposite faces were flattened. However, all of the original projections seen in CTEM images could be recovered as projections of the 3D reconstructed particle. The square shape is recovered in Figure 2.13 (a) and (c) and the hexagonal projection can be recovered as in Figure 2.13 (b). In this case, the particles were found to be polycrystalline, as shown in Figure 2.12 (b).

In sample (ii), the shape of the particles was not found to be homogeneous in the projections, although they were found to be monocrystalline. In Figure 2.14, the shape distribution found in the sample can be observed, which cannot be attributed directly to any regular polyhedron. Two different tomographic reconstructions were acquired. The results are shown in Figure 2.15 and Figure 2.16 respectively. The reconstructions show two irregular particles, with facets of different shapes. From projections of the reconstructed particles it was not possible to recover the shapes of all the particles present in the CTEM images. The particles are thus irregular, and not homogeneous in shape.

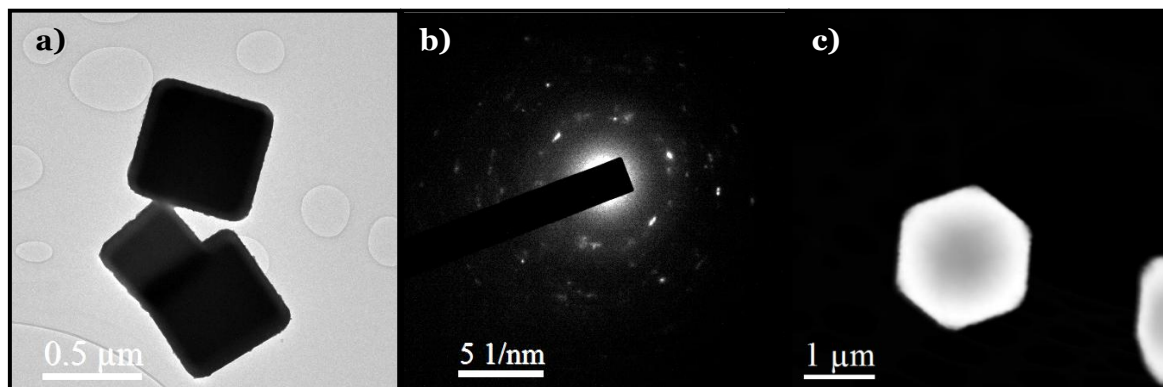


**Figure 2.12:** **a)** CTEM image of three particles and **b)** corresponding diffraction pattern of the upper particle. **c)** HAADF STEM image of the particle used in the reconstruction at  $-66^\circ$

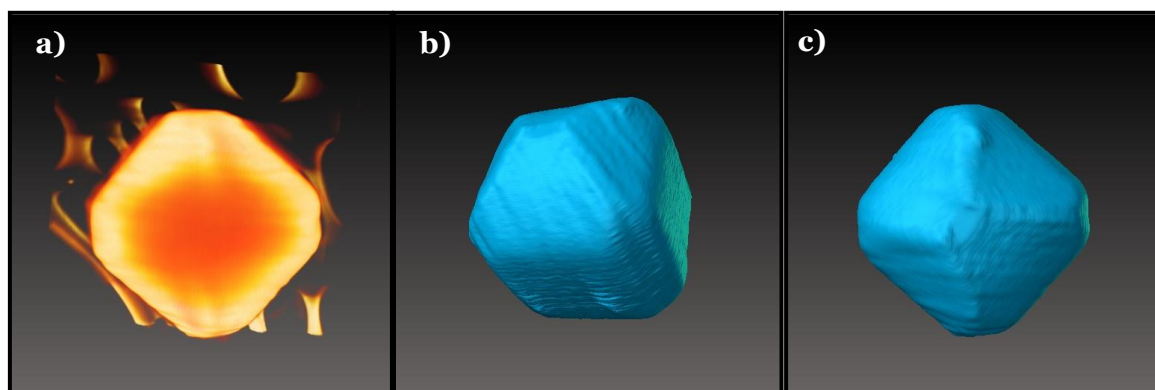


**Figure 2.13:** **a)** Voltex visualization of the reconstructed particle, oriented to match the projections in Figure 2. (a). **b)** and **c)** surface rendering of the reconstructed particle.

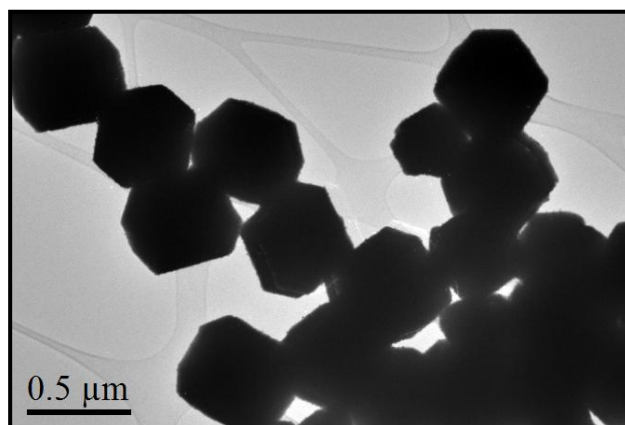


**Figure 2.14:** CTEM image of a group of particles.

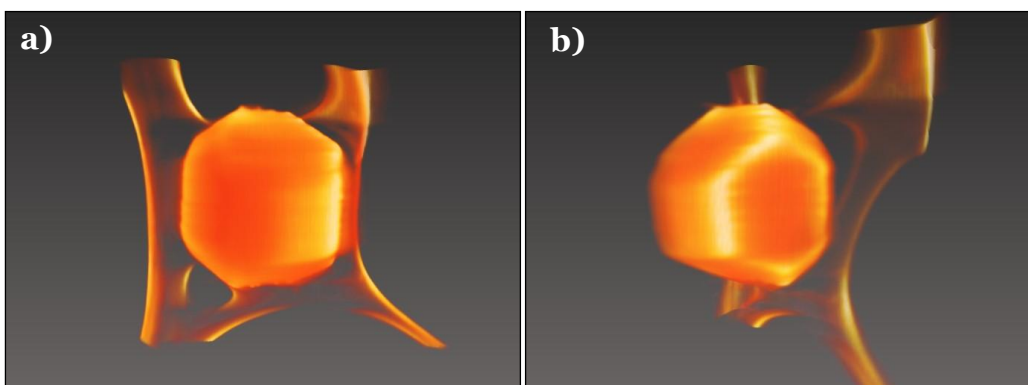


**Figure 2.15:** Voltex visualization of a reconstructed particle from a HAADF STEM tilt series ranging from  $-66^{\circ}$  to  $70^{\circ}$ .

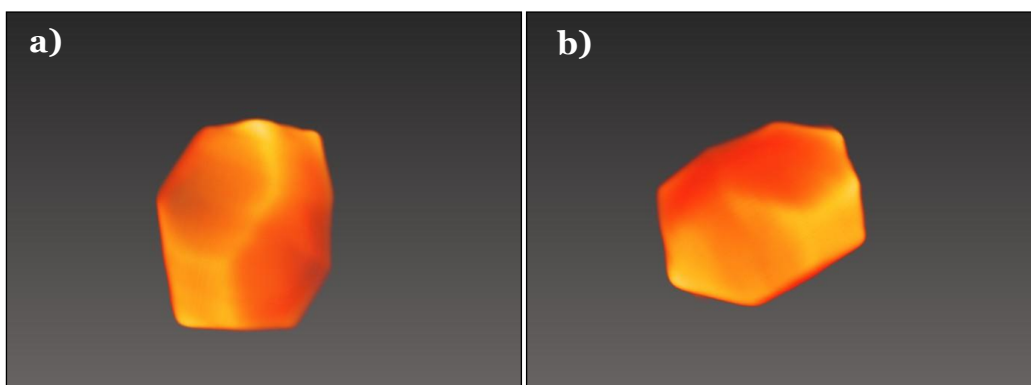


**Figure 2.16:** visualization of a reconstructed particle from a HAADF STEM tilt series ranging from  $-74^{\circ}$  to  $70^{\circ}$ .

The TEM images of sample (iii) showed 3 different morphologies, in projection: rhombohedral (Figure 2.17 (a)), hexagonal (Figure 2.18 (a)) and square (Figure 2.19 (a)). The results of the reconstruction are shown in Figure 2.17 (b) and (c). From the 3D visualizations, it becomes clear that the sample consists on regular octahedra with truncated vertices. The next step is to recover the shapes in the original CTEM images from different projections of the reconstructed polyhedron.

An hexagonal shape was observed in many particles, such as the one in Figure 2.18 (a). This corresponds to the octahedra observed perpendicularly to one of the triangular facets, as shown in Figure 2.18 (c). In Figure 2.19 the square shaped particles are found to correspond to the projections of the octahedra when observed parallel to the vertices.

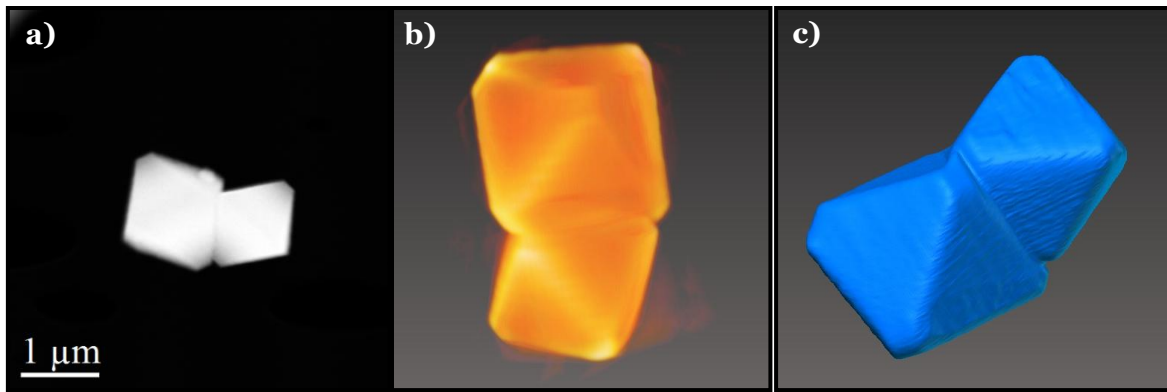


**Figure 2.17:** Images of the 3D reconstruction of two nanoparticles. **a)** HAADF STEM image at  $-70^\circ$  before reconstruction. **b)** Voltex visualization of the reconstructed particles and **c)** surface rendering of the truncated octahedra.

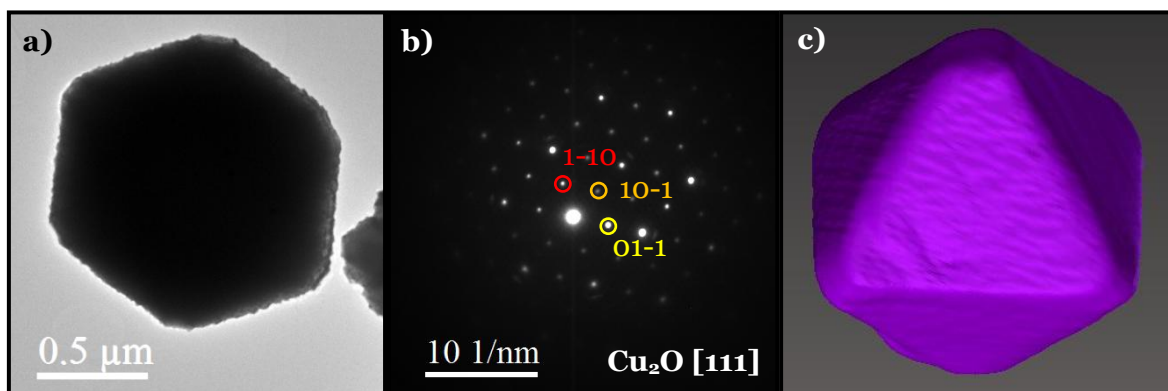


**Figure 2.18:** **a)** CTEM image of one particle and **b)** corresponding diffraction pattern. The zone axis (ZA) is found to be  $[111]$ . **c)** Reconstructed particle oriented to match the projection in **a)**; in this image, one particle facet is perpendicular to the viewing direction, meaning that the bigger facets correspond to  $(111)$  planes.

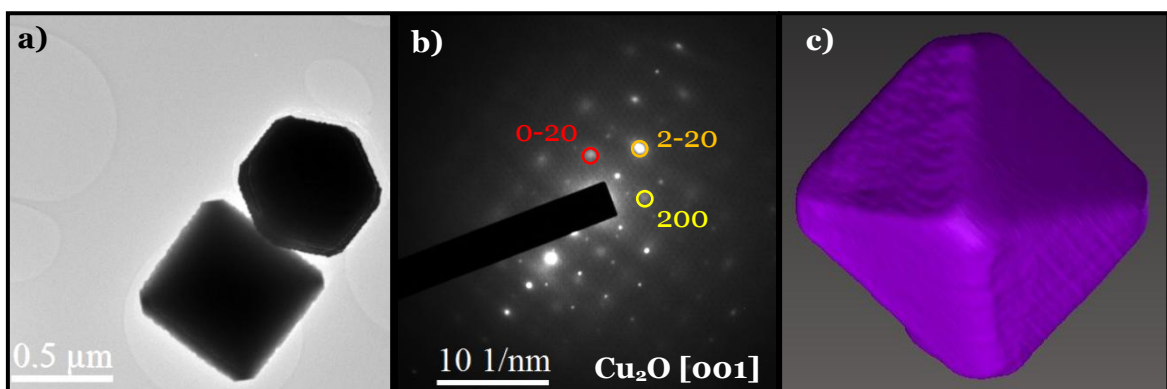


**Figure 2.19:** **a)** CTEM image of two particles and **b)** diffraction pattern of the lower particle. The zone axis (ZA) is found to be  $[001]$ . **c)** Reconstructed particle oriented to match the projection in **a)**; in this image one truncated vertex is perpendicular to the viewing direction.

Diffraction patterns were acquired for the square and hexagonal projected shapes (Figure 2.18 (b) and Figure 2.19 (b) respectively). The zone axes were found to be [111] and [001] respectively. As Cu<sub>2</sub>O crystallizes in the spatial group  $Pn\bar{3}m$ , which is cubic, the angle between both zone axes is 45°, exactly the same rotation needed in the 3D reconstruction to recover the projections in the CTEM images.

From the reconstructions and the diffraction patterns, we can deduce that the faces of the octahedron, constituting the surface, correspond to {111} planes, and the truncated vertices are small {001} facets. As a sanity check, the structure of the particles was simulated using Rhodius<sup>53, 54</sup>. In Figure 2.20, a Cu<sub>2</sub>O particle is simulated as observed from different crystal orientations ([001], [110] and [111], respectively) to recover the square (a), rhombohedral (b) and hexagonal (c) projections.

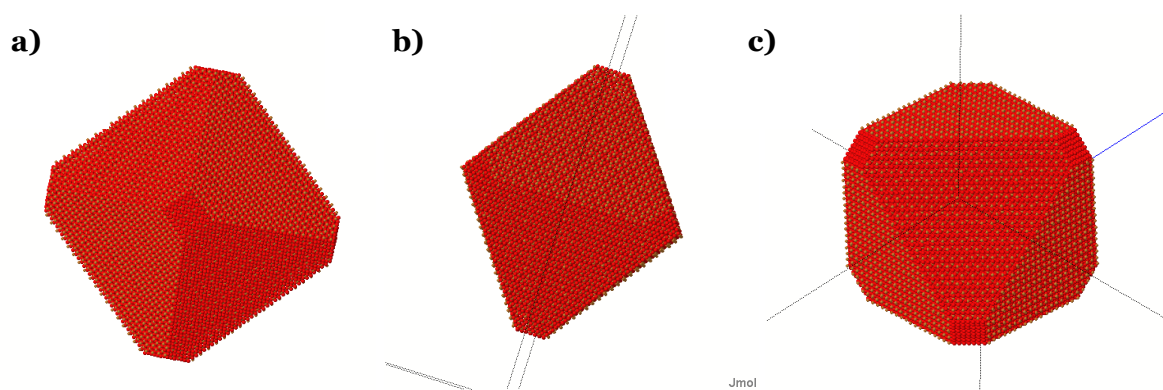


**Figure 2.20:** Simulations of the particles in Rhodius, viewed along the **a)** [001], **b)** [110] and **c)** [111] zone axes.

### 2.4.3. Conclusions

Electron tomography was applied to solve an important problem in nanoparticle growth: the determination of the faceting of the particles. Three different kinds of Cu<sub>2</sub>O nanoparticles were studied. The first kind presented a regular homogeneous shape, but was polycrystalline. The second kind of particles was monocrystalline, but irregular and

inhomogeneous in shape. The third sample consisted on octahedral monocrystalline nanoparticles with facets corresponding to the  $\{111\}$  and  $\{001\}$  planes of  $\text{Cu}_2\text{O}$ .

The results of these analyses are of great importance for the understanding of the properties of the nanoparticles once they are tested for their final use.

This section has been an example of the conventional use of electron tomography in the TEM for shape reconstruction. The rest of this thesis is devoted to follow the necessary steps to add a fourth, chemical, dimension to the reconstructions.

## 2.5. References

1. Batenburg, K. J., et al. 3D imaging of nanomaterials by discrete tomography. *Ultramicroscopy* **109**, 730-740 (2009).
2. Roelandts, T., et al. Accurate segmentation of dense nanoparticles by partially discrete electron tomography. *Ultramicroscopy* **114**, 96-105 (2012).
3. Thomas, J. M., Leary, R., Midgley, P. A. & Holland, D. J. A new approach to the investigation of nanoparticles: Electron tomography with compressed sensing. *J.Colloid Interface Sci.* **392**, 7-14 (2013).
4. de Rosier, D. & Klug, A. Reconstruction of 3 Dimensional Structures from Electron Micrographs. *Nature* **217**, 130-134 (1968).
5. Crowther, R., de Rosier, D. & Klug, A. Reconstruction of 3 Dimensional Structure from Projections and its Application to Electron Microscopy. *Proceedings of the Royal Society of London Series A-Mathematical and Physical Sciences* **317**, 319-340 (1970).
6. Nyquist, H. Certain topics in telegraph transmission theory (Reprinted from Transactions of the A. I. E. E., February, pg 617-644, 1928). *Proc IEEE* **90**, 280-305 (2002).
7. Vainshtein, B. Finding Structure of Objects from Projections. *Soviet Physics Crystallography, USSR* **15**, 781 (1971).
8. Radermacher, M., Wagenknecht, T., Verschoor, A. & Frank, J. A New 3-D Reconstruction Scheme Applied to the 50s Ribosomal-Subunit of Escherichia-Coli. *J.Microsc.-Oxf.* **141**, RP1-RP2 (1986).
9. Radermacher, M., Wagenknecht, T., Verschoor, A. & Frank, J. 3-Dimensional Reconstruction from a Single-Exposure, Random Conical Tilt Series Applied to the 50s-Ribosomal Subunit of Escherichia-Coli. *Journal of Microscopy-Oxford* **146**, 113-136 (1987).
10. Radermacher, M. Weighted Back-projection Methods. 245-273 (2006).
11. Hoppe, W., Schramm, H., Sturm, M., Hunsmann, N. & Gassman, J. 3-Dimensional Electron-Microscopy of Individual Biological Objects .1. Methods. *Zeitschrift Fur Naturforschung Section A-a Journal of Physical Sciences* **31**, 645-655 (1976).
12. Bracewell, R. N. Two-dimensional aerial smoothing in radio astronomy. *Australian Journal of Physics* **9**, 297-314 (1956).

13. Gordon, R., Bender, R. & Herman, G. T. Algebraic Reconstruction Techniques (ART) for three-dimensional electron microscopy and X-ray photography. *J.Theor.Biol.* **29**, 471-481 (1970).
14. Gilbert, P. Iterative methods for the three-dimensional reconstruction of an object from projections. *J.Theor.Biol.* **36**, 105-117 (1972).
15. Gupta, A. K. & Gupta, M. Synthesis and surface engineering of iron oxide nanoparticles for biomedical applications. *Biomaterials* **26**, 3995-4021 (2005).
16. Lobel, B., Eyal, O., Kariv, N. & Katzir, A. Temperature controlled CO<sub>2</sub> laser welding of soft tissues: Urinary bladder welding in different animal models (rats, rabbits, and cats). *Lasers Surg.Med.* **26**, 4-12 (2000).
17. Scherer, F., et al. Magnetofection: Enhancing and targeting gene delivery by magnetic force in vitro and in vivo. *Gene Ther.* **9**, 102-109 (2002).
18. Martinez-Boubeta, C., et al. Learning from Nature to Improve the Heat Generation of Iron-Oxide Nanoparticles for Magnetic Hyperthermia Applications. *Scientific Reports* **3**, 1652 (2013).
19. Hawkes, P. W. The Electron Microscope as a Structure Projector. 83-111 (2006).
20. Singhal, A., et al. Copper(I) Oxide Nanocrystals - One Step Synthesis, Characterization, Formation Mechanism, and Photocatalytic Properties. *European Journal of Inorganic Chemistry* 2640-2651 (2013).
21. Briskman, R. N. A Study of Electrodeposited Cuprous-Oxide Photovoltaic Cells. *Solar Energy Mater.Solar Cells* **27**, 361-368 (1992).
22. Minami, T., Nishi, Y., Miyata, T. & Nomoto, J. High-Efficiency Oxide Solar Cells with ZnO/Cu<sub>2</sub>O Heterojunction Fabricated on Thermally Oxidized Cu<sub>2</sub>O Sheets. *Applied Physics Express* **4**, 062301 (2011).
23. Nishi, Y., Miyata, T. & Minami, T. Effect of inserting a thin buffer layer on the efficiency in n-ZnO/p-Cu<sub>2</sub>O heterojunction solar cells. *Journal of Vacuum Science & Technology a* **30**, 04D103 (2012).
24. Ruehle, S., et al. All-Oxide Photovoltaics. *Journal of Physical Chemistry Letters* **3**, 3755-3764 (2012).
25. Casado, A. L. & Espinet, P. Quantitative evaluation of the factors contributing to the "copper effect" in the Stille reaction. *Organometallics* **22**, 1305-1309 (2003).
26. Dubbaka, S. R. & Vogel, P. Palladium-catalyzed stille cross-couplings of sulfonyl chlorides and organostannanes. *J.Am.Chem.Soc.* **125**, 15292-15293 (2003).
27. Gallagher, W. P., Terstiege, I. & Maleczka, R. E. Stille couplings catalytic in tin: The "Sn-O" approach. *J.Am.Chem.Soc.* **123**, 3194-3204 (2001).
28. Kim, W. S., Kim, H. J. & Cho, C. G. Regioselectivity in the Stille coupling reactions of 3,5-dibromo-2-pyrone. *J.Am.Chem.Soc.* **125**, 14288-14289 (2003).

29. Mazzola, R. D., Giese, S., Benson, C. L. & West, F. G. Improved yields with added copper(I) salts in carbonylative Stille couplings of sterically hindered vinylstannanes. *J.Org.Chem.* **69**, 220-223 (2004).
30. Mee, S. P. H., Lee, V. & Baldwin, J. E. Significant enhancement of the Stille reaction with a new combination of reagents-copper(I) iodide with cesium fluoride. *Chemistry-a European Journal* **11**, 3294-3308 (2005).
31. Allred, G. D. & Liebeskind, L. S. Copper-mediated cross-coupling of organostannanes with organic iodides at or below room temperature. *J.Am.Chem.Soc.* **118**, 2748-2749 (1996).
32. Beletskaya, I. P. & Cheprakov, A. V. Copper in cross-coupling reactions - The post-Ullmann chemistry. *Coord.Chem.Rev.* **248**, 2337-2364 (2004).
33. Falck, J. R., Bhatt, R. K. & Ye, J. H. Tin-Copper Transmetalation - Cross-Coupling of Alpha-Heteroatom-Substituted Alkyltributylstannanes with Organohalides. *J.Am.Chem.Soc.* **117**, 5973-5982 (1995).
34. Hassan, J., Sevignon, M., Gozzi, C., Schulz, E. & Lemaire, M. Aryl-aryl bond formation one century after the discovery of the Ullmann reaction. *Chem.Rev.* **102**, 1359-1469 (2002).
35. Kang, S. K., Kim, J. S. & Choi, S. C. Copper- and manganese-catalyzed cross-coupling of organostannanes with organic iodides in the presence of sodium chloride. *J.Org.Chem.* **62**, 4208-4209 (1997).
36. Mohapatra, S., Bandyopadhyay, A., Barma, D. K., Capdevila, J. H. & Falck, J. R. Chiral alpha,beta-dialkoxy- and alpha-alkoxy-beta-aminostannanes: Preparation and copper-mediated cross-coupling. *Org.Lett.* **5**, 4759-4762 (2003).
37. Li, J., et al. Reusable copper-catalyzed cross-coupling reactions of aryl halides with organotin in inexpensive ionic liquids. *J.Org.Chem.* **71**, 7488-7490 (2006).
38. Poizot, P., Laruelle, S., Grugeon, S., Dupont, L. & Tarascon, J. M. Nano-sized transition-metaloxides as negative-electrode materials for lithium-ion batteries. *Nature* **407**, 496-499 (2000).
39. Liu, D., et al. Preparation of 3D nanoporous copper-supported cuprous oxide for high-performance lithium ion battery anodes. *Nanoscale* **5**, 1917-1921 (2013).
40. Paoletta, A., et al. Colloidal Synthesis of Cuprite (Cu<sub>2</sub>O) Octahedral Nanocrystals and Their Electrochemical Lithiation. *Acs Applied Materials & Interfaces* **5**, 2745-2751 (2013).
41. Zhang, J. T., Liu, J. F., Peng, Q., Wang, X. & Li, Y. D. Nearly monodisperse Cu<sub>2</sub>O and CuO nanospheres: Preparation and applications for sensitive gas sensors. *Chemistry of Materials* **18**, 867-871 (2006).
42. Li, X. D., Gao, H. S., Murphy, C. J. & Gou, L. F. Nanoindentation of Cu<sub>2</sub>O nanocubes. *Nano Letters* **4**, 1903-1907 (2004).
43. Laskowski, R., Blaha, P. & Schwarz, K. Charge distribution and chemical bonding in Cu<sub>2</sub>O. *Physical Review B* **67**, 075102 (2003).

44. Chang, Y., Teo, J. J. & Zeng, H. C. Formation of colloidal CuO nanocrystallites and their spherical aggregation and reductive transformation to hollow Cu<sub>2</sub>O nanospheres. *Langmuir* **21**, 1074-1079 (2005).
45. Ramirez-Ortiz, J., et al. A catalytic application of Cu<sub>2</sub>O and CuO films deposited over fiberglass. *Appl.Surf.Sci.* **174**, 177-184 (2001).
46. Hara, M., et al. Cu<sub>2</sub>O as a photocatalyst for overall water splitting under visible light irradiation. *Chemical Communications* 357-358 (1998).
47. Ikeda, S., et al. Mechano-catalytic overall water splitting. *Chemical Communications* 2185-2186 (1998).
48. Walker, A. V. & Yates, J. T. Does cuprous oxide photosplit water? *J Phys Chem B* **104**, 9038-9043 (2000).
49. Barreca, D., et al. The Potential of Supported Cu<sub>2</sub>O and CuO Nanosystems in Photocatalytic H<sub>2</sub> Production. *Chemsuschem* **2**, 230-233 (2009).
50. Montini, T., et al. Nanostructured Cu/TiO<sub>2</sub> Photocatalysts for H<sub>2</sub> Production from Ethanol and Glycerol Aqueous Solutions. *Chemcatchem* **3**, 574-577 (2011).
51. Gombac, V., et al. CuOx-TiO<sub>2</sub> Photocatalysts for H<sub>2</sub> Production from Ethanol and Glycerol Solutions. *Journal of Physical Chemistry a* **114**, 3916-3925 (2010).
52. Kuo, C. & Huang, M. H. Morphologically controlled synthesis of Cu<sub>2</sub>O nanocrystals and their properties. *Nano Today* **5**, 106-116 (2010).
53. Perez-Omil, J. A. Interpretación sistemática de imágenes de microscopía electrónica de alta resolución de materiales policristalinos. Estudio de catalizadores metálicos soportados. (1994).
54. Bernal, S., et al. The interpretation of HREM images of supported metal catalysts using image simulation: profile view images. *Ultramicroscopy* **72**, 135-164 (1998).

### ***3. Electron Energy Loss Spectroscopy***



<b>3.1. Scope of the chapter.....</b>	<b>101</b>
<b>3.2. Core-loss EELS. Physics of electron scattering.....</b>	<b>102</b>
3.2.1. Elastic scattering .....	102
3.2.2. Lenz formalism of inelastic scattering .....	104
3.2.3. Bethe Theory .....	106
3.2.4. Generalized Oscillator Strength calculations.....	110
3.2.5. Single, Plural and Multiple Scattering. Poisson's law. Effects of plural scattering .....	111
3.2.6. ELNES.....	113
<b>3.3. Quantification of the core-loss edges.....</b>	<b>116</b>
3.3.1. Background to core loss edges .....	120
<b>3.4. Precession assisted EELS.....</b>	<b>123</b>
3.4.1. Electron precession and EELS .....	123
3.4.2. Considered EELS edges and methods.....	126
3.4.3. Signal enhancement as a function of precession angle.....	126
3.4.4. Conclusions .....	129
<b>3.5. Oxide Wizard .....</b>	<b>130</b>
3.5.1. Procedures to determine oxidation states from the ELNES.....	131
3.5.2. Steps of the analysis .....	134
3.5.3. Calibration test on $Mn_xO_y$ oxides .....	141
3.5.4. Application: Mn oxidation state determination in core-shell nanoparticles.....	143
3.5.5. Conclusions .....	147
<b>3.6. References .....</b>	<b>148</b>



## **3.1. Scope of the chapter**

In this chapter, the physical principles of electron energy loss spectroscopy, with a focus on the core-loss region, will be presented. Then, the application of beam precession to obtain a signal enhancement in EELS will be discussed. Finally, a homemade script for Digital Micrograph, is proven to quantitatively characterize the energy-loss near edge structure of transition metal edges, which is directly related to their oxidation state.

## 3.2. Core-loss EELS. Physics of electron scattering

The signal in the core-loss region contains the edges corresponding to electron transitions from core levels, as well as multiple contributions from other phenomena, namely the background onto which the edges are superimposed. The interpretation of the spectrum relies on the knowledge of the physics behind the observed signal and the mathematical tools available to make the most of the information in the spectrum. In Figure 3.1, the spectrum, up to 800 eV energy loss, of a manganese oxide is shown. In the schema of the transitions, we can see how core losses (red levels) are related to a specific energy change associated to the excitation from a core state to states above the Fermi level ( $E_F$ ).

### 3.2.1. Elastic scattering

Before we deal with inelastic scattering, let us consider elastic scattering first. Elastic scattering refers to a scattering event with a loss of energy which cannot be empirically detectable. In our case, it mostly refers to the interactions between fast electrons and the electrostatic potential of the nuclei of the atoms in the material.

The simplest way of describing the elastic scattering is the differential cross section per unit solid angle  $d\sigma/d\Omega$ , which means the probability of changes in angular distribution of the electron beam. Assuming that electrons are only scattered by nuclei (Rutherford scattering), we have<sup>1</sup>

$$d\sigma/d\Omega = \frac{4\gamma^2 Z^2}{a_0^2 q^4} \quad , \quad [3.1]$$

where  $Z$  is the atomic number,  $a_0 = 0.529 \cdot 10^{-10}$  m is the Bohr radius,  $\gamma = (1 - \frac{v^2}{c^2})^{-1/2}$  and  $q$  is the magnitude of the scattering vector  $q = 2k_0 \sin(\theta/2)$  where  $\hbar k_0$  is the momentum of the incident electron and  $\hbar q$  the momentum transferred to the nucleus. For small scattering angles, equation [3.1] is proportional to  $\theta^{-4}$ , meaning a highly forward scattered peak.

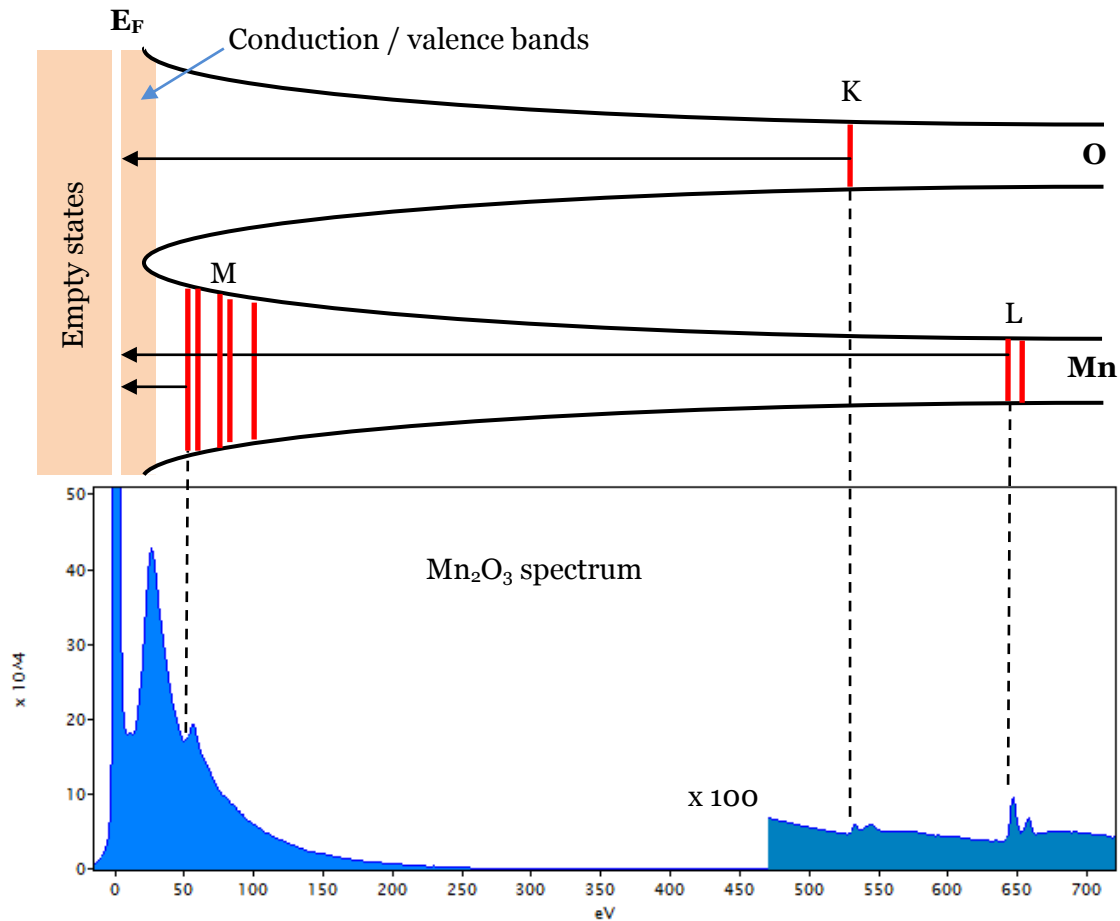


**Figure 3.1:** Schematic relationship between the EELS spectrum and the energy bands of a manganese oxide around two atoms of oxygen and manganese.

Rutherford scattering does not take into account the effects of screening of the nuclear electrostatic field by the electron cloud; it overestimates the elastic scattering at small angles and yields an infinite cross section if integrated over all possible angles.

A way of correcting for the screening is through the incorporation of a Yukawa potential, where the nuclear potential is exponentially attenuated as a function of distance  $r$  from the nucleus:

$$\phi(r) = [Ze/4\pi\epsilon_0 r]e^{-\frac{r}{r_0}} \quad , \quad [3.2]$$

where  $r_0$  is the screening radius. Then, the differential cross section equation [3.1] becomes

$$d\sigma/d\Omega = \frac{4\gamma^2}{a_0^2} \left( \frac{Z}{q^2 + r_0^{-2}} \right)^2 \quad . \quad [3.3]$$

### 3.2.2. Lenz formalism of inelastic scattering

By analogy with elastic scattering, let us deal with the inelastic scattering of a single atom in the same terms of differential cross section  $d\sigma_i/d\Omega$ .

Modifying Morses theory of elastic scattering, Lorenz obtained an expression for the differential cross section which can be expressed as:

$$\frac{d\sigma_i}{d\Omega} = \frac{4\gamma^2 Z}{a_0^2 q^4} \left( 1 - \frac{1}{(1 + (qr_0)^2)^2} \right) \quad , \quad [3.4]$$

where all the parameters are defined as in the previous section and the screening radius is  $r_0 = a_0 Z^{-1/3}$ , assuming the Thomas-Fermi model.  $\vec{q}$  is the scattering vector  $\vec{q} = \vec{k}_f -$

$\vec{k}_0$ , where  $\vec{k}_f, \vec{k}_0$  are the final and initial momenta of the incident electron, respectively, as shown in Figure 3.2.

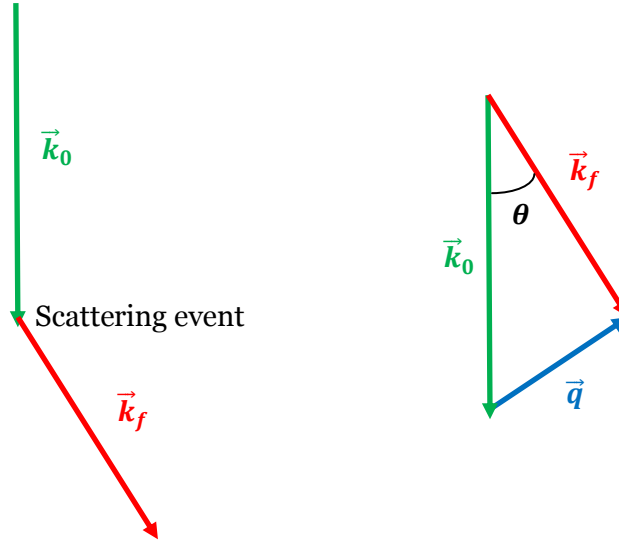


**Figure 3.2:** Schematic representation of the initial and final momenta of the incident electron, with  $\vec{q}$  the scattering vector and  $\theta$  the scattering angle.

The magnitude of  $\vec{q}$  can be approximated by  $q^2 \approx k_0^2(\theta^2 + \theta_E^2)$  [3.5], being  $\vec{k}_0$  the initial wavevector of the incident electron,  $\theta$  the scattering angle and  $\theta_E$  the characteristic scattering angle  $\theta_E = E/2E_0$ , with  $E_0$  the initial energy and  $E$  the energy loss.

The differential inelastic cross section can be written now in the form:

$$\frac{d\sigma_i}{d\Omega} \approx \frac{4\gamma^2 Z}{a_0^2 k_0^4} \frac{1}{(\theta^2 + \theta_E^2)^2} \left( 1 - \frac{\theta_0^4}{(\theta^2 + \theta_E^2 + \theta_0^2)^2} \right), \quad [3.6]$$

with  $\theta_0 = 1/k_0 r_0$ .

From this equation we can see that for angles comprised in the range  $\theta_E < \theta < \theta_0$ , the cross section is proportional to  $1/\theta^2$ , while above  $\theta_0$  it falls to  $1/\theta^4$ . This means that inelastic scattering is concentrated in small forward angles.

Spectrometers cannot collect the whole solid angle of scattered electrons, but only up to a given collection semi-angle  $\beta$  (see Figure 3.3). This must be taken into account when calculating the cross sections, as they depend on that angle.

Thus, we should integrate the cross section up to a scattering angle  $\beta$ :

$$\sigma_i(\beta) \approx \frac{8\pi\gamma^2 Z^{\frac{1}{3}}}{k_0^2} \ln \left( \frac{(\beta^2 + \theta_E^2)(\theta_0^2 + \theta_E^2)}{\theta_E^2(\beta^2 + \theta_0^2 + \theta_E^2)} \right) . \quad [3.7]$$

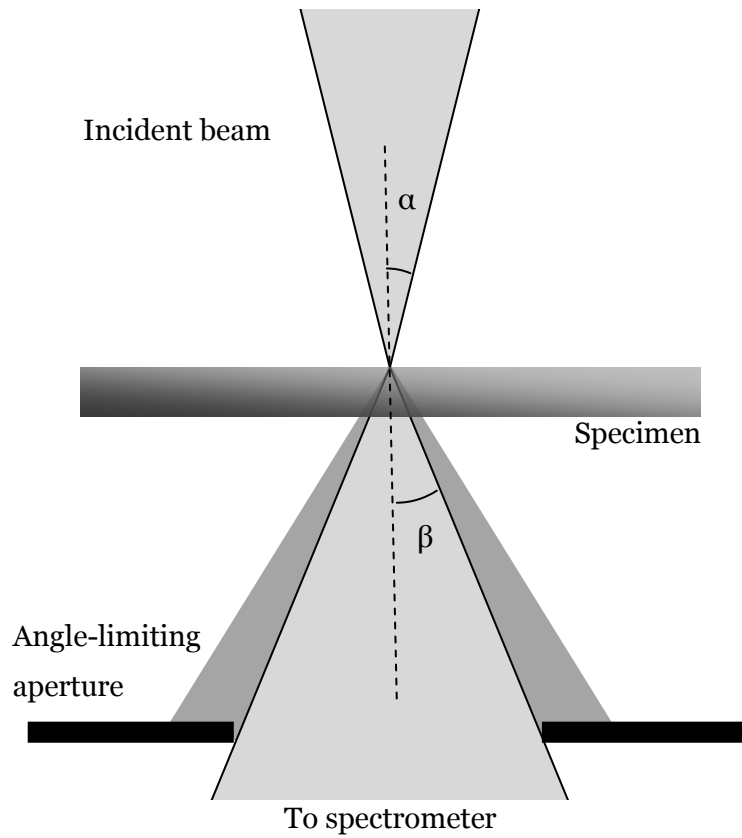


**Figure 3.3:** Schematic of the collection semiangle ( $\beta$ ) in the TEM. Convergence semiangle ( $\alpha$ ) is also indicated.

### 3.2.3. Bethe Theory

In a quantum mechanical approach, the behavior of single atomic electrons can be described in terms of a transition from an initial state of wavefunction  $\psi_0$  to a final state of wavefunction  $\psi_n$ . The first Born approximation can be used as the interaction

with the atom can be regarded as a perturbation for the fast electron (which is reasonable in EELS). Then we obtain a differential cross section of the form

$$\frac{d\sigma_n}{d\Omega} = \left(\frac{m_0}{2\pi\hbar^2}\right)^2 \frac{k_1}{k_0} \left| \int V(\vec{r}) \psi_0 \psi_n^* e^{i\vec{q}\cdot\vec{r}} d\tau \right|^2, \quad [3.8]$$

where  $k_0$  and  $k_1$  are the moduli of the wavevectors of the incident electron before and after the scattering event,  $\vec{q}$  is the scattering vector, and, therefore,  $\hbar\vec{q} = \hbar(\vec{k}_1 - \vec{k}_0)$  is the momentum transferred to the atom.  $\vec{r}$  is the coordinate of the fast electron,  $V(\vec{r})$  is the potential responsible for the interaction and  $d\tau$  is a volume element within the atom.

The electrostatic forces between the atom and the incident electron can be written as:

$$V(\vec{r}) = \frac{Ze^2}{4\pi\epsilon_0 r} - \frac{1}{4\pi\epsilon_0} \sum_{j=1}^Z \frac{e^2}{|\vec{r} - \vec{r}_j|}, \quad [3.9]$$

where  $\vec{r}_j$  is the position of the  $j$ -th electron in the atom. The first term corresponds to the Coulomb attraction by the nucleus and the second is a sum of the repulsive effects from each individual electron in the atom.

$V(\vec{r})$  is usually referred to as a potential. However,  $V(\vec{r})$  is related to the electrostatic potential  $\phi$  by  $V = e\phi$ .  $V(\vec{r})$  is not a proper potential but the negative of the potential energy.

Note that nuclear contribution in eq [3.8] amounts to zero when integrated because of the orthogonality of initial and final state wavefunctions in inelastic scattering. Therefore, inelastic scattering is only an electron-electron interaction. More intuitively, only electrons in the atom have a comparable mass to the fast electron, and, therefore, energy transfer is only allowed with these.

Combining the two previous equations, the differential cross section can be written as

$$\frac{d\sigma_n}{d\Omega} = \left(\frac{4\gamma^2}{a_0^2 q^4}\right) \frac{k_1}{k_0} |\epsilon_n(q)|^2, \quad [3.10]$$

where the first term (into parentheses) is the Rutherford cross section for a single scattering from a single free electron ( $Z=1$ ). The term  $k_1/k_0$  is close to unity whenever the energy loss is much less than the incident energy and  $\varepsilon_n$  is the dynamical structure factor or inelastic form factor.

$$\varepsilon_n = \left\langle \psi_n \left| \sum_j \exp(i\vec{q} \cdot \vec{r}_j) \right| \psi_0 \right\rangle = \int \psi_n^* e^{i\vec{q} \cdot \vec{r}} \psi_0 d\tau \quad . \quad [3.11]$$

A convenient quantity which can be defined is the generalized oscillator strength (GOS):

$$f_n(q) = \frac{E_n |\varepsilon_n(q)|^2}{R (qa_0)^2} \quad , \quad [3.12]$$

where  $E_n$  is the energy loss of the transition and  $R = \frac{m_0 e^4 / 2}{(4\pi\epsilon_0 \hbar)^2} = 13.6 \text{ eV}$  is the Rydberg energy. Then, the differential cross section can be written in the form:

$$\frac{d\sigma_n}{d\Omega} = \frac{4\gamma^2 R k_1}{E_n q^2 k_0} f_n(q) \quad . \quad [3.13]$$

Notice that in the limit  $q \rightarrow 0$  the GOS reduces to the dipole oscillator strength  $f_n$ , which characterizes optical absorption.

Knowing that the energy loss spectrum is a continuous function of the energy loss, it is necessary to define the GOS per unit energy loss. Then we obtain a double differential cross section:

$$\frac{d^2\sigma_n}{d\Omega dE} = \frac{4\gamma^2 R k_1}{E q^2 k_0} \frac{df}{dE}(q, E) \quad . \quad [3.14]$$

To obtain the angular distribution of inelastic scattering, eq [3.6] can be recovered, obtaining:

$$\frac{d^2\sigma_n}{d\Omega dE} \approx \frac{4\gamma^2 R}{E k_0^2} \left( \frac{1}{\theta^2 + \theta_E^2} \right) \frac{df}{dE} \quad . \quad [3.15]$$

The GOS is a function of the energy ( $E$ ) and momentum ( $\hbar q$ ) transferred to the atom, and can be represented as a surface plot called a Bethe surface, as the one

displayed in Figure 3.4. In this representation, the horizontal coordinate is related to the scattering angle. Most interestingly, this plot also shows qualitatively the behavior of the double differential cross section, which is proportional to  $E^{-1}q^{-2}df/dE$ . For energy losses close to the inner shell binding energy, the angular distribution is forward peaked. For higher losses, the scattering is concentrated around the so-called Bethe ridge. This ridge is centred around a value satisfying

$$(qa_0)^2 = \frac{E}{R} + \frac{E^2}{(2m_0c^2R)} \approx \frac{E}{R} . \quad [3.16]$$

Then the scattering angle is given by

$$\sin^2\theta_r = \frac{E}{E_0} \left[ 1 + \frac{E_0 - E}{2m_0c^2} \right]^{-1} , \quad [3.17]$$

which can be estimated as  $\theta_r \approx (E/E_0)^{1/2} \approx (2\theta_E)^{1/2}$  for small  $\theta$  and nonrelativistic incident electrons.

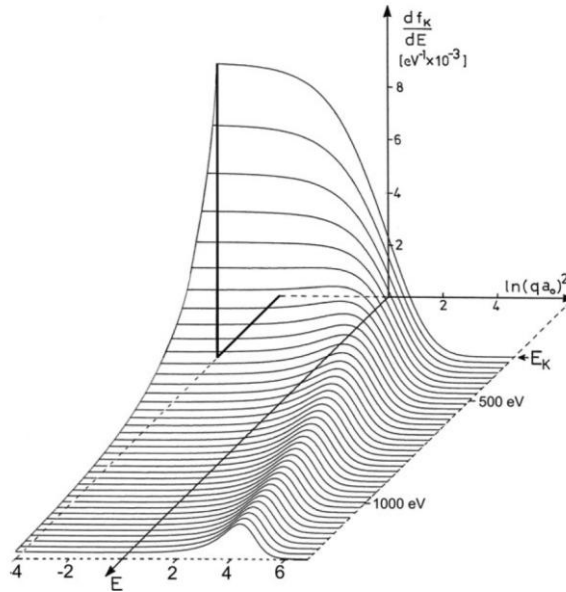


**Figure 3.4:** Bethe surface for the K-shell of carbon, calculated with a hydrogenic model (adapted from Egerton<sup>2</sup>).

This theory, based on single atoms or gas specimens, applies to inner atomic shells of electrons, where the solid state effects can be treated as perturbations in  $df/dE$ . For outer shell electrons, chemical bonding affects their states, and therefore this formalism cannot be used.

### 3.2.4. Generalized Oscillator Strength calculations

The key quantity in Bethe's theory is the generalized oscillator strength (GOS), describing the response of a single atom suffering the collision of a fast electron. Two models are here considered: the hydrogenic model and the Hartree-Slater method.

- *The hydrogenic model*

In the hydrogenic model, the GOS is estimated by reducing the actual atom with atomic number  $Z$  to a hydrogen atom with an effective atomic number  $Z_S$ . The simplicity of the model arises from the fact that solutions of the Schrödinger equation are available for the hydrogen atom.

This  $Z_S$  takes into account the charge of the nucleus as well as the screening effects from other electrons. In the case of K-shell excitations, the second 1s electron produces a screening of the nucleus, and the effective charge is reduced by  $0.3e$ :  $Z_S = Z - 0.3$ . In the case of L-shell excitations, two K-shell and seven L-shell electrons screen the nucleus, by  $0.85e$  and  $0.35e$  respectively.

Outer electrons are assumed to form a shell of charge which reduces the inner shell binding energy by an amount  $E_S$ . The final observed threshold for inner shell ionization is

$$E_k = Z_S^2 R - E_S \quad . \quad [3.18]$$

- *Hartree-Slater*

More accurate wavefunctions can be computed by iterative solutions of the Schrödinger equation. The Hartree-Slater (or Hartree-Fock-Slater) is a simplification of the Hartree-Fock procedure by assuming a spherically symmetric field within the atom. The results are close to those of Hartree-Fock, but with much less computing required.

The wavefunction of the several electrons in an atom is described by a Slater determinant containing the  $N$  wavefunctions of the  $N$  electrons. Each wavefunction is an eigenfunction of the Hartree-Fock operator, taking into account the potential created by the nucleus and all the electrons in the atom.

Hartree-Slater cross sections can be parametrized as a function of energy loss and scattering angle, and used to calculate  $\sigma_k(\beta, \Delta)$  for a wide range of  $Z, E_0, \Delta$  and  $\beta$ , as it is done in the Digital Micrograph software.

### 3.2.5. Single, Plural and Multiple Scattering. Poisson's law. Effects of plural scattering

Inelastic scattering, in terms of data interpretation, can be divided into three regimes depending on the number of scattering events:

- Single scattering: fast electrons undergo one scattering only.
- Plural scattering: incoming electrons undergo between 1 and 20 interactions while going through the specimen
- Multiple scattering: fast electrons undergo more than 20 scattering events, which makes the sample unfit for EELS analysis.

The first regime is the most favorable one, as it makes interpretation of the spectra much simpler. For a very thin specimen, single scattering is the most probable event. In this case, the intensity of the spectrum  $J^1(E)$  approximates a single-scattering distribution  $S(E)$ :

$$J^1(E) \approx S(E) = I_0 n_a t (d\sigma/dE) + I_0 (dP_S/dE) \quad , \quad [3.19]$$

where  $I_0$  is the zero-loss intensity (which is approximately equal to the total intensity under the energy loss spectrum),  $n_a$  is the number of atoms per unit volume and  $t$  is the thickness of the sample. The last term refers to intensity arising from surface modes.

However, in most cases spectra are formed by plural scattering. Considering plural scattering as a series of independent events, it should obey Poisson statistics. Therefore the probability of an electron suffering  $n$  events is:

$$P_n = \frac{m^n e^{-m}}{n!} \quad , \quad [3.20]$$

where  $m$  is the mean number of events undergone by the fast electron. We can define here  $\lambda$  as the mean free path for inelastic scattering, the mean distance travelled by an electron between inelastic events. Therefore  $m = t/\lambda$ , which is also referred to as the scattering parameter of the specimen. The probability of  $n$ -th fold scattering is then:

$$P_n = \frac{I_n}{I_t} = \frac{(t/\lambda)^n e^{-t/\lambda}}{n!} \quad , \quad [3.21]$$

where  $I_n$  is the integrated  $n$ -th fold scattering and  $I_t$  is the total integrated intensity. Note that for an unscattered beam ( $n=0$ ), i.e. the zero-loss peak, we have

$$P_0 = \frac{I_0}{I_t} = e^{-t/\lambda} \quad , \quad [3.22]$$

which allows the measurement of the thickness of the sample, as introduced in eq. [1.4].

It is important to notice that for these statistics to apply, the scattering angles have to be small, so that all the electrons travel the same  $t$  through the sample.

If we consider different energy loss processes within the sample, each characterized by its own mean free path  $\lambda_j$ , the effective scattering parameter will be

$$\frac{t}{\lambda} = \sum_j \frac{t_j}{\lambda_j} \quad , \quad [3.23]$$

where  $t_j$  is the whole thickness of the sample if the different scattering events occur over a single layer specimen or the layer thickness if the electron passes through a layered sample.

- *Effect of Plural scattering*

Although in the low-loss region plural scattering makes significant contributions to the signal, at core loss energies, the probability of plural scattering involving only plasmons contributing to the background is negligible.  $P_n$  becomes extremely small due to the  $n!$  denominator.

In the same way, for two or more inelastic events at higher and comparable energies, the probability of both events taking place is very low, being the probability of each of them of the form  $AE^{-r}$ .

However, the probability of two dissimilar energy losses taking place, such as low-loss and core-loss, is appreciable. Taking one single electron and  $n$  plasmon events, the intensity of the spectrum is:

$$J^{1+n}(E) = A(E - nE_p)^{-r} (t/\lambda)^n e^{-\frac{t}{\lambda n}} \quad . \quad [3.24]$$

As this double scattering is delayed at an energy  $E = E_k + E_p$ , the presence of plural scattering is clearly seen as a rise in the intensity after the core-loss edge. The resulting edge ( $J_k(E)$ ) can be seen as the convolution of the low loss spectrum (zero loss and plasmon region  $J_l(E)$ ) to the single scattering distribution of the core loss ( $K^1(E)$ ).

$$J_k(E) = K^1(E) * \frac{J_l(E)}{I_0} \quad . \quad [3.25]$$

Therefore, the single scattering distribution can be recovered by deconvolving the low loss region. Moreover, this procedure, called Fourier-ratio because in Fourier space the deconvolution is done by dividing the transforms of the core loss edge and the low loss spectrum, also takes into account the instrumental broadening.

### 3.2.6. ELNES

The shape of most edges differs from the one they would have according to the atomic models we have considered thus far. Usually, there are strong oscillations in the

region of 30-50 eV after the onset of the edge, which are called the energy loss near edge structure (ELNES).

When an electron is promoted from the inner shell of the atom to an excited state, leaving a hole, it may not receive enough energy to escape to the vacuum level. Then it will still be attracted to the nucleus. In this situation, the final state of the electron will be one of the possible energy levels above the Fermi energy ( $E_F$ ), as it is shown in Figure 3.1. The Fermi level is the boundary between the filled and the unfilled states in the weakly bound conduction or valence bands. In a metal,  $E_F$  is located in the conduction band, while in semiconductors or insulators, it is located between the valence and the conduction band. The possible final states for the electrons of the core levels are determined by the availability of empty energy states.

The probability of an electron ending up in an empty state is not equal for all of them. The distribution of unfilled energy levels is called the density of states (DOS). When there is a high DOS region above  $E_F$ , the ELNES intensity will be greater. Therefore, the ELNES will mirror the DOS above  $E_F$ . The importance of the DOS resides in its sensitivity to the bonding or the valence state of the atom.

The simplest way to use the ELNES is by fingerprinting, comparing it with spectra of reference samples of well known electronic configurations. Fingerprinting can also be used to compare an experimental structure with a simulated one. Interestingly, ELNES can also be used to calculate the oxidation state of a transition metal, as the DOS is closely related to it.

$L_{2,3}$  edges in transition metals and  $M_{54}$  edges in rare earths show sharp peaks arising from transitions to well defined energy states instead of broad continuums, which are the so called white lines. The L shell in transition metals is divided into three different energy levels because of the spin-orbit splitting. As the electrons in L shell levels 2 and 3 are in the p state, quantum theory restricts the sum ( $j$ ) of spin ( $s$ ) and angular-momentum ( $l$ ) quantum numbers to  $1/2, 3/2, 5/2$ , etc. due to Pauli exclusion principle. The spin quantum number can only be  $s = \pm \frac{1}{2}$ . Thus, the more tightly bound  $L_2$  shell can only have two p electrons with  $j = \pm \frac{1}{2}$  while the  $L_3$  shell can have four p electrons with  $j = \pm \frac{1}{2}, \pm \frac{3}{2}$ . Therefore we can expect twice as many electrons coming from the  $L_3$  shell than the  $L_2$  shell. Then, in the spectrum, the  $L_3$  line should be twice as intense as the  $L_2$ . However, in actual spectra the ratio changes from 0.8 to 3 in pure metals.

These deviations from 2 in  $L_3/L_2$  ratio arise from the DOS above  $E_F$ . Due to the dipole selection rule, the change in  $l$  angular momentum quantum number can only be  $\pm 1$ . As the p state (of the p electrons in the L shell) has  $l=1$ , the final states that are either s ( $l=0$ ) or d ( $l=2$ ). Moreover, the ejected core electrons end primarily in the unoccupied d states, as they are more available than the s. Therefore, the density of d states above  $E_F$  will determine the ratio.

The cause of  $L_1$  edge being so weak and broad is that the electrons are in the s state ( $l=0$ ) and can only be excited to p states ( $l=1$ ). In transition metals, there are few unoccupied p states in the conduction band, and they are much more spread in energy.

The energy width of the white lines, primarily related to the energy spread of the final states, is also affected by the time it takes for the ionized state to decay. Rapid decays are related to wide peaks (because of Heisenberg uncertainty principle).

### 3.3. Quantification of the core-loss edges

For angles below 1 rad, which is the case in TEM, the energy-differential cross section can be obtained from [3.15], and integrating up to  $\beta$ :

$$\frac{d\sigma}{dE} \approx \frac{4R\hbar^2}{Em_0^2v^2} \int_0^\beta \frac{df(q, E)}{dE} \frac{2\pi\theta}{(\theta^2 + \theta_0^2)} d\theta \quad . \quad [3.26]$$

Supposing we are in the dipole region, where  $(qa_0)^2 < 1$ , we can consider the GOS constant and therefore

$$\frac{d\sigma}{dE} = \frac{4\pi R^2\hbar^2}{ETm_0^2v^2} \frac{df(0, E)}{dE} \ln[1 + (\beta/\theta_E)^2] \quad . \quad [3.27]$$

$df(0, E)/dE$  is the optical value. Outside the dipole region,  $df/dE$  is calculated for each angle  $\theta$ . The approximate logarithmic behavior for the cross section is  $d\sigma/dE \propto E^{-s}$ , where  $s$  is the downward slope and is found to be constant over a range of energy-loss.

The intensity  $J_k^1(\beta, E)$  of the inner shell contribution for a single scattering event is:

$$J_k^1(\beta, E) = NI_0(d\sigma/dE) \quad , \quad [3.28]$$

where  $N$  is the number of atoms per unit area which contribute to the ionization.

- *Partial cross sections*

In order to quantify the elements in a sample, intensities of the inner shell excitations are integrated over a finite range  $\Delta$  beginning at the edge onset. In the single scattering case

$$I_k^{\Delta}(\beta, \Delta) = NI_0\sigma_k(\beta, \Delta) \quad , \quad [3.29]$$

where  $\sigma_k(\beta, \Delta)$  is the partial cross section and can be defined as

$$\sigma_k(\beta, \Delta) = \int_{E_k}^{E_k+\Delta} \frac{d\sigma}{dE} dE \quad . \quad [3.30]$$

- *Beam convergence correction*

Equation [3.29] assumes that the collection semi-angle is the only magnitude affecting angular distribution of the scattered electrons. However, this condition is easily broken by using a focused electron beam, as done in STEM mode. Then, the convergence semi-angle (see Figure 3.3) must also be taken into account.

The angular distribution of the core loss intensity can be calculated as a convolution of the inner shell intensity  $dI_k(\alpha = 0)/d\Omega$  by an incident electron angular distribution  $dI_i/d\Omega$ .

If we assume the inner shell scattering to be a Lorentzian function of width  $\theta_E = \langle E \rangle / (\gamma m_0 v)$ ,  $\langle E \rangle$  being the mean energy loss in the integration window, we obtain

$$I_k(\alpha, \beta, \theta_E) \propto \int_0^{\beta} 2\pi\theta d\theta \int_0^{\alpha} \theta_0 d\theta_0 \int_0^{2\pi} \frac{dI_i}{d\Omega} \frac{1}{\theta^2 + \theta_0^2 - 2\theta\theta_0 \cos\phi + \theta_E} d\phi \quad . \quad [3.31]$$

Considering that the incident intensity is a constant  $I_i$  up to the semi-angle  $\alpha$ , and zero for higher angles we obtain

$$\frac{dI_k}{d\Omega} \propto \ln \left[ \frac{\psi^2 + (\psi^4 + 4\theta^2\theta_E^2)^{1/2}}{2\theta_E^2} \right] , \quad [3.32]$$

with  $\psi^2 = \alpha^2 + \theta_E^2 - \theta^2$ . Then this intensity can be related to that of parallel illumination

$$F_1 = \frac{I_k(\alpha, \beta, \Delta)}{I_k(0, \beta, \Delta)} = \frac{2}{\alpha^2 \ln [1 + (\beta/\theta_E)^2]} \int_0^\beta \ln \left[ \frac{\psi^2 + (\psi^4 + 4\theta^2\theta_E^2)^{1/2}}{2\theta_E^2} \right] \theta d\theta . \quad [3.33]$$

The reduction of core loss intensity due to the convergence of the incident beam is simplified in factor  $F_1 (<1)$ , which depends on the ionization edge.

Finally, the effect of beam convergence can be alternatively expressed in terms of an effective collection angle  $\beta^*$  so that

$$I_k(\alpha, \beta, \Delta) = F_2 I_k(\beta, \Delta) = I_k(\beta^*, \Delta) . \quad [3.34]$$

To quantify the edges, it is only necessary to integrate their intensity over an appropriate energy window, subtracting the background, as in Figure 3.1.

Following equation [3.29] the quantification for two elements will be given by:

$$\frac{N_a}{N_b} = \frac{I_{ka}(\beta, \Delta) \sigma_{jb}(\beta, \Delta)}{I_{jb}(\beta, \Delta) \sigma_{ka}(\beta, \Delta)} , \quad [3.35]$$

where  $N$  is the areal density of atoms,  $I$  the integrated intensity over  $\Delta$  of an edge for a given collection semiangle  $\beta$  and  $\sigma$  are the partial cross-sections, which can be obtained experimentally from reference samples or calculated from models. We are making the assumption that the plasmon excitation contribution redistributes intensities towards higher energy losses. Thus, if plural scattering is not deconvolved, integration windows for all edges should be the same and wide enough to take this effect into account.

The background over which the edge is superimposed is usually estimated in the 50 eV preceding the edge, fitted by a power law function of the form  $Ae^{-rE}$ , where  $E$  is the energy and  $A$  and  $r$  are the fitting parameters.

This technique can only be applied if the edges do not overlap. In the case of overlapping edges, other techniques such as peak fitting to a parametric model, multivariate analysis or edge simulation have to be used.

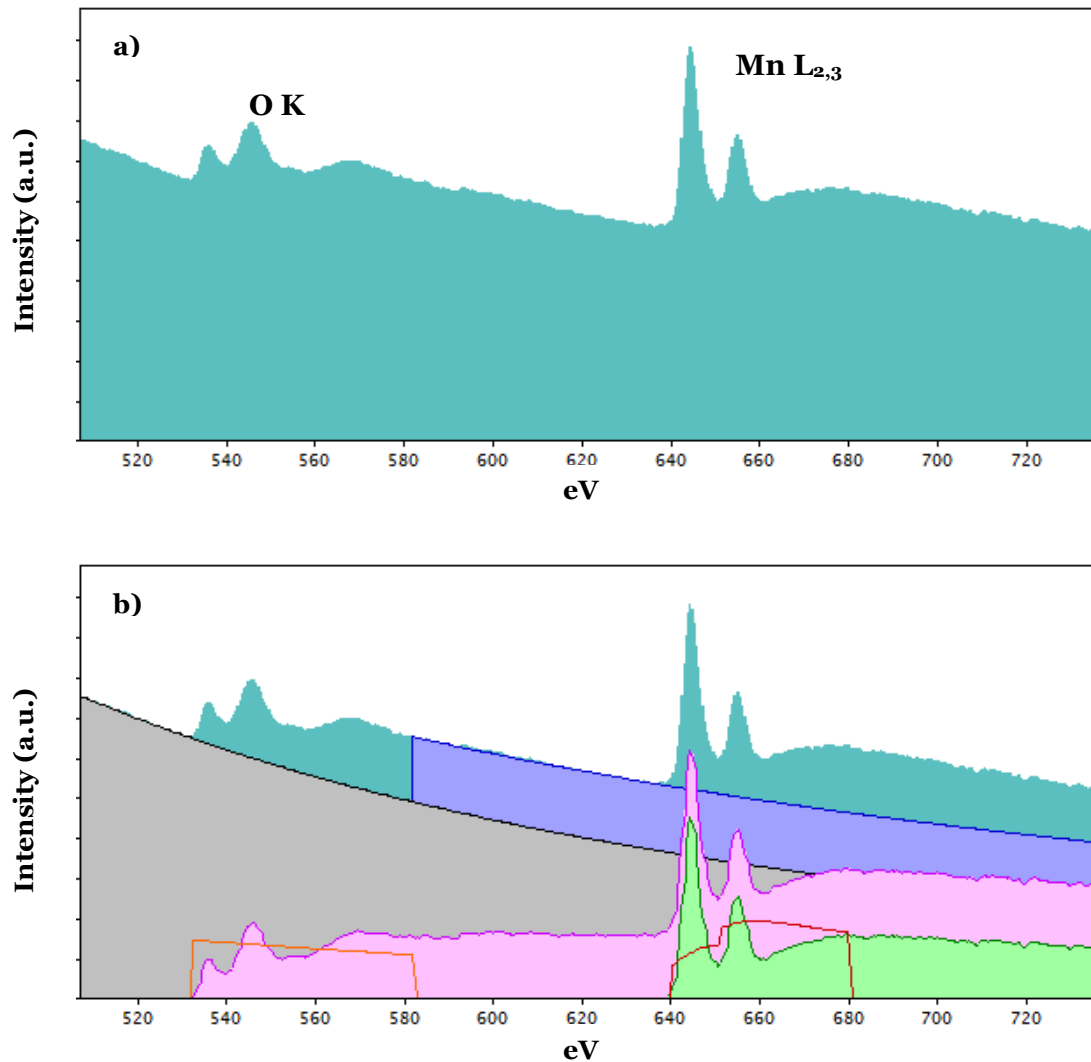


**Figure 3.1:** Extraction of information for quantification for a manganese oxide. In **a)**, the original spectrum is presented, with O K and Mn L<sub>2,3</sub> edges. In **b)**, the modeling (in grey) and the subtraction (in pink) of the background before the oxygen K edge. In blue and green, the modeling of the background and the subtracted signal of the Mn L<sub>2,3</sub> edge. The orange and red lines represent the calculated Hartree-Slater cross sections for both edges.

### 3.3.1. Background to core loss edges

Core loss edges are superimposed on a decreasing background arising from excitations at lower energies. In order to analyze the edges, this background needs to be subtracted. As this background is in the order of magnitude of the edges or even larger, it is important to know the mechanisms giving rise to the background and the ways to model it

- *Outer shell scattering*

In the range of 10-30 eV plasmon peaks usually occur. Their intensity falls proportionally to  $E^{-3}$  for large energies following the Drude model. However, at high energy loss, scattering is more appropriately described by Bethe theory, and the exponent is in the order of 4 or 5 for small values of  $\beta$ .

Far away in the energy loss dimension, plasmon losses are not forward peaked, but rather concentrated at the Bethe ridge. This high angle scattering corresponds to “hard” collisions (interactions at short distances) of the fast electron with the electrostatic field of an outer shell electron. The resulting losses from this interaction not only correspond to an energy loss, but also to a great momentum transfer. Therefore most of the background of core losses arises from these interactions. The higher the energy loss (higher momentum transfer), the higher the angle of the Bethe ridge. Binding energy of outer shell electrons is much lower than the energy of core losses, which means that the maximum cross-section will be at higher scattering angles while the inner shell electrons with large binding energies will have a forward peaked distribution. This means that for the same energy loss, a smaller collection angle will enhance the core-loss signal compared to the background (SBR). However, this also means a weaker signal and, thus, a lower signal to noise ratio (SNR).

- *Tails of core-loss edges*

Like valence electrons, inner shell edges with lower binding energies also contribute to the background. As we have seen, if they are far away from the studied edge, their angular distribution will present a maximum at higher scattering angles. This means that a smaller collection angle will help minimize its effects. Conversely, if the preceding edge has a binding energy close to the analyzed edge, its distribution will be forward peaked and changing the collection angle will prove less successful.

- *Bremsstrahlung*

Bremsstrahlung is an electromagnetic radiation which arises from electrons being decelerated when undergoing centripetal acceleration in the nuclear field of an atom. In x-ray spectroscopy, bremsstrahlung forms a continuous background to the characteristic emission peaks.

If we consider the differential cross section into angles below  $\beta$ , neglecting screening from electrons:

$$\frac{d\sigma}{dE} = \frac{CZ^2}{E(v/c)^2} \ln[1 + (\beta/\theta_E)^2] \quad , \quad [3.36]$$

with  $C = 1.55 \cdot 10^{-31}$  m<sup>2</sup> per atom, we can see that for energy losses below 4 keV the contribution of bremsstrahlung to the spectrum is much lower than that of electronic excitations.

- *Plural scattering*

As already explained, the probability of two dissimilar energy losses taking place is appreciable. Therefore, when studying core loss edges, there is a probability of the electron having also undergone a plasmon excitation loss, which will appear in the spectrum as a rise in the intensity after the edge. Any rise in the tails of the edges will contribute to an increased background in following edges.

Signal to background ratio (SBR) is always maximum for thin specimens, as plural scattering can be avoided. Yet the signal will be very weak in relation to the noise (SNR). The SNR is maximized at an optimum thickness not far from  $t/\lambda = 1$ .

## 3.4. Precession assisted EELS

### 3.4.1. Electron precession and EELS

Electron beam precession is a relatively new method developed for electron diffraction. Instead of illuminating the sample with a beam perpendicular to the surface, the illumination is tilted and the beam is rocked about the optical axis of the microscope on the sample. After the sample, the beam needs to be de-rocked onto the plane of the diffraction pattern. It is, thus, a system which subjects the beam to a double cone surface motion where the sample is placed at the tip (as schematized in Figure 3.2).

This type of illumination is based on the previous hollow cone diffraction (also called conical diffraction), where a circular aperture was used below C2. This type of illumination allowed obtaining ring patterns for large grained materials. In the seventies, the same kind of illumination was obtained by electronically rocking the beam onto the sample instead of inserting an annular aperture<sup>3</sup>. In the eighties it was demonstrated that this type of illumination could also improve bright field images, as phase contrast noise was suppressed and the resolution was increased<sup>4</sup>.

Precession was first envisaged in the TEM by Vincent and Midgley in 1993<sup>5</sup> as an approach to reduce dynamical scattering and recover more kinematic diffraction patterns, which has been the most usual application up to date. When in zone axis, many reflections are excited, increasing the probability of multiple diffraction. Precession allows exciting only a few reflections simultaneously, strongly reducing dynamical effects. Moreover, when precessing the beam, more reflections are excited,

and their intensity is integrated along the excitation error vector, resulting in more complete and accurate datasets for crystal structure determination.

Electron energy-loss spectroscopy (EELS) performed in the transmission electron microscope (TEM) provides chemical and electronic information about the considered solid state sample, through the determination of the energy lost by the incident electrons, with an extraordinary spatial resolution, that can be as high as one atomic column in aberration-corrected instruments<sup>6-96, 7, 7</sup>.

If one solves the Schrödinger equation for an electron in a crystalline potential, the resulting wavefunctions are Bloch waves. When a number of Bragg beams are excited, the same number of Bloch waves propagate in the crystal. In the most simple case, in the two beam condition, two Bloch waves are present: one that is peaked at the specimen atoms (type 1) and another that is peaked at half way between the atoms (type 2), both with the same intensity. When tilting the specimen out of the exact Bragg condition, if the beam-crystal plane angle is reduced, type 1 wave is enhanced, and, if the aforementioned angle is increased, then, the type 2 wave is enhanced. The orientation dependence of Bloch waves amplitude is a generalized phenomenon and may affect the relative intensity of the EELS edges, depending on the position of the different atoms in the unit cell respective to the exact Bragg plane, which is sometimes used to determine the polarity of a thin film or nanostructure<sup>10</sup>.

When in exact zone axis, the Bloch wave description may not be the most suitable one. It is well established that, when a crystal is viewed parallel to the atom columns, the obtained high resolution images show a one-to-one correspondence with the actual atom positions if the balance between the resolution of the instrument and the atomic distance is favourable enough; thus, in this case, the exiting wave function mainly depends on the projected structure, and the physical explanation for this to occur has been proposed<sup>11, 12</sup> to be the channelling of the electrons along the atom columns parallel to the beam direction: through the positive electrostatic potential of the atoms, a column acts as a channel for the electron, within which it can scatter dynamically without leaving the column. This elastic and highly directed incident electron-atom interaction is bound to strongly reduce the EELS signal<sup>13, 14</sup>.

The obvious answer to this is to remain off-axis to perform EELS experiments. Now, this is not always possible. Consider, for instance, the EELS analysis of a region delimited by one or several interfaces, where getting away from the zone axis means collecting signal from outside this region. More interestingly, when working in aberration-corrected microscopes, one does want to keep the zone axis condition in

order to allow for the chemical analysis of one given atomic column. In this case, electron channelling may give rise to further experimental problems. Artefacts may be encountered, especially if the sample is thick enough. If an inelastic scattering event is suffered by an electron channelling down an atomic column, there is a non-null probability of this electron swapping to the next atomic column and, thus, giving some chemical information about the wrong atomic column. Precession can be considered to overcome the problems associated with channelling: if one combines EELS with precession, it is possible to recover an effective two-beam condition while remaining in the zone axis<sup>5, 15, 16</sup>.

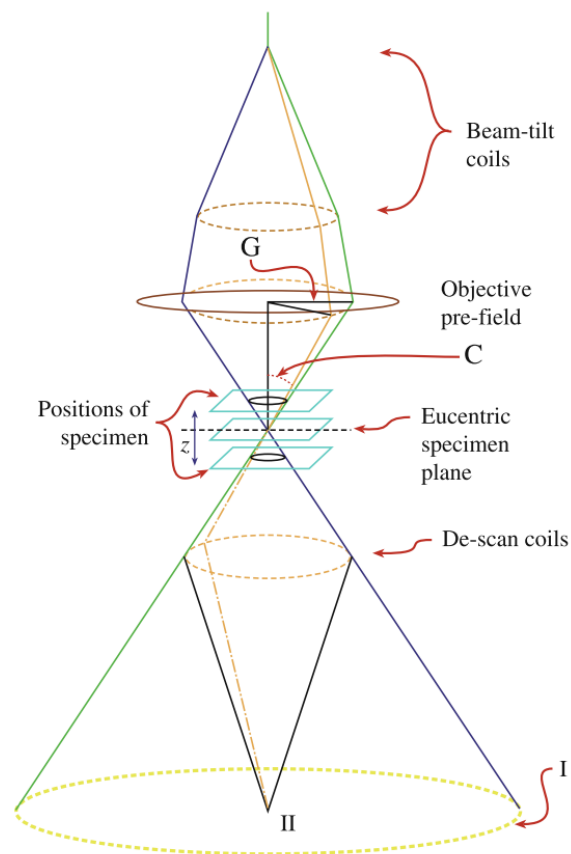


**Figure 3.2:** Schematic ray diagram of electron precession in the TEM, adapted from Williams&Carter<sup>1</sup>. The hollow cone is presented by radius  $G$  and precession angle  $C$ .

### 3.4.2. Considered EELS edges and methods

To prove this precession-assisted signal enhancement, several EEL spectra were obtained in a Jeol J2010F coupled with a GIF spectrometer and a SpinningStar precession system. The considered EELS edges for testing the hypothesis were the Si  $L_{2,3}$  edge in Si and the O K and Ti  $L_{2,3}$  edges in SrTiO<sub>3</sub> (STO). The used probe size was 0.5 nm, convergence and collection semiangles were 9 mrad and 10 mrad, respectively, and the acquisition time was of 3 s for the Si  $L_{2,3}$  edge in Si and 6 s for the O K and Ti  $L_{2,3}$  edges in STO. Sample thicknesses were determined from low-loss EELS to be about 30 nm for the Si sample, and about 35 nm for the STO sample.

### 3.4.3. Signal enhancement as a function of precession angle

A Si crystal in the [011] zone axis was first studied, Si  $L_{2,3}$  edge was acquired for precession angles between 0° and 1.92°. An example of the resulting effect is shown in Figure 3.3, where the signal increase for an angle of 0.48° is already observed. An EEL spectrum was acquired every 0.125° precession angle. Then, the background before the edge was extracted and the signal integrated over a 100 eV energy window to obtain intensity  $I$ . We define the signal enhancement ( $SE$ ) for a given precession angle  $\alpha$  as:

$$SE(\alpha) = (I(\alpha) - I(0))/I(0) \quad [3.1]$$

where  $I(0)$  is the intensity obtained without precession, so that  $SE$  is expressed as a percentage.

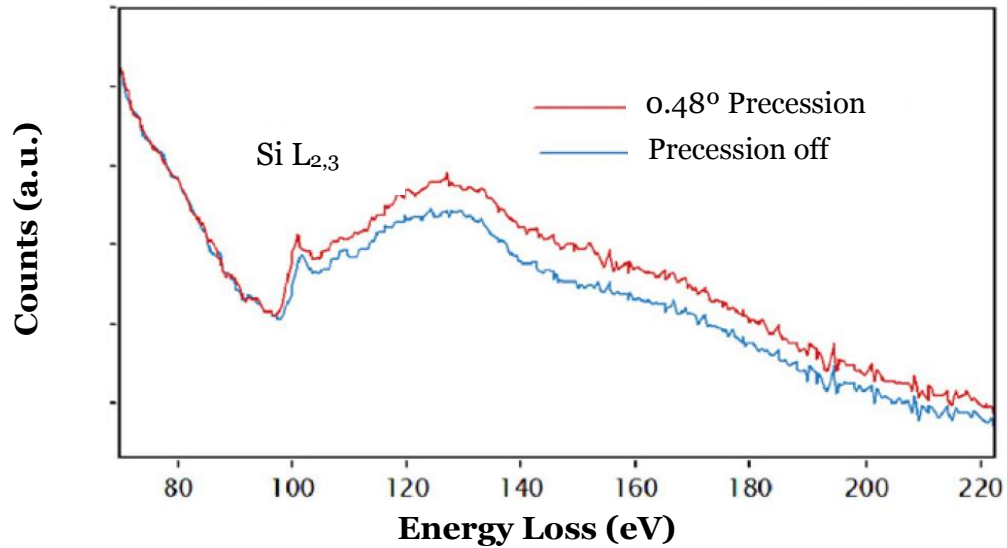


**Figure 3.3:** Comparison between the Si  $L_{2,3}$  edge acquired in zone axis conditions without precession and with  $0.48^\circ$  precession angle.

The  $SE(\alpha)$  plot in Figure 3.4 shows an enhancement in EELS signal that saturates around 12.5% at angles as low as  $0.5^\circ$ . This enhancement compensates for the signal loss due to channeling when in the zone axis, which means that for precession angles over  $\alpha \sim 0.5^\circ$  the signal is equivalent to that obtained off-zone-axis.

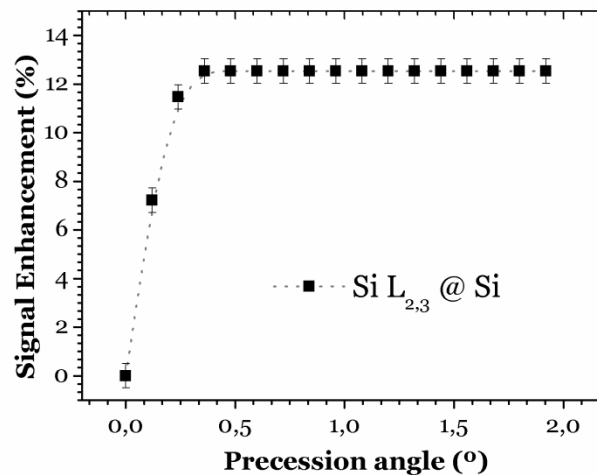


**Figure 3.4:** Signal enhancement as a function of precession angle for the Si  $L_{2,3}$  edge in a Si crystal in  $[011]$  zone axis conditions.

For the SrTiO<sub>3</sub> (STO) crystal oriented in the [001] zone axis, we carry out the same investigation in the oxygen K edge and the titanium L<sub>2,3</sub> edge. Again, precession angles were investigated between 0° and 1.92°, with an integration window of 50 eV. The results are shown in Figure 3.5. While the plots are considerably noisier than for the previous, Si, example, the same kind of enhancement is found for both edges: a rapid increase in signal saturating for angles as low as  $\alpha \sim 0.5^\circ$ . In this case, the enhancement of Ti L<sub>2,3</sub> is comparable to that of the Si edge, around 14% in this case. However, the K edge of oxygen is enhanced to around 37%.

These results clearly prove that precession can compensate for the reduction of EELS signal when in zone axis. In addition to allowing to obtain higher signal-to-noise ratios, electron precession can also help to compare EELS data with simulations, where channeling effects are rarely taken into account.

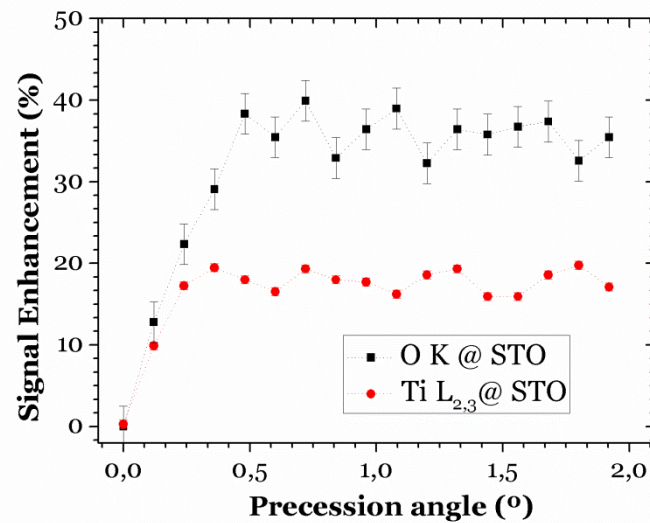


**Figure 3.5:** Signal enhancement as a function of precession angle for the O K and Ti L<sub>2,3</sub> edges in a STO crystal in [001] zone axis conditions.

### 3.4.4. Conclusions

In this section, the combination of EELS and electron precession has been proposed to overcome the loss of signal when in zone axis conditions. Experimentally, the signal enhancement due to precession has been observed for the Si L<sub>2,3</sub> edge of a pure Si sample oriented in [011] zone axis and for the O K and Ti L<sub>2,3</sub> edges in [001] oriented STO.

These observations have led to the obtention of a patent (european patent number 1559 / 2642279), in collaboration with Nanomegas SL and Appfive Inc., regarding the application of electron precession to enhancing the signal in analytical TEM.

## 3.5. Oxide Wizard

Transition metal (TM) oxides have kept the interest of researchers for decades due to their appealing physiochemical properties, which have resulted in many different applications in a broad variety of fields. Interestingly, many of these properties stem directly from their many possible oxidation states. Manganite perovskites, for example, have attracted much attention for their colossal magnetoresistance (CMR) properties, leading to applications such as magnetoresistive tunnel junctions<sup>17</sup>. Actually, CMR is closely related to the electronic inhomogeneity and double exchange ensuing from the  $Mn^{+3}/Mn^{+4}$  mixed valence present in some doped manganites. Other fields where the TM valence is of great importance include mineralogy<sup>18-21</sup>, catalysis<sup>22</sup>, electro-chemistry<sup>23</sup> or 2D superconducting materials<sup>24</sup> among many others.

The oxidation state can be defined as the number of electrons a given atom contributes to the bond, i.e. the hypothetical charge the atom would have in a purely ionic picture<sup>25</sup>, and it is directly linked to the occupation of the 3d energy bands near the Fermi level of the material. However, the formal oxidation state differs from the actual charge of the TM atom<sup>26</sup>, as the bonds have a marked covalent character.

The accurate characterization of complex TM oxides to properly understand their functional properties requires reliable measurements of their oxidation state, i.e.: their 3d band occupation. Electron energy-loss spectroscopy (EELS) has been routinely used to obtain information on this electronic property, and there are a vast number of publications about the link between the oxidation state and the energy-loss near-edge structure (ELNES) of the  $L_{2,3}$  edges ( $2p \rightarrow 3d$  – like transitions)<sup>18, 19, 27-44</sup>. Many methods have been reported to relate the  $L_{2,3}$  ELNES to the oxidation state, mainly through the measurements of  $L_{2,3}$  intensity ratios. However, most of these methods are not reliable when the signal-to-noise ratio (SNR) is poor, as is typically the case in EEL spectrum images with short acquisition times per pixel. In the framework of this Thesis, Oxide Wizard has been developed, a script for Digital Micrograph which characterizes the

shape and position of the transition metal edge and reliably and reproducibly produces maps of the oxidation state of transition metals.

### 3.5.1. Procedures to determine oxidation states from the ELNES

Driven by the relevance of the accurate determination of oxidation state in these materials, several procedures exist in order to correlate the features in the ELNES of the TM absorption edges with the oxidation state. Here we describe some of those procedures, based on the analysis of the  $L_{2,3}$  edge or the O  $K$  edge, which are already reported in the literature:

- *White line ratio*: in the case of TMs there are two clear peaks near the  $L_{2,3}$  edge onset. These are the so-called white lines (WL), its name arising from the fact that they appeared as bright, overexposed stripes in x-rays and still appear as bright stripes in EEL spectra<sup>45</sup>. They originate in transitions from the 2p to the 3d bands and their separation corresponds to the spin-orbit splitting from the ground states of the transition ( $2p_{3/2} \rightarrow 3d$ ) and ( $2p_{1/2} \rightarrow 3d$ ). Intuitively, the ratio between the two peaks should correspond to the occupation of the ground states (2:1) if the final density of states was the same for all electrons. Experimentally, the ratios usually differ from 2:1. The changes in this ratio have been successfully related to oxidation states. Quite generally, the ratio will be maximum for  $3d^5$  occupancy and a decrease towards either  $3d^{10}$  or  $3d^0$  is observed<sup>46</sup>. A clear example is found in the case of Mn. The ratio for  $Mn^{2+}$  is around 5, while it decreases to 2 for  $Mn^{4+}$  or  $Mn^0$ . There are several methods for extracting the WL intensities. Amongst them, the Pearson or step function method<sup>47, 48</sup>, where a linear model of the continuum is subtracted; the curve fitting method with Hartree-Slater cross sections<sup>49</sup>, where Gaussian or Lorentzian curves are fitted to the WL after the removal of the Hartree-Slater cross-section; or the Walsh-Dray method<sup>50</sup>, where the continuum is estimated with H edge functions. The measurement of the  $L_{2,3}$  intensity ratios has been one of the most used techniques for oxidation state investigations, but it is very important to keep in mind that other characteristics beyond oxidation state, such as spin state, coordination geometry and ligand types,

may also play an important role<sup>42, 51</sup>. Moreover, WL ratio increases with increasing thickness of the sample, but this effect can be removed by deconvolution of the low-loss spectrum<sup>52</sup>. Methods based on the second derivative<sup>36</sup> of the spectrum have also been used.

- *TM L edge onset (chemical shift)*: the onset of edges will roughly (as the final DOS is convolved with the core-hole) correspond to the lowest energy of the final state. The position of the edge will change with changes in binding energy of the core level. In general, the edges move to higher energies for higher oxidation states<sup>30, 32, 42, 51, 53</sup>. This energy shift is usually referred to as chemical shift<sup>2</sup>. The relationship between the formal oxidation state and the chemical shift of the TM edge is often difficult to ascertain, as the maximum shift is usually below the 2 eV. Also, the very measurement of the peak onset differs amongst the authors. While sometimes the maximum of the  $L_3$  peak has been taken as the onset of the edge<sup>27, 42</sup>, or the point where some fraction of the maximum is reached<sup>52</sup>, it is much more common to use the inflexion point of the rise as a threshold<sup>34</sup>. The results for any of the different techniques for which some point of the rise is taken might be different, but the final trend in the results is maintained.

- *O K onset*: even if the nominal oxidation state of oxygen atoms is -2, the position of the K edge can be substantially different for different compounds. In manganese compounds, the position of the oxygen K edge moves monotonically to lower energies for higher oxidation states of the cation<sup>51, 52, 54</sup>, but this trend is not maintained for all TM oxides. Therefore, calibrating the spectrum for absolute energy positions using the O-K edge can be misleading. However, it is another feature of the spectrum that can be used to identify the oxidation state of the TM.

- *$L_3$  FWHM*: two important aspects influence the width of the  $L_3$  peak: the oxidation state and the mixture of oxidation states. A slight change in the width of the peak with oxidation state was shown by Riedl et al.<sup>32</sup> while it had been previously calculated by Sherman<sup>55</sup>, and Kurata and Colliex<sup>49</sup>. However, the sensitivity to the oxidation state is very low, around 20% as calculated by Riedl, with a good SNR. However, the width of the peak contains information about mixed valences. The  $L_{2,3}$  edges for materials containing TMs in different oxidation states can be regarded as the superposition of two edges of the different oxidation states rather than a single edge of the average valence. Therefore, the chemical shift in this case is that of the lower valence, which onset appears before. This may be misleading, but the  $L_3$  peak will be larger, as it starts with the lower valence but ends with the higher valence. If the width of the peak is notoriously larger than a single oxidation state for a TM, it can indicate the presence of two oxidation states. It is a way of telling a mixed case from a single

valence case when the average is the same. Generally, the width of the Mn  $L_{2,3}$  white lines obtained from experimental EEL spectra is governed by the lifetime of the core-hole and of the excited electron as well as by non-lifetime effects such as solid state effects, exchange interactions between core-hole and 3d electrons, and experimental broadening due to energy resolution and dispersion<sup>56</sup>. The dependence of the  $L_3$  line width on the Mn valence can be explained in the molecular orbital model<sup>57</sup> with the energetic arrangement of the electronic levels near the Fermi level, which are the destination of the excited inner shell electrons.

- *TM L to O K energy distance*: taking into account that the oxygen K edge onset and that of the TM both shift, the relative distance between the two of them is an interesting feature of the spectrum, particularly when no absolute energy positions can be determined. This quantity is related to the energy difference between the 1s level of the oxygen and the  $2p_{3/2}$  level of the TM. While it may be equivalent to the TM edge onset if the O 1s state remains the same<sup>40</sup>, this quantity is generally different due to the non-monotonicity between the oxidation state and the O K edge position. There are some works on identifying the oxidation states of chromium and manganese with this edge difference<sup>20, 32, 40, 42</sup>.

- *$L_2$ - $L_3$  energy distance*: the difference in energy between the  $L_3$  and the  $L_2$  peaks is a feature rarely used in previous work. The separation of the peaks arises from the spin-orbit splitting from the ground states of the transitions ( $2p_{3/2} \rightarrow 3d$ ) and ( $2p_{1/2} \rightarrow 3d$ ). Therefore, any change in the separation is related to the changes in the ground states. Zhang et al.<sup>20</sup> measured those changes in manganese oxides.

- *O K peak-separation method*: The energy separation between the O K pre-peak and the edge main peak is a highly successful and accurate approach to measure oxidation states, which has been tested both experimentally<sup>44</sup> and theoretically<sup>58</sup>. This method, however, is difficult to use in complex heterosystems such as interfaces between two oxides due to beam broadening and cross-talk effects.

All these methods yield consistent results when used on data with good SNR. However, a good SNR is rather uncommon when working with complex data sets such as two dimensional spectrum images. Thanks to the recent advances in electron microscopes<sup>59</sup> the number of spectra available in a single spectrum image (SI) is rapidly increasing. Therefore, a procedure to extract reliable oxidation state information from a great number of spectra at a time is needed. In order to address this need, we have developed the Oxide Wizard software, an automated routine for Gatan Digital Micrograph (DM). As we will show, our approach offers a method for

characterizing the white lines of transition metals in a reproducible, reliable manner, including all the necessary tools in a single interface.

### 3.5.2. Steps of the analysis

The script, written in Digital Micrograph scripting language, is divided in several sequential steps which are summarized in the flow chart in Figure 3.6. The first three steps are optional, and consist of a low-loss deconvolution, spectra binning and drift correction. Afterwards, the oxygen K edge onset is measured, followed by the TM edge. The results are shown for a single spectrum, and, if satisfactory, applied to the full spectrum image.

The first step consists on the **deconvolution** of the low-loss region of the spectrum. Core-loss edges are usually broadened because of the effects of multiple scattering. If the sample is not thin enough, it is likely that the electrons suffering core-loss inelastic scattering will also undergo at least a plasmon excitation, broadening the ELNES and, hence, changing the shape of the continuum. Some authors have shown that the measurements that will follow are dependent on the thickness of the sample because of multiple scattering. If the measurements are carried out in a thin specimen or in an area of the sample with constant thickness and only used for comparison purposes, low-loss deconvolution is not necessary. Otherwise, deconvolution of the low-loss region is typically required. This step is strongly recommended in order to compare the results between different samples with better accuracy. In Figure 3.7, an example of the input of the script is given for a  $\text{Mn}_2\text{O}_3$  spectrum line. The low-loss spectrum is shown in Figure 3.7 (a) and the core-loss spectrum in Figure 3.7 (b). Prior to deconvolution, the background before the first edge is better extracted, as shown in Figure 3.7 (c) using the DM built-in function. The result of the deconvolution is shown in Figure 3.8 (a), where the gain in sharpness can be observed. Binning can be achieved by summing spectra, and it can be helpful when the dataset is very noisy or when performing test runs on very large spectrum images.

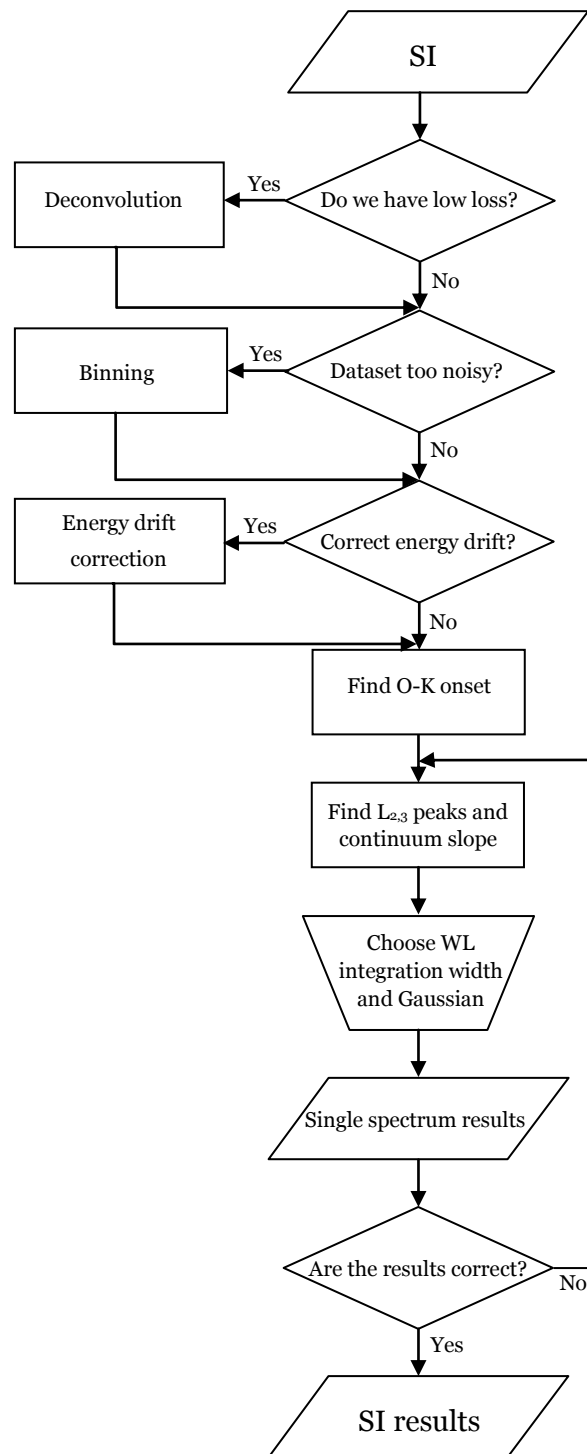


**Figure 3.6:** Flow chart of the script, starting with an spectrum image and ending in the results.

Next, an **energy drift correction** procedure can be carried out. This step is based on the presence of peaks other than the TM or the oxygen in the spectra. It consists on choosing an edge in one single spectrum with a region of interest (ROI) tool provided by the script. The energy drift is calculated using a cross correlation of that region of the reference spectrum and the rest of the spectra. A new, drift-corrected spectrum image is created. As it can be observed in Figure 3.7 (b), the input spectrum image has a lot of instabilities in energy. If it is not possible to use an edge other than the oxygen or the TM, drift correction is still useful. If the energy drift is too large, the adequate ROI for a single spectrum will be inadequate for the whole set of spectra and the analysis can fail. In Figure 3.8 (b) the drift corrected core loss can be observed. The absolute peak position of the TM edge is lost if we apply the drift correction procedure on it, but the relative position to O K edge may still be valuable.

Subsequently, the **onset of the oxygen K edge** is analyzed. The onset is located at the minimum of the rise. Choosing the first peak of the oxygen with a ROI (Figure 3.9), the onset is found as a minimum in a modified second derivative, equivalent to the second derivative filter in DM, where maxima in the original function correspond to maxima in the filtered version, as in the inset of Figure 3.10. The modification inverts the second derivatives in order to locate maxima that correspond to minima in the actual second derivative of the function.

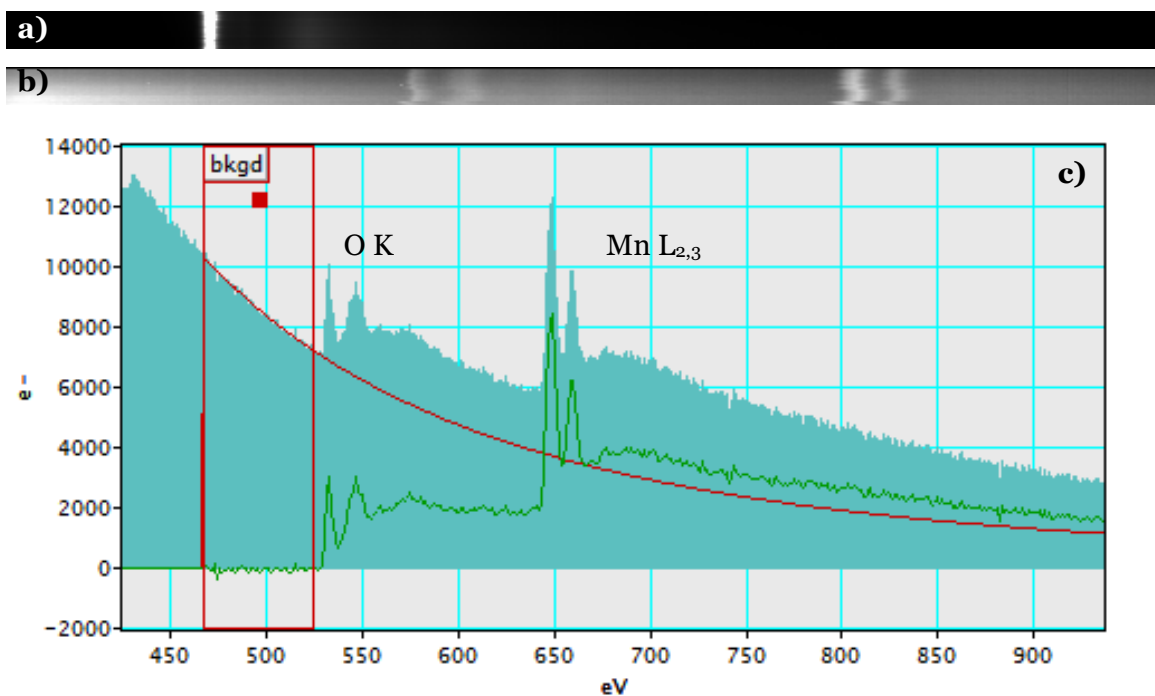


**Figure 3.7:** Input of the script. **a)** Low-loss spectrum line, **b)** core-loss spectrum line and **c)** single spectrum extracted from the core-loss spectrum line, with the procedure to extract the signal (in green) from the background (in red).

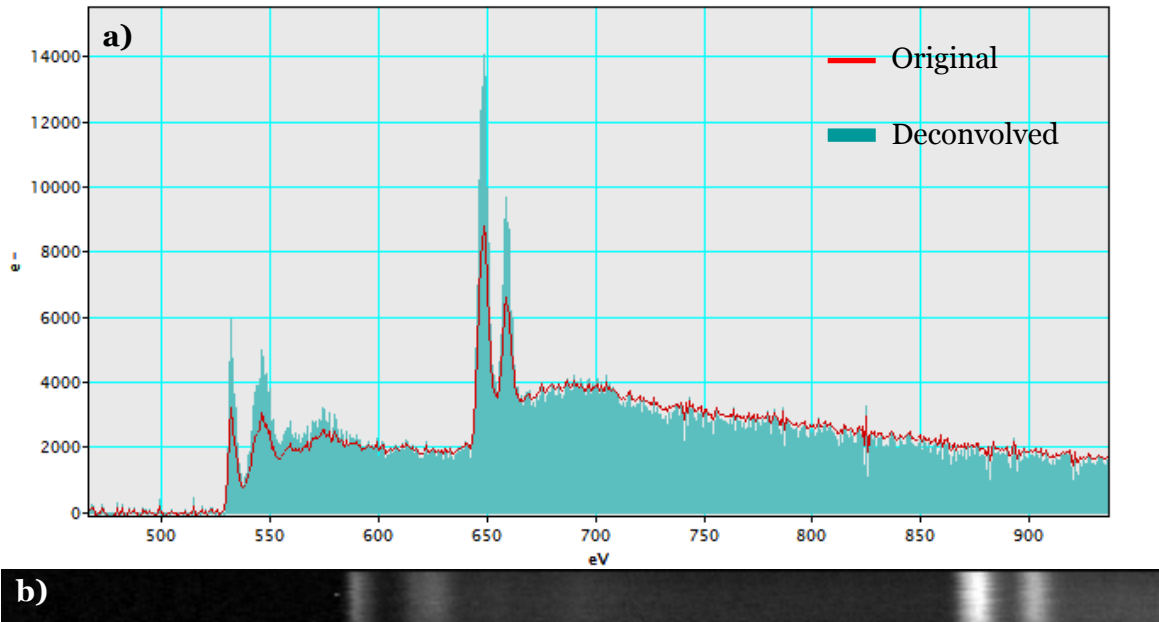


**Figure 3.8:** Deconvolution and drift correction. **a)** Single spectrum before (in red) and after (in filled green) deconvolution with its low loss. **b)** Core-loss spectrum image after energy drift correction.

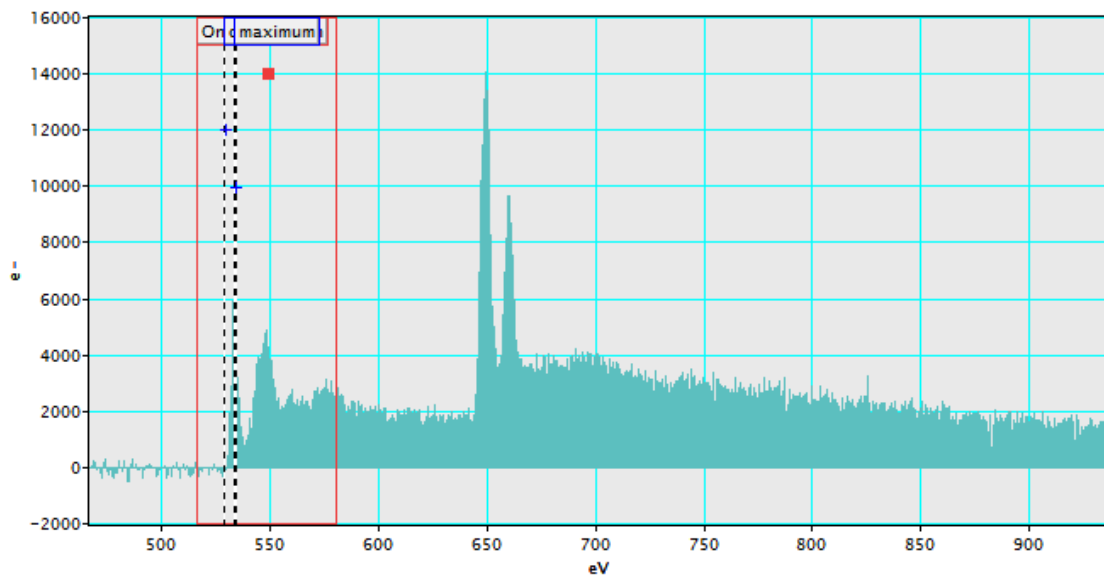


**Figure 3.9:** Location of the onset of the O K edge. The ROI is set in red, while the onset and maximum of the first oxygen peak are tagged

Finally, the **ELNES of the TM** is characterized by finding the positions of the maxima of the two white lines, the onset of the  $L_3$ , the minimum in between and the end of the  $L_2$ . It must be noticed that, before this analysis, the background needs to be subtracted (by using power-law fits in DM or other models). After placing a ROI on the

white lines of a single spectrum, the script calculates the second derivative, finds the maximum and fits a Gaussian curve to it. (Figure 3.10, inset). This maximum corresponds to the first white line. This curve is then used to calculate the position of the features in the WL by cross correlating it with the second derivative of the spectrum. A cross-correlation is used since it is easily and rapidly calculated in DM, and it is robust against noise and it enhances actual white line peaks in the second derivative against local maxima and minima.

The cross-correlation has a few distinct features: a global maximum placed at zero position and a series of peaks which match the greater features of the second derivative of the spectrum. The minimum before the first white line is taken as the onset of the edge. The global maximum not corresponding to the zero position, found as the maximum of the cross-correlation after a few eV from the zero, corresponds to the second white line. The two other features are less important for the analysis, but are calculated anyway for further data treatment. The valley between the WL and the end of the ELNES are found as the minima after the first and second white lines respectively. The result is shown as in Figure 3.10, and can be used to detect any error in the peak detection.

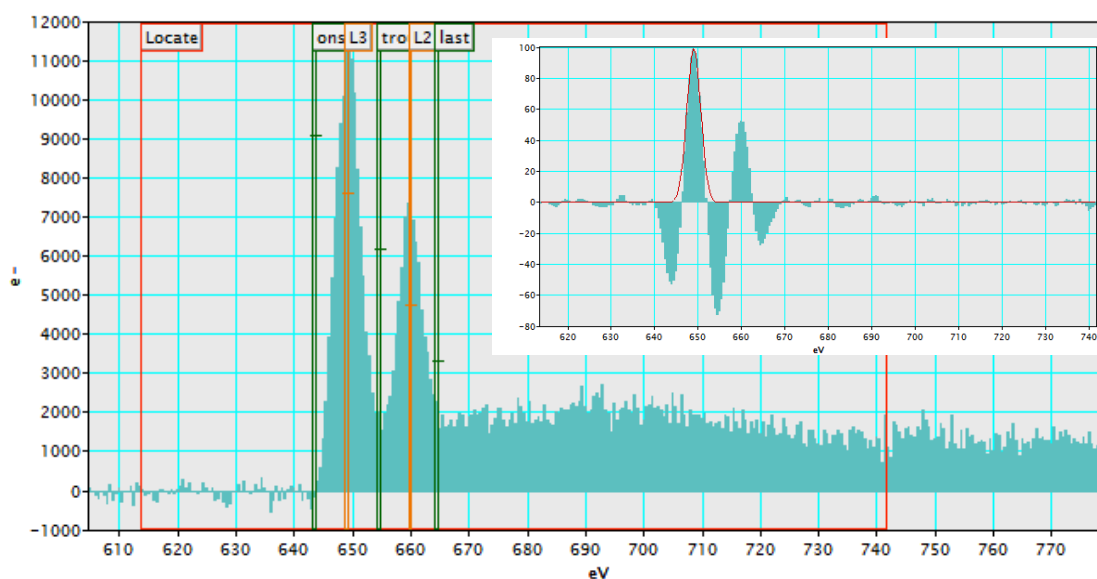


**Figure 3.10:** Location of the peaks in the  $L_{2,3}$  ELNES. In the inset, second derivative of the area marked in the red ROI of the main image is shown. The red line in the inset is the Gaussian fit of the  $L_3$  second derivative peak used for cross correlation. In the main image, the peaks are marked with orange, while the minima are marked in green.

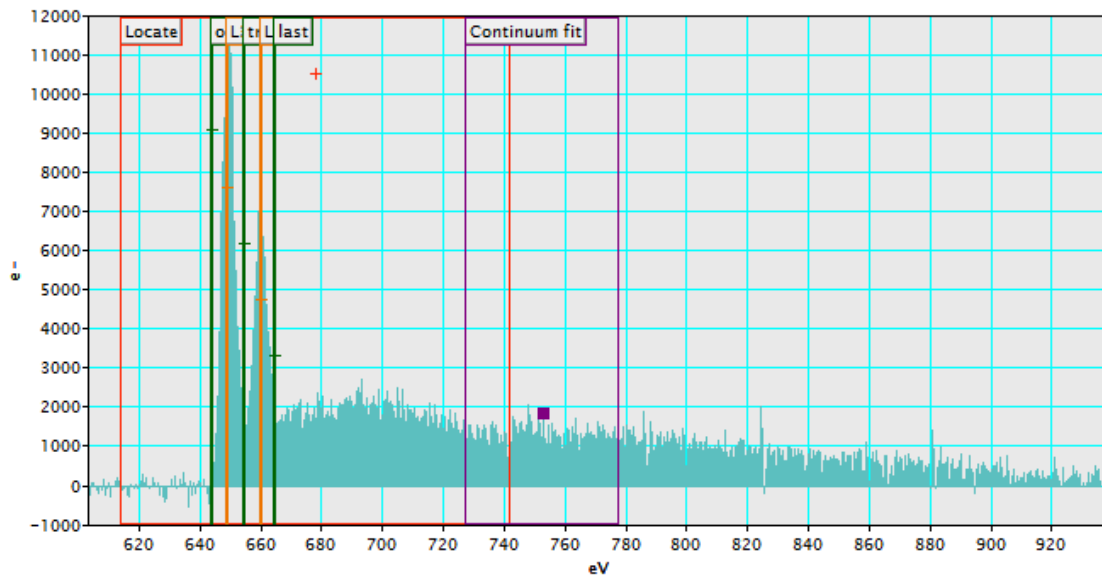


**Figure 3.11:** Continuum fit ROI.

Once the features of the ELNES are located, we already have the information concerning the absolute positions of the lines. However, if we want to integrate the areas under the peaks, it is necessary to remove the influence of the continuum<sup>47</sup>. A few methods have been devised for this purpose, such as modeling it with Hartree Slater or hydrogenic cross sections (Walsh-Dray method). This method calculates the the continuum with a neutral atom cross section. However, a simpler alternative is a linear fitting of the continuum, i.e., the Pearson method, which has been chosen for its simplicity and for yielding results similar to those of Walsh Dray<sup>47</sup>. For this method, the continuum is modeled as a two step function with the steps centered under the peaks (Figure 3.12), with a height ratio of 2:1 from first to second and with a slope calculated by a linear fit of the continuum after the peaks (Figure 3.11), as we want to calculate the deviations from the 2:1 ratio of the lines. This function is subtracted from the data as the intensity under the peaks is calculated. The script allows the user to decide the width of the integrating windows and also the continuum modeling region.

The script can present the results for a single spectrum or for the whole spectrum image. In both cases the results can be refined by fitting the peaks after the continuum subtraction with two Gaussian curves (Figure 3.13). Final results provided by the script are the TM edge onset, the white line ratio, the energy split between the two WL, the energy between the O K and the TM edge and the FWHM of the first WL.

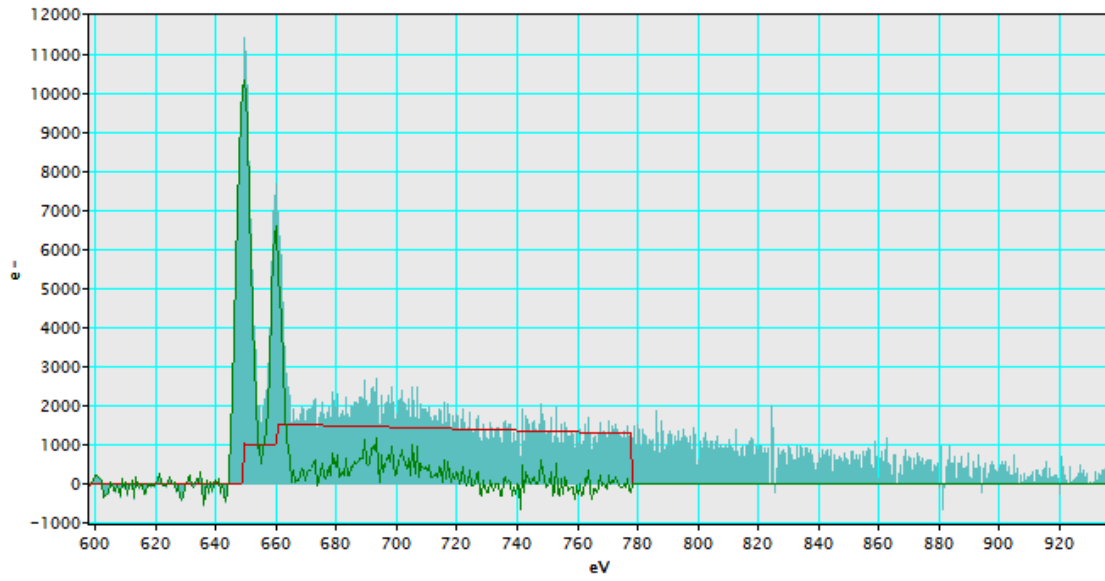


**Figure 3.12:** The continuum measured in the ROI shown in Figure 3.11 is extrapolated to a two step function (red line) and subtracted from the edge (in green, filled)

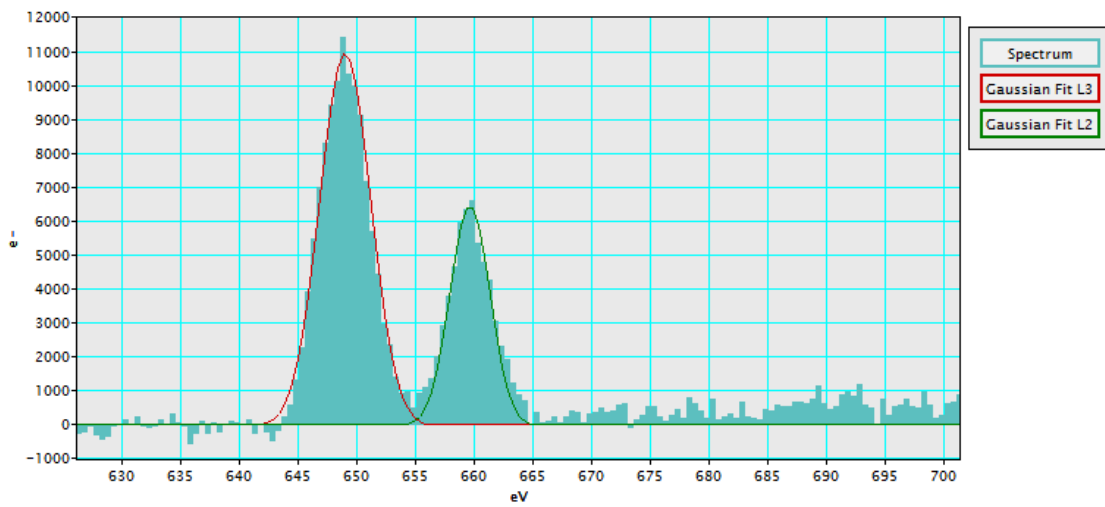


**Figure 3.13:** Gaussian curves fitting the two white lines.

### 3.5.3. Calibration test on $Mn_xO_y$ oxides

Importantly, to calibrate the script, bulk materials with known oxidation states were necessary. In our case, since we were interested in the Mn oxidation states, a number of different bulk manganese oxides ( $MnO$ ,  $Mn_3O_4$ ,  $Mn_2O_3$  and  $MnO_2$ , kindly provided by Dr. Elena Xuriguera from the Electronics Department and the Department of Materials Science and Metallurgical Engineering of the University of Barcelona) were obtained. The structure of the samples was confirmed by x-ray diffraction. In Figure 3.14, single spectra for the four different bulk manganese oxides considered are shown. The differences in the O K edges and the Mn  $L_{2,3}$  edges are clear, the  $L_3/L_2$  ratio decreases with oxidation state and the O K onset position increases.

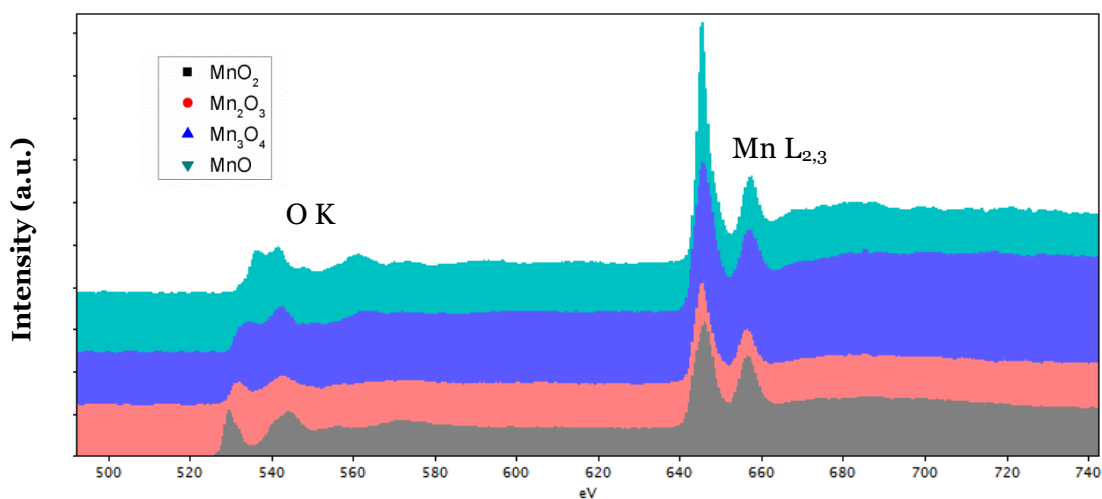


**Figure 3.14:** Single spectra used for reference data extraction for Mn oxidation states ranging from 2 to 4, displaced in the intensity direction. The spectra are aligned for the Mn  $L_{2,3}$  edge

Rather than calibration curves, we have preferred the two-parameter method introduced by Daulton et al.<sup>42</sup> in chromium and performed by Tan et al. on manganese and iron oxides<sup>52</sup>. This method presents the results of the two WL features in the same plot. While a single parameter can be misleading, the two-parameter method makes the characterization easier.

The Mn  $L_{2,3}$  onset is discarded, as there was no absolute measure of the position. Similarly, the  $L_3 - L_2$  distance is not used since it did not show relevant changes in the data. The white line ratio did show the expected changes; in Figure 3.15, it is plotted

against the O K to Mn L<sub>3</sub> distances, which also showed a large change between oxidation states. In the chart, although the different formal oxidation states are separated, the Mn<sub>3</sub>O<sub>4</sub> (in red) and Mn<sub>2</sub>O<sub>3</sub> (in blue) show data clouds very close to one another, with some data points overlapping. To avoid ambiguity in the analysis, a third parameter, FWHM of L<sub>3</sub> peak, is introduced. As it can be clearly seen in Figure 3.16, in this case all the data clouds, and particularly Mn<sub>3</sub>O<sub>4</sub> and Mn<sub>2</sub>O<sub>3</sub> ones, are well separated.

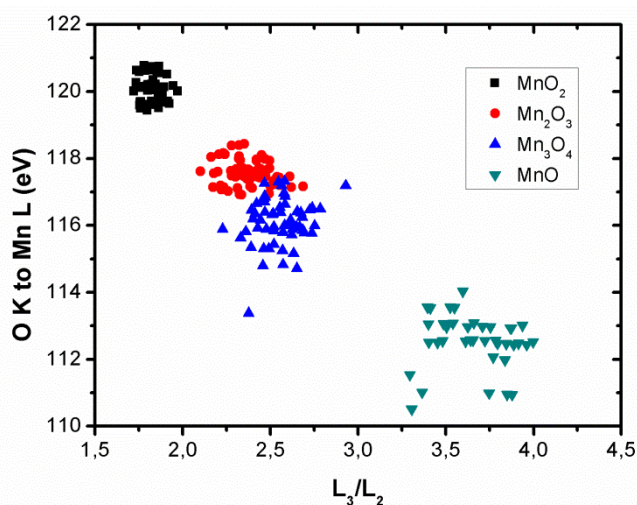


**Figure 3.15:** Two parameter chart combining white line ratios and O K to Mn L<sub>3</sub> energy distances for Mn oxidation states ranging from 2 to 4.

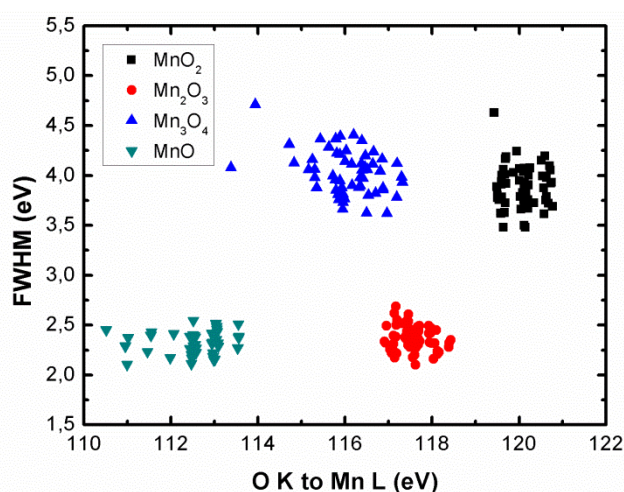


**Figure 3.16:** Two parameter chart combining O K to Mn L<sub>3</sub> energy distances and FWHM of the L<sub>3</sub> peak for Mn formal oxidation states ranging from 2 to 4.

$\text{Mn}_2\text{O}_3$  has a single oxidation state, as  $\text{Mn}^{3+}$ , while  $\text{Mn}_3\text{O}_4$  contains a mixture of  $\text{Mn}^{3+}$  and  $\text{Mn}^{2+}$  in a two-to-one ratio. The measured edge can be seen as a superposition of both oxidation states. The onset of the edge for  $\text{Mn}_3\text{O}_4$  is, therefore close to that of the  $\text{Mn}_2\text{O}_3$  edge, both given by the  $\text{Mn}^{3+}$  contribution. However, there is a variation in O K position, so the distance between O and Mn edges does show a change. The white line ratio is also very close for the two compositions. However, the FWHM of the mixed oxide is expected to be larger, since the  $L_3$  will be a superposition of two displaced peaks. The experimental results corroborate this point.

#### **3.5.4. Application: Mn oxidation state determination in core-shell nanoparticles**

Once the parameters for the edges of the different manganese oxide reference materials have been established, the routine can be applied to a sample of unknown oxidation state. The sample consists of core-shell nanoparticles, where the core corresponds to an iron oxide and the shell to a manganese oxide.

For the synthesis of the sample, in a first step, spherical iron oxide nanoparticles were obtained by dissolving a given amount of iron (III) oleate and 1 mmol of oleic acid in 36 mL of 1-octadecene. The mixture was heated under magnetic stirring up to 320 °C (at 3 °C/min) and kept for 30 min. The slurry was removed from the heating source and allowed to cool down to room temperature. A surfactant-to-metal molar ratio,  $[\text{S}]/[\text{M}]$ , of 1 was used, leading to iron oxide seeds of and 17(1) nm. In a second step the iron oxide seeds were used to heterogeneously growth a manganese oxide layer. Briefly, a solution of 200 mg of iron oxide seeds and 50 ml of dibenzyl ether was degassed with several cycles of vacuum/argon gas at 100 °C. Subsequently it was heated up to 220 °C, in which a solution containing 0.8 mmol (0.2g) of manganese (II) acetylacetonate, 0.8 mmol of 1,2-hexadecanediol, 1.6 mmol of oleylamine, 0.6 mmol of oleic acid and 10 mL of dibenzyl ether was added at a fast injection rate. The slurry was maintained at 220°C during 1 hour under magnetic stirring after the fast injection. Finally, the reaction flask was removed from the heating source and cooled down in argon to room temperature.

A high angle annular dark field (HAADF) image of a nanoparticle is shown in Figure 3.17 (a). In this image, the core and the inhomogeneous shell are difficult to tell apart. If we carry out a multiple linear least squares (MLLS) fitting of the EELS spectrum image for the iron and manganese edges, we can obtain a composite image with compositional contrast, as shown in Figure 3.17 (b). In this figure, the iron oxide core appears as a round particle presented in red, while the manganese oxide grows as discontinuous crystallites around the core.

The samples were grown by Dr. Marta Estrader from the Inorganic Chemistry Department of the University of Barcelona, and the data, acquired at the Nion UltraSTEM200, were kindly provide by Dr. María Varela, from Oak Ridge National Laboratory, Tennessee, and the Applied Physics III Department of the Complutense University.

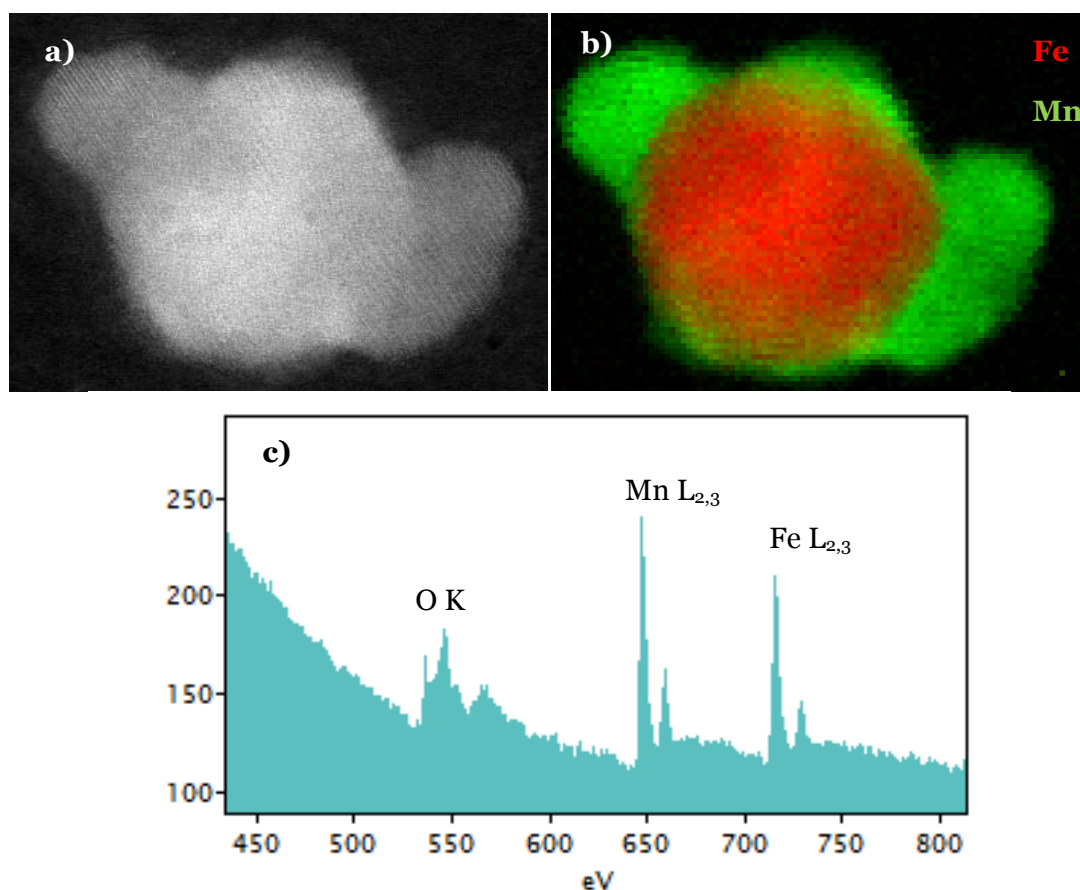


**Figure 3.17:** **a)** HAADF image of the particle and **b)** composite image of the MLLS fitting of the spectrum image to the iron and manganese  $L_{2,3}$  edges. **c)** Single spectrum showing the oxygen K, manganese  $L_{2,3}$  and iron  $L_{2,3}$  edges.

The spectrum image was fitted to two single spectra in Figure 3.18 (a) from the surface (orange) and the inner part (turquoise) of the Mn oxide shell. The two spectra had different characteristics, pointing to different oxidation states. The red spectrum, extracted from the surface region, has a higher WL ratio, a thinner  $L_3$  and an onset shifted to lower energies than the green spectrum, extracted from the inner parts of the manganese oxide shell. The result of the fitting is shown in Figure 3.18 (b), where we can observe a distribution of manganese oxidation states. However, the MLLS fitting maps offer qualitative information only. We then apply OW to quantify the results.

The spectra were rather noisy, so multivariate analysis was applied prior to OW. This kind of analysis will be explained in section 4.3.2. The script was applied to the whole spectrum image, consisting on 100x70 single spectra as the one shown in Figure 3.17 (c), both with and without low-loss deconvolution. The differences between both procedures were negligible, mainly due to the small thickness of the particle, which, along with the carbon support, added only to 0.3 inelastic mean free paths. The results of the deconvolved spectra are shown in Figure 3.19. The Mn white line ratio (Figure 3.19 (a)) in the particle ranges from 3 to 3.5. The FWHM of the  $L_3$  line (Figure 3.19 (b)) yields values between 4 and 6 eV, and the energy separation between the O K edge and the Mn  $L_{2,3}$  (Figure 3.19 (c)) goes from 112 to 115 eV.

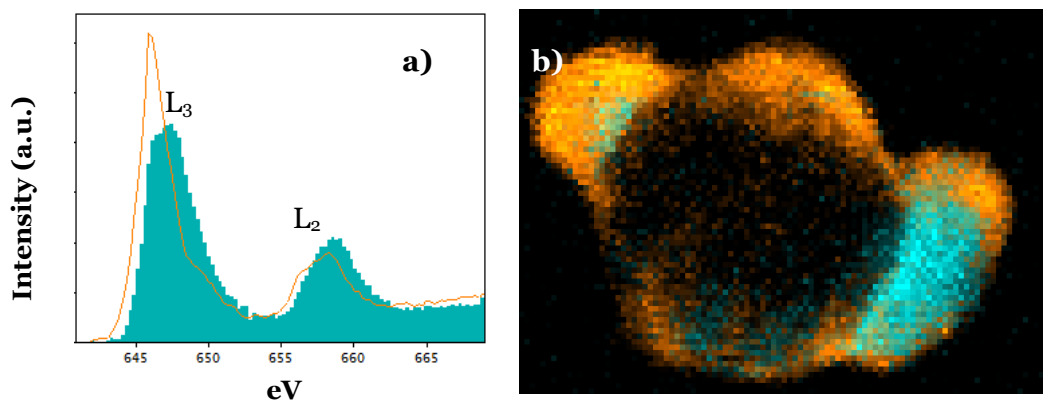


**Figure 3.18:** **a)** Mn  $L_{2,3}$  edges extracted from the border (in orange) and the inner area (in turquoise) of the manganese oxide shell and **b)** composite image of the MLLS fitting of the spectrum image to the two spectra in (a).

In the manganese oxide shell, two different regions can be seen, corresponding to the surface and the inner areas of the shell. At the surface, the values of both the WL ratio (3.5) and the O-Mn distance (112 eV) point to a MnO-like composition according

to the two parameter chart in Figure 3.15 with an oxidation state of  $\text{Mn}^{2+}$ . In the inner regions of the shell, displayed in green in Figure 3.19 (a), and in the range of green to yellow in Figure 3.19 (b), the WL ratio is around 3, and the O-Mn distance is around 115 eV. In Figure 3.15, however, these values do not correspond to any of the reference oxidation states. The values lie between  $\text{Mn}^{2+}$  and  $\text{Mn}^{2.66+}$ . The spectra for the inner regions of the manganese oxide result from a superposition of the inner and outer areas, as the electron travels through the entire thickness of the sample. Therefore, the actual oxidation state in the inner part must be higher than measured. Using the FWHM measurements, the difference between the surface and the interior of the manganese regions is of 2 eV, the same difference found between  $\text{Mn}^{2+}$  and  $\text{Mn}^{2.66+}$ . Therefore, we can assume that the oxidation state of manganese ranges from  $\text{Mn}^{2+}$  at the surface to  $\text{Mn}^{2.66+}$  in the inside. An oxidation state of +2.66 would correspond to  $\text{Mn}_3\text{O}_4$ . Consequently, our results indicate that the shell of the particles may be composed by an inhomogeneous Mn oxide, with a mixture of MnO at the surface and  $\text{Mn}_3\text{O}_4$  rich areas within the shell.

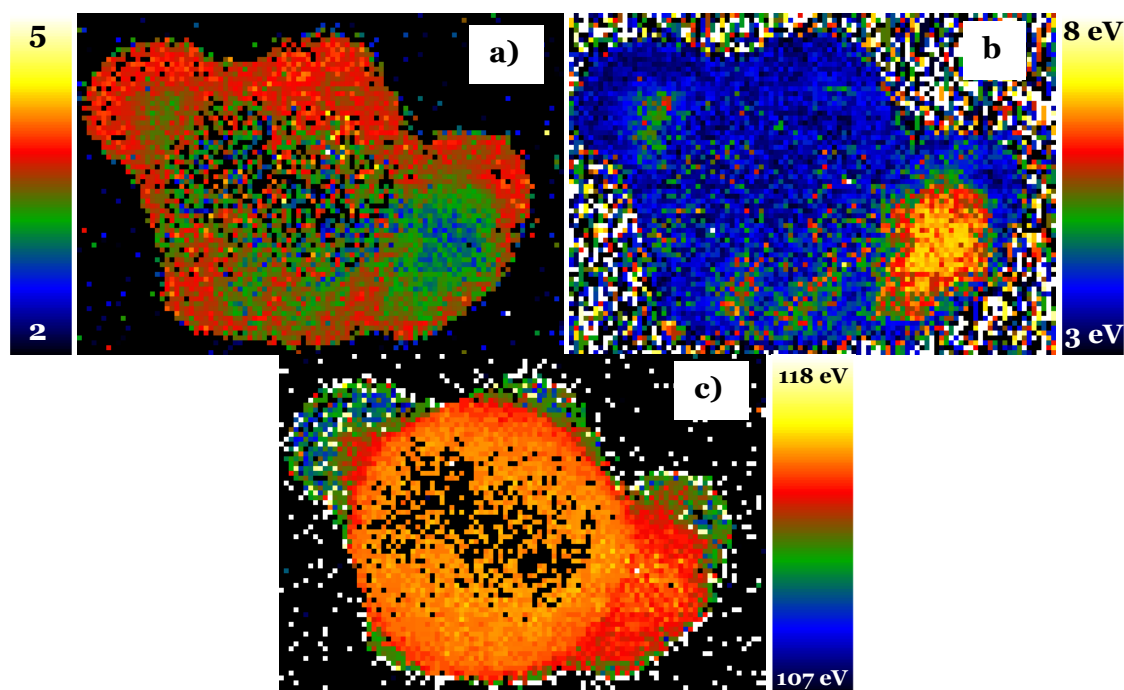


**Figure 3.19:** Different outputs of the Oxide Wizard script: **a)** WL ratio. **b)**  $L_3$  FWHM after Gaussian fitting. **c)** O K to Mn  $L_3$  distance.

In this example, it is possible to observe how unfortunate the projection of 3D information in the 2D EELS-SI can be. The oxidation state of manganese in the interior of the shell is not directly measurable, as it is completely covered by another compound with a different oxidation state. Also, the spatial resolution of the different compounds is not clear from the analyze Spectrum Image.

### 3.5.5. Conclusions

A script for Digital Micrograph, Oxide Wizard, has been developed to characterize the white lines of transition metals, dealing with large spectrum images in a systematic, reproducible, way. As an output, the script plots the white line ratio, the oxygen K edge onset, the TM edge onset, the difference between both, the FWHM of the TM first WL and the separation between the WLs. From these parameters, and using reference compounds for comparison, quantitative information on the oxidation state of unknown samples can be easily obtained. This procedure has been applied to iron oxide/manganese oxide core/shell nanoparticles with unknown manganese oxidation states. The results evidence, with sub-nm resolution, the existence nano-domains with distinct oxidation states consistent with the presence of  $\text{Mn}_3\text{O}_4$  in the interior of the shell and MnO near its surface. Hence, Oxide Wizard has been demonstrated to be a very effective and reliable script capable of dealing with large datasets which allows real time processing of data within the Digital Micrograph interface.

In this section we have seen how the oxidation state of transition metal oxides can be extracted from the EELS spectrum, but also how this information, arising from 3D structures, gets mixed when acquiring spectrum images. The next chapters will deal with the reconstruction of the information in the EEL Spectrum in 3D, to avoid this kind of superposition.

## 3.6. References

1. Williams, D. B. & Carter, B. C. *Transmission Electron Microscopy* (Springer, 2009).
2. Egerton R. F. *Electron Energy-Loss Spectroscopy in the Electron Microscope* (Springer, New York, 2011).
3. Krakow, W. & Howland, L. Method for Producing Hollow Cone Illumination Electronically in Conventional Transmission Microscope. *Ultramicroscopy* **2**, 53-67 (1976).
4. Kunath, W., Zemlin, F. & Weiss, K. Apodization in Phase-Contrast Electron-Microscopy Realized with Hollow-Cone Illumination. *Ultramicroscopy* **16**, 123-138 (1985).
5. Vincent, R. & Midgley, P. Double Conical Beam-Rocking System for Measurement of Integrated Electron-Diffraction Intensities. *Ultramicroscopy* **53**, 271-282 (1994).
6. Muller, D. A., et al. Atomic-scale chemical imaging of composition and bonding by aberration-corrected microscopy. *Science* **319**, 1073-1076 (2008).
7. Kimoto, K., et al. Element-selective imaging of atomic columns in a crystal using STEM and EELS. *Nature* **450**, 702-704 (2007).
8. Batson, P. E., Dellby, N. & Krivanek, O. L. Sub-angstrom resolution using aberration corrected electron optics. *Nature* **418**, 617-620 (2002).
9. Allen, L. J., Findlay, S. D., Lupini, A. R., Oxley, M. P. & Pennycook, S. J. Atomic-resolution electron energy loss spectroscopy imaging in aberration corrected scanning transmission electron microscopy. *Phys.Rev.Lett.* **91**, 105503 (2003).
10. Wang, Y., et al. Determination of the polarity of ZnO thin films by electron energy-loss spectroscopy. *Physics Letters a* **320**, 322-326 (2004).
11. VanDyck, D. & deBeeck, M. O. A simple intuitive theory for electron diffraction. *Ultramicroscopy* **64**, 99-107 (1996).
12. Van Aert, S., Geuens, P., Van Dyck, D., Kisielowski, C. & Jinschek, J. R. Electron channelling based crystallography. *Ultramicroscopy* **107**, 551-558 (2007).
13. Fitting, L., Thiel, S., Schmehl, A., Mannhart, J. & Muller, D. A. Subtleties in ADF imaging and spatially resolved EELS: A case study of low-angle twist boundaries in SrTiO<sub>3</sub>. *Ultramicroscopy* **106**, 1053-1061 (2006).

14. Nakafuji, A., Murakami, Y. & Shindo, D. Effect of diffraction condition on mean free path determination by EELS. *J. Electron Microsc.* **50**, 23-28 (2001).
15. Weirich, T. E., Portillo, J., Cox, G., Hibst, H. & Nicolopoulos, S. Ab initio determination of the framework structure of the heavy-metal oxide Cs<sub>x</sub>Nb<sub>2.54</sub>W<sub>2.46</sub>O<sub>14</sub> from 100 kV precession electron diffraction data. *Ultramicroscopy* **106**, 164-175 (2006).
16. Avilov, A., et al. Precession technique and electron diffractometry as new tools for crystal structure analysis and chemical bonding determination. *Ultramicroscopy* **107**, 431-444 (2007).
17. Sun, J., KrusinElbaum, L., Duncombe, P., Gupta, A. & Laibowitz, R. Temperature dependent, non-ohmic magnetoresistance in doped perovskite manganese trilayer junctions. *Appl. Phys. Lett.* **70**, 1769-1771 (1997).
18. Cave, L., Al, T., Loomer, D., Cogswell, S. & Weaver, L. A STEM/EELS method for mapping iron valence ratios in oxide minerals. *Micron* **37**, 301-309 (2006).
19. Loomer, D. B., Al, T. A., Weaver, L. & Cogswell, S. Manganese valence imaging in Mn minerals at the nanoscale using STEM-EELS. *Am. Mineral.* **92**, 72-79 (2007).
20. Zhang, S., Livi, K. J. T., Gaillot, A., Stone, A. T. & Veblen, D. R. Determination of manganese valence states in (Mn<sup>3+</sup>, Mn<sup>4+</sup>) minerals by electron energy-loss spectroscopy RID A-2569-2010. *Am. Mineral.* **95**, 1741-1746 (2010).
21. van Aken, P. A., Liebscher, B. & Styrsa, V. J. Quantitative determination of iron oxidation states in minerals using Fe L<sub>2,3</sub>-edge electron energy-loss near-edge structure spectroscopy. *Physics and Chemistry of Minerals* **25**, 323-327 (1998).
22. Suchorski, Y., et al. Evolution of oxidation states in vanadium-based catalysts under conventional XPS conditions. *Appl. Surf. Sci.* **249**, 231-237 (2005).
23. Graetz, J., Ahn, C., Ouyang, H., Rez, P. & Fultz, B. White lines and d-band occupancy for the 3d transition-metal oxides and lithium transition-metal oxides. *Phys. Rev. B* **69**, 235103 (2004).
24. Logvenov, G., Gozar, A. & Bozovic, I. High-Temperature Superconductivity in a Single Copper-Oxygen Plane. *Science* **326**, 699-702 (2009).
25. McNaught, A. D. & Wilkinson, A. *IUPAC. Compendium of Chemical Terminology (the "Gold Book")* (Blackwell Scientific Publications, Oxford, 1997).
26. Luo, W., et al. Orbital-occupancy versus charge ordering and the strength of electron correlations in electron-doped CaMnO<sub>3</sub>. *Phys. Rev. Lett.* **99**, 036402 (2007).
27. Schmid, H. K. & Mader, W. Oxidation states of Mn and Fe in various compound oxide systems. *Micron* **37**, 426-432 (2006).
28. Garvie, L. & Craven, A. High-Resolution Parallel Electron-Energy-Loss Spectroscopy of Mn L<sub>2,3</sub>-Edges in Inorganic Manganese Compounds. *Phys. Chem. Miner.* **21**, 191-206 (1994).

29. Garvie, L. A. J. & Buseck, P. R. Ratios of ferrous to ferric iron from nanometre-sized areas in minerals. *Nature* **396**, 667-670 (1998).
30. Rask, J., Miner, B. & Buseck, P. Determination of Manganese Oxidation-States in Solids by Electron Energy-Loss Spectroscopy. *Ultramicroscopy* **21**, 321-326 (1987).
31. Riedl, T., Gemming, T. & Wetzig, K. Extraction of EELS white-line intensities of manganese compounds: Methods, accuracy, and valence sensitivity. *Ultramicroscopy* **106**, 284-291 (2006).
32. Riedl, T., Gemming, T., Gruner, W., Acker, J. & Wetzig, K. Determination of manganese valency in  $\text{La}_{1-x}\text{Sr}_x\text{MnO}_3$  using ELNES in the (S)TEM. *Micron* **38**, 224-230 (2007).
33. Riedl, T., Serra, R., Calmels, L. & Serin, V. Valence sensitivity of Fe- $L_{2,3}$  white-line ratios extracted from EELS. 419-420 (2008).
34. Paterson, J. H. & Krivanek, O. L. EELS of 3d transition-metal oxides: II. Variations with oxidation state and crystal structure. *Ultramicroscopy* **32**, 319-325 (1990).
35. Turquat, C., Leroux, C., Gloter, A., Serin, V. & Nihoul, G. V-doped  $\text{HfO}_2$ : thermal stability and vanadium valence. *Int.J.Inorg.Mater.* **3**, 1025-1032 (2001).
36. Botton, G. A., Appel, C. C., Horsewell, A. & Stobbs, W. M. Quantification of the EELS near-edge structures to study Mn doping in oxides. *Journal of Microscopy-Oxford* **180**, 211-216 (1995).
37. Gloter, A., et al. Vanadium valency and hybridization in V-doped hafnia investigated by electron energy loss spectroscopy. *European Physical Journal B* **22**, 179-186 (2001).
38. Meneses, C. T., Vicentin, F. C., Sasaki, J. M. & Macedo, M. A. Influence of Li on the K-edge of O and  $L_{2,3}$  of the Mn XANES in  $\text{Li}_x\text{Mn}_2\text{O}_4$  thin films. *Journal of Electron Spectroscopy and Related Phenomena* **156**, 326-328 (2007).
39. Colliex, C., Manoubi, T. & Ortiz, C. Electron-Energy-Loss-Spectroscopy Near-Edge Fine-Structures in the Iron-Oxygen System. *Physical Review B* **44**, 11402-11411 (1991).
40. Arevalo-Lopez, A. M. & Alario-Franco, M. A. Reliable Method for Determining the Oxidation State in Chromium Oxides. *Inorg.Chem.* **48**, 11843-11846 (2009).
41. Wang, Y. Q., Maclaren, I. & Duan, X. F. EELS analysis of manganese valence states in rare-earth manganites  $(\text{La}_{1-x}\text{Y}_x)_{0.5}(\text{Ca}_{1-y}\text{Sr}_y)_{0.5}\text{MnO}_3$ . *Materials Science and Engineering A* **318**, 259-263 (2001).
42. Daulton, T. L., Little, B. J., Lowe, K. & Jones-Meehan, J. Electron energy loss spectroscopy techniques for the study of microbial chromium(VI) reduction. *J.Microbiol.Methods* **50**, 39-54 (2002).
43. Kourkoutis, L. F., Hotta, Y., Susaki, T., Hwang, H. Y. & Muller, D. A. Nanometer scale electronic reconstruction at the interface between  $\text{LaVO}_3$  and  $\text{LaVO}_4$ . *Phys.Rev.Lett.* **97**, 256803 (2006).

44. Varela, M., et al. Atomic-resolution imaging of oxidation states in manganites. *Physical Review B* **79**, 085117 (2009).
45. Leapman, R. D., Grunes, L. A. & Fejes, P. L. Study of the  $L_{2,3}$  edges in the 3d transition metals and their oxides by electron-energy-loss spectroscopy with comparisons to theory. *Phys.Rev.B* **26**, 614-635 (1982).
46. Sparrow, T., Williams, B., Rao, C. & Thomas, J.  $L_3/L_2$  White-Line Intensity Ratios in the Electron Energy-Loss Spectra of 3d Transition-Metal Oxides Rid B-1569-2009. *Chem.Phys.Lett.* **108**, 547-550 (1984).
47. Pearson, D. H., Ahn, C. C. & Fultz, B. White lines and d-electron occupancies for the 3d and 4d transition metals. *Phys.Rev.B* **47**, 8471 (1993).
48. Estrade, S., et al. Distinguishing the core from the shell in  $MnO_x/MnO_y$  and  $FeO_x/MnO_x$  core/shell nanoparticles through quantitative electron energy loss spectroscopy (EELS) analysis. *Micron* **43**, 30-36 (2012).
49. Kurata, H. & Colliex, C. Electron-Energy-Loss Core-Edge Structures in Manganese Oxides. *Physical Review B* **48**, 2102-2108 (1993).
50. Stolojan, V., Walsh, C. A., Yuan, J. & Brown, L. M. Calibration of the relationship between white-line intensity and valence states for the first transition series. *Electron Microscopy and Analysis 1999* 235-238 (1999).
51. Gilbert, B., et al. Multiple scattering calculations of bonding and X-ray absorption spectroscopy of manganese oxides RID E-3182-2010. *J Phys Chem A* **107**, 2839-2847 (2003).
52. Tan, H., Verbeeck, J., Abakumov, A. & Van Tendeloo, G. Oxidation state and chemical shift investigation in transition metal oxides by EELS. *Ultramicroscopy* **116**, 24-33 (2012).
53. Taftø, J. & Krivanek, O. L. Site-Specific Valence Determination by Electron Energy-Loss Spectroscopy. *Phys.Rev.Lett.* **48**, 560-563 (1982).
54. Laffont, L. & Gibot, P. High resolution electron energy loss spectroscopy of manganese oxides: Application to  $Mn_3O_4$  nanoparticles. *Mater Charact* **61**, 1268-1273 (2010).
55. Sherman, D. M. The Electronic-Structures of Manganese Oxide Minerals. *Am.Mineral.* **69**, 788-799 (1984).
56. Mitterbauer, C., et al. Electron energy-loss near-edge structures of 3d transition metal oxides recorded at high-energy resolution. *Ultramicroscopy* **96**, 469-480 (2003).
57. Grunes, L. A., Leapman, R. D., Wilker, C. N., Hoffmann, R. & Kunz, A. B. Oxygen-K Near-Edge Fine-Structure - an Electron-Energy-Loss Investigation with Comparisons to New Theory for Selected 3d Transition-Metal Oxides. *Physical Review B* **25**, 7157-7173 (1982).

58. Luo, W., Varela, M., Tao, J., Pennycook, S. J. & Pantelides, S. T. Electronic and crystal-field effects in the fine structure of electron energy-loss spectra of manganites. *Physical Review B* **79**, 052405 (2009).

59. Gubbens, A., et al. The GIF Quantum, a next generation post-column imaging energy filter. *Ultramicroscopy* **110**, 962-970 (2010).

## ***4. EELS Tomography***



<b>4.1. Scope of the chapter .....</b>	<b>157</b>
<b>4.2. Preliminary characterization:</b>	
<b>HAADF tomography and EELS.....</b>	<b>158</b>
4.2.1. Materials: Mesoporous $\text{Fe}_x\text{Co}_{(3-x)}\text{O}_4@\text{Co}_3\text{O}_4$ .....	158
4.2.2. HAADF STEM tomography of mesoporous.....	160
4.2.3. EEL Spectroscopy across pore walls .....	165
4.2.4. Discussion of HAADF STEM tomography and EELS as independent tools .....	168
<b>4.3. EELS Spectrum Image tomography     of mesoporous materials .....</b>	<b>169</b>
4.3.1. Acquisition of the tomographic SI series .....	170
4.3.2. Noise reduction by PCA .....	171
4.3.2.a. Principal Component Analysis (PCA) theory.....	171
4.3.2.b. Noise reduction: experimental and results.....	178
4.3.3. Edge intensity maps .....	181
4.3.4. Identification of the independent components.....	184
4.3.4.a. Blind Source Separation / Independent Component Analysis (ICA) theory.....	184
4.3.4.b. Results: independent components. ....	185
4.3.5. EELS-SI tomography reconstruction.....	188
4.3.6. Conclusions .....	190
<b>4.4. A step beyond: enhanced resolution EELS-tomography     of the mesoporous material.....</b>	<b>194</b>
4.4.1. Spectra acquisition and data treatment.....	194
4.4.2. EELS tomography resolving porous structure.....	196
4.4.3. Conclusions .....	202
<b>4.5. Conclusions .....</b>	<b>203</b>
<b>4.6. References .....</b>	<b>205</b>



## 4.1. Scope of the chapter

In the previous chapters, the use of HAADF electron tomography to reconstruct three dimensional structures and the use of EELS to extract chemical or even electronic information have been shown. However, EELS signal arises from electrons that have travelled through all the thickness of the sample; thus, EELS information is a projection of the properties of the sample. This has been shown particularly unfortunate in the case of two different materials overlapping, when they both contain the same element and it is not possible to assess which quantity of the element corresponds to each material, namely in oxides of the same transition metal.

In this chapter, we reconstruct the information extracted from EELS spectrum images (SI) in three dimensions, by acquiring a series of EELS-SI at different tilt angles. This approach was supposed to have the disadvantage of a high electron dose as well as long acquisition times. We propose to overcome this problem by acquiring spectra at low voltages and short acquisition times, and then extracting the relevant information using multivariate analysis (MVA).

In this sense, we undertake the characterization of an  $\text{Fe}_x\text{Co}_{(3-x)}\text{O}_4@\text{Co}_3\text{O}_4$  mesoporous structure, first by HAADF tomography and conventional, 2D, EELS-SI, and then by EELS-SI tomography. Concerning EELS tomography, two experiments have been carried out, the first one to show the feasibility and the capacities of the considered approach, and the second one to prove the possibility of reconstructing chemical information with high spatial resolution.

## 4.2. Preliminary characterization: HAADF tomography and EELS

### 4.2.1. Materials: Mesoporous $\text{Fe}_x\text{Co}_{(3-x)}\text{O}_4@ \text{Co}_3\text{O}_4$

Since the discovery of the first ordered mesoporous silica (OMS) in the early 1990's by the Mobil corporation<sup>1</sup>, there has been great interest in synthesizing and characterizing the different families of OMS. This interest arises from the capability of the pore structure to be tailored through the choice of surfactant, auxiliary chemicals and reaction conditions<sup>2</sup>. Tailoring of the pore structure means that new materials can be designed using the OMS as a scaffold for high surface materials. Metal oxide growth confined in the porous structure of the OMS, the so called "host-guest chemistry", followed by elimination of the silica framework is the path to obtain materials which combine the physico-chemical properties of the metal oxide with the advantages of finite size - high surface ratio pores of the OMS<sup>3</sup>.

OMS can be classified into three groups according to the topology of the pores<sup>3</sup>. The first group has channel like pores, such as SBA-15 (space group  $p6mm$ )<sup>4</sup> or KIT-6 (space group  $Ia3d$ ) structures<sup>5</sup>. The second one has cage-like cavities connected by narrow pores, like SBA-16 (space group  $Im3m$ )<sup>6</sup> or KIT-5 (space group  $Fm3m$ )<sup>7</sup>. The third one consists of a layered pore structure, like FSM-16<sup>8</sup>.

The open pore structure of the first group makes it the most suitable one for templating purposes, as the cavities can be filled with precursors of a different material from the outside. These materials include noble metals, transition metal oxides or metal chalcogenides.

Applications of these materials range from photonics, electronics, gas sensing<sup>9-11</sup>, fuel cell devices<sup>12, 13</sup> and catalysis<sup>12, 14-19</sup> to biomedical applications like drug delivery, imaging or magnetic hyperthermia<sup>20-22</sup>.

Given the intrinsic 3D structure of mesoporous materials, there are several examples of TEM tomography characterization of these systems in the literature, either in bright field<sup>23-30</sup> or HAADF<sup>31-38</sup>.

In this chapter, 3D structural and chemical information will be recovered from antiferromagnetic (AFM) mesoporous  $\text{Co}_3\text{O}_4$  nanocast replicas of  $\text{SiO}_2$  KIT-6 templates. In particular,  $\text{SiO}_2$  KIT-6 templates<sup>9, 39</sup> have a 3D cubic morphology presenting a double gyroidal mesostructure with channels running along the [100] and [111] directions, defining a 3D pore network, that are then replicated in the  $\text{Co}_3\text{O}_4$  matrix.

Mesoporous KIT-6 silica was synthesized in acidic conditions using Pluronic P123 copolymer as surfactant and tetraethyl ortosilicate as the silicon source. The hydrothermal treatment was carried out at 90°C for 24 h in a sealed container and the solid obtained was filtered, copiously washed with water and finally calcined at 550°C for 5h to remove the organics. For the synthesis of the  $\text{Co}_3\text{O}_4$  replica, a given amount of KIT-6 silica powder was put in contact with cobalt nitrate dissolved in ethanol. The mixture was stirred for 30 min in a crucible and left for ethanol evaporation overnight. The crucible was then placed in a tubular furnace and the impregnated silica was calcined at 375 °C. The silica host was removed with 30 mL of 2 M NaOH solution at 70 °C under stirring. The resulting mesoporous  $\text{Co}_3\text{O}_4$  powder was collected after centrifugation and decanted off the supernatant, copiously rinsed in ethanol, and finally dried.

The  $\text{Co}_3\text{O}_4$  replica was subsequently infiltrated with different amounts of iron (III) nitrate precursor, which underwent conversion into the corresponding oxide product at 375 °C, in the same fashion as above. The Fe(III): $\text{Co}_3\text{O}_4$  molar ratio was varied in order to achieve different degrees of filling of the  $\text{Co}_3\text{O}_4$  host:

- 0.6 Fe(III): $\text{Co}_3\text{O}_4$  molar ratio
- 1.2 Fe(III): $\text{Co}_3\text{O}_4$  molar ratio
- 2.4 Fe(III): $\text{Co}_3\text{O}_4$  molar ratio
- 3.6 Fe(III): $\text{Co}_3\text{O}_4$  molar ratio

The formation of a ferrimagnetic (FiM)  $\text{Fe}_x\text{Co}_{(3-x)}\text{O}_4$  layer is expected on the surface of the channels, as the interest of the material lays in the AFM-FiM coupling between the two transition metal oxides.

Mesoporous samples were kindly provided by Dr. Eva Pellicer, from the Physics Department of the Universitat Autònoma de Barcelona.

#### 4.2.2. HAADF STEM tomography of mesoporous

The pure  $\text{Co}_3\text{O}_4$  KIT-6 replica templates were first observed by CTEM, HRTEM and STEM in the TEM, and also at lower magnification in the scanning electron microscope (SEM). These observations showed the ordered structure of the particles, as well as their sizes (75-150 nm) and pore diameters (15 nm). In Figure 4.1 (a), the SEM image shows spherical particles, with a homogeneous size distribution, as well as a regular pore structure. These observations are confirmed in the CTEM image in Figure 4.1 (b), where all the particles present in the cluster show a rounded shape and a single orientation mesoporous structure. In Figure 4.2 (a), a HAADF STEM image has been used to measure the distance between pore walls (20 nm) with the intensity profile in the inset. In Figure 4.2 (b), the HRTEM image shows the monocrystalline nature of the particles. The KIT-6 mesostructure has  $Ia3d$  symmetry, where two channel systems are interconnected through mesoporic tunnels, which can be observed in both figures.

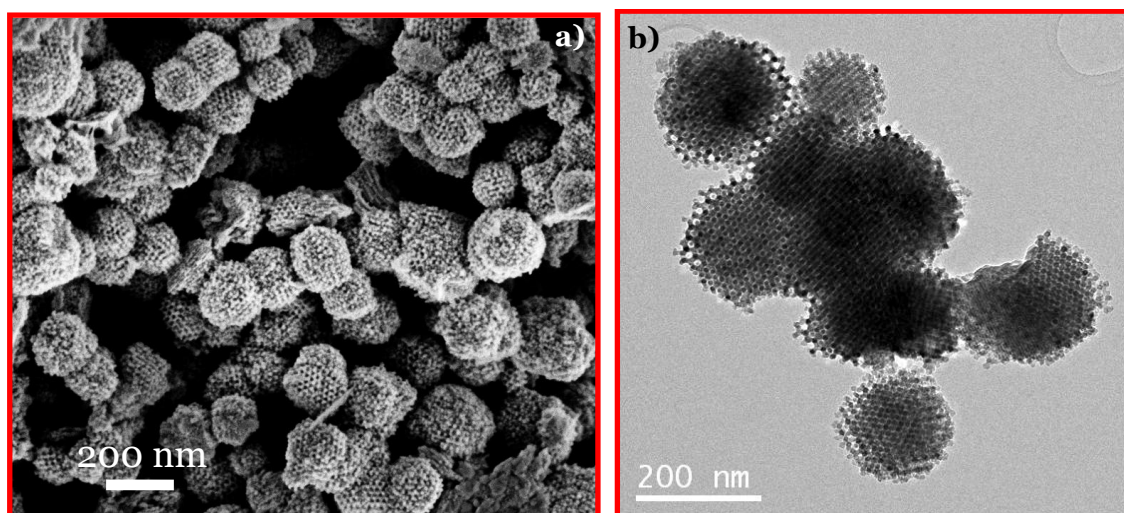


**Figure 4.1:** **a)** SEM, **b)** CTEM images of a group of mesoporous nanoparticles.

Tilt series were acquired for three different samples once an adequate particle group for each was located: a pure  $\text{Co}_3\text{O}_4$  KIT-6 replica (images framed in red) and two other samples with increasingly high iron infiltration charge, 2.4 Fe(III): $\text{Co}_3\text{O}_4$  molar ratio, (images framed in orange) and 3.6 Fe(III): $\text{Co}_3\text{O}_4$  molar ratio (images framed in yellow). The range of the acquired series was the following:

- Pure  $\text{Co}_3\text{O}_4$ :  $-64^\circ \leq \alpha \leq 64^\circ$
- 2.4 Fe(III): $\text{Co}_3\text{O}_4$  molar ratio:  $-72^\circ \leq \alpha \leq 76^\circ$
- 3.6 Fe(III): $\text{Co}_3\text{O}_4$  molar ratio:  $-68^\circ \leq \alpha \leq 72^\circ$

All of them were obtained at equal steps of  $2^\circ$  in the FEI Tecnai.

The tilt series were aligned and reconstructed with Inspect3D. The visualizations were obtained using the Amira software.

One image of the tilt series for each sample can be seen in Figure 4.3. The projections appear to be more compact with higher infiltrations. The particles show only one orientation of the mesoporous ordering in each particle except for the highest infiltration charge, where different orientations (approximately at both sides of the dashed red line) are found in the same particle.

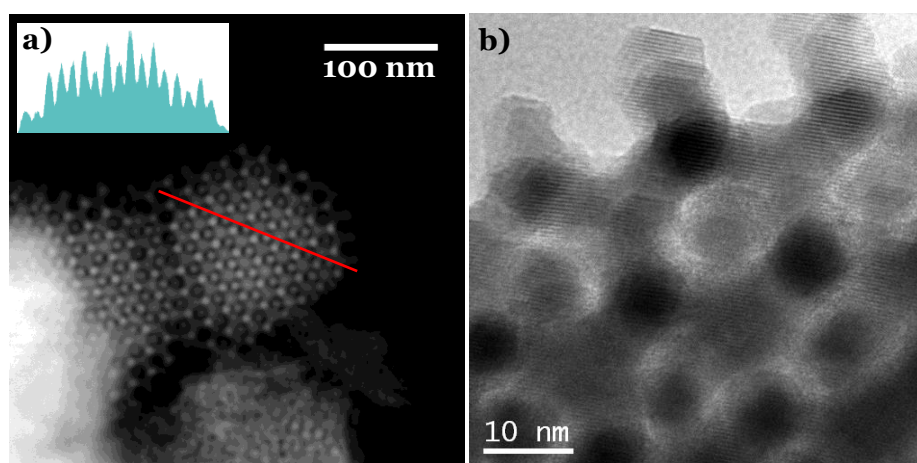


**Figure 4.2:** **a)** HAADF STEM image of a group of mesoporous nanoparticles with a line profile of intensities along the red line. **b)** HRTEM image of one of the particles.

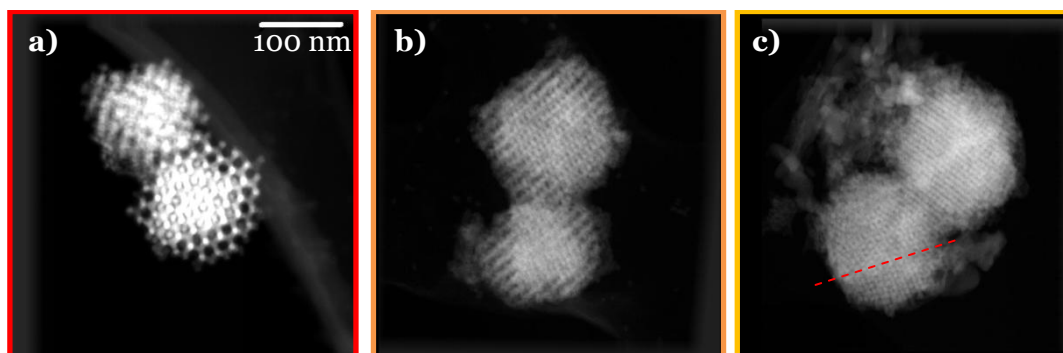


**Figure 4.3:** HAADF images from the tilt series of **a)** pure  $\text{Co}_3\text{O}_4$  KIT-6 replica, **b)** template infiltrated with iron charge 2.4  $\text{Fe(III):Co}_3\text{O}_4$  and **c)** template infiltrated with iron charge 3.6  $\text{Fe(III):Co}_3\text{O}_4$ .

After alignment and 40 iterations of SIRT algorithm, the three tilt series were reconstructed. In Figure 4.4 a direct visualization for each of the three tilt series can be observed. In the case of the highest infiltration charge, the reconstruction is less precise, due to the greater size of the particles and the multiple orientations. In the supplementary data, animations of the reconstructions for pure  $\text{Co}_3\text{O}_4$  KIT-6 replica and the template infiltrated with iron charge 2.4  $\text{Fe(III):Co}_3\text{O}_4$  can be found in movies 6 and 7, respectively.

In order to quantify the reduction in pore size, the apparent pore wall thicknesses (measure of the shortest distance between pores) were measured in slices (as those shown in Figure 4.5) through the reconstructed volumes. Table 4.1 presents the results of the quantification. For the original  $\text{Co}_3\text{O}_4$  structure, the pore wall was 5 nm thick. The thickness of the walls increased to 7.8 nm for 2.4  $\text{Fe(III):Co}_3\text{O}_4$  molar ratio charge, and was found to be the same (7.8 nm) for the highest infiltration charge, 3.6  $\text{Fe(III):Co}_3\text{O}_4$  molar ratio, indicating a saturation of the incorporation of Fe by impregnation.

The changes in pore size were apparent in the tomographic reconstructions; however, it is not possible to observe the chemical nature of the transformation. HAADF signal is proportional to  $Z$ , and can therefore tell materials with different  $Z$  numbers apart. Unfortunately, cobalt and iron have correlative atomic numbers, which makes it impossible to differentiate them using HAADF in the electron microscope. It is necessary to use analytical tools to determine the chemical composition after the filling.

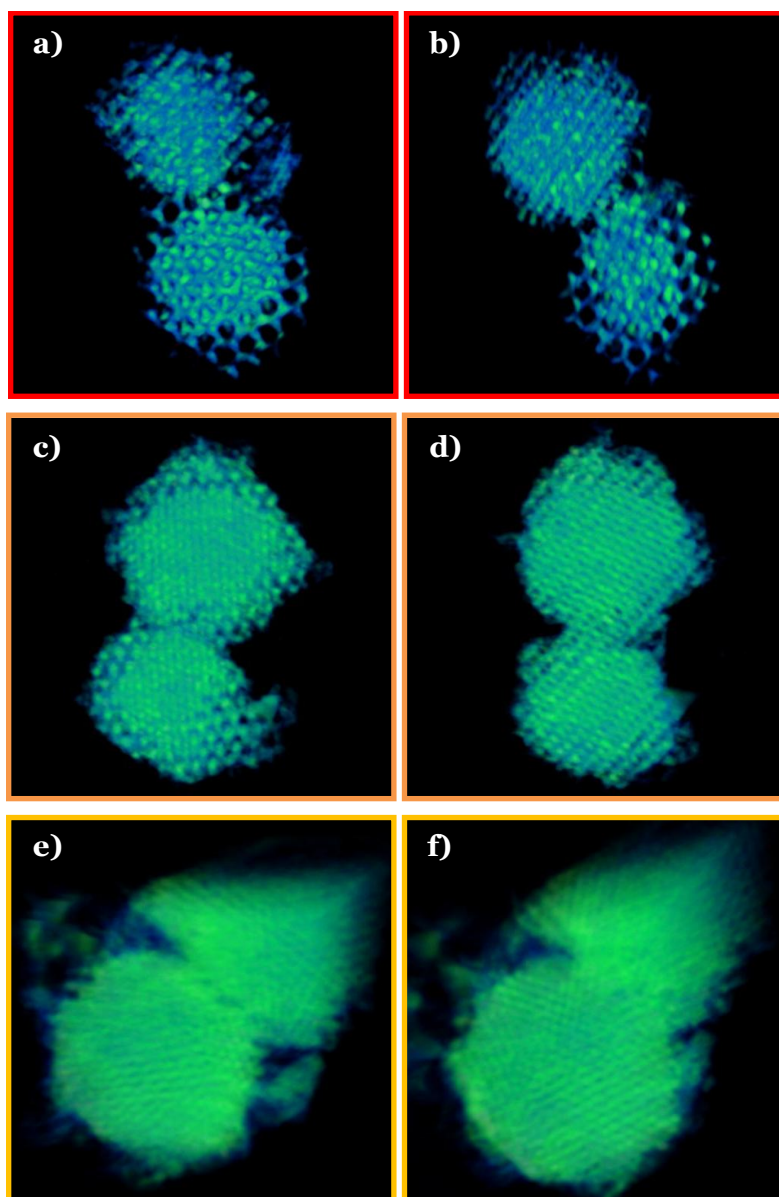


**Figure 4.4:** Direct visualization of the 3D reconstructed volume from different orientations of the pure  $\text{Co}_3\text{O}_4$  KIT-6 replica **a)** and **b)** (red), template infiltrated with iron charge 2.4 **c)** and **d)** (orange) and template infiltrated with iron charge 3.6 **e)** and **f)** (yellow).

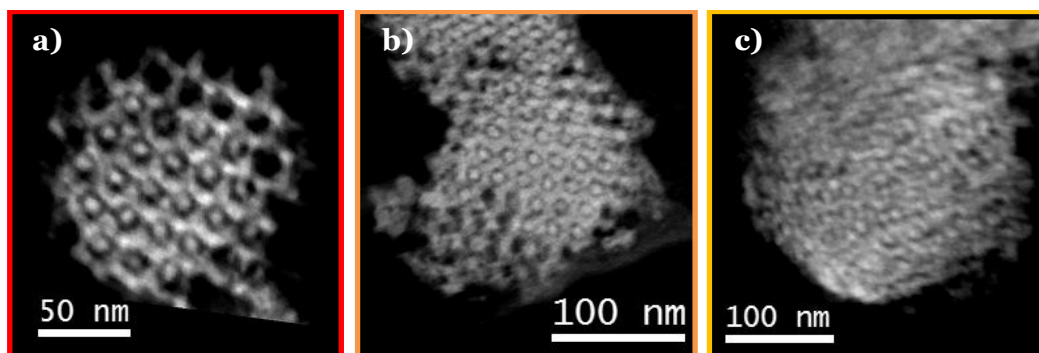


**Figure 4.5:** Slices through the 3D reconstruction of the mesoporous particles with different infiltrations: **a)** pure  $\text{Co}_3\text{O}_4$  KIT-6 replica, **b)** template infiltrated with iron charge 2.4  $\text{Fe(III):Co}_3\text{O}_4$  and **c)** template infiltrated with iron charge 3.6  $\text{Fe(III):Co}_3\text{O}_4$ .

$\text{Fe(III):Co}_3\text{O}_4$ molar ratio	Apparent pore wall thickness (nm)
0	$5.13 \pm 1.07$
2.4	$7.77 \pm 0.42$
3.6	$7.68 \pm 0.99$

**Table 4.1:** Pore wall thickness as measured in slices through the reconstructed particles.

### 4.2.3. EEL Spectroscopy across pore walls

In order to better understand the nature of the infiltration, spectroscopic investigations using EELS were performed on the samples. Spectrum images were acquired at the surface of the nanoparticles, where a pore was well oriented, for two samples infiltrated with iron charge 0.6 Fe(III):Co<sub>3</sub>O<sub>4</sub> and 1.2 Fe(III):Co<sub>3</sub>O<sub>4</sub>, in the probe corrected FEI Titan. Then, the intensities of the iron and cobalt L<sub>2,3</sub> edges were integrated and superimposed, as shown in Figure 4.6. The iron edge intensity is presented in red, while the cobalt is presented in blue. The pore structure, that was measured in the outer part of the particle, is apparently formed by a Co<sub>3</sub>O<sub>4</sub> template covered with Fe<sub>x</sub>Co<sub>(3-x)</sub>O<sub>4</sub>, as Co signal predominates in the main skeleton and Fe signal is located mainly in the vicinity of the pore system.

Several spectrum lines were acquired through the mesoporous system walls. In Figure 4.7, the position of two spectrum lines for the 0.6 Fe(III):Co<sub>3</sub>O<sub>4</sub> sample are shown, along with the corresponding elemental quantification of the results, following the method explained in section 3.3. The same outline is followed in Figure 4.8 for the 1.2 Fe(III):Co<sub>3</sub>O<sub>4</sub> sample. As observed in Figure 4.6, the iron concentration at the border of the wall is higher, and it decreases towards the interior of the structure. The spectrum lines even suggest the presence of Fe<sub>3</sub>O<sub>4</sub> at the inner side of the pores, where no cobalt could be measured. The spectrum lines in Figure 4.7 show lower iron concentration levels than the ones in Figure 4.8, which is hardly surprising due to the higher amount of iron precursor in the second figure.

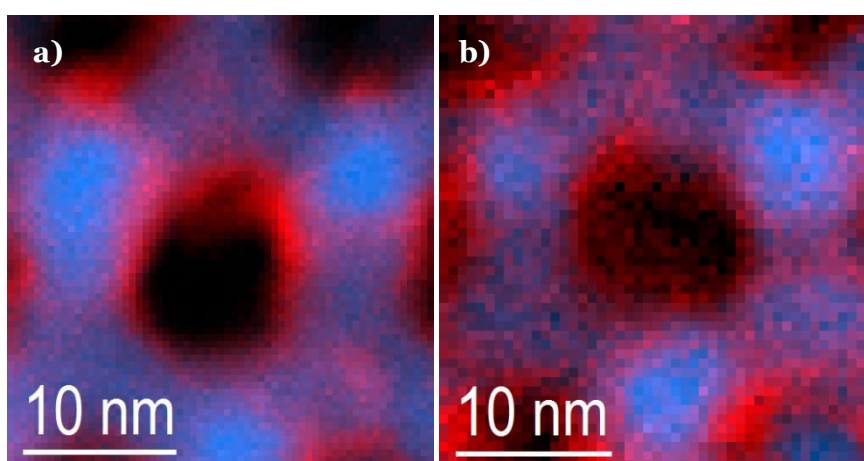


**Figure 4.6:** Color maps for the iron (red) and cobalt (blue) edge intensities for: **a)** charge 0.6 Fe(III):Co<sub>3</sub>O<sub>4</sub>, **b)** charge 1.2 Fe(III):Co<sub>3</sub>O<sub>4</sub>.

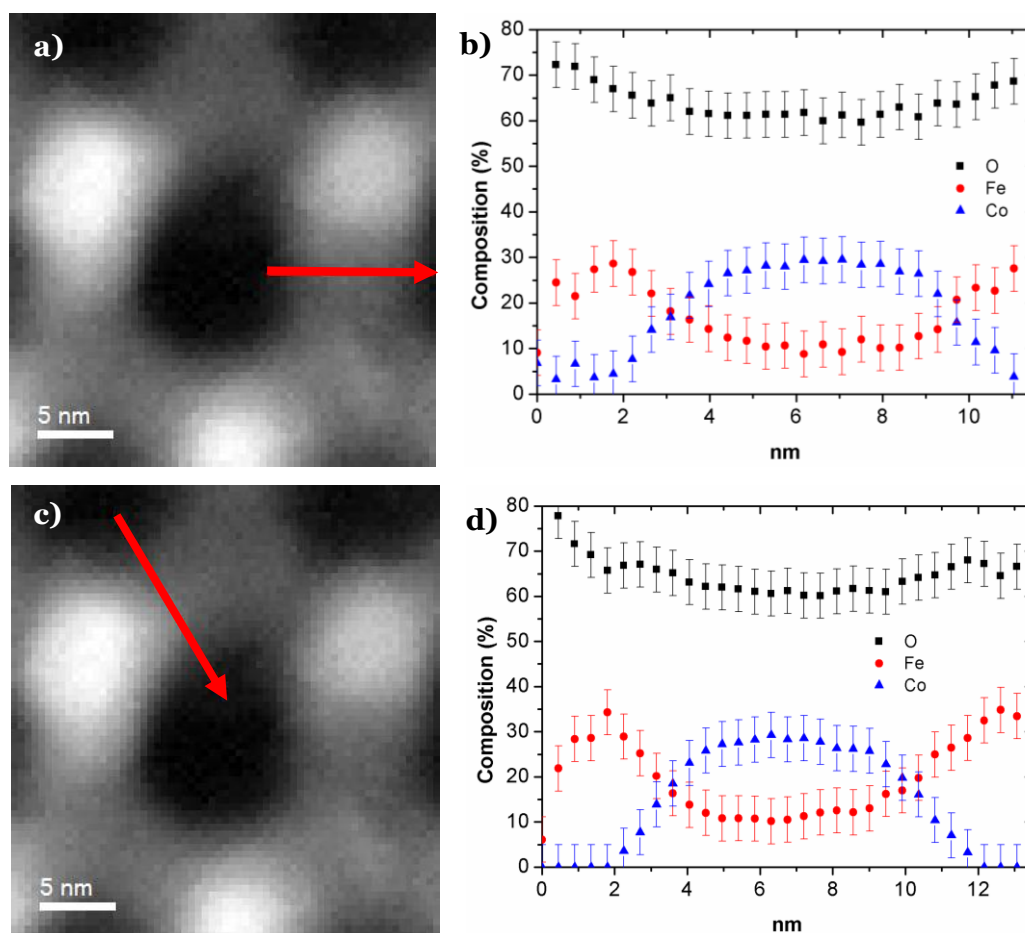


**Figure 4.7:** **a), c)** EELS spectrum images for the sample infiltrated with iron charge 0.6  $\text{Fe(III):Co}_3\text{O}_4$ ; **b), d)** quantification results along the red arrows in **a)** and **c)** respectively.

The concentration of iron changed greatly depending on the measured particle or the considered point in the particle. Therefore, we chose to report compositional ranges for the four infiltrations. Table 4.2 displays the composition ranges of the particles measured in the JEOL JEM2010F. The compositional range for each of the infiltrations is huge. Cobalt-to-iron ratio can change an order of magnitude from Co rich areas to Fe rich areas. However, for the highest infiltration charge, no higher iron concentration was found. As it was observed in the tomographic results, the deposition of new material saturates at charge 2.4, and no further incorporation of material was observed. Moreover, iron oxide nanoparticles outside the  $\text{Co}_3\text{O}_4$  matrix were detected for 2.4 and 3.6  $\text{Fe(III):Co}_3\text{O}_4$  molar ratios, which indicated the saturation limit of the pores at 2.4  $\text{Fe(III):Co}_3\text{O}_4$ .

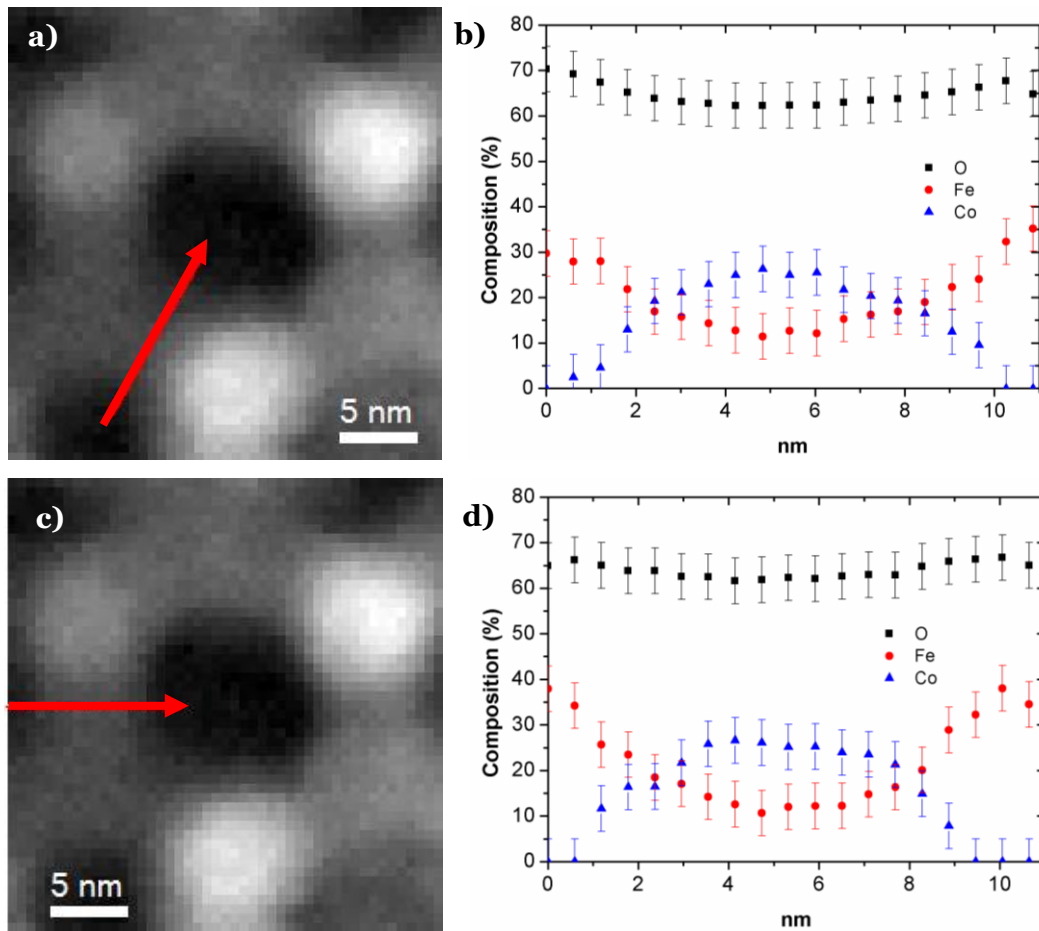


**Figure 4.8:** **a), c)** EELS spectrum images for the sample infiltrated with iron charge 1.2 Fe(III):Co<sub>3</sub>O<sub>4</sub>; **b), d)** quantification results along the red arrows in a) and c) respectively.

<i>Fe(III):Co<sub>3</sub>O<sub>4</sub> molar ratio</i>	<i>Composition</i>
0.6	$\text{CoCo}_{1.76}\text{Fe}_{0.24}\text{O}_4 \leftrightarrow \text{FeFe}_{0.53}\text{Co}_{1.47}\text{O}_4$
1.2	$\text{CoCo}_{1.34}\text{Fe}_{0.66}\text{O}_4 \leftrightarrow \text{FeFe}_{0.72}\text{Co}_{1.28}\text{O}_4$
2.4	$\text{FeFe}_{0.53}\text{Co}_{1.47}\text{O}_4 \leftrightarrow \text{FeFe}_{1.39}\text{Co}_{0.61}\text{O}_4$
3.6	$\text{CoCo}_{1.13}\text{Fe}_{0.87}\text{O}_4 \leftrightarrow \text{FeFe}_{0.76}\text{Co}_{1.24}\text{O}_4$

**Table 4.2:** Composition ranges calculated from single EEL spectra acquired near the border of the particles for the different infiltration charges.

#### 4.2.4. Discussion of HAADF STEM tomography and EELS as independent tools

In the considered mesoporous particles, the relevance of HAADF STEM tomography is clear, as no projection of the particles can offer information about the shape of the pores. Even if KIT-6 mesoporous structure is well known, tomography allows an assessment of the quality of the structure and the possible presence of domains. Moreover, the slices enable measuring the width of the pores. As the mesoporous  $\text{Co}_3\text{O}_4$  particles are infiltrated with an iron precursor and the formation of an iron and cobalt mixed oxide is expected, the changes in structure width can be associated with iron deposition. The results obtained in the particles without iron and two more of particles infiltrated with different iron precursor charges, nominally 2.4 Fe(III): $\text{Co}_3\text{O}_4$  molar ratio and 3.6 Fe(III): $\text{Co}_3\text{O}_4$  molar ratio, show how the apparent width of the pore walls increased by more than 50% when infiltrated with charge 2.4. However, no increase in pore wall thickness was measured for greater infiltrations. This means that the structure is saturated at charge 2.4, and that attempts to further charge the structure with iron using the same technique will prove unsuccessful, as the iron will remain outside the particles.

Electron energy loss spectroscopic analysis performed on a greater series of infiltration charges also suggests that the iron infiltration maximum load for infiltration avoiding the growth of material outside the host structure is charge 2.4, as no higher iron composition in the structure is measured from that point on. EEL spectra also shed light on the nature of the new material grown on the original framework. Measurements on the particles revealed that the new material is a mixed iron cobalt oxide. This can be understood by the formation of an initial iron oxide phase on the  $\text{Co}_3\text{O}_4$  mesoporous template and subsequent ion diffusion into the host, forming an intermediate layer of mixed cobalt iron spinel,  $\text{Fe}_x\text{Co}_{(3-x)}\text{O}_4$ , where the Fe concentration is related to the amount of iron salt precursor.

We have shown that HAADF STEM tomography is able to extract structural information of the mesoporous particles in 3D, and that EELS is capable of extracting chemical information in two dimensions. However, as we are interested in knowing how the iron is incorporated into the structure, there is a need for a three dimensional characterization which contains information about the distribution of the elements. Therefore, we proceed to perform tomography with the chemical information contained in the spectrum.

## 4.3. EELS Spectrum Image tomography of mesoporous materials

As already introduced in section 1.3, 3D chemical characterization in the TEM has been usually performed by energy filtered TEM (EFTEM). In EFTEM, the images are acquired using an energy selecting slit, and discarding all energies outside the slit width. Only a few images per element and tilt angle are needed. When compared to EELS-SI, the acquisition time and the electron dose received by the sample are reduced, which is more favourable for sample stability<sup>40-42</sup>. However, EFTEM has a low energy resolution, limited by the slit. EELS-SI retains all the information in the spectrum during the acquisition, but presents the drawback of higher acquisition times (as a full SI per tilt angle is needed) and, thus, higher electron dose onto the sample.

We propose reducing the acquisition times to reduce the dose received by the sample in EELS-SI and recovering the information in the spectra by means of multivariate analysis (MVA)<sup>43, 44</sup>. More precisely, we propose to use principal component analysis (PCA) to reduce the noise of the spectra acquired with short acquisition times (and low voltage if need be). PCA is able to separate components in the spectrum according to their variance. Provided that the signal has higher variance than the noise, one can keep the signal and discard the noise. Moreover, independent component analysis (ICA) can recover uncorrelated components with physical meaning. In addition to the extracted edge intensities and MLLS fitting (already considered by Jarausch et al.<sup>45</sup>), we propose direct elemental quantification from EEL spectra, and ICA to retrieve complementary information, to reconstruct 3D volumes of chemical data. Both MVA techniques are explained in the following sections 4.3.2 and 4.3.4.

The use of statistical procedures to make noisy data suitable for reconstruction and expand the range of signals fulfilling the projection requirement opens the prospect of EELS-SI tomography becoming a widespread tool for 3D chemical characterization

in the nanosciences, in addition to the usual high-angle annular dark field (HAADF) tomography<sup>32, 46-48</sup>.

### 4.3.1. Acquisition of the tomographic SI series

The data set consisted of 48 SI ranging from  $68.99^\circ$  to  $-64.74^\circ$  following a saxton scheme angle step with  $55 \times 55$  spectra each, acquired for 0.1 s. Each spectrum was acquired in the region of 480 – 890 eV at an energy dispersion of 0.2 eV, with an  $E_0$  of 80 kV. High angle annular dark field (HAADF) signal was acquired simultaneously. The three data sets obtained per tilt angle are presented in Figure 4.9 for the  $0^\circ$  tilt, at the middle of the acquisition: the HAADF survey image (Figure 4.9 (a)), used for spatial drift correction during SI acquisitions, the coacquired HAADF image (Figure 4.9 (b)) and the EELS-SI (Figure 4.9 (c)). The spectra were corrected for detector background. Standard Gatan procedure was applied for minimizing/correcting dark count readout and the channel-to-channel variation in the gain response. These artifacts, thus, are negligible.

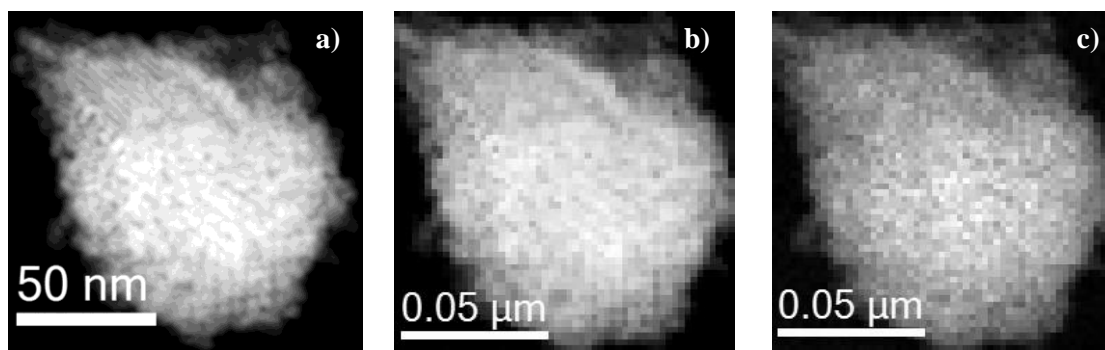


**Figure 4.9: a)** HAADF projection at  $0^\circ$  tilt of the particle used in the analysis. The HAADF signal was acquired in order to correct for spatial drift during EELS data collection. **b)** HAADF image at  $0^\circ$  tilt obtained during the acquisition of the EELS-SI. These data were reconstructed in order to compare it to the EELS extracted signals. **c)** EELS SI obtained at  $0^\circ$  tilt.

Because of the low voltage and the short acquisition times, the signal-to-noise ratio (SNR) is very low. As shown in Figure 4.10, the noise content in the spectra is too high to allow a direct quantification, particularly in the thickest part of the particle (as shown in Figure 4.10 (c)), where the elemental edges are hardly visible. Therefore, there is a need to get rid of the noise.

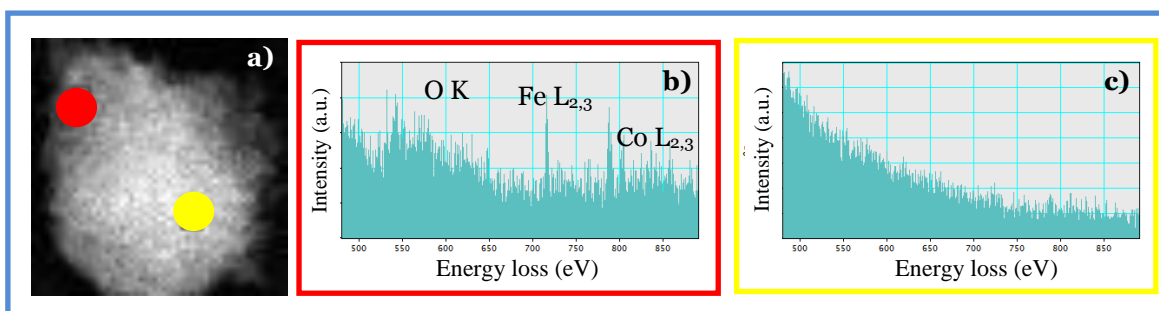


**Figure 4.10:** **a)** Spectrum image at 68.99° as acquired. **b)** Single spectrum from the area at the border of the particle, highlighted in red, and **c)** single spectrum from the area at the center of the particle, highlighted in yellow.

## 4.3.2. Noise reduction by PCA

### 4.3.2.a. Principal Component Analysis (PCA) theory

When acquiring an EELS-SI, in addition to the useful signal, the image contains “useless information” such as the background and the noise. This is a general problem in images, not a specific problem of EELS. In the next few paragraphs, the basics of principal component analysis will be explained, following the formulation of Trebbia and Bonnet<sup>49</sup>, who reported the first application of PCA to an EELS-SI.

- **Contrast and variance:**

Let two pixels of an image be  $(i, j)$  and  $X_i$  and  $X_j$  their contents (the number of electrons detected). The mean value  $\langle X \rangle$  can be defined as

$$\langle X \rangle = (X_i + X_j)/2 \quad , \quad [4.1]$$

and the variance is

$$s^2 = \langle X^2 \rangle - \langle X \rangle^2 = \left( \frac{X_i - X_j}{2} \right)^2 \quad . \quad [4.2]$$

The standard deviation  $s$  is defined as

$$s = |(X_i - X_j)/2| \quad . \quad [4.3]$$

The contrast  $\mathfrak{C}$  between the two pixels is defined as <sup>50</sup>:

$$\mathfrak{C} = \frac{|X_i - X_j|}{X_i + X_j} = \frac{s}{\langle X \rangle} \quad , \quad [4.4]$$

if  $\langle X \rangle \neq 0$ . This means that  $X_i$  and  $X_j$  both have to be different to zero, as they cannot be negatives.

Therefore, the local contrast between two pixels is directly proportional to the standard deviation, which is the square root of the variance. As a consequence, the analysis of contrast can be carried out through the analysis of the variance.

- **Information:**

As proposed by Shannon<sup>51, 52</sup>, the information  $I(E)$  associated with an event  $E$  is defined as the cologarithm of the probability of that event occurring before it happened:

$$I(E) = -\log[\text{Prob}(E)] \quad . \quad [4.5]$$

Information is always a positive number, or zero when we know a priori that the event will certainly occur. The consequence of this property is that information only increases with new events occurring.

- **Entropy:**

Let  $E$  be a random variable with possible values  $E_k (k = 1, \dots, N)$  and  $Prob(E)$  the probability law governing the variable. The entropy  $S(Prob)$  of the probability law is defined as the expectation of the information carried by the  $N$  possible events:

$$S(Prob) = \sum_k I(E_k) Prob(E_k) = - \sum_k Prob(E_k) \log[Prob(E_k)] . \quad [4.6]$$

The entropy has some interesting properties, namely:

- $S(Prob)$  is always positive or null.
- $S(Prob)$  is only null if there is only a  $E_k$ , with probability 1.
- $S(Prob)$  is maximum when all the  $E_k$  values have the same probability  $1/N$ ; then  $S(Prob) = \log N$  and increases with  $N$ .
- Entropy and information vary in reverse ways: the higher the information of an event, the lower the probability, and therefore the entropy, of the event. The less uniform the probability distribution, the higher the difference between the actual entropy and its maximum, and, therefore, the lower the entropy.

As an example, an image with no contrast does not carry any information, and its entropy is maximum.

- **Relative entropy:**

The previous definition of entropy follows the assumption that one among the  $N$  possible events  $E_k$  will certainly occur. If the experiment does not deliver a deterministic value, but a random variable, the relative entropy can be defined as the information associated with a change in the probability law: let  $P_1(E)$  be the a priori law controlling the event  $E$  and  $P_2(E)$  the a posteriori probability law (which is one in the previous definition). The relative entropy of  $P_2$  with respect to  $P_1$  can be expressed as:

$$H\left(\frac{P_2}{P_1}\right) = \sum_k P_2(E_k) \log \left[ \frac{P_2(E_k)}{P_1(E_k)} \right] . \quad [4.7]$$

Let  $X_{ij}$  be a matrix of two kinds of variables:  $C$  columns noted  $i$  ( $i = 1, \dots, C$ ) and  $P$  lines noted  $j$  ( $j = 1, \dots, P$ ). This matrix can be seen in two ways: either as a description of the  $C$  coordinates of  $P$  values in  $\mathbb{R}^C$  or the other way around. In the case of EELS-SI, the  $C$  columns can be seen as  $C$  filtered images (or energy channels) containing  $P$  pixels.

In general, there will be some kind of dependence between some lines and/or some columns. Therefore, some information will be redundant. The aim of the analysis will be to remove the redundancy and classify the remaining information. From the original data set  $X_{ij}$  the aim is to reduce the dimension of the original space  $\mathbb{R}^C$  by building  $Q$  eigenvectors so that<sup>49</sup>:

- they are a linear combination of the original variables,
- they are orthogonal to each other and generate a new  $\mathbb{R}^Q$  vectorial space,
- they are normalized to the unity, and
- the axes created by the eigenvectors describe the most of the information conveyed by  $X_{ij}$ .

The eigenvectors are calculated so that the associated axes are as close as possible to the actual variables.

PCA makes a clear distinction between the variables: the columns are not treated in the same way as the lines. Another important point is that it uses an Euclidean metric to measure the distance between points. In order to use PCA, the original data set  $X_{ij}$  has to be transformed to a new data set  $Y_{ij}$ , in which the formulation is symmetrical with respect to  $i$  and  $j$ , and the original  $\chi^2$  metric should be equivalent to an Euclidian metric.

The building of the  $Y_{ij}$  matrix is carried out in three steps:

(i) The values in  $X_{ij}$  are related to counting numbers. In order to be able to compare lines and/or columns, the values have to be normalized.

$$X_i = \sum_j X_{ij}, \quad X_j = \sum_i X_{ij}, \quad X = \sum_i X_i = \sum_j X_j \quad . \quad [4.8]$$

In the case of column normalization:

$$X'_{ij} = X_{ij} / X_i \quad . \quad [4.9]$$

As  $\sum_j X'_{ij} = 1$ , the number of independent variables is reduced from  $P$  to  $P - 1$ . This reduction in the dimension of vectorial space will give an eigenvalue equal to one.

(ii) The  $X'_{ij}$  has to be changed to  $X''_{ij}$  so that the  $\chi^2$  distance between two  $X'_{ij}$  will be equal to the Euclidean distance between the relevant  $X''_{ij}$ .

$$d_{ii}^2_{\chi^2} = \sum_j X (X'_{ij} - X'_{i'j})^2 / X_j \quad . \quad [4.10]$$

To make it Euclidean (a space where distances are defined by the Pythagorean formula, as the square root of the sum of square differences) it must be transformed to:

$$X''_{ij} = X'_{ij} \sqrt{X/X_j} = \frac{X_{ij} \sqrt{X}}{X_i \sqrt{X_j}} \quad [4.11]$$

and

$$d_{ii}^2_{Euclidean} = \sum_j X (X''_{ij} - X''_{i'j})^2 \quad . \quad [4.12]$$

(iii) The last transformation is carried out to ensure the symmetry between the two kinds of variables by using the weighting factor  $\sqrt{X_i/X}$ :

$$Y_{ij} = X_{ij} \sqrt{X_i/X} \quad . \quad [4.13]$$

In order to build the variance-covariance matrix which contains the contrast information, the  $Y_{ij}$  matrix has to be multiplied by its transposed  $Y_{ij}^t$ . The eigenvalues and eigenvectors of the resulting symmetrical matrix  $S$  are then computed. If we assume  $C$  smaller than  $P$  we have:

$$Y^t Y \rightarrow S_{ii'} = \sum_j (Y_{ij} Y_{i'j}) = \frac{1}{\sqrt{X_i X_{i'}}} \sum_j \frac{X_{ij} X_{i'j}}{X_j} . \quad [4.14]$$

- **Properties of the S matrix:**

(i) All the eigenvalues of  $S$  are positive and less or equal to one.

(ii) The sum of the eigenvalues of  $S_{ii'}$  (including the trivial one which is equal to 1) is equal to the trace of that matrix. The eigenvalues,  $\lambda$ , can be given in decreasing order  $\lambda_\alpha$  ( $\alpha = 1, \dots, C$ ):

$$\lambda_\alpha \leq \lambda_{\alpha-1} \quad \text{and} \quad \lambda_1 = 1 \quad [4.15]$$

$$\sum_{\alpha=1}^C \lambda_\alpha = 1 + \sum_{\alpha=2}^C \lambda_\alpha = \sum_{\alpha=1}^C S_{ii} = \text{trace}(S) \quad [4.16]$$

$$\sum_{\alpha=1}^C \lambda_\alpha = \sum_i \left( \frac{1}{X_i} \sum_j \frac{X_{ij}^2}{X_j} \right) . \quad [4.17]$$

- **Eigenvalues and Eigenvectors:**

When we apply PCA over the columns or the lines, the non-trivial and non-zero eigenvalues have been noted as  $\lambda_\alpha$ , with  $\alpha$  ranging from 2 to the minimum of the numbers  $C$  or  $P$ .

The relevant eigenvalues are expressed as linear combinations of the variables. If we consider the lines as variables, the eigenvectors are noted  $u_\alpha = \{u_{\alpha j}\}$ . If we consider the columns as variables, the eigenvectors are noted  $v_\alpha = \{v_{\alpha i}\}$ . The diagonalization of the  $S_{ii'}$  matrix yields the values of the  $\lambda_\alpha$  and the  $C$  coordinates of the  $v_{\alpha i}$  associated eigenvectors.

The  $P$  coordinates  $u_{\alpha j}$  of the  $u_\alpha$  eigenvector are related to  $v_{\alpha i}$  by the relationship

$$u_{\alpha j} = \frac{1}{\sqrt{\lambda_\alpha}} \sum_i Y_{ij} v_{\alpha i} = \frac{1}{\sqrt{\lambda_\alpha}} \sum_i \frac{X_{ij}}{\sqrt{X_i X_j}} v_{\alpha i} . \quad [4.18]$$

The non-trivial  $\lambda_\alpha$  values are organized by decreasing value (from now on we omit the trivial 1 and start  $\lambda_\alpha$  at  $\lambda_1 \neq 1$ ). Each of the eigenvectors is supported by a factorial axis with an arbitrary orientation. Each axis  $\alpha$  contains a part  $C_\alpha$  of the total variance:

$$C_\alpha = \lambda_\alpha / \sum_\alpha \lambda_\alpha \quad . \quad [4.19]$$

With increasing  $\alpha$  the  $C_\alpha$  coefficients decrease, and so does the variance. At a given point, we can consider that only the components with a variance above a particular threshold convey the important part of the total information.

Let  $Q$  be the number of factorial axes which we consider as relevant. Then

$$\sum_1^Q C_\alpha \leq 1 \quad . \quad [4.20]$$

And the resulting vectorial space will contain the important part of the information and will be fully described by the first  $Q$  eigenvectors  $u_\alpha$  (or  $v_\alpha$ ).

In order to describe the initial  $X_{ij}$ , it is necessary to calculate the coordinates of the points representing the variables in the new axes:

the value of the projection of the  $i$ th column on axis  $\alpha$  is

$$M_{\alpha i} = \sqrt{\frac{X\lambda_\alpha}{X_i}} u_{\alpha i} \quad , \quad [4.21]$$

and the value of the projection of the  $j$ th line on axis  $\alpha$  is

$$N_{\alpha j} = \sqrt{\frac{X\lambda_\alpha}{X_j}} u_{\alpha j} = \sqrt{\frac{X}{X_j}} \sum_i \frac{X_{ij}}{\sqrt{X_i}} u_{\alpha i} \quad . \quad [4.22]$$

If we consider only the  $Q$  first factorial axes, the initial values can be approximately reconstructed as

$$X_{ij} \simeq \frac{X_i X_j}{X} \left( 1 + \sum_1^Q \frac{M_{\alpha i} N_{\alpha j}}{\sqrt{\lambda_\alpha}} \right) \quad . \quad [4.23]$$

If we chose  $v_\alpha$  as our eigenvectors, they will be in the form of counts in the  $i$  energy channels. They are, thus, spectra. Therefore, they can also be called eigenspectra. Reformulating [4.23], we have

$$X_{ij} = S_{jQ} \times L_{iQ}^T \quad [4.24]$$

where  $S_{jQ}$  is the so called score matrix and  $L_{iQ}$  the loading matrix. Each of the  $i$  rows of the transposed  $L^T$  matrix represents an eigenspectrum, a spectral feature orthogonal to the others. Each of the  $j$  columns in  $S$  represents the local weight of the corresponding eigenspectrum of the loading matrix. The principal components are the eigenspectra. The number of principal components is  $Q$ , and it will always be equal to or lower than the minimum of  $i$  (the number of energy channels) or  $j$  (the number of spectra).

#### 4.3.2.b. Noise reduction: experimental and results

The inputs of 3D tomographic algorithms are intensities  $I$  in a distribution of the form  $I(x, y, \theta)$  while our dataset was in the form  $I(x, y, \theta, \Delta E)$ . The approach by Jaraush et al.<sup>45</sup> consisted in integrating areas under core-loss edges, hence obtaining a series of  $I_A(x, y, \theta)$ , where  $A$  corresponds to an edge of a given element. As our dataset was too noisy to perform that transformation, we proceeded to treat it with PCA.

The first step of data treatment was merging the data together in Hyperspy<sup>53, 54</sup>, a Python based suite specially developed for SI MVA, in order to obtain a large SI onto which the statistical analysis could be applied. Therefore, the original four dimensional  $(x, y, \theta, \Delta E)$  data set was transformed to  $(x, y(\theta), \Delta E)$ , the same format as a regular SI data cube. This format transformation was necessary in the used version of Hyperspy, while more recent versions are now able to deal directly with the EELS four dimensional dataset. After energy drift correction using the 478-886 eV region, weighted PCA (wPCA) was applied to the data. The weighting of the PCA was adapted to the dominant Poissonian noise. PCA consists in finding a new parametric model for the dataset, where every spectrum can be described as a weighted sum of a finite number of components and noise. The signals are separated according to their variance<sup>55</sup>; thus, an enhanced signal-to-noise ratio can be obtained by keeping only the higher variance components and discarding most of the noise contribution.

First, spatial drift was corrected using the whole region where the edges were observed (478-886 eV). Afterwards, spikes were removed and PCA was applied

assuming poissonian noise. Figure 4.11 shows the logarithm of the variance of the components. The first components are clearly much higher in variance, and therefore, in information. The first 5 components are shown in Figure 4.12 (a), with the fifth in the inset, as its contribution is already very small, but it still contains information about the edges. Components from the sixth to the tenth are shown in Figure 4.12 b. In these components, only noise can be noticed, but for the sixth, shown in the inset. Yet, the shape observed in the sixth component does not correspond to the actual shape of a spectrum, but it is similar to its derivative. This artifact arises from slight misalignments in the energy axis. As its contribution is quite low and the noise content is high, it was not kept for further analysis. Therefore, only the first five components were retained for further analysis.

The results of noise reduction are illustrated in Figure 4.13 (a). A spectrum image acquired at  $68.99^\circ$  is shown. Two single spectra, from the border and the centre of the mesoporous particle, containing the K edge of oxygen and the  $L_{2,3}$  edges of iron and cobalt are shown in Figure 4.13 (b) and (c), respectively. The low signal-to-noise ratio prevents any further analysis. In Figure 4.13 (d), the same spectrum image after PCA assisted noise reduction shows the capabilities of the technique. The two single spectra are shown in Figure 4.13 (e) and (f) respectively. All the features of the edges are revealed, even in the spectra from the thickest part of the particle, therefore making the data suitable for further analysis.

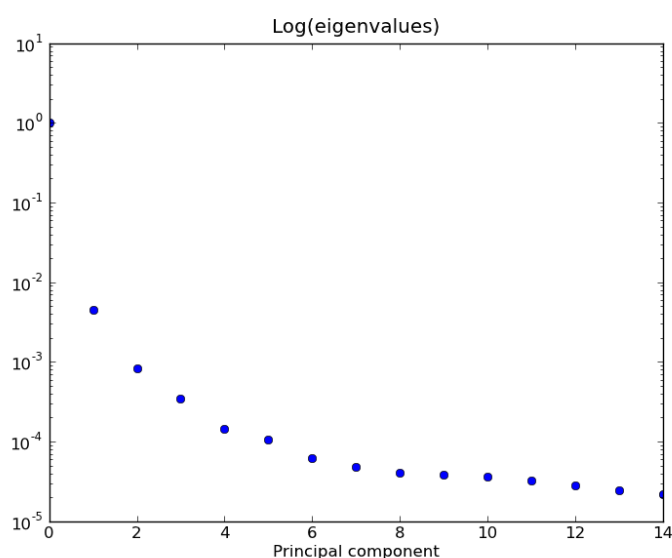


**Figure 4.11:** *Logarithm of the variance of the components obtained from PCA analysis.*

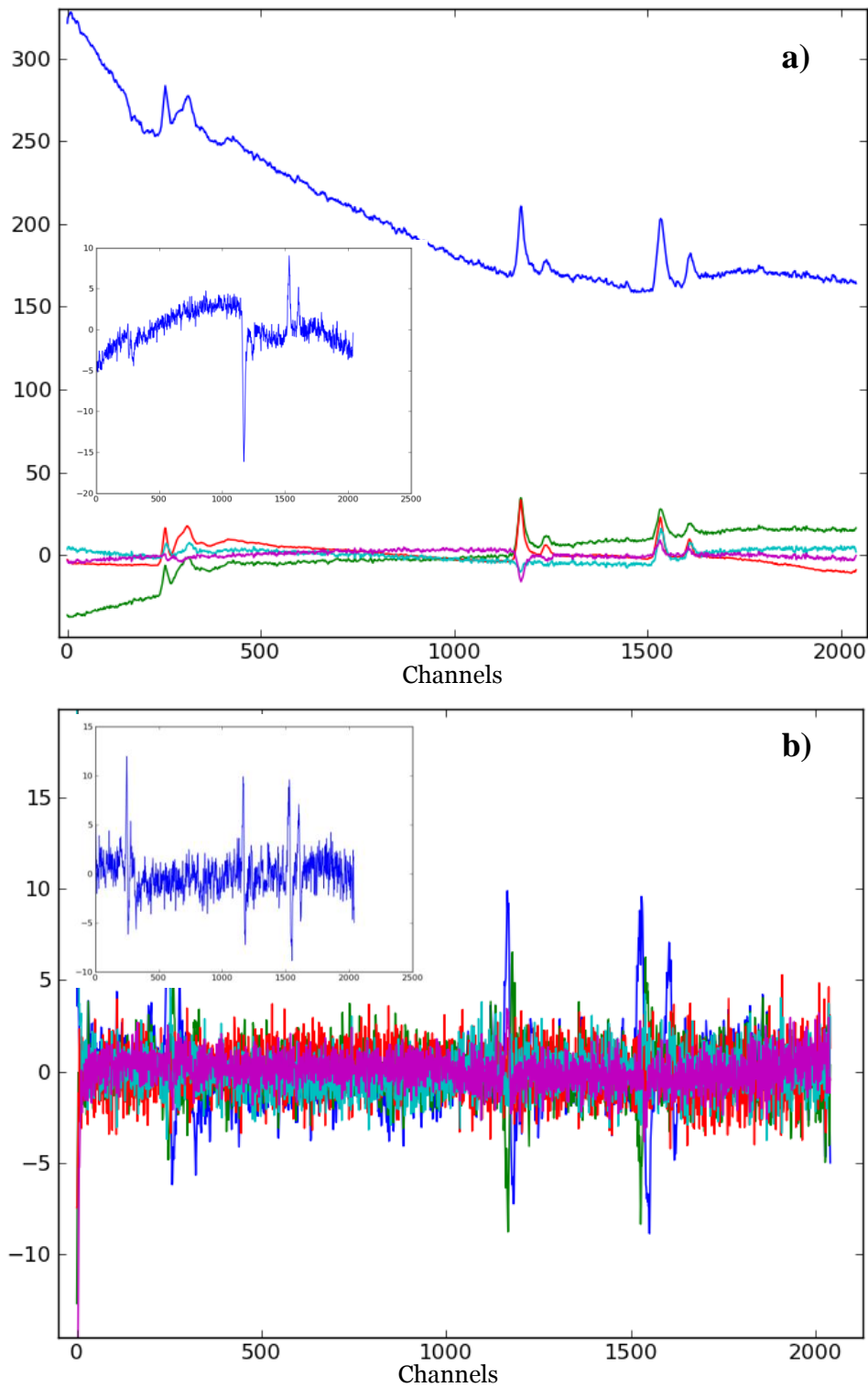


**Figure 4.12: a)** First five principal components. On the inset there is the fifth principal component, which still retains useful information about the edges in the spectra. **b)** Plot of the sixth to tenth principal components, which were discarded for noise reduction. The inset image is the sixth component, the first discarded signal. Note how the signal to noise ratio is very poor in comparison with the first five components.

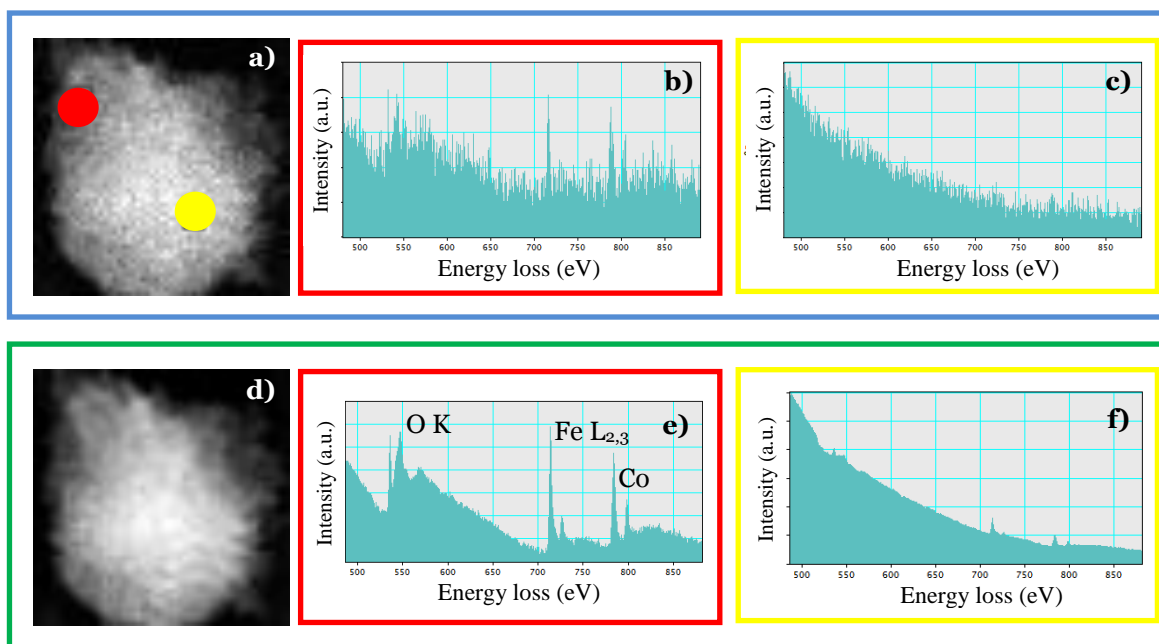


**Figure 4.13:** Spectrum images at  $68.99^\circ$  before ( **a**) framed in blue and equivalent to Figure 4.10) and after ( **d**) framed in green) PCA assisted noise reduction. Individual spectra from the border of the particle ( **b**) and ( **e**), in red) and a thicker region ( **c**) and ( **f**), in yellow). Signal-to-background is much higher at the border of the particle, but it can be seen that the noise level in the as acquired spectra is excessively high for any further quantification at both positions.

### 4.3.3. Edge intensity maps

The noise-reduced data were then transformed back to the original four dimensions  $I(x, y, \theta, E)$  in order to proceed to traditional core loss extraction using the Egerton method<sup>56</sup>. Following background removal, edge intensities were experimentally determined by integrating the area under the edges.

The experimental results for the extracted intensity maps of the three edges for a particular projection ( $-27.15^\circ$ ) are shown in Figure 4.14, revealing a drop in intensity at the centre of the particle, again a clear indication of thickness effects. Plural scattering (convolution of the ionization edges with the low loss region) appears to be responsible for the loss of intensity. The effects of plural scattering are avoided for

thickness ( $t$ ) of the sample  $t/\lambda \leq 0.3$ <sup>56</sup>, where  $\lambda$  is the inelastic scattering mean free path. The thickness of the particle is around 100 nm (as seen in Figure 4.9) and the inelastic scattering mean free path in the experimental conditions for iron and cobalt oxides is between 70 and 80 nm<sup>56</sup>. Those values imply that plural scattering is found for thicknesses over about 20 nm in our sample. The experimental edge maps fail to fulfil the projection requirement<sup>57</sup> near the centre of the particle, where this drop in intensity is systematically found, but this problem is not found near the surface.

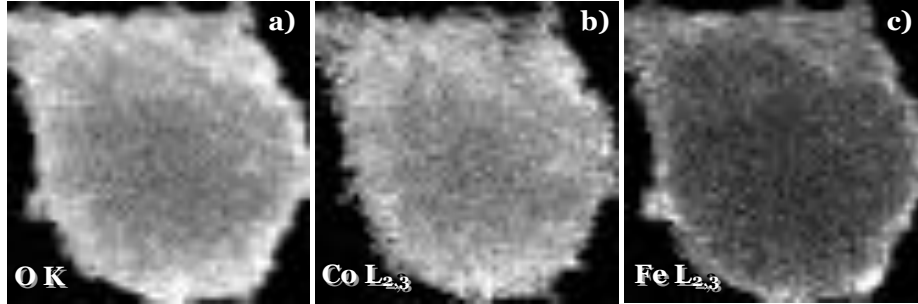


**Figure 4.14:** Edge intensity maps for **a) O K**, **b) Co L<sub>2,3</sub>** and **c) Fe L<sub>2,3</sub>**.

In order to overcome the thickness problems, we considered using elemental quantification results instead of edge intensity maps. Recovering equation [3.29], we know that the intensity of a given edge can be expressed by equation [4.25], where  $I_k^A$  is the edge intensity of a  $k$  transition for an element  $A$ ,  $N^A$  is the areal density of element  $A$ ,  $\sigma_k^A$  is the  $k$  ionization cross-section of element  $A$ ,  $I_t$  the total transmitted beam intensity,  $t$  is the sample thickness and  $\lambda$  the inelastic mean free path.

$$I_k^A(\beta, \Delta) = N^A \sigma_k^A(\beta, \Delta) I_t \quad [4.25]$$

or

$$I_k^A(\beta, \Delta) = N^A \sigma_k^A(\beta, \Delta) I_t e^{-\frac{t}{\lambda}} . \quad [4.26]$$

The absolute intensities are directly proportional to the thickness of the sample for small thicknesses, once  $t$  becomes comparable to  $\lambda$  the absolute intensities decrease (Figure 4.14).

However, the elemental concentrations can be extracted according to equation [4.27] for a three component quantification as:

$$\begin{aligned}
 [A] &= \frac{N^A}{N^A + N^B + N^C} \\
 &= \frac{I_k^A(\beta, \Delta) \left( \sigma_k^A(\beta, \Delta) I_t e^{-\frac{t}{\lambda_A}} \right)^{-1}}{I_k^A(\beta, \Delta) \left( \sigma_k^A(\beta, \Delta) I_t e^{-\frac{t}{\lambda_A}} \right)^{-1} + I_k^B(\beta, \Delta) \left( \sigma_k^B(\beta, \Delta) I_t e^{-\frac{t}{\lambda_B}} \right)^{-1} + I_k^C(\beta, \Delta) \left( \sigma_k^C(\beta, \Delta) I_t e^{-\frac{t}{\lambda_C}} \right)^{-1}} \quad [4.27] \\
 [A] &\approx \frac{\frac{I_k^A}{\sigma_k^A}}{\frac{I_k^A}{\sigma_k^A} + \frac{I_k^B}{\sigma_k^B} + \frac{I_k^C}{\sigma_k^C}},
 \end{aligned}$$

which is thickness independent.

Elemental quantification maps for a tilt angle of  $-27.15^\circ$  are shown in Figure 4.15 (a) for oxygen, (b) for cobalt and (c) for iron. As expected, in this case the intensities at the centre of the particle do not decrease. The cancelation of exponential factors is a valid approximation if the mean free path through the sample does not effectively change. Elemental quantification is a signal which approximately fulfils the projection requirement, as it changes monotonically with elemental concentration and does not depend on tilt angle<sup>47</sup>. Quantification faithfully recovers the shape of the particle as long as it is convex. This signal is kept for reconstruction, while the extracted elemental intensities are discarded. In the supporting data, movie 8, the animation of the quantification reconstruction is presented.

In order to extract more information from the dataset, finding the independent signals which compose the spectra can be of great help. We apply blind source separation to extract those independent components.

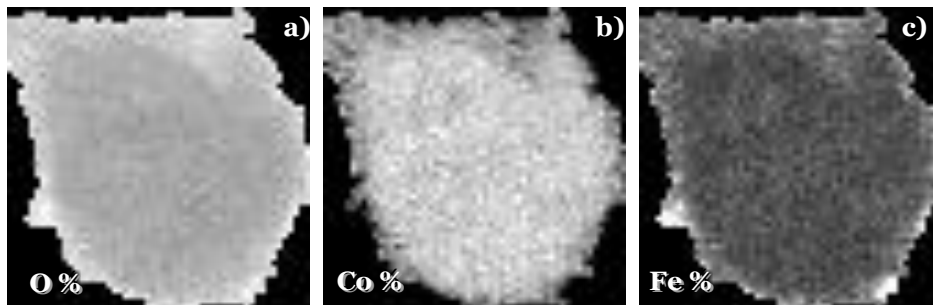


**Figure 4.15:** Elemental quantification maps for **a) O**, **b) Co** and **c) Fe**.

### 4.3.4. Identification of the independent components

#### 4.3.4.a. *Blind Source Separation / Independent Component Analysis (ICA) theory*

The decomposition of spectra in principal components (PC) is not based on any physical considerations. As a result, we obtain a series of orthogonal components ordered in descending variance. If the signal has higher variance than the noise, the data can be described as a weighted sum of signal and noise. We have shown how this is very practical for noise reduction. However, the PC can be very difficult to interpret physically.

The approach of blind source separation (BSS) consists in attempting to solve the mixture of signals originating from  $n$  sources being mixed and recorded by  $p$  sensors:

$$x_k = \sum_{i=1}^n a_{ik} s_i, \quad k = 1..p \quad [4.28]$$

where  $x_k$  is the  $k$ th recorded spectrum in the SI,  $s_i$  are the independent components and  $a_{ik}$  are the elements of the mixing matrix. As long as the sources can be considered as statistically independent, it is possible to find solutions. As BSS often involves finding an inverse filter that provides components as independent as possible, the technique is also called independent component analysis (ICA).

Unfortunately, the independent solution is difficult to find, and there are many algorithms that use different contrast functions to maximize the degree of independence between components. Given that the mutual information of a random vector is nonnegative, and zero only if the components of the vector are independent, mutual information is a function to be minimized. ICA estimation by minimization of mutual information is equivalent to maximizing the sum of the non-Gaussianity of the estimates<sup>58</sup>. Popular criteria for maximizing the non-Gaussianity are maximizing the kurtosis<sup>59</sup>

$$\text{kurt}(y) = E \{y^4\} - 3(E \{y^2\})^2 \quad , \quad [4.29]$$

where  $E \{x\}$  stands for the expected value of a random variable  $x$ ; and maximizing the negentropy

$$J(y) = H(y_{Gauss}) - H(y) \quad , \quad [4.30]$$

where  $y_{Gauss}$  is a Gaussian random variable with the same covariance as  $y$  and  $H(y)$  is the differential entropy.

In this work, KernelICA (or KICA) has been used<sup>60</sup>. This approach is not based on a single nonlinear function, but on an entire function space of candidate nonlinearities. The work is carried out with the functions in a reproducing kernel Hilbert space, and makes use of the “kernel trick” to efficiently search over this space. The use of a function space makes it possible for the algorithm to adapt to a variety of sources, making the algorithm more robust to varying source distributions.

A full description of the algorithm can be found in<sup>60</sup>.

#### 4.3.4.b. Results: independent components.

Observing the components in Figure 4.12, it is clear that they have no physical meaning and cannot be directly identified with the compounds in the sample. As ICA is much more resource consuming and noise sensitive than PCA, it was applied only to the noise filtered dataset obtained from PCA as previously mentioned. ICA was performed using KICA algorithm<sup>60</sup>, also in Hyperspy. From the five independent components (IC) shown in Figure 4.16, one can be directly interpreted as cobalt oxide signal (IC1), and another one as iron oxide signal (IC3). While containing some of information from the oxides, IC2 can be attributed mostly to the thickness of the sample. IC0 corresponds to a slight increase of the background for the last channels of the spectra, observed in the last two SI, and IC4 could also be attributed to the thickness of the sample. From the two IC containing information about the thickness of the sample, only one is kept (IC2), as the main difference between both lies in the tail of the Co edge and is considered to hold the same information about the spatial distribution of the sample thickness. Therefore, we end up with three components

(Figure 4.18) that can be identified as three orthogonal axes of our new basis: Fe oxide and Co oxide signals, and the background signal before the oxygen K edge. Every single spectrum of the dataset can be represented as a weighted sum of the independent components. Therefore, for each SI we can build three maps corresponding to the scalars of each IC, i.e., maps of iron oxide, cobalt oxide and thickness.

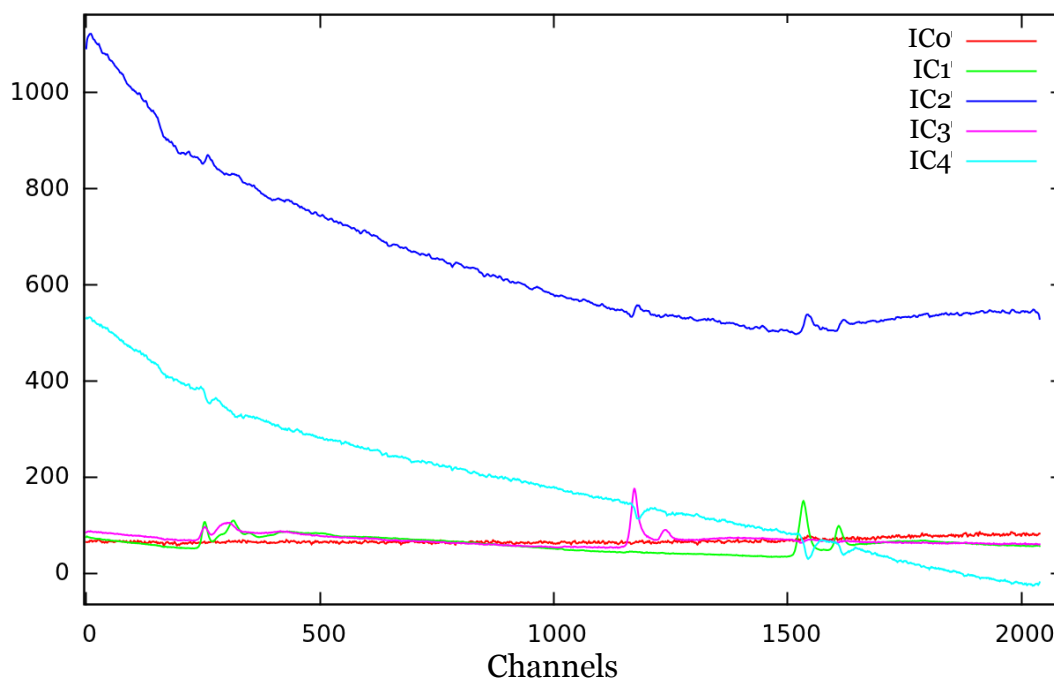


**Figure 4.16:** Independent components from the ICA. Components 1 to 3 were used for reconstructing the particle as they contained information about cobalt oxide, thickness and iron oxide respectively.

In Figure 4.18 (b) four examples are shown for the maps at a tilt angle of  $62.91^\circ$ ,  $37.45^\circ$ ,  $-27.15^\circ$  and  $-60.97^\circ$ , as well as the superposition of the maps. From these maps it can be observed that the cobalt and iron oxide related components present a drop in intensity at the centre of the particle, while the thickness related signal does not show any drop at the centre. Thus, in the combination of the maps, the thickness signal dominates the centre of the particle and the oxide signals are more pre-eminent at the border. In terms of the projection requirement<sup>57</sup>, the oxide signals fail it and the thickness signal fulfils it. Nevertheless, the oxide signals are kept for reconstruction as they contain valuable information about elemental distribution at the border of the particle, where they do fulfil the requirement (see movie 9 of the supporting data). The two oxides are not coincident all over the particle, as iron oxide is clearly seen independently at some points, unlike cobalt oxide, which is always associated to iron oxide.

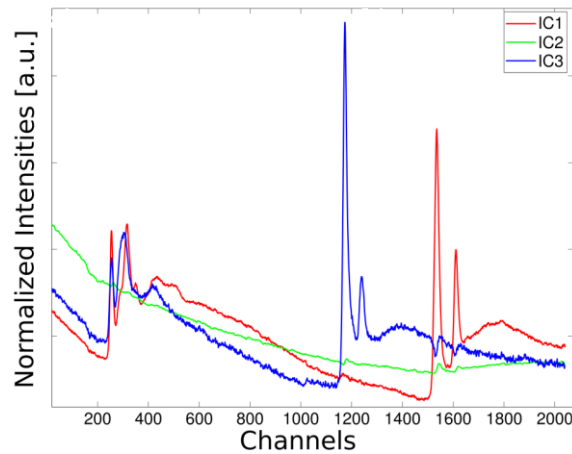


**Figure 4.17:** Independent components (unity vectors of our new basis) which are proportional to cobalt oxide (red), iron oxide (blue) and thickness of the sample (green).

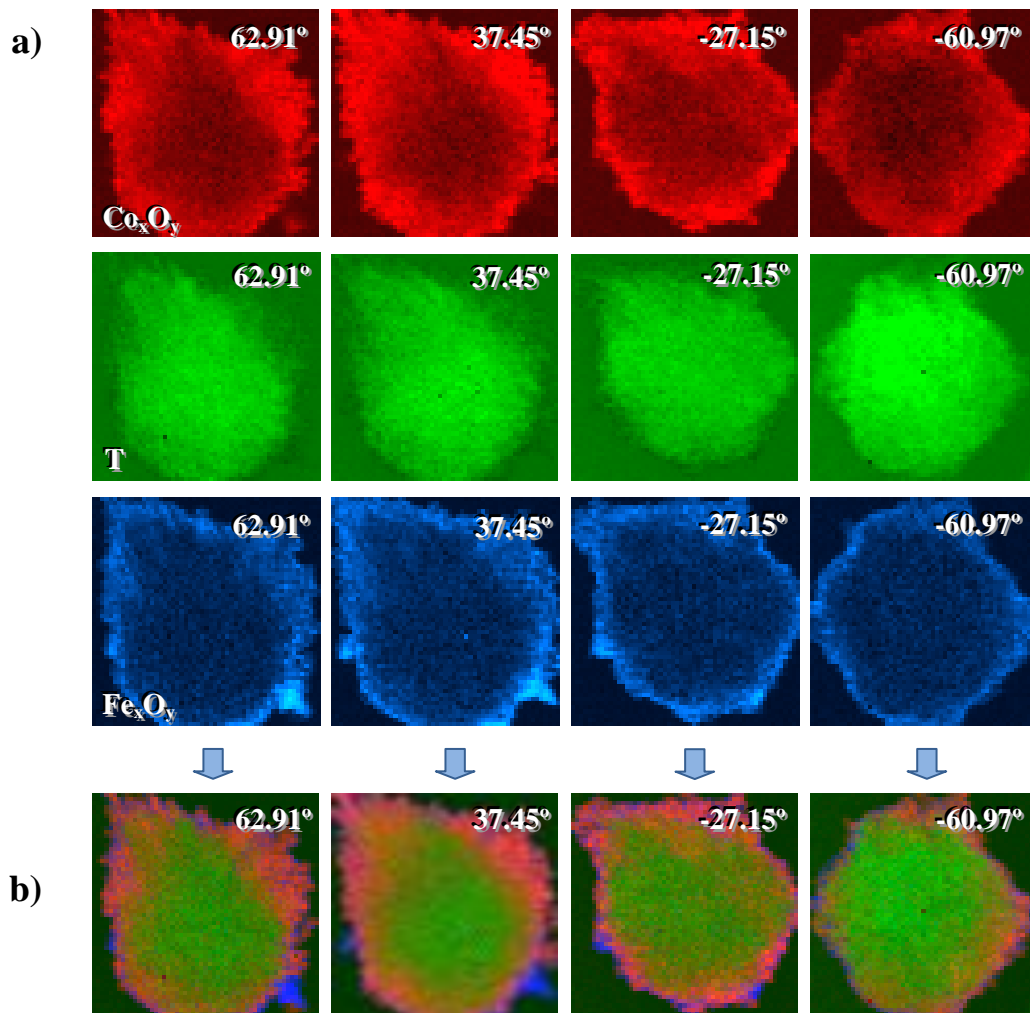


**Figure 4.18:** **a)** Extracted IC maps for four different projections ( $62.91^\circ$ ,  $37.45^\circ$ ,  $-27.15^\circ$  and  $-60.97^\circ$ ). Cobalt oxide ( $\text{Co}_x\text{O}_y$ ) is displayed in red, thickness ( $T$ ) in green and iron oxide ( $\text{Fe}_x\text{O}_y$ ) in blue. **b)** RGB composites are obtained for the four tilt angles in order to compare the spatial distribution and magnitude of each component.

As the quantification signal does not contain any information about the thickness of the sample, we combined it with the data extracted from ICA thickness maps. Hence, a new kind of signal is obtained. Pixel by pixel, the corresponding projection images are merged by multiplication. The intensity of this new signal corresponds to the contribution of each element to the thickness at every pixel, and is therefore proportional to the absolute number of atoms of that given element, fulfilling the projection requirement. Density thickness maps for a tilt angle of  $68.99^\circ$  are shown in Figure 4.19 (a) for oxygen, (b) for cobalt and (c) for iron (see movie 10 of the supporting data for the animated reconstructions)

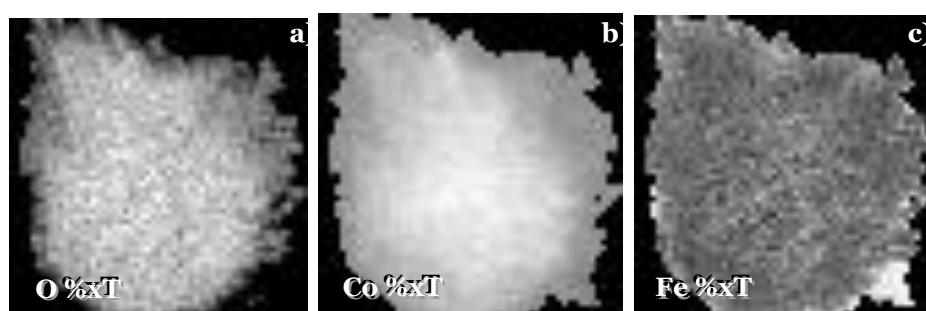


**Figure 4.19:** Density thickness maps for **a)** O, **b)** Co and **c)** Fe.

### 4.3.5. EELS-SI tomography reconstruction

Summing up the signals which were obtained from the EELS tomography dataset, we can mention the extracted signals, quantification, HAADF, sample thickness, cobalt oxide and iron oxide signal from ICA and the ICA thickness combined with core loss quantifications of Fe, Co and O. The extracted signals were not reconstructed, as they failed to fulfil the projection requirement in most of the particle. The rest of the signals were reconstructed, using the iron quantification signal to measure spatial drift in IMOD<sup>61</sup>. Imod is a free software containing many programs for image treatment specially developed for electron tomography. After failing to get a successful alignment from the commercial software, Imod was found more suitable for images with a reduced number of pixels. This spatial drift measurement was then

applied to all 9 datasets. The measure of tilt axis and reconstruction was achieved using Inspect3D software. Again, Fe quantification signal was used to determine the tilt axis, and the same correction was applied to all datasets. The chosen reconstruction algorithm was SIRT, with a number of iterations ranging from 40 to 60 in order to maximise the signal-to-background ratio.

In Figure 4.20, the results of the reconstruction for the iron related signals can be observed. In (a), an iron quantification image is given, followed by the iron quantification reconstruction in (b) and an orthoslice in (c). This signal correctly recovers the shape of the particle. The reconstruction is much better behaved than that of the iron oxide independent component. In (d), a map of the Fe IC is shown, with the intensity drop at the centre. This signal is also reconstructed (e), giving three different intensity areas, clearly observed in the orthoslice in panel (f). The areas correspond, from brighter to darker, to the border, an area where the projection requirement is still valid and the centre of the particle, with its intensity drop. Other than the centre of the particle, the results in the thinner areas are quite similar to those of the quantification signal, with a marked bright surface. Finally, the density-thickness maps show the best results. The original map in (g) shows a distribution of the intensities with two clear features: the bright border and an increase in intensity in the thicker part of the particle (to be expected in mass-thickness contrast). The reconstruction in (h) can be compared to the previous signals and is equivalent in shape, but the intensity distribution in 3D, as observed in the orthoslice in (i), presents an homogenous intensity in the inner part, with higher signal and less noise than the previous slices, and with a brighter border. This would be the kind of information expected in the core loss edge integrated intensities, which could not be used in this case due to the drop of intensities in the thicker parts of the particle. These images show how those signals can be used to reconstruct chemical information in 3D. Similar effects can be observed in the oxygen and cobalt reconstructions in Figure 4.21.

In Figure 4.22, the Fe and Co density-thickness reconstructions are superimposed. It is clearly visible in the orthoslice (Figure 4.22 (b)) that the Fe signal (in red) extends further than the Co signal (blue). This is also observed in the volume visualization (Figure 4.22 (a)). Therefore, some of the iron which is intended to penetrate the structure remains on the outer surface. However, in the inside of the particle the elemental distribution is kept constant, which means that the infiltration has been uniform.

The reconstructions from oxygen and cobalt are in good agreement with the co-acquired HAADF volume reconstruction, as shown in Figure 4.23. Conversely, Fe signals reconstruct volumes greater than those of the other elements or the HAADF.

The explanation for this phenomenon could lie in the fact that the concentration of iron is much higher at the border, and therefore iron related signals give rise to a sharp interface between the particle and the vacuum. Meanwhile, the HAADF signal is much higher at the thicker parts of the particle, and falls to background level at the border due to the small thickness. As a result, the iron signal reconstructs the edge of the particles more accurately. Finally, the thickness related IC (Figure 4.23 (d-f)) underestimates the border. This is due to the statistical nature of the signal, which assigns it a low contribution to the spectra at the border. However, the most interesting feature of this signal is that it is low sensitive to the chemistry of the sample and independent of multiple scattering, a characteristic not found in any other signal used for electron tomography.

Disregarding the effects in the centre of the particle, all chosen signals could be properly reconstructed, leading to volumes containing chemical information. Even those signals suffering from intensity loss in the centre can reconstruct volumes which keep the shape information.

### 4.3.6. Conclusions

MVA assisted EELS-SI tomography has been successfully applied to reconstruct chemical information in 3D. Amongst the MVA techniques, principal component analysis has been used to reduce the noise in the data, thus allowing for shorter acquisition times at 80 kV. Independent component analysis has been used to retrieve the uncorrelated signals which formed the spectrum, and cobalt oxide, iron oxide and thickness signal have been extracted. We have also used quantification maps to overcome the thickness problem found in the signal. Finally, thickness and elemental quantification signals have been combined to obtain chemical species distribution maps in 3D. MVA clearly expands the potential applications of analytical tomography, as it is now possible to apply it to characterize beam sensitive materials or samples with overlapping edges, where core-loss extraction using the background or EFTEM fail.

EELS tomography has been applied to  $\text{Co}_3\text{O}_4$  mesoporous particles filled with  $\text{Fe}_x\text{Co}_{(3-x)}\text{O}_4$ . It has been determined that the iron distribution is homogeneous inside the particle, and that the surface of the particle is iron rich.

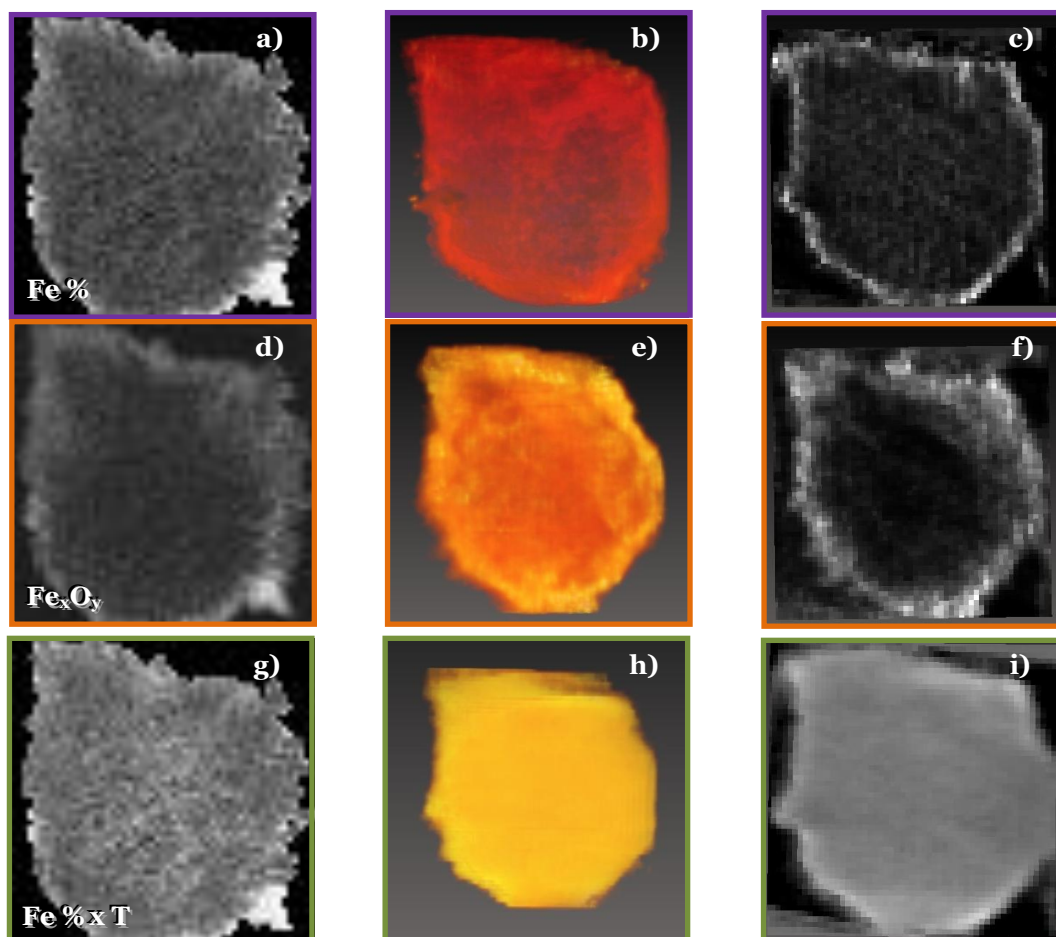


**Figure 4.20:** **a)** Iron map at  $68.99^\circ$  from Egerton quantification, **b)** voltex visualization of the reconstruction of iron maps and **c)** slice through the reconstructed volume. **d)** Iron oxide map from ICA, **e)** voltex visualization of the reconstruction of ICA iron oxide maps and **f)** slice through the reconstructed volume. **g)** Iron density-thickness map from ICA, **h)** voltex visualization of the reconstruction of ICA thickness maps related to iron quantification and **i)** slice through the reconstructed volume. All slices through the reconstructions cut through the middle of the particle.

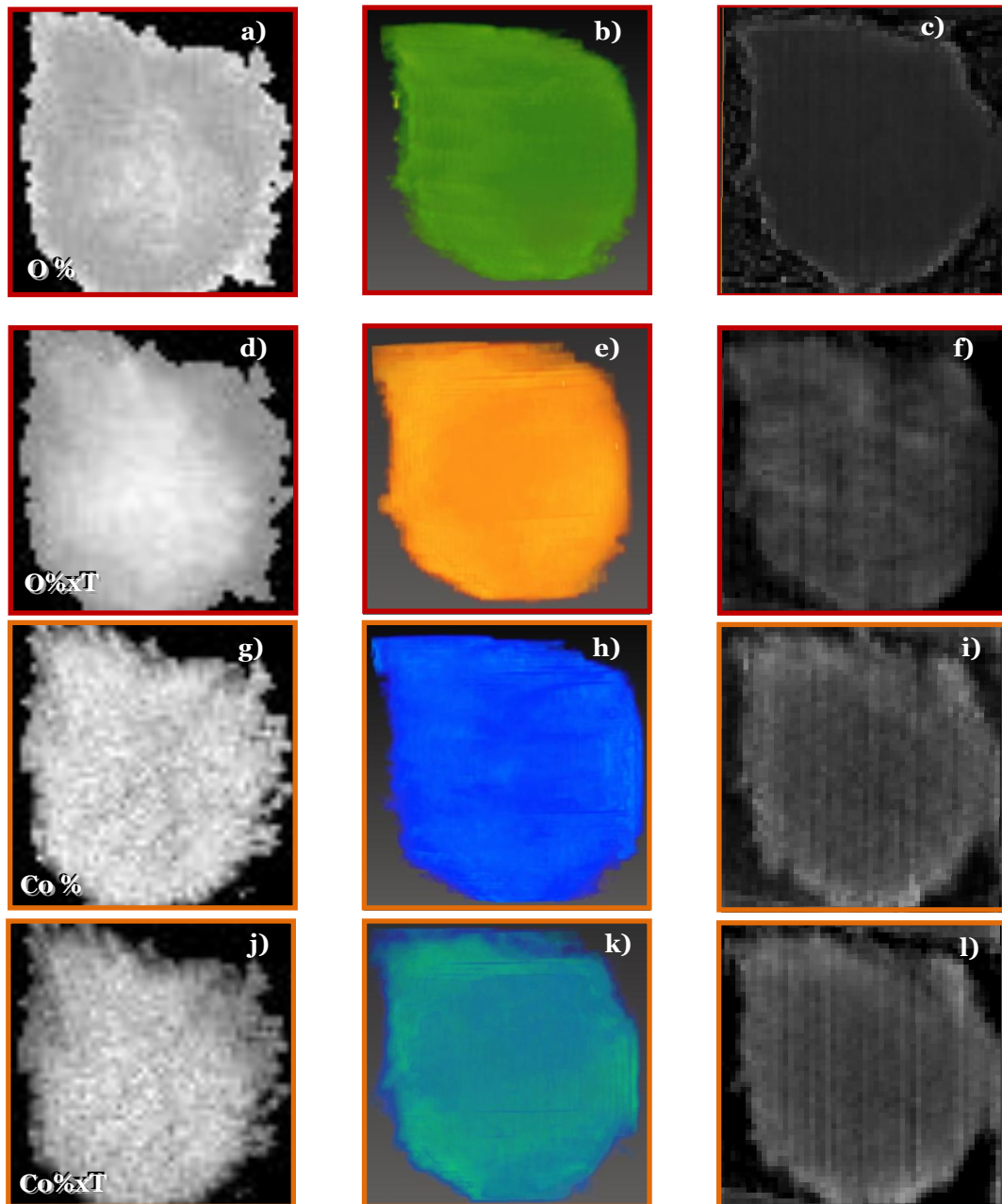


**Figure 4.21:** **a)** oxygen map at  $68.99^\circ$  from Egerton quantification, **b)** voltex visualization of the reconstruction of oxygen maps and **c)** slice through the reconstructed volume. **d)** Oxygen density-thickness map from ICA, **e)** voltex visualization of the reconstruction of ICA thickness maps related to oxygen quantification and **f)** slice through the reconstructed volume. **g)** Cobalt map at  $68.99^\circ$  from Egerton quantification, **h)** voltex visualization of the reconstruction of cobalt maps and **i)** slice through the reconstructed volume. **j)** Cobalt density-thickness map from ICA, **k)** voltex visualization of the reconstruction of ICA thickness maps related to cobalt quantification and **l)** slice through the reconstructed volume.

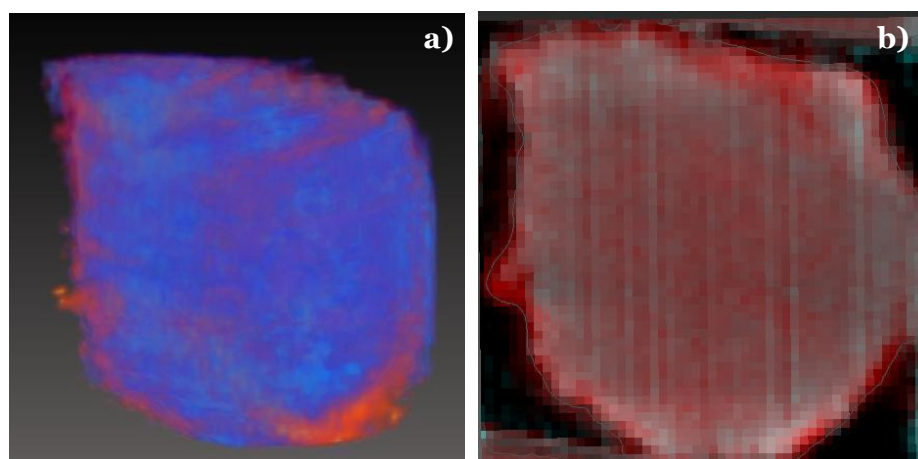


**Figure 4.22:** **a)** Voltex visualization of the reconstructed iron (red) and cobalt (blue) density-thickness maps. **b)** Orthoslice through the volumes of the reconstructed iron and cobalt density-thickness maps. It can be observed that iron has higher intensity than cobalt at the edges of the particle.

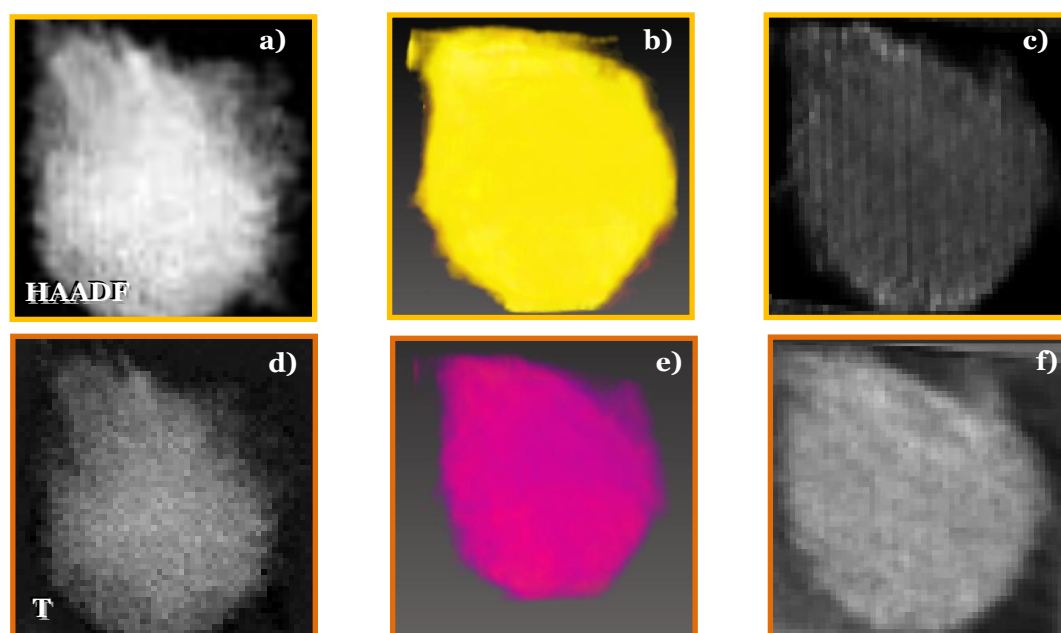


**Figure 4.23:** **a)** HAADF projection at  $68.99^\circ$ , **b)** voltex visualization of the HAADF reconstruction and **c)** slice through the reconstructed volume. **d)** Thickness map from ICA, **e)** voltex visualization of the reconstruction of ICA thickness maps and **f)** slice through the reconstructed volume.

## **4.4. A step beyond: enhanced resolution EELS-tomography of the mesoporous material**

The previous results have shown the feasibility of EELS electron tomography at low voltages and short acquisition times thanks to the application of multivariate analysis. If the sample can withstand the beam, the bottleneck of the technique is the amount of time needed for the acquisition. The 48 spectrum images used for the reconstruction of the mesoporous particle took many hours to acquire; yet, the resolution of the images was not enough to distinguish the pores.

The aim of the next experiment is to increase the resolution of the EELS-SI to recover the 3D elemental distribution in the pores. Reducing the exposition time is not the best option, as the increased noise could compromise the data extraction. Instead, as the number of spectra per image should increase, we chose to reduce the number of images to 36 SI. The results will show that the number of images is enough for a good reconstruction, and that the elemental distribution at the pores can be extracted successfully.

### **4.4.1. Spectra acquisition and data treatment**

The sample with lower iron concentration (0.6 Fe(III):Co<sub>3</sub>O<sub>4</sub>) was chosen to demonstrate the capability of low-voltage EELS-SI tomography to retrieve the

elemental distribution around the pores in an aberration corrected microscope. This sample was chosen to minimize the thickness, as it can affect the EELS signal<sup>62</sup>.

The final dataset was obtained by acquiring 36 EELS-SI from  $-67^{\circ}$  to  $72^{\circ}$ , with  $63 \times 63$  spectra each, 2048 channels per spectrum and an energy distribution of 0.2 eV per channel and an acquisition time of 0.2 s per spectrum. The data were acquired in a probe corrected FEI Titan.

We used Hyperspy to perform weighted principal component analysis (wPCA). The used version of Hyperspy is capable of dealing with the whole dataset, applying the same treatment to all the images. First of all it is necessary to align the dataset in energy. This was done using the oxygen K edge. The used GIF Tridiem EELS detector actually consists of two detectors, which, at the low integration times used, could not properly correct for gain. In order to correct this offset, which was measured to be always below 50 counts, the data was separated into two spectral ranges, removing 8 eV around the area where the intensity jump is found. Afterwards, the data were spliced together, rescaling the data to avoid the intensity jump. Also, to avoid negative values caused by the noise in order to use Poissonian normalization in the wPCA decomposition, a constant intensity translation was used. For wPCA decomposition, a sparse algorithm was used, masking some of the data. The masked area lay where the intensity jump correction was applied, in the 660-668 eV range. From this analysis, four components were chosen to reconstruct a clean dataset.

From this clean dataset the elemental maps can be extracted. Taking into account the number of images that required elemental extraction, the process was simplified by creating a script for Digital Micrograph (DM) which removed the background contribution and integrated the areas under the oxygen, iron and cobalt edges. As a result, repetitive maps of the three elements for every image could be extracted, plus an image using the background before the oxygen edge. In order to simplify the alignment, the pixels in the images were oversampled using a bilinear interpolation in DM. Signals were reconstructed in three dimensions using Inspect 3D and 40 iterations of SIRT algorithm.

### 4.4.2. EELS tomography resolving porous structure

First of all, to check the possibility to correctly align the data, the HAADF survey images were used for reconstruction. The results are shown in Figure 4.24. The voltex visualization of the reconstructions shows the preservation of the pore structure. Therefore, it should be possible to align the EELS data.

Due to the low electron beam voltage and short acquisition times used to avoid sample damage during such a long experiment, the data sets were found to be very noisy. As in the previous section, Multivariate analysis (MVA), was efficiently applied to separate most of the noise from the signal in the EELS-SI.

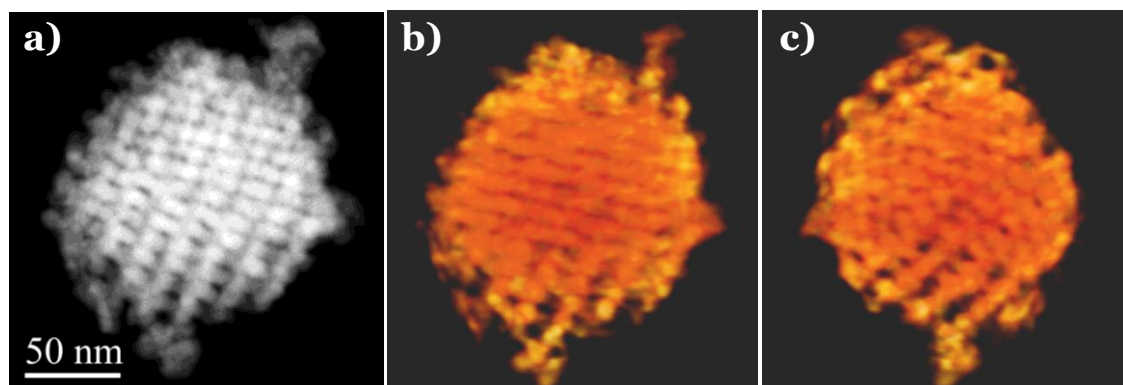


**Figure 4.24:** **a)** HAADF image acquired at  $-4^\circ$ , half through the acquisition series. **b)** and **c)** two different views of the 3D reconstruction of the HAADF images. The porous structure is clearly visible in the reconstruction.

Spectra before and after the noise cleaning process are shown in Figure 4.25. After noise reduction, the images were thresholded to eliminate the intensities in areas outside the particle. The shown spectra result from the sum of four spectra in the images. Single spectra in the original SI are even noisier, but MVA accurately extracts the actual information contained in the data, as observed in the spectrum from the same area after MVA.

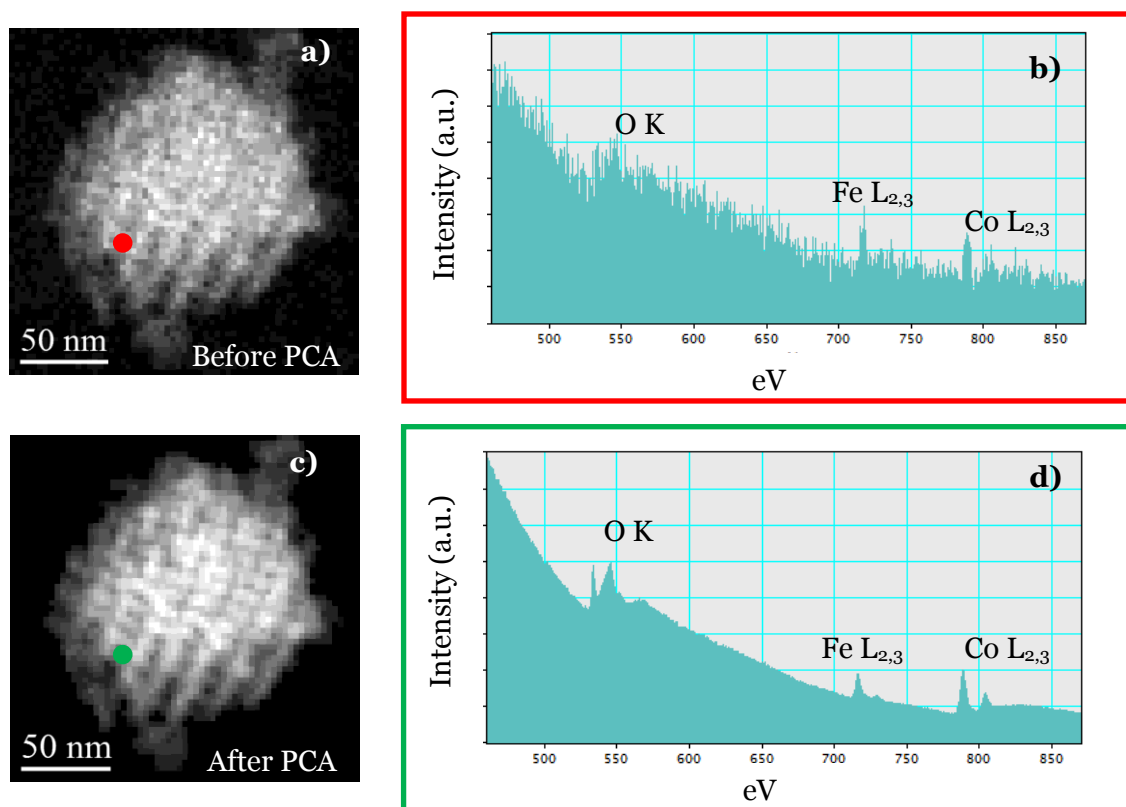


**Figure 4.25:** **a)** SI at  $-4^\circ$  as acquired with corresponding sum of four spectra **b)** from the area highlighted in red. **c)** SI at  $-4^\circ$  after PCA noise reduction with corresponding sum of four spectra **d)** from the area highlighted in green. Not only is the noise in the spectra reduced, but also in the images.

Then, from this clean dataset, the elemental edge intensity maps can be extracted, through background removal and integration of the areas under the oxygen K, iron L<sub>2,3</sub> and cobalt L<sub>2,3</sub> edges, as illustrated in Figure 4.26 (a). As a result, repetitive maps of the three elements for every image could be extracted, plus an image using the background before the oxygen edge (Figure 4.26 (b-e)). To a first approximation, the background before the O K edge is only proportional to the thickness of the sample and the integrated area under the edges is proportional to the thickness and the concentration of a given element. These four signals were successfully reconstructed in 3D, as shown in Figure 4.27. However, the spatial resolution of the reconstruction is not the same for all signals. Taking into account the definition of the inner pores as the main feature to be preserved in the reconstruction, the background signal gives the best spatial resolution. It can be observed in the extracted map in Figure 4.26 (b) that the pores of the structure are visible all over the particle using this signal. If we compare the different extracted signals from Figure 4.26, cobalt and iron maps show defined pores all over the projection. Only in the centre of the particle the pore structure

appears more blurred. On the other hand, oxygen signal is only accurate at the border of the particle, so the pore structure is not visible inside the particle. Concerning the resolution of the pores after 3D reconstruction, cobalt (Figure 4.27 (c) and (g)) and iron (Figure 4.27 (d) and (h)) reconstructions have a visible porous structure while this is not observed for the oxygen signal (Figure 4.27 (b) and (f)). The oxygen signal, however, can reconstruct the porous structure at the border (see movie 11 in the supporting files for the animated reconstructions).

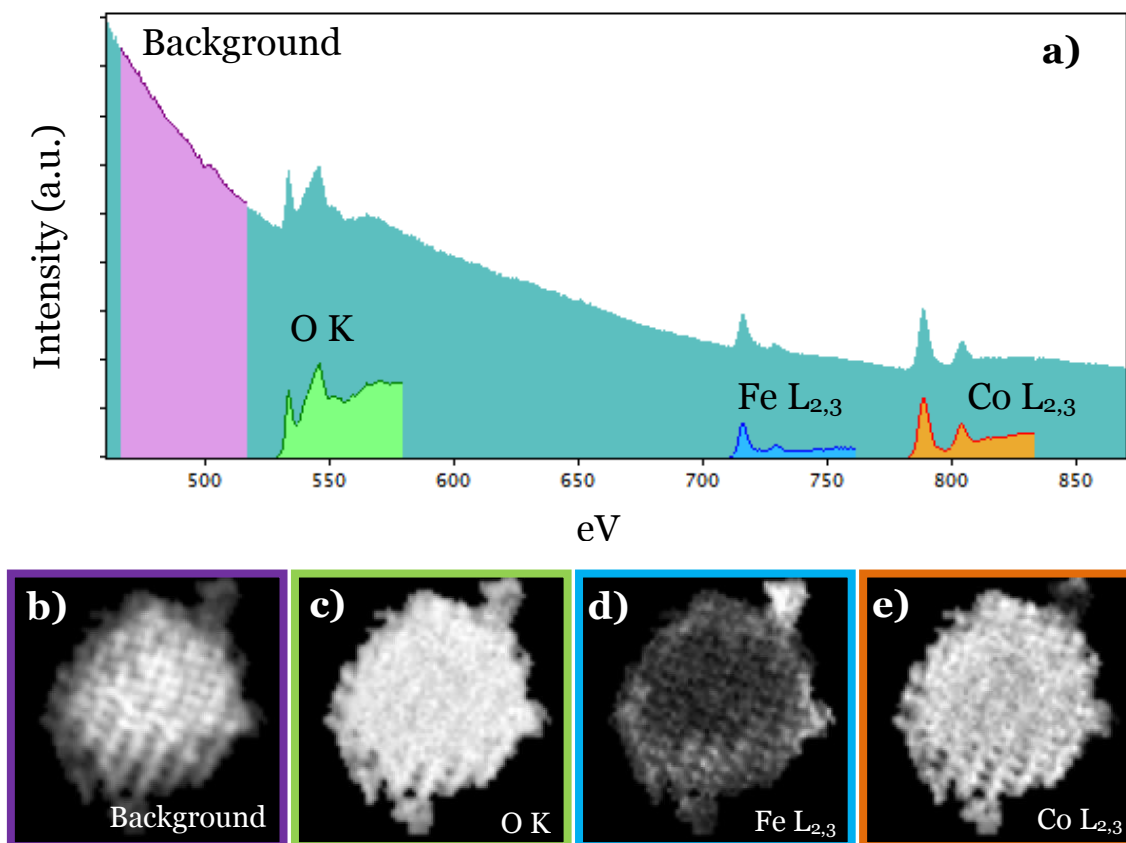


**Figure 4.26:** **a)** Single spectrum from the clean dataset at  $-4^\circ$  tilt, with the shaded areas corresponding to the integrated intensities of the background and edges. **b)** Background extracted intensities map, **c)** oxygen K edge map, **d)** iron  $L_{2,3}$  edge map and **e)** cobalt  $L_{2,3}$  edge map at  $-4^\circ$  tilt.

Iron and cobalt reconstruct the porous structure with good accuracy. It can be observed that there are two protuberances on the particle, and that one of them has a different composition from the rest of the sample. From Figure 4.26 and Figure 4.27, it is apparent that the topmost protuberance is iron rich while the bottom one has the same mean composition as the rest of the sample. This can also be observed in Figure 4.28,

where Fe and Co extracted maps are superimposed. Most interestingly, this figure shows how the pores of the mesoporous cobalt oxide template have been successfully impregnated with the mixed iron-cobalt oxide, as the signal from iron (in blue) is nicely seen inside the mesoporous structure. This observation is confirmed in Figure 4.29, where the covering of the cobalt oxide structure with iron is shown in a slice through the reconstructed volume, obtaining in this case information from the inside of the particle only, which would be unobtainable by means of any other technique.

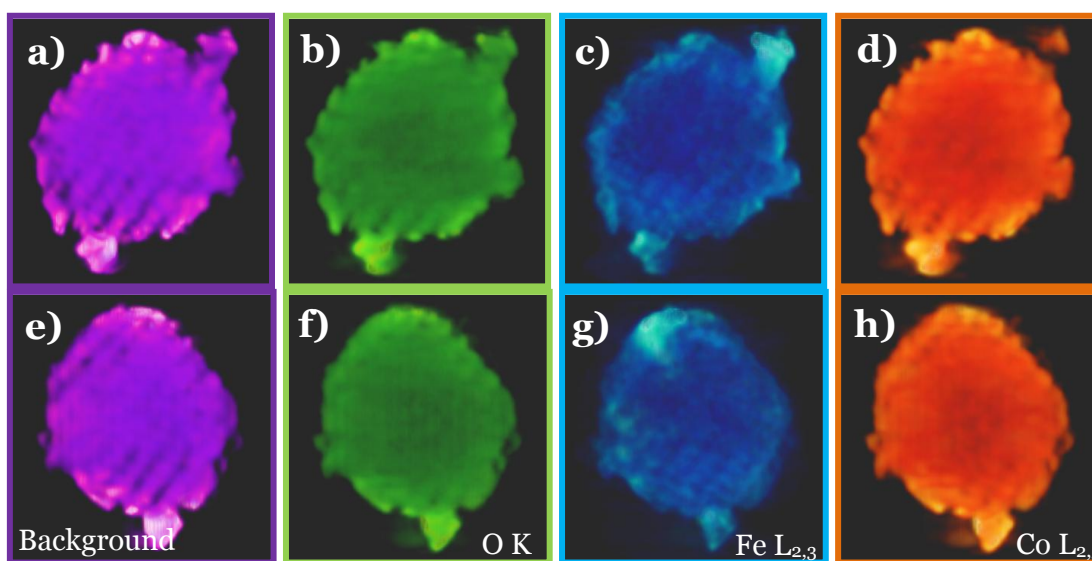


**Figure 4.27:** Voltex visualizations of the reconstructed volume from the extracted intensities of the background (**a** and **e**), O K edge (**b** and **f**), Fe  $L_{2,3}$  edge (**c** and **g**) and Co  $L_{2,3}$  edge (**d** and **h**).

Unlike what was found in the previous experiment, in these results, no contrast inversion is found in the centre of the particle. The main reason for this is the smaller size of the particle and the lower charge of iron, which further reduces the effective thickness of the sample, as the pores are wider than those in the previous experiment. Recovering equation [4.26], we stated that the effects of plural scattering are avoided for thicknesses ( $t$ ) of the sample  $t/\lambda \leq 0.35^6$ , where  $\lambda$  is the inelastic scattering mean free path. The thickness of the particle is around 100 nm (as seen in Figure 4.24) and due to the porosity it can be effectively reduced to 50 nm; the mean free path is around 80 nm. Therefore, plural scattering can be expected. However, we can consider that the signal still behaves monotonically with thickness while  $t/\lambda < 2^{45}$ , but giving rise to the so called cupping artefact, found when the monotonic relationship is not linear, and

observed at the centre of the reconstructions in Figure 4.27, which has intensities somewhat lower than the borders. This is important to interpret the images, as the brighter lower protuberance in the reconstruction and the borders of the particle are expected to have the same mean composition as the inner parts, as revealed by the original projections in Figure 4.26. Once the artefact is recognised, it does not further hinder the interpretation of the results.

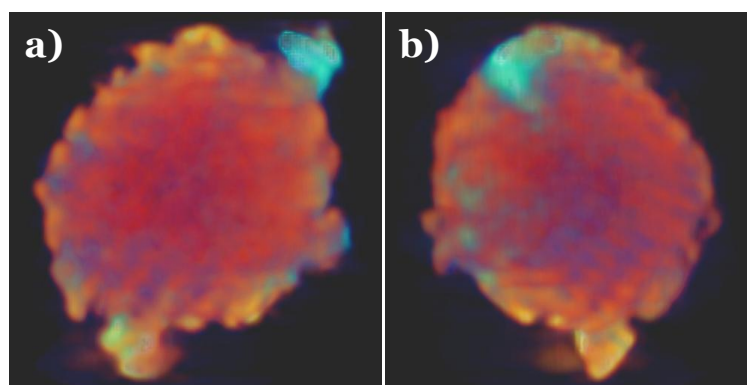


**Figure 4.28:** Comparison of the cobalt (orange) and iron (blue) reconstructions, where the presence of iron inside the pores can be observed.

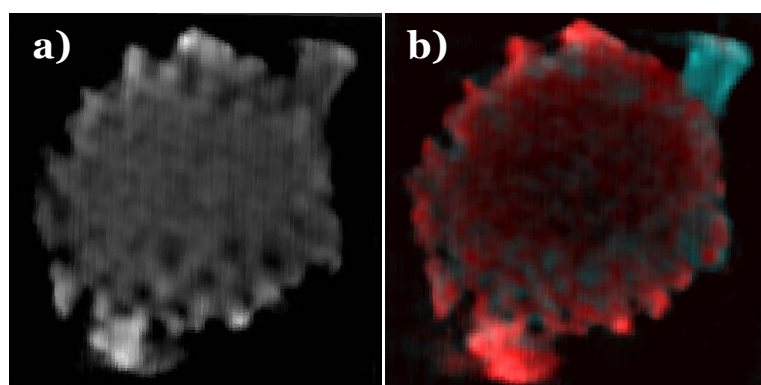


**Figure 4.29:** **a)** Slice through the reconstructed volume of the background signal and **b)** the combined cobalt (red) and iron (blue) signals. It can be observed how the inner sides of the pores are richer in iron, as it was expected from the infiltration procedure.

As for the integrated background previous to the O K edge, we can assume that it is only caused by the tail of the low loss region, dominated by the bulk plasmon. Cobalt and iron are consecutive elements and the oxides present in the sample are both spinels with very close unit cell size. Therefore, the new material grown on top of the original cobalt oxide structure, either iron cobalt mixed oxide or iron oxide, grows epitaxially. As a result, the plasmons in the sample can be considered to be roughly uniform. We thus consider that only the thickness of the material is involved in the

intensity of the plasmon tail and, thus, in the intensity of the background prior to the first core loss edge.

Finally, observing the original HAADF projection in Figure 4.24, it can be noted that the particle has in fact two grains of the mesoporous order, dividing the particle in two halves. This phenomenon can hinder the 3D visualization, as the area around the grain boundary tends to appear blurred. Nevertheless, the used signals properly reconstructed the mesoporous structure of the particle to a great extent.

Blind source separation was also applied to the data set after PCA noise cleaning. Three components could be directly linked to iron oxide, cobalt oxide and thickness, just as in the previous experiment. The results, however, had lower spatial resolution than the intensities extracted by the Egerton method. In Figure 4.30, an original map for each component can be observed. When comparing them to the extracted maps in Figure 4.26, as they are projections at the same angle, it becomes clear that the three component maps appear more blurred than the extracted edge intensities. The thickness component compares well with the background extracted intensity, but the iron and cobalt oxide components mix the transition metal and the oxygen information. As observed in Figure 4.26, the oxygen had a lower spatial resolution than the metals. This can be an explanation for the loss of spatial resolution in the BSS components.

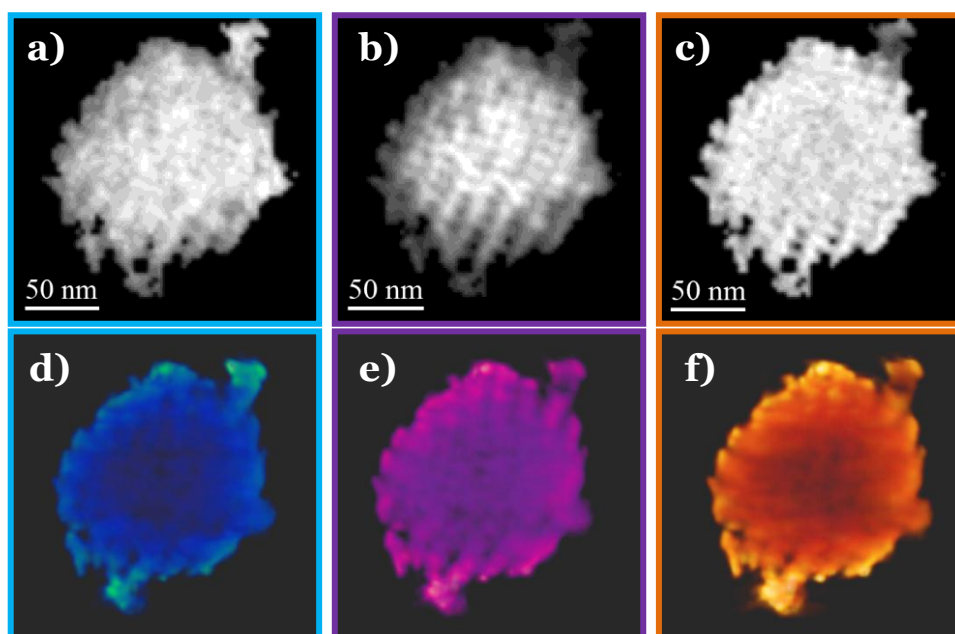


**Figure 4.30:** Results of the BSS **a)** iron oxide component map, **b)** thickness component map and **c)** cobalt oxide component map at  $-4^\circ$  tilt. Voltex visualizations of the **d)** iron oxide maps, **e)** thickness maps and **f)** cobalt oxide maps.

To sum up, EELS-SI tomography allowed us to confirm that the nominal AFM-FiM structure is obtained (Figure 4.29). This technique yielded 3D reconstructions of the particle using chemical sensitive signals, therefore obtaining 3D representations of the elemental distribution in the sample. In these 3D representations, the higher concentration of iron in the pore walls is observed, but, most importantly, it is possible to extract punctual chemical information from the inside of the particle confirming the expected structure.

### 4.4.3. Conclusions

In this experiment, we have shown that EELS signal can reconstruct the three dimensional structure of  $\text{Fe}_x\text{Co}_{(3-x)}\text{O}_4@ \text{Co}_3\text{O}_4$  mesoporous nanoparticles down to pore resolution. The use of multivariate analysis has been necessary to reduce the noise in the dataset. This statistical treatment has enabled the extraction of edge intensities, in a manner similar to EFTEM. Moreover, the EELS background has been used for the first time to reconstruct the structure, resolving the pores. The EELS edges have also been used to reconstruct the structure, the  $L_{2,3}$  edges showing less delocalization than the oxygen K edge.

Thanks to the enhanced spatial resolution obtained even at low voltages (80kV) using a probe aberration corrected instrument, and the ability of multivariate analysis to extract useful information from noisy data, it has been possible for the first time to prove that the  $\text{Fe}_x\text{Co}_{(3-x)}\text{O}_4$  was grown on top of  $\text{Co}_3\text{O}_4$  in the inner pores of the structure.

## 4.5. Conclusions

In this chapter, we have introduced the combination of electron tomography and electron energy loss spectroscopy to recover 3D chemical maps. Focusing on the characterization of  $\text{Fe}_x\text{Co}_{(3-x)}\text{O}_4@\text{Co}_3\text{O}_4$  mesoporous nanoparticles, we have first shown the possibilities of HAADF STEM tomography to recover the 3D structural information of the samples and the ability of EELS SI to extract chemical information in 2D maps. Following this characterization, EELS SI tomography experiments have been carried out. In order to avoid damaging sample, low voltages (80 kV) and low acquisition times per spectrum (100-200 ms) were applied, which lead to very noisy datasets. We proposed the use of multivariate analysis to overcome this problem and enable short acquisition times.

In a first experiment, principal component analysis (PCA) was applied to reduce the noise in the data, and independent component analysis (ICA) was used to extract the uncorrelated components forming the spectra. Then, quantification results were reconstructed in 3D, as well as the independent components and a new kind of signal, here called density-thickness map, was built using the quantification and the thickness related independent component. Quantification was able to reconstruct the shape of the particle and density-thickness maps were demonstrated to overcome the inversion contrast at the centre of the particle found in the EELS signal.

A second experiment was carried out, to push the resolution of the technique further. As the considered material was mesoporous, we aimed at resolving the pores in the reconstructed volumes of the different components. As in the previous experiment, the data underwent MVA to reduce the noise content. In this case, the oxygen, iron and cobalt integrated signals were reconstructed in 3D, successfully preserving the porous structure in the reconstruction. Moreover, the background prior to the oxygen K edge was also integrated and reconstructed yielding the best spatial resolution of the EELS extracted signals.

In summary, EELS-SI tomography has been proven to be a useful and useful tool for the characterization of nanostructures. Multivariate analysis has been the key to enable the use of the technique in beam sensitive materials with high spatial resolution. Moreover, the independent component analysis of the data opens the possibility to analyze materials with overlapping edges, where EFTEM would fail.

## 4.6. References

1. Kresge, C., Leonowicz, M., Roth, W., Vartuli, J. & Beck, J. Ordered Mesoporous Molecular-Sieves Synthesized by a Liquid-Crystal Template Mechanism. *Nature* **359**, 710-712 (1992).
2. Beck, J., et al. A New Family of Mesoporous Molecular-Sieves Prepared with Liquid-Crystal Templates. *J.Am.Chem.Soc.* **114**, 10834-10843 (1992).
3. Cabo, M., et al. Synthesis of compositionally graded nanocast NiO/NiCo<sub>2</sub>O<sub>4</sub>/Co<sub>3</sub>O<sub>4</sub> mesoporous composites with tunable magnetic properties. *Journal of Materials Chemistry* **20**, 7021-7028 (2010).
4. Zhao, D. Y., et al. Triblock copolymer syntheses of mesoporous silica with periodic 50 to 300 angstrom pores. *Science* **279**, 548-552 (1998).
5. Kleitz, F., Choi, S. H. & Ryoo, R. Cubic Ia3d large mesoporous silica: synthesis and replication to platinum nanowires, carbon nanorods and carbon nanotubes. *Chemical Communications* 2136-2137 (2003).
6. Zhao, D. Y., Huo, Q. S., Feng, J. L., Chmelka, B. F. & Stucky, G. D. Nonionic triblock and star diblock copolymer and oligomeric surfactant syntheses of highly ordered, hydrothermally stable, mesoporous silica structures. *J.Am.Chem.Soc.* **120**, 6024-6036 (1998).
7. Kleitz, F., et al. Large cage face-centered-cubic Fm3m mesoporous silica: Synthesis and structure. *J Phys Chem B* **107**, 14296-14300 (2003).
8. Tanaka, S., Tate, M. P., Nishiyama, N., Ueyama, K. & Hillhouse, H. W. Structure of mesoporous silica thin films prepared by contacting PEO106-PPO70-PEO106 films with vaporized TEOS. *Chemistry of Materials* **18**, 5461-5466 (2006).
9. Rossinyol, E., et al. Synthesis and Characterization of Chromium-Doped Mesoporous Tungsten Oxide for Gas Sensing Applications. *Advanced Functional Materials* **17**, 1801-1806 (2007).
10. Prim, A., et al. A novel mesoporous CaO-loaded In<sub>2</sub>O<sub>3</sub> material for CO<sub>2</sub> sensing. *Advanced Functional Materials* **17**, 2957-2963 (2007).
11. Francioso, L., et al. Nanostructured In<sub>2</sub>O<sub>3</sub>-SnO<sub>2</sub> sol-gel thin film as material for NO<sub>2</sub> detection. *Sens.Actuator B-Chem.* **114**, 646-655 (2006).

12. Rossinyol, E., et al. Gadolinium doped Ceria nanocrystals synthesized from mesoporous silica. *Journal of Nanoparticle Research* **10**, 369-375 (2008).
13. Cabo, M., et al. Hydrogen sorption performance of MgH<sub>2</sub> doped with mesoporous nickel- and cobalt-based oxides. *Int J Hydrogen Energy* **36**, 5400-5410 (2011).
14. Sahoo, B., Sahu, S. K., Nayak, S., Dhara, D. & Pramanik, P. Fabrication of magnetic mesoporous manganese ferrite nanocomposites as efficient catalyst for degradation of dye pollutants. *Catalysis Science & Technology* **2**, 1367-1374 (2012).
15. Song, B. Y., Eom, Y. & Lee, T. G. Removal and recovery of mercury from aqueous solution using magnetic silica nanocomposites. *Appl.Surf.Sci.* **257**, 4754-4759 (2011).
16. Tao, S., Wang, C., Ma, W., Wu, S. & Meng, C. Designed multifunctionalized magnetic mesoporous microsphere for sequential sorption of organic and inorganic pollutants. *Microporous and Mesoporous Materials* **147**, 295-301 (2012).
17. Ursachi, I., Stancu, A. & Vasile, A. Magnetic alpha-Fe<sub>2</sub>O<sub>3</sub>/MCM-41 nanocomposites: Preparation, characterization, and catalytic activity for methylene blue degradation. *J.Colloid Interface Sci.* **377**, 184-190 (2012).
18. Wang, Y., et al. Multifunctional Magnetic Mesoporous Silica Nanocomposites with Improved Sensing Performance and Effective Removal Ability toward Hg(II). *Langmuir* **28**, 1657-1662 (2012).
19. Yuan, C., Huang, Z. & Chen, J. Mesoporous Titanium-Silica Composite Encapsulated gamma-Fe<sub>2</sub>O<sub>3</sub>: Novel Magnetically Recyclable Heterogeneous Catalysts for Olefin Epoxidation Reactions. *Catalysis Letters* **141**, 1484-1490 (2011).
20. Chen, Y., et al. Structure-property relationships in manganese oxide - mesoporous silica nanoparticles used for T-1-weighted MRI and simultaneous anti-cancer drug delivery. *Biomaterials* **33**, 2388-2398 (2012).
21. Ma, M., et al. Au capped magnetic core/mesoporous silica shell nanoparticles for combined photothermo-/chemo-therapy and multimodal imaging. *Biomaterials* **33**, 989-998 (2012).
22. Wu, H., et al. pH-responsive magnetic mesoporous silica nanospheres for magnetic resonance imaging and drug delivery. *Reactive & Functional Polymers* **72**, 329-336 (2012).
23. Gommers, C. J., Friedrich, H., Wolters, M., de Jongh, P. E. & de Jong, K. P. Quantitative Characterization of Pore Corrugation in Ordered Mesoporous Materials Using Image Analysis of Electron Tomograms. *Chemistry of Materials* **21**, 1311-1317 (2009).
24. Martines, M. U., et al. Hexagonal mesoporous silica nanoparticles with large pores and a hierarchical porosity tested for HPLC. *Comptes Rendus Chimie* **8**, 627-634 (2005).

25. Yao, Y., Czymmek, K. J., Pazhianur, R. & Lenhoff, A. M. Three-dimensional pore structure of chromatographic adsorbents from electron tomography. *Langmuir* **22**, 11148-11157 (2006).
26. Wang, H., et al. Supra-assembly of siliceous vesicles. *J.Am.Chem.Soc.* **128**, 15992-15993 (2006).
27. Han, Y., Zhao, L. & Ying, J. Y. Entropy-driven helical mesostructure formation with achiral cationic surfactant templates. *Adv Mater* **19**, 2454-2459 (2007).
28. Yuan, P., et al. Solving complex concentric circular mesostructures by using electron tomography. *Angewandte Chemie-International Edition* **47**, 6670-6673 (2008).
29. Ersen, O., et al. Direct Observation of Stacking Faults and Pore Connections in Ordered Cage-Type Mesoporous Silica FDU-12 by Electron Tomography. *J.Am.Chem.Soc.* **130**, 16800-16806 (2008).
30. Vercaemst, C., et al. Periodic Mesoporous Organosilicas Consisting of 3D Hexagonally Ordered Interconnected Globular Pores. *Journal of Physical Chemistry C* **113**, 5556-5562 (2009).
31. Midgley, P., Weyland, M., Thomas, J. & Johnson, B. Z-Contrast tomography: a technique in three-dimensional nanostructural analysis based on Rutherford scattering. *Chem.Commun.* 907-908 (2001).
32. Weyland, M., Midgley, P. A. & Thomas, J. M. Electron Tomography of Nanoparticle Catalysts on Porous Supports: A New Technique Based on Rutherford Scattering. *The Journal of Physical Chemistry B* **105**, 7882-7886 (2001).
33. Thomas, J. M., Johnson, B. F. G., Raja, R., Sankar, G. & Midgley, P. A. High-performance nanocatalysts for single-step hydrogenations. *Acc.Chem.Res.* **36**, 20-30 (2003).
34. Thomas, J. M., et al. The Chemical Application of High-Resolution Electron Tomography: Bright Field or Dark Field? *Angewandte Chemie* **116**, 6913-6915 (2004).
35. Thomas, J. M. & Midgley, P. A. High-resolution transmission electron microscopy: the ultimate nanoanalytical technique. *Chemical Communications* 1253-1267 (2004).
36. Midgley, P. A., et al. High-resolution scanning transmission electron tomography and elemental analysis of zeptogram quantities of heterogeneous catalyst. *J Phys Chem B* **108**, 4590-4592 (2004).
37. Yates, T. J. V., et al. Three-dimensional real-space crystallography of MCM-48 mesoporous silica revealed by scanning transmission electron tomography. *Chemical Physics Letters* **418**, 540-543 (2006).
38. Weyland, M., Yates, T., Dunin-Borkowski, R., Laffont, L. & Midgley, P. Nanoscale analysis of three-dimensional structures by electron tomography. *Scr.Mater.* **55**, 29-33 (2006).

39. Tian, B., et al. Facile Synthesis and Characterization of Novel Mesoporous and Mesorelief Oxides with Gyroidal Structures. *J. Am. Chem. Soc.* **126**, 865-875 (2004).
40. Möbus, G., Doole, R. C. & Inkson, B. J. Spectroscopic electron tomography. *Ultramicroscopy* **96**, 433-451 (2003).
41. Weyland, M. & Midgley, P. A. Extending Energy-Filtered Transmission Electron Microscopy (EFTEM) into Three Dimensions Using Electron Tomography. *Microscopy and Microanalysis* **9**, 542-555 (2003).
42. Leapman, R. D., Kocsis, E., Zhang, G., Talbot, T. L. & Laquerriere, P. Three-dimensional distributions of elements in biological samples by energy-filtered electron tomography. *Ultramicroscopy* **100**, 115-125 (2004).
43. Bosman, M., Watanabe, M., Alexander, D. T. L. & Keast, V. J. Mapping chemical and bonding information using multivariate analysis of electron energy-loss spectrum images. *Ultramicroscopy* **106**, 1024-1032 (2006).
44. Yamazaki, T., Kotaka, Y. & Kataoka, Y. Analysis of EEL spectrum of low-loss region using the Cs-corrected STEM-EELS method and multivariate analysis. *Ultramicroscopy* **111**, 303-308 (2011).
45. Jarausch, K., Thomas, P., Leonard, D. N., Twesten, R. & Booth, C. R. Four-dimensional STEM-EELS: Enabling nano-scale chemical tomography. *Ultramicroscopy* **109**, 326-337 (2009).
46. Möbus, G. & Inkson, B. J. Three-dimensional reconstruction of buried nanoparticles by element-sensitive tomography based on inelastically scattered electrons. *Appl.Phys.Lett.* **79**, 1369-1371 (2001).
47. Midgley, P. A. & Weyland, M. 3D electron microscopy in the physical sciences: the development of Z-contrast and EFTEM tomography. *Ultramicroscopy* **96**, 413-431 (2003).
48. Arslan, I., Yates, T. J. V., Browning, N. D. & Midgley, P. A. Embedded Nanostructures Revealed in Three Dimensions. *Science* **309**, 2195-2198 (2005).
49. Trebbia, P. & Bonnet, N. EELS Elemental Mapping with Unconventional Methods .1. Theoretical Basis - Image-Analysis with Multivariate-Statistics and Entropy Concepts. *Ultramicroscopy* **34**, 165-178 (1990).
50. Jourlin, M., Pinoli, J. C. & Zeboudj, R. Contrast Definition and Contour-Detection for Logarithmic Images. *Journal of Microscopy-Oxford* **156**, 33-40 (1989).
51. Shannon, C. E. A Mathematical Theory of Communication. *Bell System Technical Journal* **27**, 379-423 (1948).
52. Shannon, C. E. A Mathematical Theory of Communication. *Bell System Technical Journal* **27**, 623-656 (1948).
53. de la Peña, F., et al. Mapping titanium and tin oxide phases using EELS: An application of independent component analysis. *Ultramicroscopy* **111**, 169-176 (2011).

54. Arenal, R., et al. Extending the analysis of EELS spectrum-imaging data, from elemental to bond mapping in complex nanostructures. *Ultramicroscopy* **109**, 32-38 (2008).
55. Cochran, R. N. & Horne, F. H. Statistically weighted principal component analysis of rapid scanning wavelength kinetics experiments. *Anal.Chem.* **49**, 846-853 (1977).
56. Egerton R. F. *Electron Energy-Loss Spectroscopy in the Electron Microscope* (Springer, New York, 2011).
57. Hawkes, P. W. The Electron Microscope as a Structure Projector. 83-111 (2006).
58. Comon, P. Independent Component Analysis, a New Concept. *Signal Process* **36**, 287-314 (1994).
59. Bonnet, N. & Nuzillard, D. Independent component analysis: A new possibility for analysing series of electron energy loss spectra. *Ultramicroscopy* **102**, 327-337 (2005).
60. Bach, F. R. & Jordan, M. I. Kernel independent component analysis. *Journal of Machine Learning Research* **3**, 1-48 (2003).
61. Kremer, J. R., Mastrorarde, D. N. & McIntosh, J. R. Computer visualization of three-dimensional image data using IMOD. *J.Struct.Biol.* **116**, 71-76 (1996).
62. Yedra, L., et al. EEL spectroscopic tomography: Towards a new dimension in nanomaterials analysis. *Ultramicroscopy* **122**, 12-18 (2012).



***5. EELS Spectrum  
Volumes***



<b>5.1. Antecedents of the spectrum volume .....</b>	<b>215</b>
<b>5.2. Materials: multiferroic nanocomposites.....</b>	<b>217</b>
<b>5.3. Sample preparation and data acquisition .....</b>	<b>219</b>
<b>5.4. EELS-SI tomography reconstruction from edge intensity maps .....</b>	<b>222</b>
<b>5.5. EELS-SI tomography from independent components .....</b>	<b>226</b>
5.5.1. Bayesian Linear Unmixing.....	227
5.5.2. 3D reconstruction from BSS components.....	228
<b>5.6. Recovering the Spectrum Volume .....</b>	<b>230</b>
<b>5.7. Conclusions .....</b>	<b>233</b>
<b>5.8. References .....</b>	<b>234</b>



## 5.1. Antecedents of the spectrum volume

As explained in previous chapters, in transmission electron microscopy (TEM), 3D tomographic reconstruction can be achieved by acquiring a series of images at different tilt angles. A different approach is obtaining 3D chemical reconstructions from energy filtered images in the TEM (EFTEM)<sup>1-3</sup>, and more recently, by acquiring EELS spectrum images (EELS-SI), each pixel containing a complete EELS spectrum<sup>4-5</sup>, as developed in chapter 4. However, in both techniques only a limited amount of information is effectively reconstructed. In this chapter we aim to derive a full EELS dataset in 4D, where every voxel of a whole volume contains a complete spectrum of energy losses, as schematized in Figure 5.1. By analogy to the spectrum image notation<sup>6</sup>, we will name this 4D dataset the EELS spectrum volume (EELS-SV).

G. Möbus et al.<sup>1</sup> suggested that the EELS-SV could be recovered by acquiring several tomography sets of EFTEM images, each set consisting in a tilted series of images filtered for a specific energy, in a single tomography experiment. Then, a tomographic reconstruction would be required for each energy-filtered tilted series. This has already been applied for a few energy slices<sup>7</sup> but to recover a large region of the spectrum would require an enormous amount of EFTEM images for every tilt angle. Typically, EELS spectra have a number of pixels around 1024 or 2048, which gives an idea of the magnitude of the number of EFTEM images required.

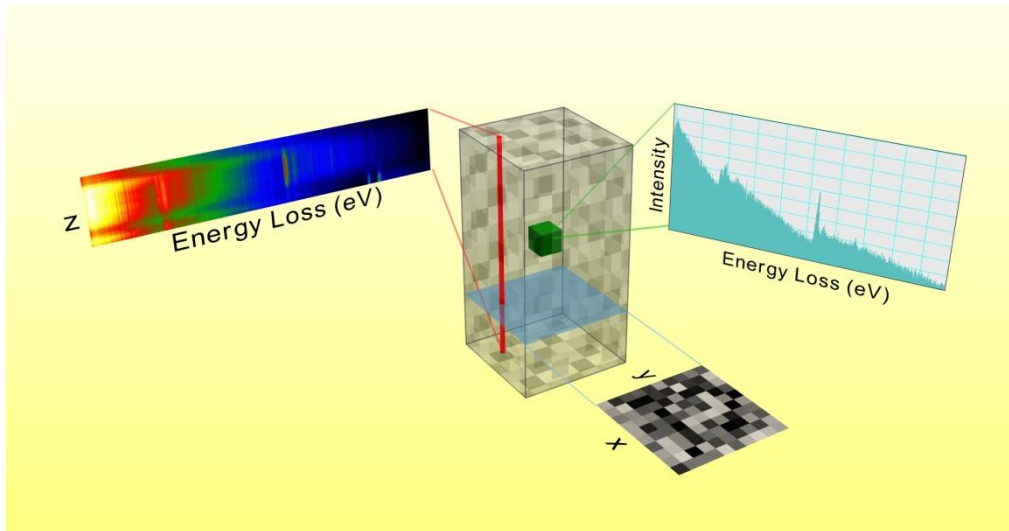


**Figure 5.1:** Schematic of the 4D dataset, the EELS spectrum volume, consisting of 3 spatial dimensions plus an additional energy loss dimension. Here it is presented along with an extracted  $xy$  spectrum image, a spectrum line along  $z$  direction and a single spectrum from an inner voxel.

Our approach to EELS-SV reconstruction is based upon SI, thus acquiring a single SI for every tilt angle. It takes advantage of Multivariate Analysis (MVA), and more precisely of blind source separation (BSS)<sup>8</sup>, to find a new spectral basis which can describe all the spectra in the dataset as a weighted sum of its components. Therefore only the 3D reconstructions of the weighting components will be necessary to recover the spectra in each voxel.

## 5.2. Materials: multiferroic nanocomposites

In the present chapter we consider FM  $\text{CoFe}_2\text{O}_4$  (CFO) nanocolumns embedded in a FE  $\text{BiFeO}_3$  (BFO) matrix grown on  $\text{LaNiO}_3$  buffered  $\text{LaAlO}_3$  substrate (BFO-CFO//LNO/LAO)<sup>9</sup>. This system, thoroughly studied<sup>10</sup>, is a prototypical multiferroic vertical nanostructure, which normally consist in a FM spinel phase epitaxially embedded in a FE matrix. It is a self assembled structure, due to the immiscibility of the two components. Studies in the past have shown the possibility of tailoring the properties of these materials by changing the substrate material, substrate orientation, ferroic phases, phase ratio, and film thickness<sup>10-22</sup>

Magnetoelectric (ME) multiferroics, as bulk single phase materials, first raised interest in the early sixties<sup>23, 24</sup>, but their scarcity and weak or far too low temperature response caused research to languish. However, significant progress in multiferroic oxide thin films and the appearance of epitaxial composite thin films, where two phases with different ferroic properties are grown at once, have triggered a renewed and now huge interest in these functional materials. In particular, the composite thin films are robust multiferroic systems at room temperature yielding high magnetoelectric coefficients due to elastic coupling between the ferroelectric (FE) and ferri/ferromagnetic (FM) phases<sup>25-27</sup>.

The final functional properties of the nanocomposite being sensitive to the local composition, EELS can be much enlightening. Chemical maps with very high spatial resolution can be obtained through EELS. Yet the aforementioned characterization is often carried out in a 2D projection. The electron beam passes through the thin sample and thus, the data in the EELS spectra is derived from the whole sample thickness, giving rise to overlapping information. This would be particularly unfortunate in the present case: an intrinsically 3D nanostructure which requires a 3D chemical characterization.

Nanocomposites with thickness around 100 nm were deposited at a rate of 0.9 Å/s on LAO(001), LNO/ LAO(001), and STO(001) at 625 °C substrate temperature by pulsed laser deposition (KrF excimer laser, 5 Hz repetition rate) using a Bi<sub>1.1</sub>FeO<sub>3</sub>CoFe<sub>2</sub>O<sub>4</sub> target with molar ratio of 65:35. The LNO buffers, around 10 nm thick, were deposited at 600 °C under an oxygen pressure of 0.1 mbar.

The samples were kindly provided by Prof. Josep Fontcuberta, Dr. Florencio Sánchez and Dr. Nico Dix from the Institut de Ciència dels Materials de Barcelona (ICMAB-CSIC).

The studies were carried out in the JEOL JEM 2010F (200kV) with a Gatan GIF EEL spectrometer, at the Scientific and Technical Centers of the University of Barcelona (CCiT-UB). Sample preparation was carried out in a FEI Strata 235 dual beam system. The sample was attached to the usual Omniprobe grid, only shortened at both ends to fit it in the Fischione 2030 ultra narrow gap tomography holder.

## 5.3. Sample preparation and data acquisition

The sample was prepared in a nanoneedle shape by Focused Ion Beam (FIB) in a FEI Strata 235 Dual Beam System (see appendix A.1.2 for more details). The nanoneedle was attached to the usual Omniprobe grid, only shortened at both ends to keep the maximum dimension below 1.5 mm in order to fit to a special sample holder (Fishione 2030 ultra-narrow gap tomography holder). The structure of the material can be observed in Figure 5.2 (a) and (b), as well as the resulting needle attached to the Omniprobe grid in a SEM image (c).

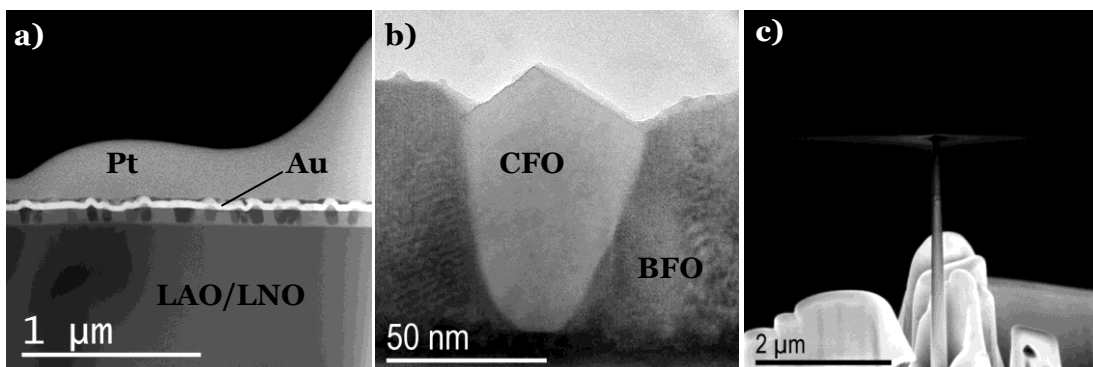


**Figure 5.2:** Sample preparation. **a)** HAADF STEM image of the multiferroic nanocomposite, where the CFO columns can be observed, covered with gold and platinum from the FIB. **b)** CFO nanocolumn in BFO and **c)** SEM image of the needle shaped sample prepared in the FIB

In order to test the suitability of the sample for EELS-SV reconstruction, a preliminary EELS-SI tomography experiment was carried out in a small area of the sample. The tilt series of the first experiment ranged from  $-65.7^\circ$  to  $61.8^\circ$ , at tilt steps of  $3^\circ$ . For each tilt step a spectrum image (SI) and a HAADF image were acquired, ending up with 44 SI consisting of  $14 \times 27$  single spectra each and 2.8 nm per pixel. Every 14

spectra (one row of the SI), sample drift was corrected using cross correlation in a HAADF survey image and exposure time was 1 second per spectrum. Figure 5.3 shows a HAADF survey image used for drift correction (a), a coacquired HAADF signal (b) and the reconstructed volume from the coacquired HAADF signal (c).

The coacquired HAADF signal was used to measure spatial drift between images and to correct for tilt axis. Moreover, as HAADF is the most used signal in electron tomography, its reconstruction can be used as a sanity check. Survey images, which are also HAADF images, but with a better spatial resolution and containing a larger area of the nanoneedle, were reconstructed as well.

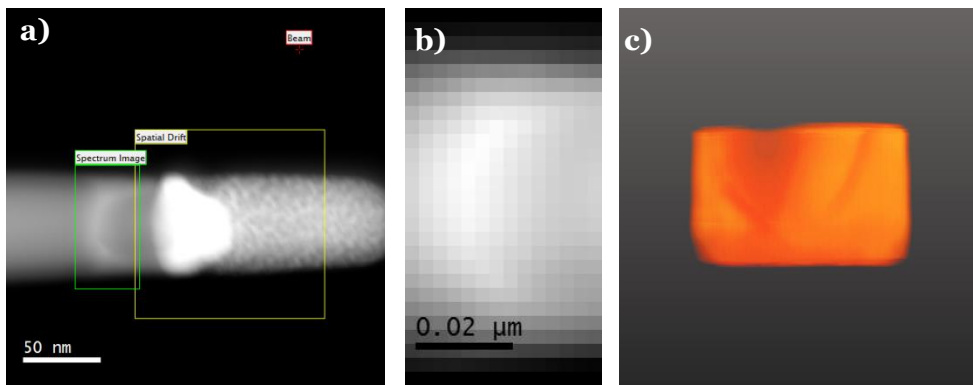


**Figure 5.3:** Areas of the nanoneedle used in the experiment. **a)** HAADF survey image used for drift correction, **b)** coacquired HAADF signal used for alignment of the images and **c)** volume reconstruction of the HAADF signal. The substrate is placed on the left, while the tip consists of the platinum deposited in the FIB.

Spectra were acquired from 424 to 936 eV, with 0.5 eV per channel for both experiments. In this range, O K edge (532 eV), Fe L<sub>2,3</sub> edge (708 eV) and La M<sub>4,5</sub> edge (832 eV) were clearly visible. Other expected edges on this range, such as Co L<sub>2,3</sub> (779 eV) and Ni L<sub>2,3</sub> (855 eV) were hardly visible. It can be explained by the lower concentration of these transition metals, the proximity to the tail of previous edges (as the sample is about 80 nm thick and thus the signal to background is reduced), low acquisition times, which lower the signal to noise ratio, and low brightness (intensity current) of the used TEM.

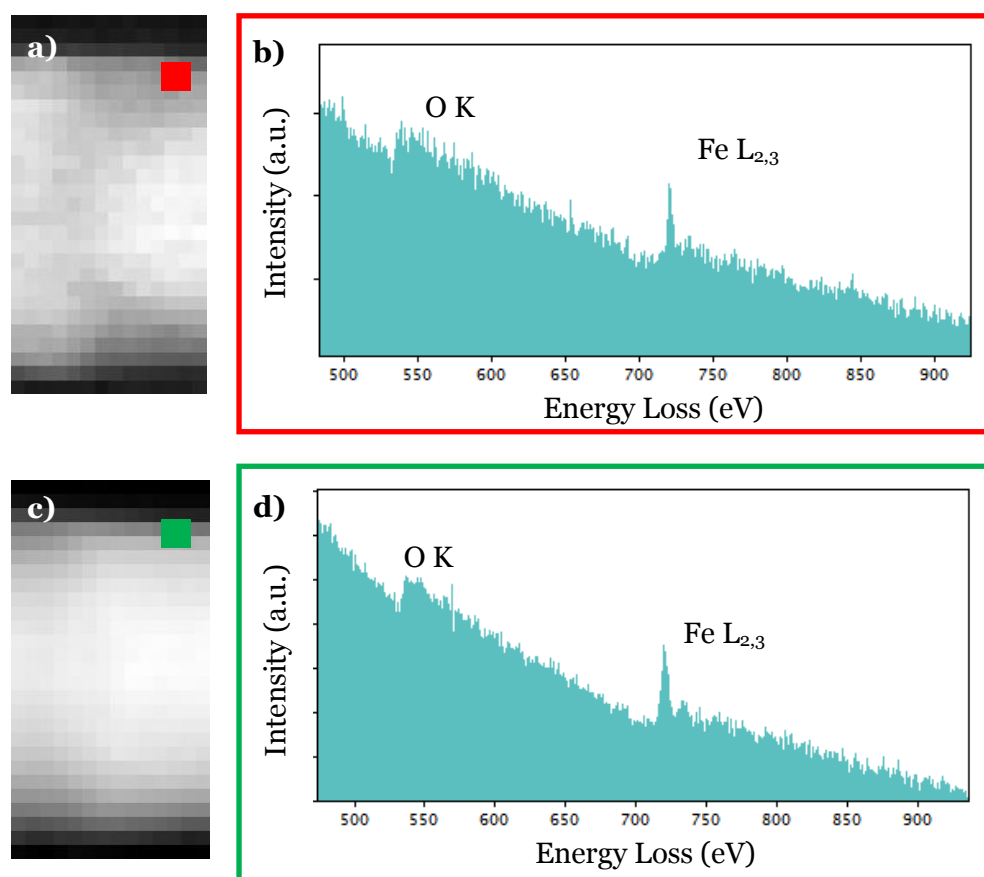


**Figure 5.4:** **a)** Spectrum image at  $-38.2^\circ$  tilt. **b)** Extracted spectrum from the highlighted area in (a). **c)** Spectrum image after PCA noise reduction and **d)** extracted spectrum from highlighted area in (c). There is a clear increase in signal to noise ratio in the data after PCA.

The spectra present a low signal to noise ratio, as observed in Figure 5.4 (b), which is due to the low acquisition times, so, in a first step, the noise level was reduced by taking advantage of Multivariate Analysis (MVA). Using Hyperspy, the energy drift of the data was corrected aligning the region around the O K edge, and the spikes present in the data set were removed. Afterwards, weighted principal component analysis (PCA)<sup>28</sup> was applied, assuming a dominant Poissonian noise in the weighting. As in previous experiments, by keeping only the higher variance components, the resulting data set is less noisy and better suited for further analysis. In Figure 5.4, in addition to an as acquired spectrum image in (a), along with a noisy single spectrum in (b), at  $-38.2^\circ$  tilt, the spectrum after PCA denoising can be observed in (c), as well as the same single spectrum with reduced noise. The noise reduction was enough to allow for edge intensity extraction, which would have been otherwise very problematic.

## 5.4. EELS-SI tomography reconstruction from edge intensity maps

Edge intensities extraction method consisted in removing the background previous to each edge approximating it by an inverse power law and then integrating the area under the edges for 40 eV. The extracted edge intensities for O K, Fe L<sub>2,3</sub> and La M<sub>4,5</sub> were measured for each EELS-SI as shown in Figure 5.5 (a). The resulting maps for the three extracted elements can be seen in Figure 5.5 (b) for O, (c) for Fe and (d) for La, as well as a mix of the three maps (e) so that it is possible to observe that the oxygen is found all over the sample. Conversely, iron and lanthanum are well separated, as expected. The extracted maps were oversampled using a bipolar interpolation, so the alignment and reconstruction software could perform cross-correlations with better accuracy. IMOD was used in this experiment for spatial drift, as it was found to be more suitable for images obtained from EELS-SI when there is lack of details. Spatial drift was measured in HAADF coacquired signal and then applied to the core-loss signals to correct SI spatial position. SIRT algorithm<sup>29</sup> with 30 iterations was used for the reconstruction.

As explained in the previous chapters, the signal must change monotonically with a property of the object<sup>30</sup>, which is the so-called projection requirement. Recovering equation [3.29], if only a single scattering event takes place, the signal is proportional to the areal density of each element, which fulfils the projection requirement. Single scattering distribution of the signal is predominant where thickness is lower than the inelastic mean free path, which in our case is over 100 nm<sup>31</sup>. Adding the influence of the plasmon losses does not change the relationship from equation [3.29]. Plasmon losses cause the intensities of the edges to be shifted to higher energies. As long as a single plasmon excitation dominates valence scattering and that the integration window is big enough, the extracted signal continues to behave

monotonically. In our case, we will assume that in our range of thicknesses this term does not affect the monotonicity of the signal.

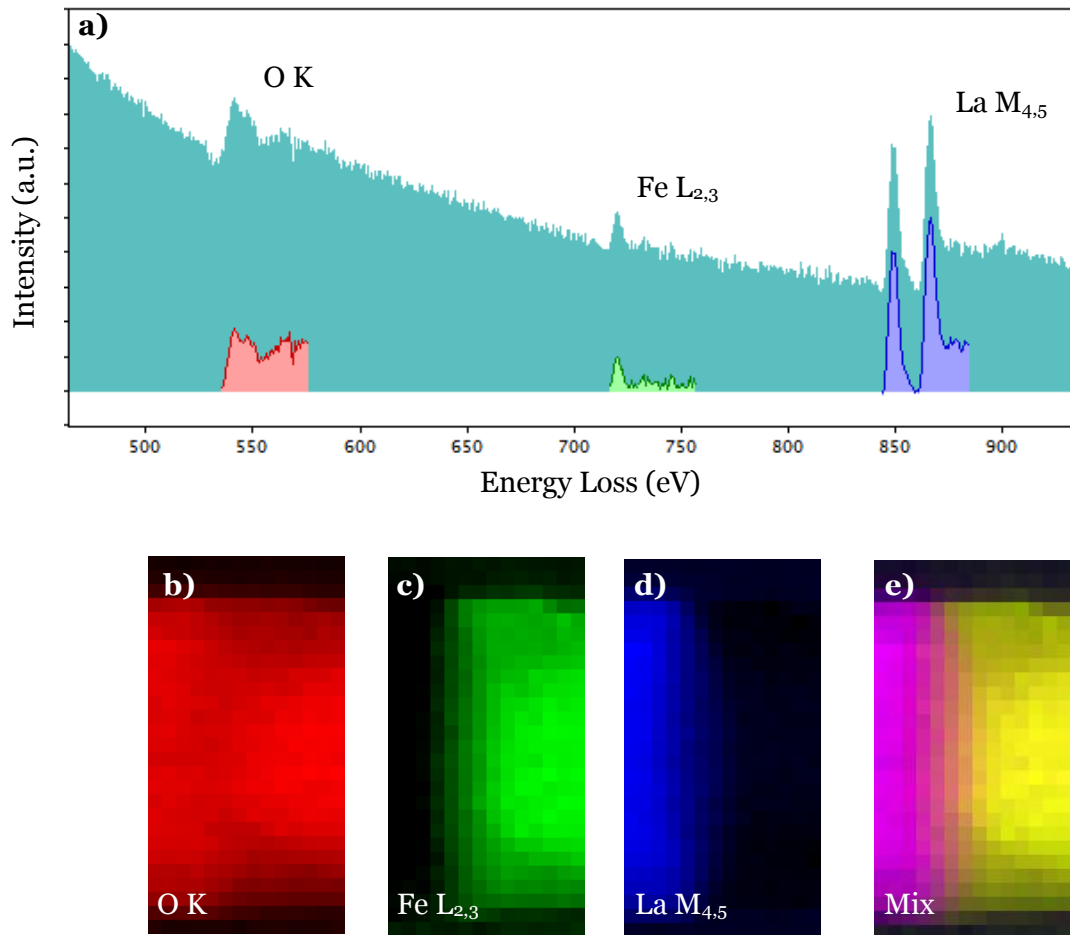


**Figure 5.5:** Extraction of edge intensities in the preliminary experiment. **a)** Single spectrum from a SI after PCA treatment at  $-38.2^\circ$ . The shaded areas represent the integrated area of the edges after background subtraction for oxygen (in red), iron (in green) and lanthanum (in blue). Maps of extracted edge intensities for **b)** O K, **c)** Fe  $L_{2,3}$  and **d)** La  $M_{4,5}$  are shown combined in **e)**.

Some other effects can make the signal fail to fulfill the projection requirement, such as diffraction contrast, which lowers the overall intensity of the spectra. In our dataset, the measured total intensity of the SI did not change substantially over the tilting process; thus, the influence of diffraction contrast is regarded as being of no importance. In summary we can consider that the edge intensity changes monotonically with thickness and with the density of each element in our sample

We can observe how the signal behaves in Figure 5.6, which displays original edge intensity maps from the projection at  $-38.2^\circ$  (a, d, g), orthoslices through the reconstructed volume (b, e, h) and a direct visualization of the reconstructed volume (e, f, i) for oxygen, iron and lanthanum, respectively. The intensities observed in Figure 5.6 can be interpreted as follows: the two higher intensities in the oxygen maps correspond to CFO and LAO/LNO, with densities of 54 atoms/nm<sup>3</sup> and 55 atoms/nm<sup>3</sup> respectively. BFO has an oxygen density of 48 atoms/nm<sup>3</sup> and therefore appears darker. The same reasoning applies to iron, with a concentration of 27 atoms/nm<sup>3</sup> in CFO and 16 atoms/nm<sup>3</sup> in BFO. Thanks to these differences in concentration the three expected regions (LAO/LNO, BFO and CFO) could be separated in EELS maps and the subsequent segmentation of the areas of interest render the volumes presented in Figure 5.7 (see movie 12 in the supporting files for the animated results).

The faceting in the results is consistent with the HRTEM characterization carried elsewhere<sup>9</sup>.

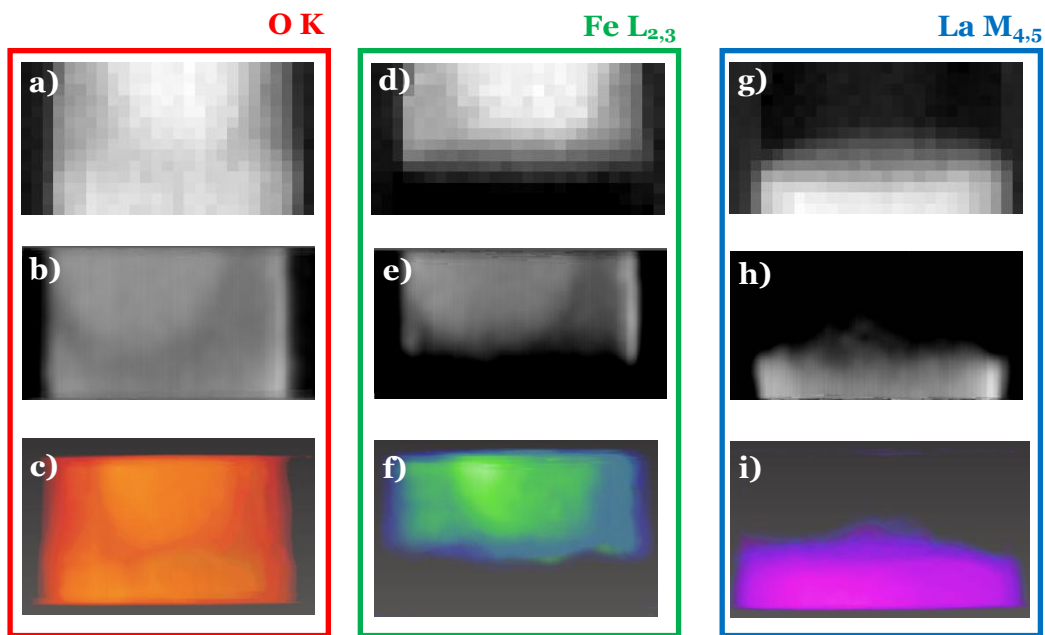


**Figure 5.6:** Original images and reconstructions in the preliminary experiment. **a)** Integrated O K signal for the image at  $-38.2^\circ$ , **b)** orthoslice through the O reconstructed volume and **c)** vortex visualization of the reconstructed O volume. **d)** Integrated Fe  $L_{2,3}$  signal for the same image, **e)** orthoslice through the reconstructed Fe volume and **f)** vortex visualization of the reconstructed Fe volume. **g)** Integrated La  $M_{4,5}$  signal, **h)** orthoslice through the reconstructed La volume and **i)** vortex visualization of the reconstructed La volume. Oxygen is found all over the sampled area, lanthanum is found at the bottom layer and iron at the top layer, where the BFO/CFO nanocomposite is.

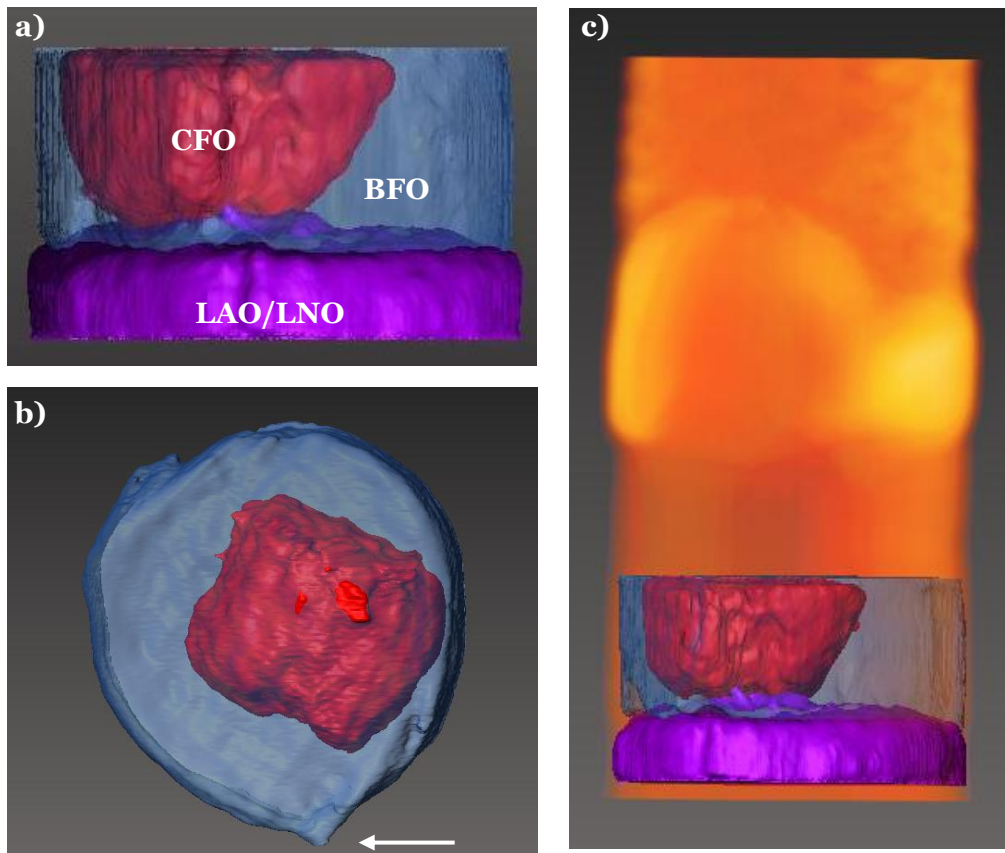


**Figure 5.7:** Visualization of the reconstruction in the preliminary EELS-SI tomography experiment. **a)** Direct visualization of the reconstructed and segmented volume. In purple, the LAO/LNO substrate, in blue, the iron and, in red, the CFO nanocolumn **b)** Axial view where the square section of the nanocolumn is observed (the bottom right side marked with the arrow is distorted due to the proximity to the limits of the reconstructed volume). **c)** Position of the area reconstructed from EELS signal with respect to the tip of the nanoneedle reconstructed from the HAADF survey image.

## 5.5. EELS-SI tomography from independent components

As the sample stability was confirmed (despite the long duration of the experiment to acquire the whole tilt series of EELS-SI) and the EELS signal was proven adequate for tomographic reconstruction of the sample, a second tomographic acquisition was carried out in a wider region of the nanoneedle as shown in Figure 5.8 (a-c).

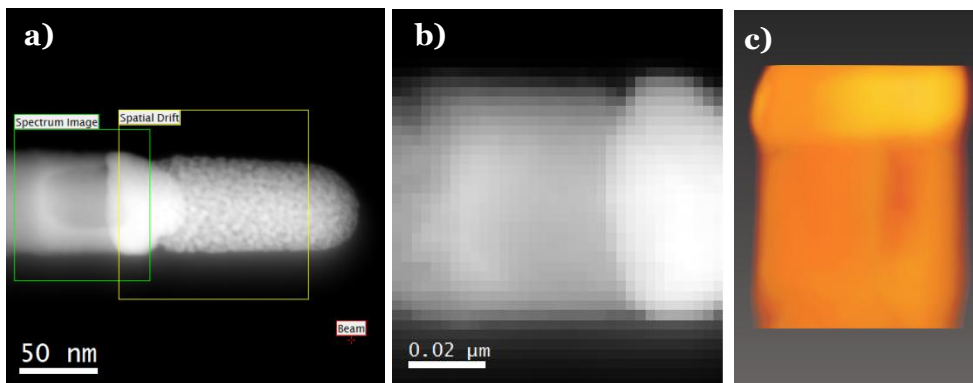


**Figure 5.8:** Areas of the nanoneedle used in the experiment. **a)** HAADF survey image used for drift correction, **b)** coacquired HAADF signal used for alignment of the images and **c)** volume reconstruction of the HAADF signal. The substrate is placed on the left, while the tip consists of platinum deposited in the FIB.

The second experiment ranged from  $-64^{\circ}.4$  to  $70^{\circ}$ , at tilt steps of  $2^{\circ}$ . The resulting data consisted of 67 SI and HAADF images of  $33 \times 39$  pixels with a resolution of 2.5 nm per pixel. In this second experiment, measure times were reduced to 0.8 seconds and sample drift was also corrected once per row. Lower acquisition times were preferred in this second experiment, as the amount of spectra to acquire was

extremely high and sample damage had to be prevented. However, further decreasing the acquisition times was found to be detrimental because the signal could not be properly separated from the noise in the subsequent multivariate statistical analysis.

### 5.5.1. Bayesian Linear Unmixing

Among the blind source separation algorithms, in this problem we chose to use the Bayesian linear unmixing (BLU) algorithm proposed by N. Dobigeon in 2009<sup>8</sup>. Spectral unmixing consists in decomposing a pixel spectrum into a collection of material spectra or endmembers, and estimating the corresponding proportions or abundances. Assuming a linear mixing model, the estimation of the unknown endmember spectra is carried out by generating a posterior distribution of abundances and endmember parameters under a hierarchical Bayesian model.

If we recover equation [4.24], the spectral unmixing problem can be described as the decomposition of the results matrix  $\mathbf{X}$  into a product matrix  $\mathbf{SA}$ , where each column in  $\mathbf{S}$  is a spectral signature or endmember and each column in  $\mathbf{A}$  is the spatial amplitude of each endmember in a pixel. To reduce the number of possible solutions, additional constraints to  $\mathbf{A}$  and  $\mathbf{S}$ , are introduced. First, all the elements in both matrices are assumed positive, and, as the columns in  $\mathbf{A}$  represent proportions, their sum is constrained to one. The constrained matrix factorization, from a geometrical point of view, consists in identifying the vertices of a lower dimensional simplex formed by the observed data.

In the BLU, the simplex of the data set is identified using PCA, while the endmembers can be identified using the N-FINDR algorithm<sup>32</sup>, which includes the positivity and sum-to-one constraints. The outputs of N-FINDR are the prior distributions of endmembers  $p(\mathbf{S})$  and abundances  $p(\mathbf{A})$ . Based on these prior models and the assumption of Gaussian likelihood  $p(\mathbf{X}|\mathbf{S}, \mathbf{A})$ , the joint posterior distribution  $p(\mathbf{S}, \mathbf{A}|\mathbf{X})$  is computed using a Bayes paradigm. As the posterior distribution is too complex to derive in closed-form expressions, BLU contains a Markov chain Monte Carlo algorithm which generates samples  $\mathbf{A}^{(t)}$  and  $\mathbf{S}^{(t)}$   $t = (1, \dots, n)$  asymptotically

distributed according to the posterior of interest. The endmember matrix  $\mathbf{S}$  and the abundance matrix  $\mathbf{A}$  are approximated using the  $n$  generated samples.

The full description of the algorithm can be found in<sup>8</sup>.

### 5.5.2. 3D reconstruction from BSS components

For this second EELS-SI dataset comprising the whole multiferroic structure, the aim of data treatment was the reduction of the dataset to independent components. PCA followed by blind source separation (BSS) was performed using the Bayesian Linear Unmixing software by N. Dobigeon<sup>8</sup>. As explained in<sup>32</sup>, we limited the number of separated components to 4, chose the NFINDR geometrical algorithm for generating the prior estimations and let a maximum number of unmixing iterations of 50.

The main three independent components of the dataset, assigned to background contribution, iron oxide and lanthanum oxide, respectively, are shown in Figure 5.9 (a). If we assume that each spectrum image is a weighted sum of these three independent components, each EELS-SI can be decomposed in three images (Figure 5.9 (b)) corresponding to the weighting of the three independent components. In this way, the whole EELS SI dataset was transformed into three new datasets suitable for tomographic reconstruction algorithms. The results of these reconstructions are shown in Figure 5.9 (c) for the three components as labeled in Figure 5.9 (a), together with their superposition, which clearly corresponds to the whole volume in Figure 5.3 (f) (see movie 13 in the supporting files for the animated results). A fourth component representing the noise in the vacuum was also retained for calculations, but its contribution is not presented in the reconstructions.

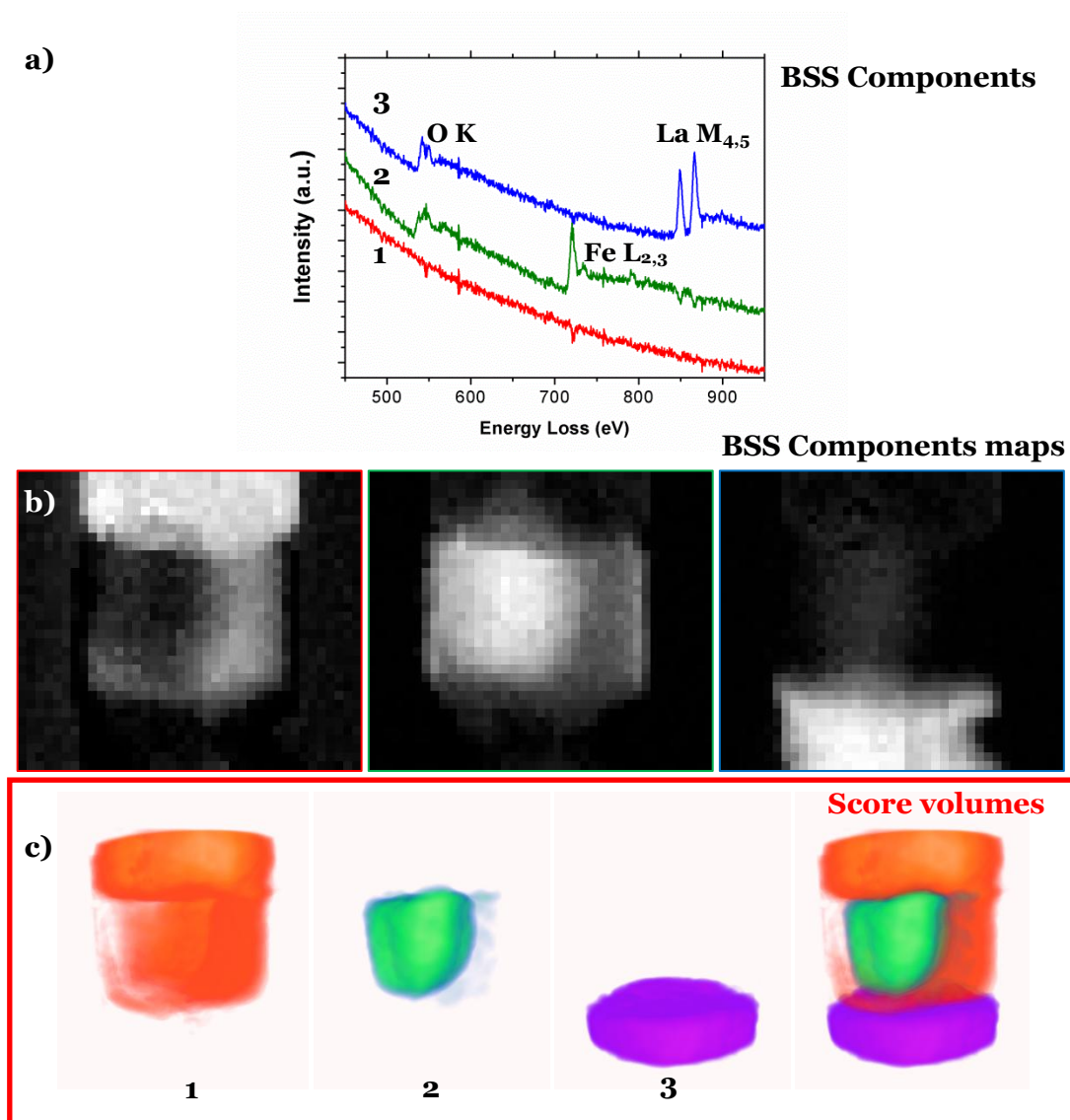


**Figure 5.9:** EELS-SV reconstruction procedure. **a)** Components of the spectrum according to BSS numbered as 1 – Thickness, 2 – Fe oxide and 3 – La oxide. **b)** BSS components score images at  $0^\circ$  tilt angle. **c)** 3D reconstructions of the 3 components extracted from Blind Source Separation (BSS), corresponding to the 3D score matrixes of the components, plus an overlapped image of the three.

## 5.6. Recovering the Spectrum Volume

The recovery of a full EELS-SV starts from the initial BSS problem, which can be expressed as

$$\mathbf{D}_{(x,y,E),\theta} = \sum_{i=1}^k \mathbf{A}_{(x,y),i,\theta} \mathbf{S}_{E,i}^T \quad , \quad [5.1]$$

where  $\mathbf{D}_{(x,y,E),\theta}$  is the dataset, formed by the SI( $x, y, E$ ) acquired at the different tilt angles  $\theta$ . The dataset can be expressed after BSS as the weighted sum of  $k$  eigenspectra (endmembers).  $\mathbf{S}_{E,i}^T$  is the  $i$ th eigenspectrum, which relative intensity for each tilt  $\theta$  is given by the abundance matrix  $\mathbf{A}_{(x,y),i,\theta}$  corresponding to the 2D component maps . The problem can be reformulated as:

$$\mathbf{D}_{x,y,z,E} = \sum_{i=1}^k \mathbf{A}_{(x,y,z),i} \mathbf{S}_{E,i}^T \quad , \quad [5.2]$$

by reconstructing the 3D abundances from 2D abundances.

At this point, the EELS-SV is already available, as the spectrum in each voxel can be calculated as a linear combination of three components. We can retrieve an EELS-SI in any section of the EELS-SV. From the SV of 32x32x36 spectra schematically reconstructed in in Figure 5.10 (a), the transversal orthoslice shows the plane  $z=16$  (Figure 5.10 (b)), with a single spectrum extracted at the (15,12,16) voxel in Figure 5.10 (d). A spectrum line along the red arrow in the transversal orthoslice  $y=16$  (Figure 5.10 (c)) is shown in Figure 5.10 (e) with its background subtracted by a power law.

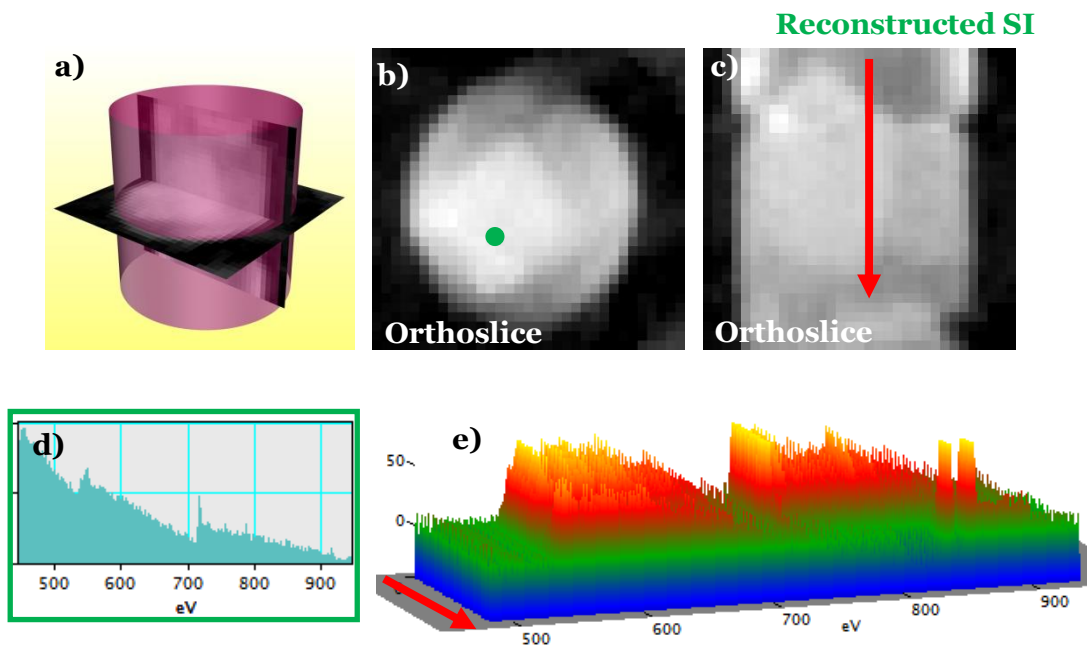


**Figure 5.10:** *a)* Schematic representation of two orthoslices. *b)* reconstructed SI for a transversal orthoslice ( $z=16$ ) and *c)* longitudinal orthoslice ( $y=16$ ). *d)* Single spectrum extracted from the transversal orthoslice (green spot) and *e)* spectrum line along the red arrow in the longitudinal orthoslice reconstructed SI, with its background subtracted by a power law before the O K edge.

To prove the validity of the spectrum volume calculations, we compare the results with the best reference that we have: the original EELS-SI. As the EELS-SI are projections of the sample, we calculate a new projection of the EELS-SV. This is done by integrating along the thickness of the EELS-SV, and, more simply, by projecting the 3D weighting maps of the BSS components and then recovering the EELS-SI using the projections as weighting. In Figure 5.11, elemental maps of edge intensities for O, Fe and La extracted according to Figure 5.5 from the original SI corresponding to a  $0^\circ$  tilt in (a). Then, in (b), the equivalent extracted intensities are obtained from the SI reduced to the BSS components (by combining (a) and (b) in Figure 5.9). Finally, in Figure 5.11 (c), the edge intensities extracted from the new projection of the EELS-SV.

The distribution of the elements (O, Fe and La) and the shape of the CFO nanocolumn remain unaltered when reconstructed after the MVA analysis, as well as the new EELS-SI from the projection of the reconstructed dataset compared to the original one. The small differences, observed in the border of the CFO nanocolumn, can be attributed to the alignment and reconstruction process, which results in a slight delocalization of the signals.

Regarding thickness related problems, the importance of nanoneedle-shaped preparation<sup>33,34</sup> through FIB is to be stressed, as the thickness of the sample was kept roughly constant throughout the experiment, therefore avoiding the signal drop at high angle expected in a conventional lamella preparation due to an increase in effective thickness as a consequence of the tilt angle. The intensity drop would have affected the monotonicity of the signals related to thickness, invalidating the reconstruction process. On the other hand, it must be noted that the spectrum calculated for each voxel contains information about the whole thickness of the sample, as it is reflected in the BSS components. However, we have proven that the elemental information is not compromised.

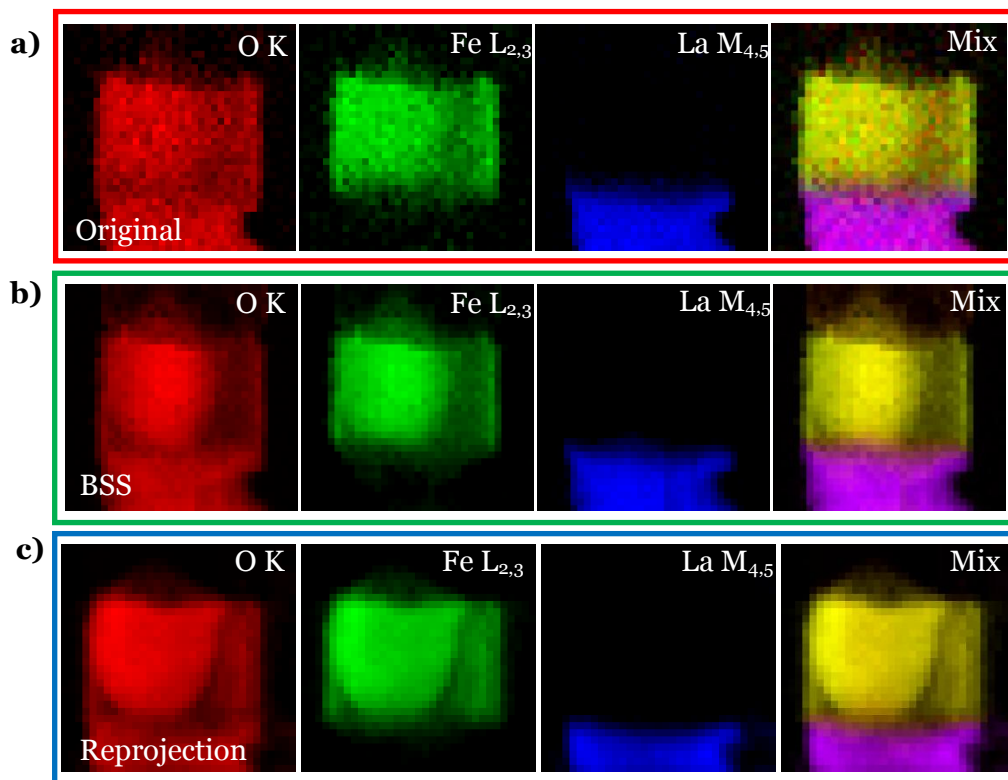


**Figure 5.11:** Comparison of the extracted edge intensities between **a)** the original projection at  $0^\circ$  tilt angle, **b)** the spectrum image at  $0^\circ$  built from the BSS components and **c)** the spectrum image built from projections of the EELS-spectrum volume (in all the images it can be observed that the gold deposited on the tip of the needle for FIB preparation masked the EELS signal at the top of the CFO nanocolumn).

## 5.7. Conclusions

In summary, EELS SI tomography has been shown capable of reconstructing the three dimensional structure of a nanocomposite sample as in conventional STEM-HAADF tomography, but adding a fourth dimension corresponding to chemical composition in a quantitative approach. In this case, CFO columns were properly reconstructed in a BFO matrix grown on a LNO/LAO substrate. Moreover, the feasibility of reconstructing EELS spectrum volumes (EELS-SV) such as those in Figure 5.1 has been shown and applied to extract single spectra from the inside of the nanocomposite sample, a step beyond EELS-SI tomography and more accurate if compared to conventional SI, which integrates information all along the thickness of the sample. This approach could be extended to other spectroscopies.

The present work proves the great potential of EELS tomography for the characterization of nanostructured materials, especially if we take into account that the results shown here were not acquired using an ultrafast reading spectrometer, neither an aberration-corrected TEM.

## 5.8. References

1. Möbus, G., Doole, R. C. & Inkson, B. J. Spectroscopic electron tomography. *Ultramicroscopy* **96**, 433-451 (2003).
2. Weyland, M. & Midgley, P. A. Extending Energy-Filtered Transmission Electron Microscopy (EFTEM) into Three Dimensions Using Electron Tomography. *Microscopy and Microanalysis* **9**, 542-555 (2003).
3. Leapman, R. D., Kocsis, E., Zhang, G., Talbot, T. L. & Laquerriere, P. Three-dimensional distributions of elements in biological samples by energy-filtered electron tomography. *Ultramicroscopy* **100**, 115-125 (2004).
4. Jarausch, K., Thomas, P., Leonard, D. N., Twesten, R. & Booth, C. R. Four-dimensional STEM-EELS: Enabling nano-scale chemical tomography. *Ultramicroscopy* **109**, 326-337 (2009).
5. Yedra, L., et al. EEL spectroscopic tomography: Towards a new dimension in nanomaterials analysis. *Ultramicroscopy* **122**, 12-18 (2012).
6. Jeanguillaume, C., Trebbia, P. & Colliex, C. About use of Electron Energy-Loss Spectroscopy for Chemical Mapping of Thin Foils with High Spatial-Resolution. *Ultramicroscopy* **3**, 237-242 (1978).
7. Gass, M. H., Koziol, K. K. K., Windle, A. H. & Midgley, P. A. Four-Dimensional Spectral Tomography of Carbonaceous Nanocomposites. *Nano Letters* **6**, 376-379 (2006).
8. Dobigeon, N., Moussaoui, S., Coulon, M., Tourneret, J. & Hero, A. O. Joint Bayesian Endmember Extraction and Linear Unmixing for Hyperspectral Imagery. *Ieee Transactions on Signal Processing* **57**, 4355-4368 (2009).
9. Dix, N., et al. Selectable Spontaneous Polarization Direction and Magnetic Anisotropy in BiFeO<sub>3</sub>-CoFe<sub>2</sub>O<sub>4</sub> Epitaxial Nanostructures. *Acs Nano* **4**, 4955-4961 (2010).
10. Zheng, H., et al. Multiferroic BaTiO<sub>3</sub>-CoFe<sub>2</sub>O<sub>4</sub> nanostructures. *Science* **303**, 661-663 (2004).
11. Zheng, H., et al. Controlling self-assembled perovskite-spinel nanostructures. *Nano Lett.* **6**, 1401-1407 (2006).

12. Zheng, H., et al. Three-dimensional heteroepitaxy in self-assembled BaTiO<sub>3</sub>-CoFe<sub>2</sub>O<sub>4</sub> nanostructures. *Appl.Phys.Lett.* **85**, 2035-2037 (2004).
13. Zavaliche, F., et al. Electric field-induced magnetization switching in epitaxial columnar nanostructures. *Nano Letters* **5**, 1793-1796 (2005).
14. Zavaliche, F., et al. Electrically assisted magnetic recording in multiferroic nanostructures. *Nano Letters* **7**, 1586-1590 (2007).
15. Levin, I., Slutsker, J., Li, J., Tan, Z. & Roytburd, A. L. Accommodation of transformation strains in transverse multiferroic nanostructures CoFe<sub>2</sub>O<sub>4</sub> -PbTiO<sub>3</sub>. *Appl.Phys.Lett.* **91**, 062912 (2007).
16. Levin, I., Li, J., Slutsker, J. & Roytburd, A. L. Design of self-assembled multiferroic nanostructures in epitaxial films. *Adv Mater* **18**, 2044-2047 (2006).
17. Slutsker, J., Tan, Z., Roytburd, A. L. & Levin, I. Thermodynamic aspects of epitaxial self-assembly and magnetoelectric response in multiferroic nanostructures. *J.Mater.Res.* **22**, 2087-2095 (2007).
18. Zhan, Q., et al. Structure and interface chemistry of perovskite-spinel nanocomposite thin films. *Appl.Phys.Lett.* **89**, 172902 (2006).
19. Li, J., et al. Self-assembled multiferroic nanostructures in the CoFe<sub>2</sub>O<sub>4</sub> - PbTiO<sub>3</sub> system. *Appl.Phys.Lett.* **87**, 072909 (2005).
20. Ren, S., Briber, R. M. & Wuttig, M. Diblock copolymer based self-assembled nanomagnetoelectric. *Appl.Phys.Lett.* **93**, 173507 (2008).
21. Zhang, J. X., et al. A novel nanostructure and multiferroic properties in Pb(Zr<sub>0.52</sub>Ti<sub>0.48</sub>)O<sub>3</sub>/CoFe<sub>2</sub>O<sub>4</sub> nanocomposite films grown by pulsed-laser deposition. *J.Phys.D* **41**, 235405 (2008).
22. Bachelet, R., et al. Self-Assembly of SrTiO<sub>3</sub>(001) Chemical-Terminations: A Route for Oxide-Nanostructure Fabrication by Selective Growth. *Chem.Mat.* **21**, 2494-2498 (2009).
23. Folen, V. J., Rado, G. T. & Stalder, E. W. Anisotropy of Magnetoelectric Effect in Cr<sub>2</sub>O<sub>3</sub>. *Phys.Rev.Lett.* **6**, 607-608 (1961).
24. Rado, G. T. & Folen, V. J. Observation of Magnetically Induced Magnetoelectric Effect and Evidence for Antiferromagnetic Domains. *Phys.Rev.Lett.* **7**, 310-311 (1961).
25. Ramesh, R. & Spaldin, N. A. Multiferroics: progress and prospects in thin films. *Nature Materials* **6**, 21-29 (2007).
26. Nan, C., Bichurin, M. I., Dong, S., Viehland, D. & Srinivasan, G. Multiferroic magnetoelectric composites: Historical perspective, status, and future directions. *J.Appl.Phys.* **103**, 031101 (2008).
27. Yan, L., et al. Review of magnetoelectric perovskite-spinel self-assembled nano-composite thin films. *J.Mater.Sci.* **44**, 5080-5094 (2009).

28. Cochran, R. N. & Horne, F. H. Statistically weighted principal component analysis of rapid scanning wavelength kinetics experiments. *Anal.Chem.* **49**, 846-853 (1977).
29. Gilbert, P. Iterative methods for the three-dimensional reconstruction of an object from projections. *J.Theor.Biol.* **36**, 105-117 (1972).
30. Hawkes, P. W. The Electron Microscope as a Structure Projector. 83-111 (2006).
31. Egerton R. F. *Electron Energy-Loss Spectroscopy in the Electron Microscope* (Springer, New York, 2011).
32. Dobigeon, N. & Brun, N. Spectral mixture analysis of EELS spectrum-images. *Ultramicroscopy* **120**, 25-34 (2012).
33. Miller, M., Russell, K. & Thompson, G. Strategies for fabricating atom probe specimens with a dual beam FIB. *Ultramicroscopy* **102**, 287-298 (2005).
34. Goris, B., Bals, S., Van den Broek, W., Verbeeck, J. & Van Tendeloo, G. Exploring different inelastic projection mechanisms for electron tomography. *Ultramicroscopy* **111**, 1262-1267 (2011).

## ***6. Conclusions***



The main goal of this thesis is to combine electron tomography and electron energy loss spectroscopy (EELS) in the TEM, in order to obtain chemical and electronic information in 3D in the nanoscale.

Tomography in the TEM has been discussed and the advantages and disadvantages of HAADF STEM tomography have been analyzed.

- A  $\text{Fe}_3\text{O}_4$  nanocube sample has been considered to illustrate the acquisition, alignment, tilt axis assessment, reconstruction and visualization processes.
- HAADF STEM tomography has been used to reconstruct the shape of a series of  $\text{Cu}_2\text{O}$  nanoparticles. For one of the samples, the facets of the  $\text{Cu}_2\text{O}$  nanoparticles, octahedral in shape, have been found to correspond to  $\{111\}$  planes.
- In one of the samples, the octahedral sample could be correlated to the crystal structure of  $\text{Cu}_2\text{O}$  using electron diffraction. The facets of the octahedra corresponded to  $\{111\}$  planes.

The physics and the data analysis methods of core-loss EELS have been briefly summarized. Two relevant contributions have been made:

- The effects of beam precession on EELS have been investigated. A signal enhancement due to electron beam precession in the TEM when in zone axis conditions has been discovered for the first time.
  - It has been proposed that the fact that an effective two beam condition is kept while precessing the beam avoids channeling of the electrons when observing the sample in zone axis.
- A homemade software, Oxide Wizard, for valence state determination of transition metals has been developed.
  - The parameters for Mn oxidation state quantification have been calibrated using samples of known oxidation state through two parameter plots.
  - The software has been applied to map the Mn oxidation state of a  $\text{MnO}_x/\text{FeO}_y$  nanoparticle.
  - The  $\text{MnO}_x$  shell of the nanoparticles has been found to consist in a two-layer structure, with  $\text{Mn}^{2.66+}$  in the inner layer and  $\text{Mn}^{2+}$  closest to the surface.

EELS spectrum imaging and electron tomography have been combined to recover chemical information in 3D for  $\text{Fe}_x\text{Co}_{(3-x)}\text{O}_4@\text{Co}_3\text{O}_4$  mesoporous nanoparticles.

- The samples have been first characterized by HAADF STEM tomography and EELS.
  - Both techniques have shown a saturation in Fe intake for 2.4 Fe(III): $\text{Co}_3\text{O}_4$  molar ratio impregnation.
  - EELS chemical information is, of course, limited to 2D maps, while only structural information is recovered in 3D form HAADF tomography.
- An EELS-SI tilt series has been acquired at 80 kV and low acquisition times, resulting in a very noisy dataset.
  - Principal component analysis (PCA) has been used to separate the noise from the signal.
  - Extracted edge intensities show an inversion in the centre of the particle due to the thickness of the sample.
  - Quantifications of the O, Fe and Co signals have been reconstructed, and the shape of the particle recovered.
  - From the noise clean dataset, components with physical meaning (iron oxide, cobalt oxide and thickness) have been extracted using independent component analysis (ICA), and reconstructed in 3D.
  - Iron oxide and cobalt oxide independent components have also been found to fail the projection requirement in the centre of the particle. The thickness component has been properly reconstructed.
  - A new kind of signal with chemical and thickness information has been obtained by combining the thickness component with the quantification results. This signal is able to properly reconstruct the chemical structure of the sample in 3D, detecting a higher presence of iron in the surface, and an even distribution of Fe inside of the particle.
- Another EELS-SI tilt series has been acquired at 80 kV and low acquisition times with enough spatial resolution to resolve the porous structure.
  - The noise has been reduced using PCA.

- Four signals extracted from the spectrum have been reconstructed: the integrated edge intensities for oxygen, iron and cobalt, and the integrated background prior to the oxygen edge.
- The oxygen signal has been found to have the poorest spatial resolution, but the porous structure remains visible in the other three reconstructions. From these 3D reconstructions, it has been possible to observe that the iron signal covers the cobalt oxide structure in the pores.

EELS-SI tomography has been applied to reconstruct  $\text{CoFe}_2\text{O}_4$  (CFO) nanocolumns embedded in a  $\text{BiFeO}_3$  (BFO) matrix grown on  $\text{LaNiO}_3$  buffered  $\text{LaAlO}_3$  substrate (BFO-CFO//LNO/LAO).

- The nanocomposite sample has been prepared in a nanoneedle shape by means of focused ion beam (FIB). This preparation has the advantage of keeping the thickness of the sample constant throughout the tilting experiment. The nanoneedle contains an island of CFO in a matrix of BFO, as well as the LNO/LAO substrate.
- The noise has been discarded using PCA.
- The oxygen, iron and lanthanum edges intensities have been extracted and reconstructed.

A new kind of data hypercube, the Spectrum Volume, has been proposed. Just as a Spectrum Image contains a spectrum per pixel, a Spectrum Volume is to contain a spectrum per voxel.

EELS-SI tomography has been applied to successfully acquire a spectrum volume (SV) of the (BFO-CFO//LNO/LAO) system.

- PCA has been used to discard the noise and Bayesian linear unmixing (BLU) has been used to extract independent components (eigenspectra).
- Each eigenspectrum has a 2D weighting map for each tilt; weighting maps have been reconstructed into 3D weighting volumes.
- Full single spectra for any point in the reconstructed space can now be recovered as a weighed sum of eigenspectra, using the 3D weighting distributions. This approach is used to extract single spectra, spectrum lines and spectrum images from the inside of the sample.

- A projection of the EELS-SV at  $0^\circ$  tilt has been obtained and compared to the original dataset, showing a good agreement.

Thanks to the application of MVA, EELS data has been shown to yield several signals suitable for tomographic reconstruction. The validity of EELS intensities in terms of the projection requirement is assured as long as the thickness of the sample is kept below the mean free path of the incident electrons, as the integrated signals under the edges can be considered to increase monotonically with the thickness of the sample. When this condition is not met, relative quantification can still be considered for reconstruction. The possible loss of intensity at certain tilt angles when in a major zone axis condition has not been observed and its influence in the reconstruction can be considered of no importance when the number of images is high.

In the context of this thesis, tomography and EELS-SI have been combined to successfully recover chemical information in 3D at the nanoscale, and a new kind of data hypercube, the Spectrum Volume, has been proposed and experimentally recovered.

# *Appendixes*



<b>A.</b>	<b><i>Experimental</i></b> .....	<b>247</b>
<b>A.1.</b>	<b><i>Nanoparticles</i></b> .....	<b>247</b>
<b>A.2.</b>	<b><i>Focused Ion Beam</i></b> .....	<b>249</b>
<b>B.</b>	<b><i>Resum en català</i></b> .....	<b>253</b>
<b>C.</b>	<b><i>Scientific curriculum</i></b> .....	<b>257</b>



# ***A. Experimental***

## **A.1. Nanoparticles**

Nanoparticle samples are usually found as powder. So that they can be observed in the TEM, the preparation begins with the suspension of the particles in an organic solvent, namely hexane, with the aid of sonication. Once the sample is suspended in the solvent, one or two drops are deposited on a copper grid with a holey carbon film. The sample is allowed to dry and the particles remaining on the amorphous carbon are ready for observation. Nevertheless, any remaining organic components used either in sample growth or preparation are very beam sensitive, which means that they can evaporate and redeposit as amorphous carbon on the specimen. This redeposition of carbon increases its thickness and can make the sample unsuitable for observation. As for tomography, contamination is one of its main hinderings, as the sample is to remain many hours under the beam. If a sample contaminates at an excessive rate, the acquisition must be halted, as the images will fail to reconstruct the volume. In Figure A.1 the effects of contamination throughout a tilt series acquisition can be observed.

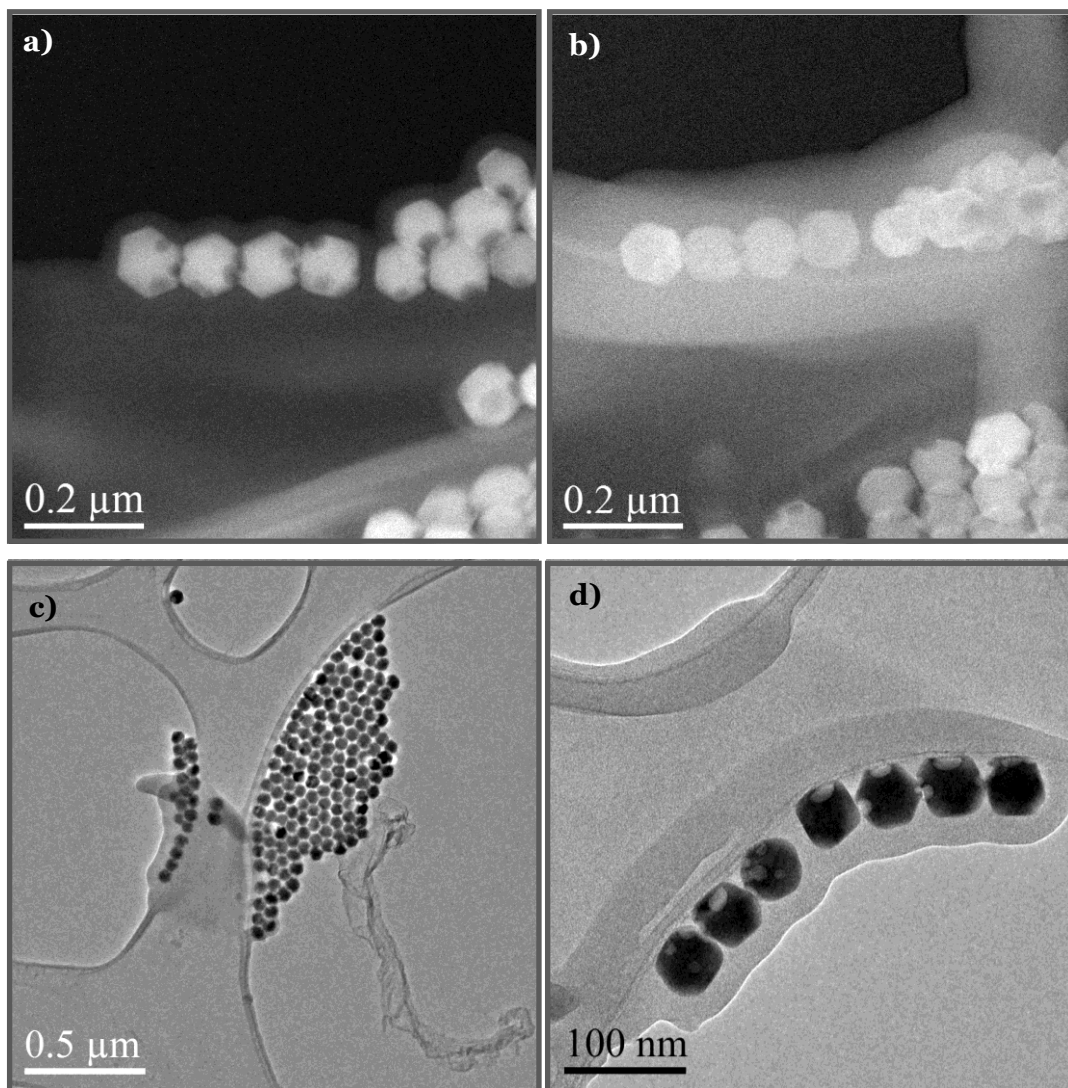


**Figure A.1:** HAADF STEM images of copper sulfide nanoparticles which were used for tomographic reconstruction. **a)** and **b)** HAADF STEM images of a nanoparticle cluster after a few degrees of tilt and halfway through a tilt series respectively. Contamination imposed abortion of the procedure. **c)** Image of the contamination on the particles in CTEM. **d)** CTEM image of a different nanoparticle cluster after acquisition of a full tilt series. In this case, contamination was not excessive as the sample was plasma cleaned for a longer time and the series was successfully acquired.

Therefore, there is a great need to use plasma cleaning, as it removes most of the organic remains, even if it also damages the holey carbon film. There must be a compromise in order to clean the sample without weakening too much the supporting film, lest it should collapse under the beam.

Nevertheless, the plasma, made of argon with 25% oxygen, can attack the sample, as was first noticed in the case of the copper sulfide particles in Figure A.1. Those particles observed in the SEM showed no holes on their surface, but the holes were present in all TEM observations. The generation of pores due to plasma cleaning was later demonstrated with the particles in Figure A.2. This effect, though uncommon, needs to be ruled out when one intends to use plasma cleaning, and is particularly unfortunate because most of the nanoparticles are synthesized using organic compounds and need the plasma cleaning to remove carbon, so they can be used for tomography experiments.

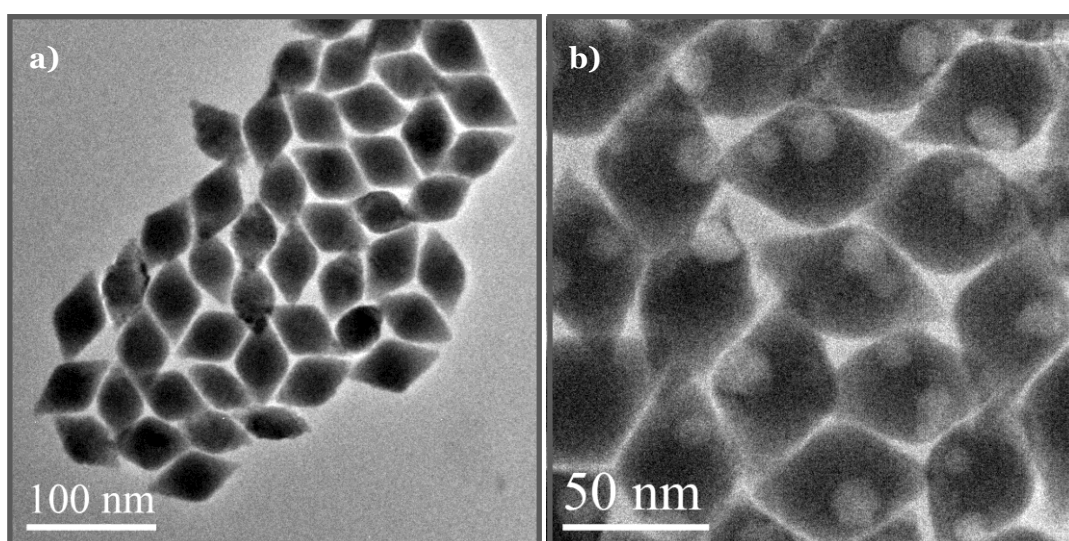


**Figure A.2:** CTEM images of copper sulfide nanoparticles a) before and b) after 10 seconds of plasma cleaning.

## A.2. Focused Ion Beam

In the case of bulk samples, they need to be thinned to electrotransparency (some tens of nanometers). In particular, for tomography, the sample has to be tilted to high angles in the transmission electron microscope, so we have chosen to prepare the samples in the shape of a nanopillar using the focused ion beam (FIB), in our case, a

FEI Strata 235 dual beam system. The ion beam is formed at an angle of  $52^\circ$  with respect to the electron beam, as shown in Figure A.3 (a), and it is used for either gas assisted deposition or sample milling. Compared to traditional sample grinding preparation, FIB has the advantage of preparing a localized area of the sample, which can be chosen by the user. At any rate, it is the only possible method for nanoneedle sample preparation.

The preparation of the sample starts by depositing a thin layer of gold, if it is non-conductive. This layer avoids any charging effects in the SEM. A SEM image of the sample considered in chapter 5 is presented in Figure A.3 (b), where the square section of the cobalt ferrite (CFO) islands in the bismuth ferrite (BFO) matrix can be observed.

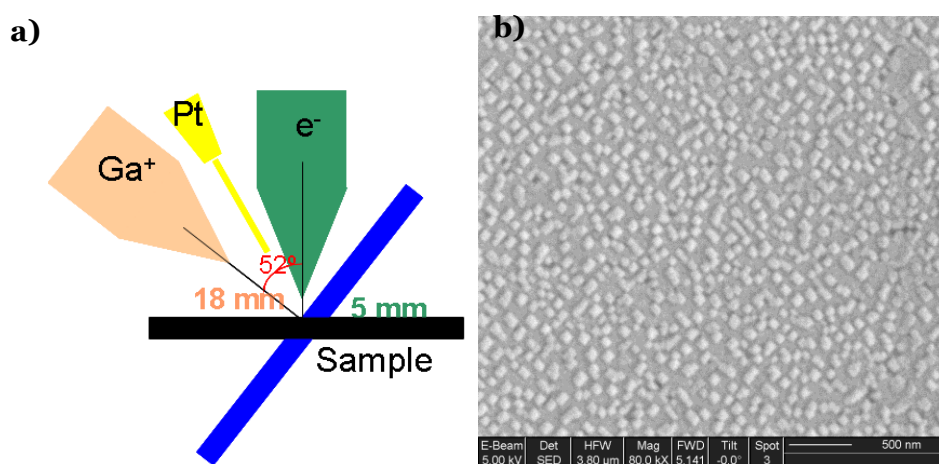


**Figure A.3:** **a)** Schematic of the relative position of the electron beam, the ion beam and the needle which injects a platinum organic precursor. **b)** SEM image of the CFO/BFO sample parallel to the growth direction. The lighter grey areas correspond to the CFO islands, and the darker gray areas to the BFO matrix. A cross section of the sample is shown in Figure 5.2.

Then, a specific area of the sample is chosen. The electrons first, and then the ions are used to grow a protecting layer of Pt on top of the chosen feature. This layer will protect the surface when the ions are used to mill around the area. A lamella from the sample is extracted and deposited on top of an Omniprobe copper grid, as shown in Figure A.4 (a). Then, this lamella is further milled to extract a single pillar, as the one in Figure A.4 (b). This pillar only has to be thinned with ions at lower accelerations in progressive steps to obtain a thin needle. The decrease in ion energy is necessary to reduce the formation of an amorphous layer at the surface of the needle.

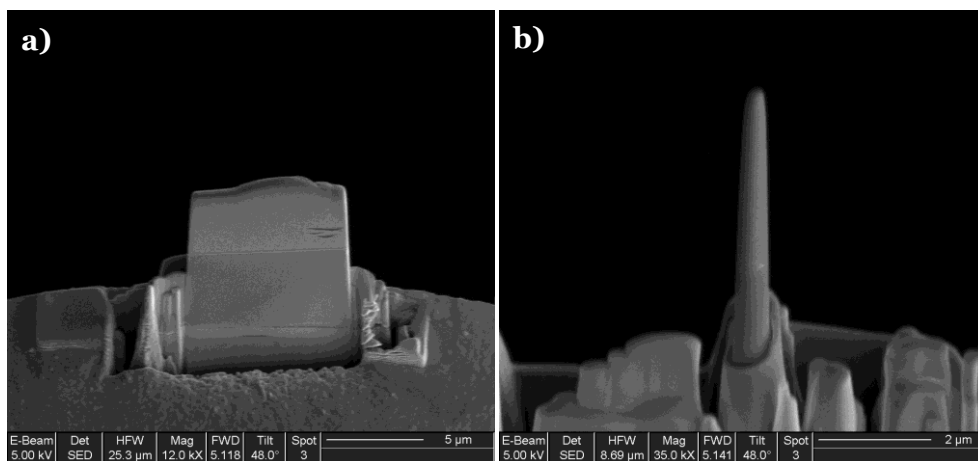


**Figure A.4:** **a)** Lamella of the sample attached to an Omniprobe grid. **b)** Pillar milled from the lamella, prior to the final thinning.



## ***B. Resum en català***

En el microscopi electrònic de transmissió (TEM), es poden obtenir imatges d'una mostra des de diferents angles i posteriorment reconstruir aquestes imatges en tres dimensions (3D). Per altra banda, les interaccions dels electrons del feix amb els electrons de la mostra poden ser analitzades mitjançant l'espectroscòpia de pèrdues d'energia dels electrons (EELS), obtenint així informació química de la mostra. L'objectiu d'aquesta tesi és la combinació de l'espectroscòpia EELS amb la tomografia electrònica per obtenir informació química en 3 dimensions a la nanoescala.

S'han explicat les bases de la tomografia electrònica, fent especial atenció als mètodes de reconstrucció i a als requisits que ha de satisfer un senyal per poder ser reconstruït en tres dimensions. Com que la tomografia electrònica ha estat utilitzada al llarg de tota aquesta tesi, el procediment de la reconstrucció ha estat il·lustrat amb una mostra de nanocubs d'òxid de ferro. Posteriorment, s'ha aplicat la tomografia electrònica amb detector anular de camp fosc d'alt angle (HAADF) a una sèrie de nanopartícules de  $\text{Cu}_2\text{O}$  per tal de descriure'n la forma. Amb una de les mostres ha estat possible correlacionar l'estructura octaèdrica amb l'orientació cristal·logràfica de l'òxid cuprós gràcies a la difracció d'electrons.

També s'ha explicat la física en què es basa l'EELS, fent especial atenció als llindars d'altres pèrdues d'energia. A continuació, s'ha mostrat l'augment del senyal obtingut amb precessió electrònica al TEM quan la mostra es troba en condicions d'eix de zona. Quan s'observa una mostra en condicions d'eix de zona, una situació habitual quan s'observen interfícies o quan es treballa amb microscopis amb aberració esfèrica corregida, l'acanalament dels electrons al llarg de les columnes atòmiques redueix el senyal. La precessió electrònica manté condicions efectives de dos feixos, cosa que evita aquest acanalament. Seguint amb les aplicacions d'EELS, s'ha explotat la possibilitat de caracteritzar els estats d'oxidació dels metalls de transició. Mitjançant un programa propi, escrit per a Digital Micrograph i anomenat Oxide Wizard, els estats d'oxidació

del manganès han estat correlacionats amb la forma del llinar, les característiques línies blanques. Amb mostres d'estat d'oxidació conegut, s'han realitzat gràfiques de calibratge, per a posteriorment, caracteritzar una mostra d'estat d'oxidació desconegut. S'ha estudiat una mostra, consistent en una estructura de nucli d'òxid de ferro i capa discontinua d'òxid de manganès. S'ha trobat que la capa està dividida en dues zones, una capa més superficial de MnO i una zona més profunda de  $Mn_3O_4$ .

Una vegada la tomografia electrònica i l'espectroscòpia de pèrdues d'energia dels electrons han estat explicades, i el seu potencial exemplificat, hem anat un pas més enllà per demostrar la possibilitat de combinar les dues tècniques. El material triat han estat partícules mesoporoses de  $in\ Co_3O_4$  crescudes com a rèpliques en motlles de sílice, i on posteriorment s'hi ha crescut  $Fe_xCo_{(3-x)}O_4$ . Primerament, les mostres s'han caracteritzat amb tomografia HAADF i EELS per separat. Ambdues tècniques han mostrat com el creixement de l'òxid mixt arriba a un punt de saturació, a partir del qual no és possible créixer més material dins de la mostra. Tanmateix, la informació d'EELS està limitada a mapes bidimensionals, mentre podem recuperar la informació estructural en tres dimensions. És per això que volem combinar l'EELS i la tomografia per reconstruir informació química en 3D. En un primer experiment, s'ha adquirit una sèrie d'espectres imatge(SI) d'EELS a diferents angles de gir. Per evitar de malmetre la mostra, hem adquirit els espectres a 80 kV de tensió d'acceleració i baixos temps d'adquisició. Aleshores, per tal de tractar la gran quantitat de soroll present als espectres, s'han utilitzat eines d'anàlisi multivariable per extraure la informació rellevant. L'anàlisi de components principals (PCA) s'ha utilitzat per separar el soroll del senyal. Si es mantenen les components principals amb major variància es pot desestimar el soroll. Després d'aquest tractament, s'ha integrat el senyal sota els llinars d'EELS un cop extret el fons. Aquest senyal integrat és equivalent al del TEM filtrat en energia (EFTEM) amb el mètode de les tres finestres, però, a diferència de l'EFTEM, les EELS-SI retenen tota la informació de l'espectre, que pot ser analitzada posteriorment. Pel que fa als requisits que ha de complir el senyal per tal d'esser reconstruït, aquest senyal integrat pateix dels efectes del gruix de la mostra perquè els electrons sofreixen múltiples xocs inelàstics a les zones més gruixudes. Aquest senyal absolut, aleshores, ha estat quantificat per tal d'eliminar la informació del gruix i reconstruït en 3D. Aquest mètode és vàlid mentre la mostra sigui convexa i només mostra informació sobre forma de la distribució dels elements a la mostra. Posteriorment, a les dades sense soroll, s'hi ha aplicat anàlisi de components independents (ICA), que dóna components interpretables físicament. D'aquest anàlisi, s'han extret components relacionats amb l'òxid de ferro, l'òxid de cobalt i el gruix de la mostra i s'han reconstruït. Els senyals d'òxid de cobalt i d'òxid de ferro també

incompleixen els requeriments de projecció a les zones més gruixudes. Tanmateix, el senyal de gruix reconstrueix el volum correctament. Per últim, s'han combinat el senyal de gruix amb les quantificacions elementals per tal d'obtenir un nou senyal amb informació química i de gruix que compleix el requeriment de projecció. Aquest senyal ha estat reconstruït correctament, donant la distribució espacial dels elements.

Una vegada s'han demostrat les capacitats de l'anàlisi multivariable aplicat a la tomografia EELS, s'ha dissenyat un segon experiment per reconstruir una mostra mesoporosa amb senyal d'EELS amb prou resolució espacial per resoldre l'estructura del porus. En aquest experiment, s'ha reduït el nombre d'imatges per permetre un augment en el temps d'exposició dels espectres. Tanmateix, el PCA encara ha estat necessari per reduir el soroll. En aquest cas, s'han extret de l'espectre quatre senyals que han estat reconstruïts en 3D: les intensitats integrades dels llinars de l'oxigen, el ferro i el cobalt, i el senyal de fons integrat just abans del llinar de l'oxigen. Entre tots, el senyal de l'oxigen ha estat amb el que s'ha obtingut una pitjor resolució espacial. Amb la resta de senyals, l'estructura porosa es manté a la reconstrucció. En aquestes reconstruccions, s'ha pogut observar que el senyal de ferro envolta el de cobalt als porus.

Un cop demostrat que l'anàlisi multivariable permet la reconstrucció tridimensional d'informació extreta d'imatges EELS a baixos voltatges i baixos temps d'adquisició, els últims experiments s'han dissenyat per provar que és possible recuperar tot l'espectre EELS en tres dimensions, és a dir, tenir un conjunt de dades tetradimensional amb les tres dimensions de l'espai i un espectre complet per vòxel. En aquest cas, s'ha preparat una mostra de nanocompòsit en forma d'agulla mitjançant un feix focalitzat d'ions (FIB). Aquesta preparació proporciona l'avantatge de mantenir el gruix de la mostra constant durant tot el gir de l'experiment. La nanoagulla conté una illa de ferrita de cobalt envoltada de ferrita de bismut, tots dos materials crescuts sobre òxid de lantà alumini i òxid de lantà níquel.

En un primer experiment, s'han obtingut espectres només d'una fracció del nanocompòsit per tal de provar que la reconstrucció 3D fos possible. S'ha fet servir PCA per eliminar el soroll. S'ha pogut obtenir mapes d'intensitat d'oxigen, ferro i lantà per a cada angle de gir i s'ha pogut reconstruir. Aquesta informació s'ha utilitzat per reconstruir l'estructura, però un segon experiment cobrint tot el nanocompòsit amb un nombre més elevat d'espectres ha donat millor informació espectral. En aquest segon conjunt de dades s'ha aplicat separació lineal Bayesiana (BLU). D'aquest anàlisi, s'obté un sistema d'espectres propis amb les seves respectives distribucions espacials. D'aquesta manera, tot espectre pot ser recuperat com una combinació lineal d'espectres

propis, amb pesos que s'extreuen de les distribucions espacials. Com que els espectres propis són directament interpretables físicament, els mapes de pesos es poden considerar proporcionals al gruix  $i$  a una característica de la mostra  $i$ , per tant, reconstruir en 3D. Aleshores, és possible recuperar l'espectre corresponent a cada unitat d'espai com la combinació dels espectres propis amb els pesos corresponents a aquestes distribucions reconstruïdes en 3D. Els espectres recuperats corresponen a la contribució de cada unitat de volum als espectres projectats. Aquest nou tipus de dades permet extreure espectres de l'interior d'una mostra.

Finalment, doncs, s'ha pogut combinar amb èxit la tomografia electrònica i 'EELS per obtenir informació química en tres dimensions a la nanoescala.

# ***C. Scientific curriculum***

## **C.1.1. Academic training**

Materials Engineering, triple graduate in the following centers:

- ETSEIB (Technical School of Industrial Engineering of Barcelona), Polytechnic University of Catalonia, Barcelona (Spain), 2009
- EEIGM (European School of Materials Science Engineering), Lorraine National Polytechnic Institute, Nancy (France), 2008
- Universität des Saarlandes (Saarland University), Saarbrücken (Germany), 2009.

Master in Biomedical Engineering, University of Barcelona and Polytechnic University of Catalonia, 2011

## **C.1.2. Professional experience**

February 2010-October 2011: LENS (Laboratory of Electron Naoscopies) research assistant. Electronics Department, University of Barcelona

October 2011 to date: Scientific and Technical Centers of the University of Barcelona (CCiT-UB). TEM research assistant in materials and biomedical applications.

### C.1.3. Journal Publications

1. J.M. Rebled, L. Yedra, S. Estrade, J. Portillo, F. Peiro, A new approach for 3D reconstruction from bright field TEM imaging: Beam precession assisted electron tomography, *Ultramicroscopy*. 111 (2011) 1504-1511.
2. S. Estrade, L. Yedra, A. Lopez-Ortega, M. Estrader, G. Salazar-Alvarez, M.D. Baro, J. Nogues, F. Peiro, Distinguishing the core from the shell in MnOx/MnOy and FeOx/MnOx core/shell nanoparticles through quantitative electron energy loss spectroscopy (EELS) analysis, *Micron*. 43 (2012) 30-36.
3. S. Estrade, J. Portillo, L. Yedra, J. Manuel Rebled, F. Peiro, EELS signal enhancement by means of beam precession in the TEM, *Ultramicroscopy*. 116 (2012) 135-137.
4. L. Yedra, A. Eljarrat, R. Arenal, E. Pellicer, M. Cabo, A. Lopez-Ortega, M. Estrader, J. Sort, M. Dolors Baro, S. Estrade, F. Peiro, EEL spectroscopic tomography: Towards a new dimension in nanomaterials analysis, *Ultramicroscopy*. 122 (2012) 12-18.
5. L. Almar, B. Coldeforns, L. Yedra, S. Estrade, F. Peiro, A. Morata, T. Andreua, A. Tarancon, High-temperature long-term stable ordered mesoporous Ni-CGO as an anode for solid oxide fuel cells, *Journal of Materials Chemistry a*. 1 (2013) 4531-4538.
6. J.M. Kiat, C. Bogicevic, P. Gemeiner, A. Al-Zein, F. Karolak, N. Guiblin, F. Porcher, B. Hehlen, L. Yedra, S. Estrade, F. Peiro, R. Haumont, Structural investigation of strontium titanate nanoparticles and the core-shell model, *Physical Review B*. 87 (2013) 024106.
7. C. Martinez-Boubeta, K. Simeonidis, A. Makridis, M. Angelakeris, O. Iglesias, P. Guardia, A. Cabot, L. Yedra, S. Estrade, F. Peiro, Z. Saghi, P.A. Midgley, I. Conde-Leboran, D. Serantes, D. Baldomir, Learning from Nature to Improve the Heat Generation of Iron-Oxide Nanoparticles for Magnetic Hyperthermia Applications, *Scientific Reports*. 3 (2013) 1652.
8. Pellicer, E.; Cabo, M.; Lopez-Ortega, A.; Estrader, M.; Yedra, L.; Estrade, S.; Peiro, F.; Saghi, Z.; Midgley, P.; Rossinyol, E.; Golosovsky, I. V.; Mayoral, A.; Prades, J. D.; Surinach, S.; Baro, M. D.; Sort, J.; Nogues, J, Controlled 3D-coating of the

pores of highly ordered mesoporous antiferromagnetic  $\text{Co}_3\text{O}_4$  replicas with ferrimagnetic  $\text{Fe}_x\text{Co}_{3-x}\text{O}_4$  nanolayers, *Nanoscale* 12 (2013), 5561-5567.

#### **C.1.4. Patents**

Estrade, S.; Portillo, J.; Peiro, F.; Rebled, J.M.; Yedra, L.; Nicolopoulos, S.; Kim, S.; Weiss, J.K.; Method and system for improving characteristic peak signals in analytical electron microscopy; **Patent number:** 1559 / 2642279; **First priority country:** European Union; **Date of priority:** 2012 **Main institution:** EPAO - European Patent Office.

#### **C.1.5. Research stages abroad**

1. Stage at High Resolution Electron Microscopy (HREM) group, Dept. of Material Sciences and Metallurgy, Cambridge (United Kingdom), 3 months (2010)
2. Stage at Appfive Inc. Tempe (AZ, United States), 6 weeks 2012

#### **C.1.6. Attendance to TEM schools**

1. Workshop on Aberration Corrected STEM, 3 – 5 June 2010 Warrington (United Kingdom), SuperSTEM
2. Electron Crystallography School – New Methods and Applications, 16 – 20 June 2012, Stockholm (Sweden), University of Stockholm.
3. 15th Ad Hoc Workshop on Jana2006 Electron diffraction, 6 – 7 December 2012, Prague (Czech Republic), Institute of Physics.

#### **C.1.7. Conference contributions**

1. Authors: Rebled, J.M.; Yedra, L.; Portillo, J.; Estradé, S.; Peiró, F.; Title: Combination of Electron Tomography and Electron Beam Precession applied to Sn precipitates in Al matrix; Kind of participation: Presentation of communication; Conference: 17th International Microscopy Conference; Rio de Janeiro (Brasil) 2010.
2. Authors: Yedra, L.; Estradé, S.; Pellicer, E.; Cabo, M.; López-Ortega, A.; Estrader, M.; Saghi, Z.; Midgley, P.; Rossinyol, E.; Golosovsky, I.V.; Prades, J.D.; Suriñach, S.; Baró, M.D.; Sort, J.; Nogués, J.; Peiro, F.; Title: Tomografía electrónica de

- materiales mesoporosos; Kind of participation: Presentation of communication; Conference: 2nd Workshop of IMAGINE, meeting of the Consolider Project CSD2009-00013; Madrid (Spain) 2010.
3. Authors: Rebled, J.M.; Yedra, L.; Portillo, J.; Estradé, S.; Peiró, F.; Title: Combination of Electron Tomography and Electron Beam Precession applied to Sn precipitates in Al matrix; Kind of participation: Poster; Conference: 2<sup>a</sup> Jornada del Instituto de Nanociencia y Nanotecnología In2UB Col·legi Oficial de Metges de Barcelona, Barcelona (Spain) 2010.
  4. Authors: Yedra, L.; Estradé, S.; Peiró, F.; Title: Development of a new Software application for oxidation state quantification in manganites; Kind of participation: Presentation of communication; Conference: Journées EELS 2011; Les Diablerets (Switzerland) 2011.
  5. Authors: Yedra, L.; Estrade, S.; Peiro, F.; Title: Manganitas: Development of a new application to quantify oxidation state in Manganites; Kind of participation: Presentation of communication; Conference: 3rd Workshop of IMAGINE, meeting of the Consolider Project CSD2009-00013; Barcelona (Spain) 2011.
  6. Authors: E. Pellicer; A. López-Ortega; M. Cabo, M. Estrader; J. Sort; L. Yedra; S. Estradé; S. Suriñach; Z. Saghi; P.A. Midgley; F. Peiró; M.D. Baró; J.Nogués; Title: Ferrimagnetic  $\text{FexCo}_{(3-x)}\text{O}_4$  nanostructures embedded in highly ordered antiferromagnetic  $\text{Co}_3\text{O}_4$  mesoporous templates; Kind of participation: Presentation of communication; Conference: E-MRS 2011 Fall meeting; Warsaw (Poland) 2011.
  7. Authors: Estradé, S.; Yedra, L.; Peiró, F.; Title: Oxide Wizard: development of a new software application for oxidation state quantification in transition metal oxides; Kind of participation: Presentation of communication; Conference: Microscopy at the Frontiers of Science 2011, 2nd Joint Congress of the Portuguese and Spanish Microscopy Societies; Aveiro (Portugal) 2011.
  8. Authors: Yedra, L.; Estradé, S.; Pellicer, E.; Cabo, M.; López-Ortega, A.; Estrader, M.; Nogués, J.; Baró, M.D.; Saghi, Z.; Midgley, P.A.; Peiró, F.; Title: HAADF STEM Tomography of ferromagnetic  $\text{FexCo}_{(3-x)}\text{O}_4$  nanostructures embedded in highly ordered antiferromagnetic  $\text{Co}_3\text{O}_4$  mesoporous templates; Kind of participation: Presentation of communication; Conference: Microscopy at the Frontiers of Science 2011, 2nd Joint Congress of the Portuguese and Spanish Microscopy Societies; Aveiro (Portugal) 2011.
  9. Authors: Rebled, J.M.; Yedra, L.; Estradé, S.; Portillo, J.; Peiró, F.; Title: Beam precession assisted electron tomography in bright field mode; Kind of participation: Presentation of communication; Conference: Microscopy at the Frontiers of Science

- 2011, 2nd Joint Congress of the Portuguese and Spanish Microscopy Societies; Aveiro (Portugal) 2011.
10. Authors: Yedra, L.; Estrade, S.; Pellicer, E.; Cabo, M.; Lopez-Ortega, A.; Estrader, M.; Nogues, J.; Baro, D.; Saghi, Z.; Midgley, P.A.; Peiro, F.; Title: HAADF STEM Tomography of Ferrimagnetic  $\text{FexCo}_{(3-x)}\text{O}_4$  Nanostructures Embedded in Highly Ordered Antiferromagnetic  $\text{Co}_3\text{O}_4$  Mesoporous Templates; Kind of participation: Poster; Conference: MRS Fall Meeting: 2011; Boston (United States) 2011
  11. Authors: López-Ortega, A.; Pellicer, E.; Cabo, M.; Estrader, M.; Sort, J.; Yedra, L.; Estradé, S.; Suriñach, S.; Peiró, F.; Baró, M.D.; Nogués, J.; Title: Ferrimagnetic  $\text{FexCo}_{(3-x)}\text{O}_4$  nanostructures embedded in highly ordered antiferromagnetic  $\text{Co}_3\text{O}_4$  mesoporous templates; Kind of participation: Presentation of communication; Conference: Villa Conference on Interactions Amongst Nanostructures; Las Vegas (United States) 2011.
  12. Authors: Yedra, Ll.; Estradé, S.; Pellicer, E.; Cabo, M.; López-Ortega, A.; Estrader, M.; Nogués, J.; Baró, M.D.; Saghi, Z.; Midgley, P.A.; Peiró, F.; Title: HAADF STEM Tomography of ferrimagnetic  $\text{FexCo}_{(3-x)}\text{O}_4$  nanostructures embedded in highly ordered antiferromagnetic  $\text{Co}_3\text{O}_4$  mesoporous templates; Kind of participation: Poster; Conference: 6th EEIGM International Conference on Advanced Materials Research; Nancy (France) 2011.
  13. Authors: Yedra, Ll.; Estradé, S.; Rebled, J.M.; Gačević, Ž.; Fernández-Garrido, S.; Calleja, E.; Heidari, H.; Goris, B.; Bals, S.; Peiró, F.; Title: Tomography of multilayered materials for optoelectronic applications; Kind of participation: Presentation of communication; Conference: 2011 MRS Meeting; Boston (United States) 2011
  14. Authors: Pellicer, E.; López-Ortega, A.; Cabo, M.; Estrader, M.; Rossinyol, E.; Sort, J.; Yedra, L.; Estradé, S.; Golosovsky, I.; Saghi, Z.; Midgley, P.A.; Prades, J.D.; Suriñach, S.; Peiró, F.; Baró, M.D.; Nogués, J.; Title: Ordered exchange coupled ferrimagnetic-antiferromagnetic mesoporous magnetic materials; Kind of participation: Invited conference; Conference: International Workshop on Nanostructured ceramics and other Nanomaterials; Delhi (India) 2012.
  15. Authors: Pellicer, E.; López-Ortega, A.; Cabo, M.; Estrader, M.; Rossinyol, E.; Sort, J.; Yedra, L.; Estradé, S.; Golosovsky, I.; Saghi, Z.; Midgley, P.A.; Prades, J.D.; Suriñach, S.; Peiró, F.; Baró, M.D.; Nogués, J.; Title: Tunable magnetic properties in ordered mesoporous magnetic materials; Kind of participation: Invited conference; Conference: 2012 MRS Spring Meeting; San Francisco (United States) 2012.

16. Authors: Pellicer, E.; López-Ortega, A.; Cabo, M.; Estrader, M.; Rossinyol, E.; Sort, J.; Yedra, L.; Estradé, S.; Golosovsky, I.; Saghi, Z.; Midgley, P.A.; Prades, J.D.; Suriñach, S.; Peiró, F.; Baró, M.D.; Nogués, J.; Title: Tunable magnetic properties in ordered mesoporous magnetic materials; Kind of participation: Invited conference; Conference: Workshop on Nanomagnetism and Spintronics; Donostia (SPAIN) 2012.
17. Authors: Yedra, L.; Eljarrat, A.; Arenal, R.; Cabo, M.; López-Ortega, A.; Estrader, M.; Pellicer, E.; Nogués, J.; Estradé, S.; Peiró, F.; Title: EEL spectroscopic tomography: towards a new dimension in nanomaterials analysis; Kind of participation: Presentation of communication; Conference: European Microscopy Congress; Manchester (United Kingdom) 2012.
18. Authors: Yedra, L.; Eljarrat, A.; Arenal, R.; Cabo, M.; López-Ortega, A.; Estrader, M.; Pellicer, E.; Baró, M.D.; Estradé, S.; Peiró, F.; Title: Accessing a new dimension of nanomaterials: EEL spectroscopic tomography; Kind of participation: Presentation of communication; Conference: Journées EELS (JEELS) 2012; Aix-les-Bains (France) 2012.
19. Authors: Yedra, L.; Eljarrat, A.; Arenal, R.; Cabo, M.; López-Ortega, A.; Estrader, M.; Pellicer, E.; Baró, M.D.; Estradé, S.; Peiró, F.; Title: Accessing new dimensions of nanomaterials: EEL spectroscopic tomography; Kind of participation: Presentation of communication; Conference: MRS Fall meeting 2012; Boston (United States) 2012.
20. Authors: Estradé, S.; Yedra, L.; Peiró, F.; Title: EELS analysis of SrMnO<sub>3</sub> crystallites; Kind of participation: Presentation of communication; Conference: 4th Workshop of IMAGINE, Materials at Sub-Ångstrom resolution, meeting of the Consolider Project CSD2009-00013; Madrid (Spain) 2012.
21. Authors: Estradé, S.; Portillo, J.; Yedra, L.; Rebled, J.M.; Peiró, F.; Title: EELS signal enhancement by means of beam precession in the TEM; Kind of participation: Presentation of communication; Conference: 5th Workshop of IMAGINE, Materials at Sub-Ångstrom resolution, meeting of the Consolider Project CSD2009-00013; Bilbao (Spain) 2012.
22. Authors: Estrade, S.; Rebled, J.M.; Yedra, L.; Eljarrat, A.; López-Conesa, L.; Peiró, F.; Title: Advanced Transmission Electron Microscopy Solutions for Nanoscience Problems; Kind of participation: Presentation of communication; Conference: 36th International Conference and Exposition on Advanced Ceramics and Composites (ICACC); Daytona Beach (United States) 2012.
23. Authors: Pellicer, E.; López-Ortega, A.; Cabo, M.; Estrader, M.; Rossinyol, E.; Sort, J.; Yedra, L.; Estradé, S.; Golosovsky, I.; Saghi, Z.; Midgley, P.A.; Prades, J.D.;

- Suriñach, S.; Peiró, F.; Baró, M.D.; Nogués, J.; Title: Tunable magnetic properties in ordered mesoporous magnetic materials; Kind of participation: Presentation of communication; Conference: NordicSpin 12, Third Nordic Workshop on Spintronics and Nanomagnetism; Varberg Kurort (Sweden) 2012
24. Authors: Estradé, S.; Portillo, J.; Yedra, L.; Rebled, J.M.; Peiró F.; Title: Enhancing EELS signal by means of beam precession; Kind of participation: Poster; Conference: European Microscopy Congress; Manchester (United Kingdom) 2012.
25. Authors: Estradé, S.; Portillo, J.; Yedra, L.; Rebled, J.M.; Peiró, F.; Title: EELS signal enhancement by means of beam precession in the TEM; Kind of participation: Presentation of communication; Conference: Journées EELS (JEELS) 2012; Aix-les-Bains (France) 2012.
26. Authors: Yedra, L.; Estradé S.; Pellicer, E.; Cabo M.; López-Ortega, A.; Estrader, M.; Nogués, J.; Baró, M.D.; Saghi Z.; Midgley, P.A.; Peiró, F.; Title: HAADF STEM tomography of ferrimagnetic  $\text{Fe}_x\text{Co}_{(3-x)}\text{O}_4$  nanostructures embedded in highly ordered antiferromagnetic  $\text{Co}_3\text{O}_4$  mesoporous templates; Kind of participation: Poster; Conference: Frontiers in electronic Materials; Aachen (Germany) 2012.
27. Authors: Yedra, L.; Eljarrat A; Arenal, R.; S.; Estradé, S.; Peiró, F.; Title: Electron energy loss spectroscopic tomography: the fourth dimension in nanomaterials analysis; Kind of participation: Presentation of communication; Conference: XXVIII Trobades Científiques de la Mediterrània: Òxids multifuncionals: de la captació de l'energia a la nanoelectrònica Maó (Spain) 2012
28. Authors: Yedra, L.; Xuriguera, E.; López-Ortega, A.; Estrader, M.; Varela, M.; Nogués, J.; Suriñach, S.; Baró, M.D.; Estradé, S.; Peiró, F.; Title: Oxide Wizard: Development of a New Software Application for Oxidation State Quantification in Transition Metal Oxides; Kind of participation: Poster; Conference: EDGE 2013; Sainte-Maxime (France) 2013.
29. Authors: Yedra, L.; Eljarrat, A.; Rebled, J.M.; Dix, N.; Sánchez, F.; Fontcuberta, F.; Estradé, S.; Peiró, F.; Title: Nanostructure tomography: an EELS approach to the 4th dimension; Kind of participation: Presentation of communication; Conference: EDGE 2013; Sainte-Maxime (France) 2013.
30. Authors: Estradé, S.; Yedra, L.; López-Ortega, A.; Estrader, M. ; Salazar-Alvarez, G.; Baró, M.D.; Nogués, J.; Peiró, F.; Title: Telling the core from the shell in tricky magnetic nanoparticles: EELS saves the day; Kind of participation: Presentation of communication; Conference: International Magnifyco (International Magnetic nanocontainers for combined hyperthermia and controlled drug release); Barcelona (Spain) 2013.

31. Authors: Almar, L.; Morata, A.; Coldeforns, B.; Yedra, L.; Estradé, S.; Peiro, F.; Andreu, T.; Tarancon, A.; Title: Thermal Stabilization of Ordered Mesoporous Metal Oxides: A Case Study as Electrodes for Solid Oxide Fuel Cells; Kind of participation: Presentation of communication; Conference: MRS Spring Meeting 2013, Symposium S: Nanostructured Metal Oxides for Advanced Applications; San Francisco (United States) 2013.
32. Authors: Yedra, L.; Eljarrat, A.; Arenal, R.; Pellicer, E.; Cabo, M.; López-Ortega, A.; Estrader, M.; Sort, J.; Baró M.D.; Estradé, S.; Peiró, F.; Title: EEL spectroscopic tomography: a new dimension to nanomaterials analysis; Kind of participation: Presentation of communication; Conference: 9th Spanish Conference on Electronic Devices, Valladolid (Spain) 2013.

### **C.1.8. Teaching**

1. Academic year 2011-2012:
  - a. Microscopy Techniques, Master in Nanoscience and Nanotechnology, University of Barcelona.
2. Academic year 2012-2013:
  - a. Microscopy Techniques, Master in Nanoscience and Nanotechnology, University of Barcelona.
  - b. Applied Electronics, Physics degree, University of Barcelona.
  - c. Laboratory fundamentals, Physics Degree, University of Barcelona.

### **C.1.9. Languages**

1. English: spoken (well), read (well) and written (well), Certificate of Advanced English, Cambridge ESOL
2. French: spoken (well), read (well) and written (well)
3. German: spoken (sufficient), read (sufficient) and written (sufficient), Deutsche Sprachprüfung für den Hochschulzugang 2.

Mother languages: Catalan and Spanish.